Alma Mater Studiorum - Università di Bologna

DOTTORATO DI RICERCA IN

ASTROFISICA

Ciclo 34

Settore Concorsuale: 02/C1 - ASTRONOMIA, ASTROFISICA, FISICA DELLA TERRA E DEI PIANETI

Settore Scientifico Disciplinare: FIS/05 - ASTRONOMIA E ASTROFISICA

MACROSCOPIC AND MICROSCOPIC ASPECTS OF PARTICLE ACCELERATION
BY COSMIC SHOCKS

Presentata da: Serena Banfi

Coordinatore Dottorato

Prof. Francesco Rosario Ferraro

Supervisore

Prof. Franco Vazza

Co-Supervisore

Prof. Lorenzo Sironi

Esame finale anno 2022

Abstract

Cosmic collisionless shocks are highly energetic phenomena in which different non-thermal processes take place. Above all, particle acceleration is arguably the most important, and observations of its signatures can be a powerful tool to constrain the local plasma and magnetic properties at the acceleration site. Within large-scale structures, the presence of cosmic rays can be revealed by means of different detection approaches, depending on the particle species: relativistic electrons can emit in radio via synchrotron radiation (which can be observed in radio relics), while energetic protons can interact with thermal protons of the intracluster medium and emit in the γ-ray band. Both electrons and protons in large-scale structures should in principle be accelerated by a kind of first order Fermi acceleration mechanism, known as diffusive shock acceleration: however, only evidence of cosmic-ray electrons has been detected so far in galaxy clusters, while no signatures of cosmic-ray proton acceleration have been reported. Connecting these two observational facts with a realistic view of shock formation and magnetic field evolution in cosmic structures is the main motivation of this Thesis' work. With a comprehensive analysis from 'macroscopic' to 'microscopic' scales, I address the missing γ-ray issue by means of advanced numerical simulations, in which extragalactic magnetic fields are evolved together with the dynamics of large-scale structures. In particular, I attempt to link the cosmic-ray acceleration efficiency of shocks in the cosmic web to the magnetic field topology, while also studying how different proposed scenarios for magnetogenesis can affect these properties. The primary factor at play is the shock obliquity, i.e. the angle between the shock propagation direction and the underlying magnetic field. In this work, I first determine the distribution of obliquity in large cosmological simulations as a function of the medium in which the shock takes place and identify two main categories of shocks, i.e. merger shocks typical of galaxy clusters and accretion shocks occurring in filaments. In the course of this analysis, I detect a pattern in the arrangement of the magnetic field around filaments and perform a quantitative study of the topological properties of the behavior of the magnetic field surrounding the components of the cosmic web. Finally, shocks in filaments are more closely investigated with new particle-in-cell simulations tailored to tackle this issue on much smaller scales, where the evolution of electrons and protons can be followed from first principles, and the actual acceleration efficiency by realistic shocks can be measured. The new insights obtained from these numerical simulations provide a useful tool for the correct interpretation of observations and to estimate the magnetic properties that can be inferred, e.g. from Faraday rotation measurements.

Contents

IV   Constraining cosmic web magnetic fields   114

8 Co-authored works   115

V   Thesis conclusions   120

9 Summary and conclusions   121

Part I

Introduction

1. The cosmic web

1.1 Structure formation

According to the Λ *cold dark matter* model, the recent Universe's evolution (for redshifts $z \gtrsim 0.6$) is dominated by dark energy ($\approx 68\%$ of the total energy density), responsible for its accelerated expansion, and dark matter ($\approx 27\%$), which drives the structure formation process; the remaining $\approx 5\%$ includes all forms of ordinary matter. In the *cold dark matter* scenario, inhomogeneities of the primordial density field were amplified by gravity in a 'bottom-up' scenario in which small-scale structures formed first and subsequently clustered into larger ones. Hierarchical clustering has led to the assembly of different structures, characterized by being either underdense or overdense to different extents, like voids, walls, filaments and halos. All of these elements constitute the so called *cosmic web*, a network of dark and baryonic matter, which links all kinds of structures in a distinctive, complex arrangement. The basics of the current understanding of how the cosmic web formed have been proposed by Bond et al. [1996], who combined the Zel'dovich approximation [Zel'dovich, 1970], according to which structures arise from the compression of matter along a preferential axis ('pancaking'), to the Press-Schechter formalism [Press and Schechter, 1974], which assumes that each object is formed by gravitational collapse of a density fluctuation in the primordial field: while the Zel'dovich pancaking successfully explains the anisotropy in the distribution of matter on largest scales following a linear regime, the Press-Schechter formalism is better suited for the non-linear phase of collapse, compatibly to a hierarchical clustering scenario. Following Bond's theory, matter distribution can be described by a global quadrupolar field which determines the local tidal shear at the density peaks and leads to the formation of the typical cluster-filament-cluster configuration at the base of the cosmic web's structure [Bond et al., 1996]. The formation of structure can be described by the set of equations including the *continuity equation* for mass conservation:

$$\frac{\partial \delta}{\partial t} + \frac{1}{a} \nabla \cdot (1 + \delta)\mathbf{v} = 0, \tag{1.1}$$

Euler's equation for gravitational and pressure forces:

$$\frac{\partial \mathbf{v}}{\partial t} + \frac{\dot{a}}{a}\mathbf{v} + \frac{1}{a}(\mathbf{v} \cdot \nabla)\mathbf{v} = -\frac{1}{a}\nabla \Phi, \tag{1.2}$$

and *Poisson-Newton's equation* for the gravitational potential:

$$\nabla^2 \Phi = 4\pi G \overline{\rho}_m(t) a(t)^2 \delta(\mathbf{r}, t), \tag{1.3}$$

where $\mathbf{r}$ is the comoving position, $\delta(\mathbf{r}, t) = \rho(\mathbf{r})/\rho_u - 1$ is the density fluctuation field with respect to the cosmic background total mass density ρ_u, $a(t)$ is the universe average expansion factor, $\mathbf{v}$ is the

peculiar velocity and $\Phi(\mathbf{r}, t)$ is the gravitational potential. At its early stages, time evolution of density perturbations $\delta(\mathbf{r}, \mathbf{t})$ can be condensed in the following linearized equation:

$$\frac{\partial^2 \delta}{\partial t^2} + 2\frac{\dot{a}}{a}\frac{\partial \delta}{\partial t} = \frac{3}{2}\Omega_{m0}H_0^2\frac{1}{a^3}\delta, \tag{1.4}$$

where H_0 is the Hubble constant and Ω_{m0} is the current (ordinary + dark) matter density parameter. Later stages of the gravitational clustering process are instead characterized by a non-linear growth phase where typical complex patters of the cosmic web begin to emerge [see Springel, 2005, and Figure 1.1].

1.2   Halos

When a positive density fluctuation becomes sufficiently overdense, it will accrete more and more matter until fully collapsing in a gravitationally bound object. When an approximately spherically symmetric density peak on $\sim$ Mpc scales enters the non-linear growth phase, it eventually reaches virial equilibrium, in which kinetic and gravitational forces are balanced, and a halo is formed.

Shape   Although a spherical collapse model is usually a reasonable approximation, halos are actually triaxial structures [Jing and Suto, 2000], meaning that the overdensity started collapsing along each axis at different times, namely the shortest axis collapses first, then the intermediate and eventually the longest one [Shen et al., 2006].

Mass distribution   By adopting the model of spherical collapse, we can approximately compute the number density n of dark matter halos as a function of their mass M and redshift z (*Press-Schechter model*, Press and Schechter 1974). According to this model, $n(M, z)$ is a decreasing function of mass, with an exponential decrease for large M: in particular, halos with $M \gtrsim 10^{15}\ M_\odot$ are very rare (with a frequency of approximately one in a 10^7 Mpc^3 volume, compatibly with the fact that the closest massive cluster, Coma, is about 100 Mpc away from us). The distribution of halos also depends on redshift: the minimum density contrast required for a collapse before a certain redshift increases with z proportionally to a growth factor, which is in turn dependent on the assumed cosmological model (larger for smaller Ω_m). More sophisticated mass functions can be derived considering the triaxiality of halos [Sheth and Tormen, 1999].

Density profile   As pertains to the internal halo structure, the radial mass profile can be inferred from numerical simulations. As a first approximation, we can describe a halo as the spherical region enclosed within the virial radius r_{100}, i.e. the distance from the halo center at which the average inner density is $\sim$ 100 times larger than the critical density

$$\rho_{\text{cr}} = \frac{3H^2}{8\pi G} \approx 8.5 \times 10^{-30}\ \text{g/cm}^3\ (\text{at } z = 0); \tag{1.5}$$

thus, we can also define the virial mass:

$$M_{100} = \frac{100 r_{100}^3 H^2}{G} \tag{1.6}$$

and the virial velocity, i.e. the circular velocity at the virial radius:

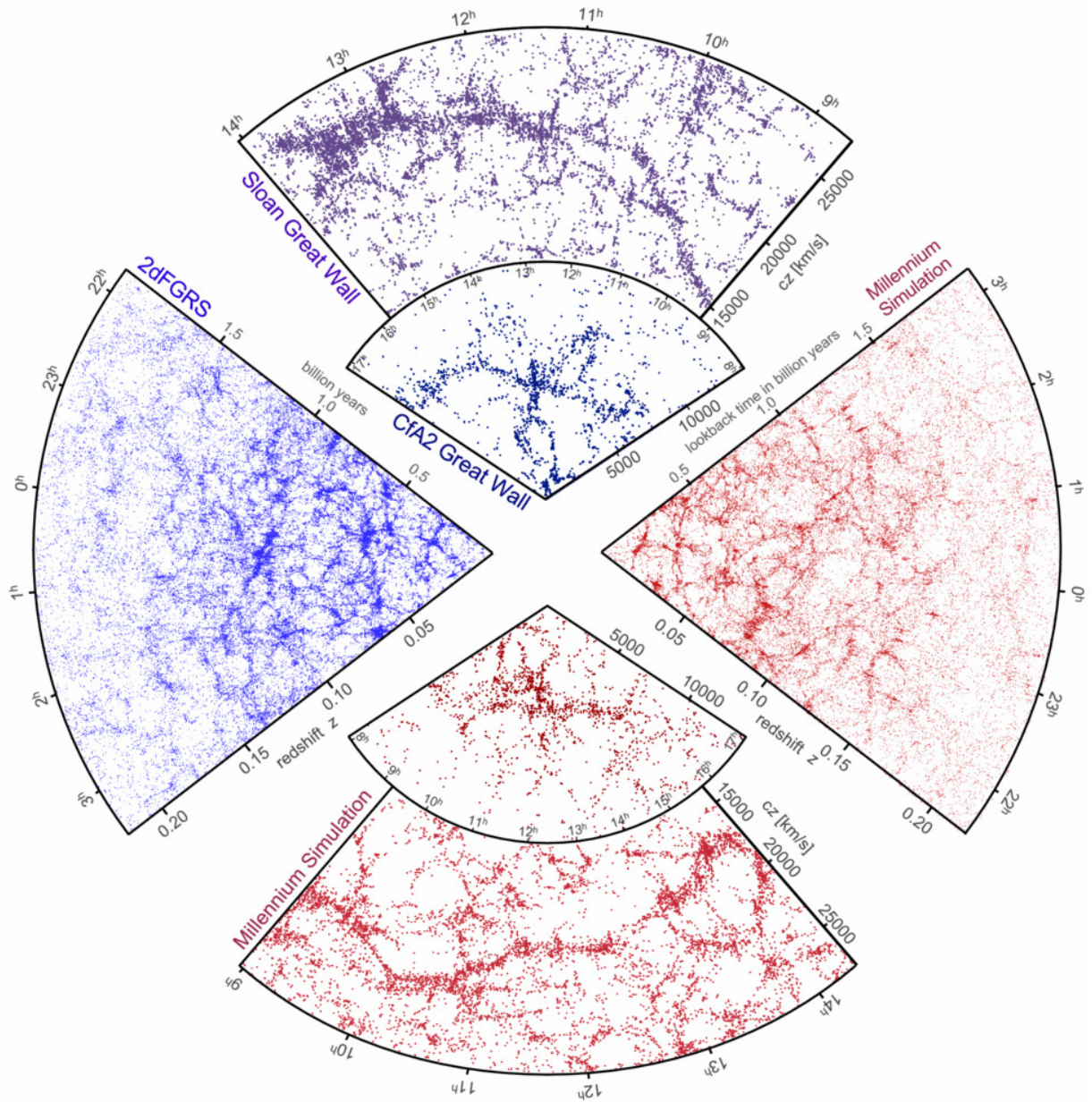$$v_{100} = \sqrt{\frac{GM}{r_{100}}}. \tag{1.7}$$

Figure 1.1: Galaxy distribution from spectroscopic redshift surveys and from mock catalogues constructed from cosmological simulations showing the typical filamentary structure of the cosmic web. *Credits:* Springel et al. [2006]

The typical dark matter density profile of halos averaged over spherical shells was proposed by Navarro et al. [1997] (*NFW-profile*), which is described by:

$$\rho_{DM}(r) = \rho_{DM,s} \left[\left(\frac{r}{r_s} \right) \left(1 + \frac{r}{r_s} \right)^2 \right]^{-1}, \tag{1.8}$$

where r_s and $\rho_{DM,s}$ are the characteristic scaling radius and density. We can define the *concentration index* of a halo as $c = r_{100}/r_s$.

Angular momentum   Halos acquire angular momentum from environmental tidal torques during the early stages of structure formation [Hoyle, 1949, Peebles, 1969], resulting in the misalignment of the inertial and tidal shear tensor. This model, named *tidal torque theory* [Doroshkevich, 1970, White, 1984], predicts an alignment between the angular momentum and the intermediate axis of the shear: in other words, this should imply that halos spin around an axis which is preferentially aligned to the direction of the wall and orthogonal to the filament. Numerical simulations [e.g. Porciani et al., 2002] have shown a good agreement with such prediction for high-mass halos, but an opposite correlation for low-mass ones. Codis et al. [2012] suggested a dynamical scenario that explains the opposed behavior of halo spins as a function of mass by taking into account that two main different processes lie behind mass acquisition, namely smooth accretion and mergers. During smooth accretion the halo mass grows in a steady process: if the halo is found within a filament, its angular momentum is built up parallel to the neighboring filament from vorticity transfer [Pichon et al., 2011]. Above a certain transition mass ($\sim 5 \times 10^{12} \, M_\odot$, e.g. Aragón-Calvo et al. [2007]), mergers dominate the acquisition of spin: drifting halos generally flow along the filament, leading to the spin orienting orthogonally to the filament. The spin acquired by halos is parameterized through the dimensionless *spin parameter*

$$\lambda = \frac{J|E|^{1/2}}{GM^{5/2}}, \tag{1.9}$$

where J, E and M are the total angular momentum, energy and mass of the halo. This parameter corresponds to the ratio of the rotational and total energy of the system, i.e. indicates the importance of angular momentum with respect to random motion.

1.2.1   Galaxy clusters

The baryons contained in dark matter halos eventually cool and condense, until galaxies are formed at the bottom of potential wells [White and Rees, 1978]. Halos hosting ~ 50 galaxies in a volume of a few Mpc^3 [Abell, 1958] are called a galaxy clusters (GCs), which are the largest gravitationally bound systems in the Universe and make up $\sim 12 - 16 \, \%$ of the cosmic mass. An undisturbed GC is expected to relax into hydrostatic equilibrium on timescales of the order of the sound crossing time [Sarazin, 2002]:

$$t_s = \frac{D}{C_s} \approx 6.6 \times 10^8 \text{yr} \left(\frac{T}{10^8 \, K} \right)^{-1/2} \left(\frac{D}{1 \, Mpc} \right), \tag{1.10}$$

where D is the diameter of the cluster and c_s in the sound speed. This time interval is much shorter than the cluster's age (of the order of the Hubble time), implying that the gas should be close to hydrostatic equilibrium. Assuming that thermal conduction is efficient, we can consider the gas in a GC to be isothermal: this, in addition to the assumption of an isotropic gaussian velocity distribution for galaxies,

allows to apply the so called β-model to the gas density distribution [Cavaliere and Fusco-Femiano, 1976]:

$$\rho_{\text{gas}}(r) = \rho_{\text{gas},0} \left[1 + \left(\frac{r}{r_c} \right)^2 \right]^{-3\beta/2}, \tag{1.11}$$

where ρ_0 is the central gas density, r is the radial coordinate and r_c is the core radius. Knowing the gas density distribution, the gas mass M_{gas} can be inferred by integrating inside a certain radius. The condition of hydrostatic equilibrium allows to estimate the total gravitational mass

$$M(r) = -\frac{r^2}{G\rho(r)} \frac{dP}{dr}. \tag{1.12}$$

The total mass of galaxies M_{gal} can be obtained from optical observations, knowing a priori the mass-to-light relation in GC [Proctor et al., 2015, Shan et al., 2015], such that also the dark matter mass can be calculated:

$$M_{\text{DM}}(r) = M(r) - M_{\text{gas}}(r) - M_{\text{gal}}(r). \tag{1.13}$$

On average, the percentages of these components are $\approx 5\,\%$, $\approx 15\,\%$ and $\approx 80\,\%$ for galaxies, gas and dark matter, respectively.

Intracluster medium

The gas component of GCs is also called intracluster medium (ICM), which is hot ($T \sim 10^7 - 10^8$ K), rarefied ($n \sim 10^{-4} - 10^{-3}$ cm^{-3}) plasma composed of fully ionized hydrogen, with a small percentage of helium and heavy elements [e.g. Sarazin and White, 1987, Ettori et al., 2009]. The ICM is typically permeated by $\sim \mu$G magnetic fields on kpc scales: the level of magnetization can be parametrized by the plasma β-parameter $\beta_P = 8\pi n k_B (T_i + T_e)/B^2$, which is usually of the order of ~ 100, where T_i and T_e are respectively the ion and electron temperature. The ICM is mostly optically thin, i.e. the mean free path of photons is large enough to allow them to escape once emitted. Numerical simulations [e.g. Ryu et al., 2008, Vazza et al., 2011a, Vallés-Pérez et al., 2021] show that turbulence is widespread in the ICM: the small-scale components of turbulence can generate dynamo action, which effectively amplify the weak magnetic field by stretching the field lines [e.g. Cho, 2014].

Thermal processes in galaxy clusters

At temperatures higher than $\sim 10^7$ K, optically thin thermal *bremsstrahlung* is the main process responsible for ICM cooling [see Sarazin, 1986, Böhringer and Werner, 2010, for reviews], which can be observed as X-ray radiation. The typical luminosity of a GC is $L_X \sim 10^{43} - 10^{45}$ erg s^{-1}. This process, also known as *free-free* radiation, is produced by the de-acceleration of electrons in the ion's Coulomb field, so its emissivity depends on electron density n_e and plasma electron temperature T_e as

$$\epsilon_\nu \propto n_e^2 T_e^{-1/2} \exp(-h\nu/k_B T_e), \tag{1.14}$$

where h is the Planck constant, ν is the radiation frequency and k_B is the Boltzmann constant. From the spectral analysis of X-ray emission, it is possible to estimate the gas temperature, density, and eventually mass: by projecting the β-model profile on the sky plane, the X-ray surface brightness distribution is found as:

$$S_X(r) = S_{X0} \left[1 + \frac{r}{r_c} \right]^{-3\beta + 0.5}, \tag{1.15}$$

11
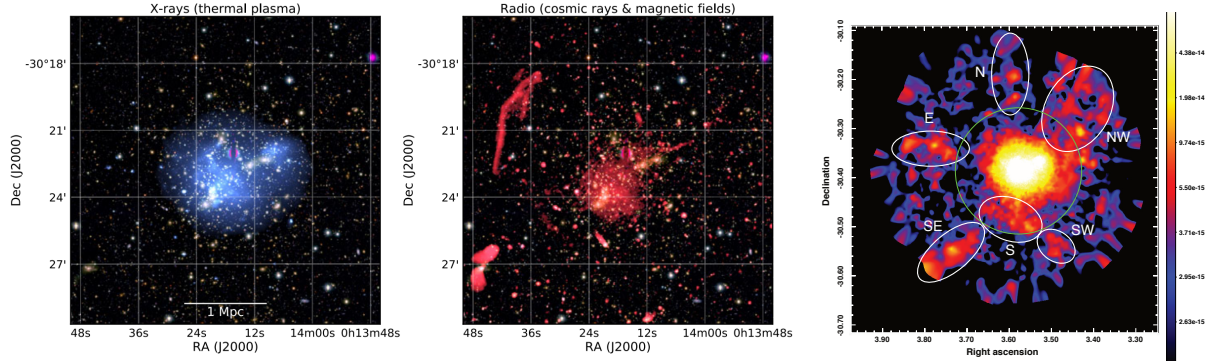
Figure 1.2: Galaxy cluster Abell 2744. *Left panel:* X-ray emission from thermal ICM (Chandra $0.5 - 2.0$ keV band). *Central panel:* $1 - 4$ GHz VLA image tracing cosmic rays and magnetic fields. *Right panel:* hot gas in the GC and the surrounding filaments (XMM-Newton/EPIC $0.5 - 1.2$ keV band). *Credits*: Pearce et al. [2017], van Weeren et al. [2019], Eckert et al. [2015].

with S_{X0} X-ray surface brightness at the center of the cluster. Based on the gas properties of GC, we can distinguish between *cool-core* clusters and *non cool-core* clusters [Molendi and Pizzolato, 2001, Sanderson et al., 2009]. In the first ones, strongly peaked X-ray emissitvity in relaxed systems can cause efficient cooling in the densest regions and determine a drop in the temperature profile of the GC. If gas cools due to X-ray emission, hydrostatic equilibrium cannot be maintained on timescales of

$$t_{\text{cool}} = 8.5 \times 10^{10} \text{ yr} \left(\frac{n_{\text{e}}}{10^{-3} \text{ cm}^{-3}} \right)^{-1} \left(\frac{T}{10^8 \text{ K}} \right)^{1/2}, \qquad (1.16)$$

which is typically longer than the Hubble time, but not in the densest regions undergoing rapid gas cooling. In order to re-establish pressure equilibrium, gas needs to flow inwards: so called *cooling flows*, however, have only been predicted theoretically, while no X-ray observation seems to validate this phenomenon. As a consequence, there has to be some alternative heating source, like a central active galactic nucleus (AGN) [Peterson and Fabian, 2006, McNamara and Nulsen, 2007]. On the other hand, non cool-core clusters are typical of disturbed systems with shallower X-ray emissitivity [Leccardi et al., 2010].

Non-thermal processes in galaxy clusters

The occurrence of non-thermal processes in GC, such as particle acceleration (see Section 2.3) or turbulence, is inferred by radio observations of diffuse synchrotron emission [see Ferrari et al., 2008, van Weeren et al., 2019, for reviews]. Based on the location and morphology of radio-emitting regions, three different kinds of diffuse emissions can be identified: halos, mini-halos and relics [Feretti and Giovannini, 1996]. Radio halos are circular regions of $\sim$ Mpc size found in the center of massive, dynamically disturbed galaxy clusters with no optical counterpart; mini-halos are smaller and are located in relaxed cool core clusters; radio relics are extended sources usually found in the cluster's periphery which show strong polarization. More detailed information about the observational signatures of these processes will be provided in Section 2.4. Figure 1.2 shows an example of galaxy cluster detection, including both thermal and non-thermal observables.

1.3 Filaments, sheets and voids

Analogously to halos, whose shape is regulated by the subsequent collapse of matter along the three axes, filaments and sheets are the outcome of an overdensity collapsing along two or one axis, respectively. The low-density regions enclosed by filaments and sheets are known as cosmic voids. They have typical diameters of $10 - 100$ Mpc and contain very few or no galaxies and up to $\sim 10 - 15\,\%$ of the total cosmic mass.

Filaments are elongated structures, up to ~ 100 Mpc long, connecting halos which are otherwise surrounded by voids. Simulations suggest that they are filled by the so called warm-hot intergalactic medium, WHIM, characterized by $T \sim 10^5 - 10^7$ K temperatures and $n_e \sim 10^{-6} - 10^{-4}$ cm^{-3} densities [Cen and Ostriker, 1999, Davé et al., 2001]. They contain up to $\sim 50\,\%$ of the entire cosmic mass [Gheller et al., 2015]. Filaments are likely to be permeated by magnetic fields and to host cosmological shock waves as a consequence of the continuous accretion of cold gas (see Section 2.2). There has been only a limited amount of direct observations of filaments in the soft X-ray band [e.g. Werner et al., 2008] and in the radio band [e.g. Farnsworth et al., 2013], as well as by staking of images in the low-frequency radio [Vernstrom et al., 2021] and in the X-ray [Tanimura et al., 2020] band. The Sunyaev-Zel'dovich effect, caused by the inverse Compton scattering of cosmic microwave background (CMB) photons with free electrons in the WHIM, has also been used to probe filaments connecting GCs [e.g. Planck Collaboration et al., 2013, Tanimura et al., 2019a, de Graaff et al., 2019]. We expect these structures to be surrounded by strong accretion shocks [e.g. Ryu et al., 2003], which makes them of great interest in view of their possible detection by, for instance, the Square Kilometre Array, as will be further discussed in Section 2.4.

2. Shocks and magnetic fields in the cosmic web

2.1   Collisionless plasmas

Particle motions in a collisionless plasma are regulated by long-range electromagnetic interactions. For a typical ICM environment [Caprioli et al., 2019],

$$\frac{\lambda_C}{\lambda_D} \sim 10^3, \tag{2.1}$$

where λ_C is the particles' mean free path against Coulomb collisions and λ_D is the Debye length, defined as the scale over which electric fields are screened out by a redistribution of the electrons. In the absence of external fields, the non-relativistic equation of motion of a particle of mass m and charge q is subjected to the electromagnetic fields produced by the other particles according to

$$m\frac{d\mathbf{u}}{dt} = q\left(\mathbf{E} + \frac{\mathbf{u}}{c} \times \mathbf{B}\right). \tag{2.2}$$

If a particle has an initial velocity $v_\perp$ perpendicular to a uniform magnetic field $\mathbf{B}$, it will move in a circle lying in the plane transverse to $\mathbf{B}$ with *cyclotron frequency* (or *gyrofrequency*)

$$\omega_c = \frac{|q|B}{mc}, \tag{2.3}$$

whose corresponding radius is called *Larmor radius* or *gyroradius*:

$$r_g = \frac{mcv_\perp}{|q|B}. \tag{2.4}$$

As a consequence, for a hydrogen plasma, electron gyroradius is ~ 2000 times smaller than ion gyroradius (and therefore electron gyrofrequency is ~ 40 times larger than ion gyrofrequency). If the initial velocity has also a component parallel to $\mathbf{B}$, the particle will at the same time perform a translation unaffected by the magnetic field: therefore, the overall orbit is given by the combination of the circular motion around a *guiding center* and the translatory motion of the guiding center. In the case there is a uniform force $\mathbf{F}$ acting on the particle perpendicularly to the uniform magnetic field, the trajectory will be modified by a drift of the guiding center in a direction perpendicular to both $\mathbf{B}$ and $\mathbf{F}$:

$$\mathbf{v}_{\text{drift}} = \frac{c}{q}\frac{\mathbf{F} \times \mathbf{B}}{B^2}. \tag{2.5}$$

For example, the force $\mathbf{F}$ at issue can be generated by the presence of a magnetic field gradient. The level of magnetization of a plasma can be parametrized by the plasma parameter β_P, as defined in Section 1.2.1.

2.1.1 Plasma waves and instabilities

Waves in plasmas can be classified as electromagnetic or electrostatic, depending on whether there is an oscillating magnetic field. Waves can also be distinguished by the oscillating species, i.e. electrons or ions. If a plasma is perturbed by the displacement of electrons from their equilibrium distribution, electric fields build up in order to pull them back to their original position and restore neutrality: this causes electrons to overshoot and oscillate around their equilibrium points (*Langmuir waves*). We define the frequency of electron density oscillations as the electron *plasma frequency*:

$$\omega_{p,e} = \sqrt{\frac{4\pi n_e e^2}{m_e}}, \tag{2.6}$$

where n_e is the particle number density. Analogously, we can obtain the same quantity $\omega_{p,i}$ for ions by substituting their mass and charge. We can now define the *plasma skin depth* as $\lambda_s = c/\omega_p$. In a magnetized fluid, magnetohydrodynamics (MHD) ion waves can be generated: based on the relative orientation of the wave vector and the magnetic field, they are called either *Alfvén waves* (transverse) or *magnetosonic waves* (longitudinal). If perturbations in a plasma grow, instead of oscillating, then an instability is generated. For the purpose of this thesis, I mention the ones that can form in the context of cosmic shocks (see Section 2.2):

- *Buneman instability* [Buneman, 1958] is the result of the interaction between cold incoming electrons and reflected ions and it generates electrostatic waves at the edge of the shock;

- *Weibel instability* [e.g. Matsumoto et al., 2015] is driven by the interaction of the incoming and reflected ions: typical elongated structures are developed during this phenomenon, which allow magnetic reconnection sites to form even in unmagnetized plasmas (see Section 2.3.2);

- *electron firehose instability* [e.g. Guo et al., 2014a] is driven by an anisotropy in the electron velocity distribution and generates waves ahead of the shock.

These make up just a small fraction of the multitude of instabilities which can develop more generally in a plasma.

2.2 Cosmological shocks

Shocks occurring on the large scales of the cosmic web are ubiquitous processes which manifest as discontinuities in the gas' thermodynamical variables and convert gravitational into (non-)thermal energy thanks to the supersonic infall of gas on structures and hierarchical clustering [e.g. Quilis et al., 1998a]: in particular, they contribute to the thermalization of gas, whose emission can potentially be observed from Earth, the amplification of magnetic fields and the acceleration of cosmic rays (see Section 2.3). Shocks are believed to first have arisen at the time of reionization ($z \sim 6-14$) [Bykov et al., 2008], when strong density inhomogeneities initially formed. Shocks launched by cosmic matter accretion events are very energetic, and their strength can be quantified with respect to the environment in which they take place by their Mach numbers. The *sonic Mach number*[1] is defined as the shock speed divided by the sound speed on the unperturbed gas:

$$M_s = \frac{v_{sh}}{c_s}, \tag{2.7}$$

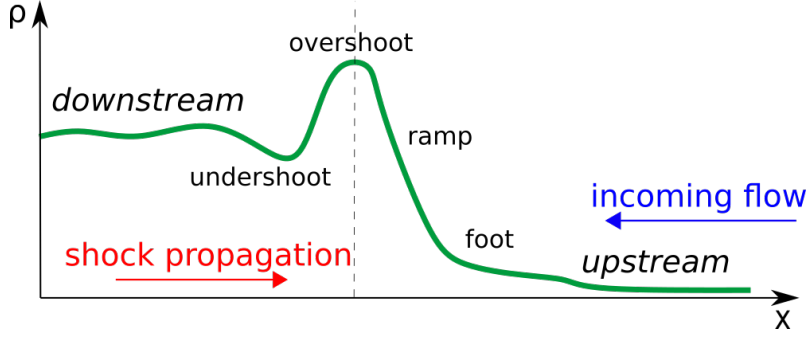[1]Unless specified, in the reminder of this thesis I will refer to the sonic Mach number simply as the Mach number.

Figure 2.1: Sketch of the shock's density as a function of the x-coordinate, along which the shock propagates. The dashed line indicates the approximate position of the shock front, separating the upstream (pre-shock) from the downstream (post-shock) regions.

where

$$c_{\text{s}} = \sqrt{\frac{\gamma k_{\text{B}} T}{m_{\text{i}}}}, \tag{2.8}$$

with γ adibatic index (generally assumed to be equal to 5/3), T pre-shock gas temperature, k_{B} Boltzmann constant and m_{i} ion mass. If a shock occurs in a magnetized medium, we can also define an *Alfvénic Mach number* as the ratio of the upstream flow velocity to the upstream Alfvén velocity v_{A}, where

$$v_{\text{A}} = \sqrt{\frac{B^2}{4\pi n m_{\text{i}}}}, \tag{2.9}$$

B is the intensity of the upstream magnetic field, n is the upstream number density and m_{i} and m_{e} are respectively the mass of ions and electrons. A schematic description of the shock structure is shown in Figure 2.1. Based on hydrodynamical simulations, cosmological shocks can be divided into two main populations [Quilis et al., 1998b, Ryu et al., 2003]: accretion (or 'external') shocks, formed by cold gas accreting on gravitationally attracting structures and characterized by high Mach numbers ($10 \lesssim M \lesssim 10^3$), and merger (or 'internal') shocks, events involving hotter merging substructures with lower Mach numbers ($2 \lesssim M \lesssim 10$), though higher kinetic flux dissipation. Figure 2.2 shows the appearance of a typical cosmic shock in a three-dimensional simulation. These shocks are expected to occur in a rarefied, collisionless plasma, meaning that physical collisions between plasma particles are negligible, so they are exclusively mediated by electromagnetic processes (see Section 2.1): as a consequence, a small fraction of particles can gain a large amount of energy and strongly deviate from the Maxwellian distribution without being quickly thermalized by collisions. More recently, high resolution cosmological simulations identified other possible sub-categories of shocks, triggered during different stages of the mass growth of self-gravitating halos (e.g. 'wind shocks', 'equatorial shocks', 'infall shocks' and 'runaway shocks', see Ha et al. 2018a,b, Zhang et al. 2020).

2.2.1 MHD approach

Within GCs - and likely also beyond them - structure formation shocks develop in a weakly magnetized environment which is suitable for a simple MHD modeling, at least on large scales.

If we consider the frame moving with the shock front, the laws of conservation for a single-fluid plasma are the following [De Hoffmann and Teller, 1950]:

$$j_n \left[\frac{\mathbf{B_t}}{\rho} \right] = B_n \left[\mathbf{u_t} \right], \tag{2.10}$$

16
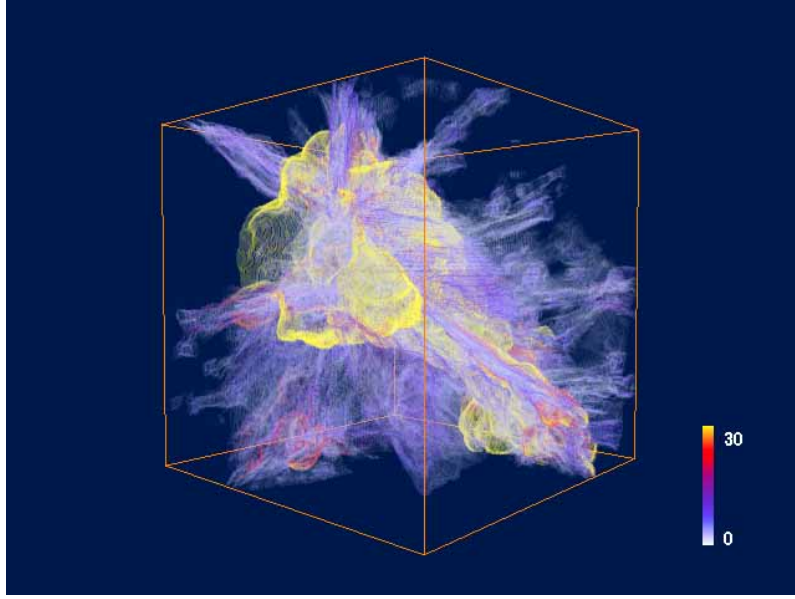
Figure 2.2: Three-dimensional rendering of shock surfaces from a cosmological simulation. The color bar shows the values of corresponding Mach numbers. *Credits:* Ryu et al. [2003].

$$j_n \left[\mathbf{u_t}\right] = \frac{B_n}{4\pi j_n} \left[\mathbf{B_t}\right], \tag{2.11}$$

$$\left[\frac{j_n^2}{\rho} + P + \frac{B_t^2}{8\pi}\right] = 0, \tag{2.12}$$

$$\left[w + \frac{j_n^2}{2\rho^2} + \frac{u_t^2}{2} + \frac{B_t^2}{4\pi\rho} - \frac{B_n}{4\pi j_n}\mathbf{B_t}\mathbf{u_t}\right] = 0, \tag{2.13}$$

where u is the bulk velocity, j is the matter flux, $w = \epsilon + P/\rho$ is the gas enthalpy, ϵ, P, ρ are the internal energy, pressure and density, the subscripts n and t indicate the normal and trasverse component respectively. Here the square brackets notation stands for $[A] = A_{\text{downstream}} - A_{\text{upstream}}$. From these equations we can obtain the variation of the hydrodynamical variables across the shock (generalized Rankine-Hugoniot jump conditions):

$$\epsilon_{\text{down}} - \epsilon_{\text{up}} + \frac{1}{2}\left(\frac{1}{p_{\text{up}}} - \frac{1}{p_{\text{up}}}\right)\left[(P_{\text{down}} + P_{\text{up}}) + \frac{1}{8\pi}\left(B_{t,\text{down}} - B_{t,\text{up}}\right)^2\right]. \tag{2.14}$$

If $\mathbf{B_t} = 0$:

$$r = \frac{\rho_{\text{down}}}{\rho_{\text{up}}} = \frac{(\gamma + 1)M_s^2}{(\gamma - 1)M_s^2 + 2}, \tag{2.15}$$

$$\frac{T_{\text{down}}}{T_{\text{up}}} = \frac{\left[2\gamma M_s^2 - (\gamma - 1)\right]\left[(\gamma - 1)M_s^2 + 2\right]}{(\gamma + 1)^2 M_s^2}, \tag{2.16}$$

where γ is the adiabatic index. The dissipative effects determine the thickness of the shock front, regardless of the nature of the dissipation mechanism: in the weak shock limit ($M_s \ll 2$) the transition layer is thick enough to be described by hydrodynamical equations [Landau and Lifshitz, 1984].

Based on the orientation of the magnetic field we can define the shock obliquity θ as the angle between the upstream magnetic field lines and the shock propagation direction. This is an important parameter that will be often mentioned in the rest of this Thesis.

2.3 Particle acceleration in shocks

Particle acceleration processes capable of generating cosmic rays (CRs) are ubiquitous in astrophysical environments, as the outcome of the presence of both electric fields and magnetic confinement. We can distinguish three kinds of particle acceleration processes: stochastic acceleration, magnetic reconnection acceleration and acceleration at flow discontinuities, i.e. shocks. From now on, I will focus on particle acceleration in shocks, which is the main topic of this work.

2.3.1 Diffusive shock acceleration

A fraction of the energy released in cosmic shock events contributes to the acceleration of charged particles in plasmas up to very high, even relativistic, energies. The main mechanisms responsible for this phenomenon is currently believed to be *diffusive shock acceleration* (DSA), which consists of the multiple reflection of charged particles across the shock front by magnetic fluctuations [see Blandford and Ostriker, 1978, for a review]. Fermi [1949] initially modelled a magnetized cloud moving with velocity $\mathbf{u}$ in the Galactic frame, in which particles move with velocity $\mathbf{v}$ and exchange energy according to $\Delta E / E = -2\mathbf{v} \cdot \mathbf{u}/c^2$, where ΔE corresponds to the work exerted by the Lorentz force. Since heads-on ($\mathbf{v} \cdot \mathbf{u} > 0$) collisions are more likely, this mechanism results into a net energy gain which scales as v^2 (*second-order Fermi acceleration*). If a shock wave is included in this scenario, both the upstream and the downstream medium see the opposite side arriving at the same speed $\Delta u = (r - 1) v_{\mathrm{sh}}/r$ (with r compression ratio and v_{sh} shock speed). Assuming that magnetic turbulence efficiently scatters off and isotropizes the particles, their mean velocity follows the local flow velocity, so particles undergo a regular Fermi acceleration, which averaged over all angles gives a mean energy gain

$$\langle \frac{\Delta E}{E} \rangle = \frac{4}{3} \frac{v_{\mathrm{sh}}}{c}, \tag{2.17}$$

which is instead a first-order increase (*first-order Fermi acceleration*). The fractional energy gain from each shock crossing is a constant and it only depends on the shock strength: the resulting energy spectrum is a power law $\mathrm{d}N(E)/\mathrm{d}E \propto E^{-p}$ with spectral index $p \gtrsim 2$, solely dependent on the compression ratio $r = \rho_{\mathrm{down}}/\rho_{\mathrm{up}}$ (≈ 4 for strong shocks).

Non-linear DSA

Extensions of DSA have been introduced in order to account for certain observational features, such as the acceleration of galactic CRs by supernova remnants. In particular, the magnetic field in the vicinity of supernova shocks appears to be amplified, to values much larger ($\sim 10^2$ or more) than the one of the average interstellar medium. To account for this, non-linear DSA has been introduced [e.g. Caprioli et al., 2010, Amato, 2014, Arbutina and Zeković, 2021]: in this theory, three sources of non-linearity are included, i.e. 1) the dynamical effect of the CR pressure on the shock, 2) the waves generated by accelerated particles in the shock's upstream and 3) the dynamical reaction of the amplified magnetic field on the system. The presence of particles much faster than the shock introduces a non negligible CR pressure term, which is increasingly stronger in the proximity of the shock. As a consequence, the ideal shock discontinuity smoothens even on large scales, and a so called 'sub-shock' region is formed: however, the overall compression ratio can now exceed the typical factor of 4 for strong shocks (see Section 2.2). Due to the sub-shock, particles with a different energy (hence with a different gyro-radius) can effectively probe different compression factors across the shock transition, and the spectrum of accelerated particles deviates from a power-law and can show much steeper (and harder) features. Another consequence of

particles streaming ahead of the shock is the generation of unstable Alfvén waves, which in turn provide amplification of the magnetic field. While such effects may in principle be relevant also in strong external accretion shocks, in this Thesis they are neglected for simplicity.

2.3.2 The injection problem

Based on the DSA model, only the high energy end of the particle distribution crossing a shock wave can undergo multiple scatter and become relativistic, since only particles with a larger enough gyration radius can experience the steep velocity gradient at the two sides of the shock. For this, they need to have a mean free path which is larger than the width of the shock front (usually ~ a few thermal ion Larmor radii). Especially for thermal electrons, some pre-acceleration is required, because if they are in kinetic equilibrium with protons, their Larmor radius is $\sqrt{m_\mathrm{p}/m_\mathrm{e}}$ times smaller than the proton gyro radius, and hence than the shock thickness. The issue of identifying the mechanisms responsible for the extraction of electrons from the thermal pool is known as the *injection* problem. Extensive studies have been conducted on this matter [e.g. Guo et al., 2014b, Matsumoto et al., 2015, Park et al., 2015, Matsumoto et al., 2017, Bohdan et al., 2017, 2019a, Arbutina and Zeković, 2020, Xu et al., 2020], but there is no definite answer yet. Several pre-acceleration mechanisms have been proposed to justify the injection of electrons into DSA, whose occurrence is strictly dependent on the shock's characteristics, which allow the manifestation of different kinds of plasma instabilities. Among these, I will elaborate on *shock drift acceleration* (SDA), *shock surfing acceleration* (SSA) (both of which rely on the effect of the convective electric field $\mathbf{E} = -\mathbf{u}/c \times \mathbf{B}$ induced by the magnetic field gradient at the shock discontinuity, where $\mathbf{u}$ is the flow motion) and *magnetic reconnection*.

Shock drift acceleration

In SDA, electrons initially belonging to the upstream perform quasi-ordered Larmor gyration in the proximity of the shock front: due to the magnetic field being amplified by shock compression in the downstream, the particle alternately perceives a larger or smaller magnetic field, which respectively reduces or increases its gyroradius (Equation 2.4). As a consequence, the orbit described by the electron becomes a cycloid, whose drift velocity is obtained as

$$\mathbf{v}_\mathrm{drift} = \frac{m_\mathrm{e}c v_\perp^2}{2eB^3}\mathbf{B} \times \nabla B, \tag{2.18}$$

where $v_\perp$ is the electron velocity component perpendicular to the magnetic field. While electrons drift along the shock front, they are energized by the motional electric field and eventually reflected to the upstream. In order for this process to be repeatedly fostered, electrons need to be maintained in the proximity of the shock front: based on the properties of the shock, this can happen via different mechanisms. For instance, Guo et al. [2014b] found that for low-Mach number shocks, electron temperature anisotropy self-consistently generates upstream waves that scatter the electrons back to the shock front in a Fermi-like process. The final energy gain due to SDA is

$$\Delta\gamma_\mathrm{SDA} = -\frac{e}{m_\mathrm{e}c^2}\frac{v}{c}B \sin\theta Z, \tag{2.19}$$

where v is the electron speed and Z is the travelled distance. The magnetic field topology is therefore fundamental, as the efficiency of SDA is much larger for perpendicular shocks.

Shock surfing acceleration

In SSA, electrons are accelerated by the convective electric field after being trapped in the electrostatic field at the ramp of high-M shocks: a particle is accelerated along the shock front until its kinetic energy along the shock normal exceeds the electrostatic potential. This potential can be generated by different phenomena, including Buneman instability (see Section 2.1.1). As for SDA, SSA also is most effective in quasi-perpendicular shocks, due to the fact that, in quasi-parallel shocks, gyration is partially inhibited (or totally suppressed, in the limit of exactly parallel shocks), and particles tend to go straight through the shock, therefore developing a low electrostatic barrier.

Magnetic reconnection

Magnetic reconnection is a process occurring in magnetized plasmas, in which the topological rearrangement of magnetic-field lines determines the conversion of magnetic energy into other forms of energy, including particle acceleration. This happens when the fluid has a finite resistivity (see Section 3.1), such that in regions hosting large current densities (*current sheets)* field lines are not frozen in the plasma, but can change their pattern of connectivity. The simplest model of magnetic reconnection [*Sweet-Parker reconnection*, Sweet, 1958, Parker, 1957] involves oppositely directed magnetic fields and relies on Ohmic diffusion over the contact region: the typical reconnection velocity is constrained by the mass conservation condition to be much lower that the Alfvén speed, which is orders of magnitude too small to explain the observed rates [e.g. Zhu et al., 2016]. In the presence of turbulence, however, a stochastic component is introduced to the magnetic field, and reconnection rates are severely increased [Goldreich and Sridhar, 1995]. Reconnection is by itself a viable mechanism for particle energization in different contexts [e.g. Hoshino, 2012], but was also found to be an intrinsic aspect of high-Alfvénic Mach number shocks [Matsumoto et al., 2015], where turbulence folds magnetic-field lines until *magnetic islands* are formed along current sheets in the shock transition region. A mixed second order Fermi-like model involving reconnection and turbulence has been recently proposed to explain the diffuse radio emission in intracluster bridges [Brunetti and Vazza, 2020].

2.3.3   The role of obliquity

The role of obliquity θ, i.e. the angle formed by the shock propagation direction and the upstream magnetic field, can be summarized by stating that (quasi-)parallel shocks ($\theta < 45°$) are able to accelerate ions via DSA, while electrons require pre-acceleration mechanisms (see Section 2.3.2), which usually occur in (quasi-)perpendicular shocks ($\theta > 45°$). At quasi-parallel shocks, ions are able to propagate back in the upstream plasma and interact with the incoming flow, hence exciting magnetic perturbations, which favor the diffusion of ions back and forth across the shock (DSA) [Caprioli and Spitkovsky, 2014a]. On the other hand, at quasi-perpendicular shocks, DSA cannot operate spontaneously, since particles are not able to seed the upstream plasma with self-generated waves beyond one ion gyroradius from the shock front. Therefore, ion acceleration at quasi-perpendicular shocks can still take place, for example in the presence of magnetic turbulence, but it may not self-sustain [Giacalone et al., 1994].

2.4   Observational evidence

From Section 2.3, we know that both electrons and ions can be accelerated by Fermi mechanisms occurring in cosmological shocks where a magnetic field is present, but the observational counterpart produced by these energetic particles is different depending on the particle's species.
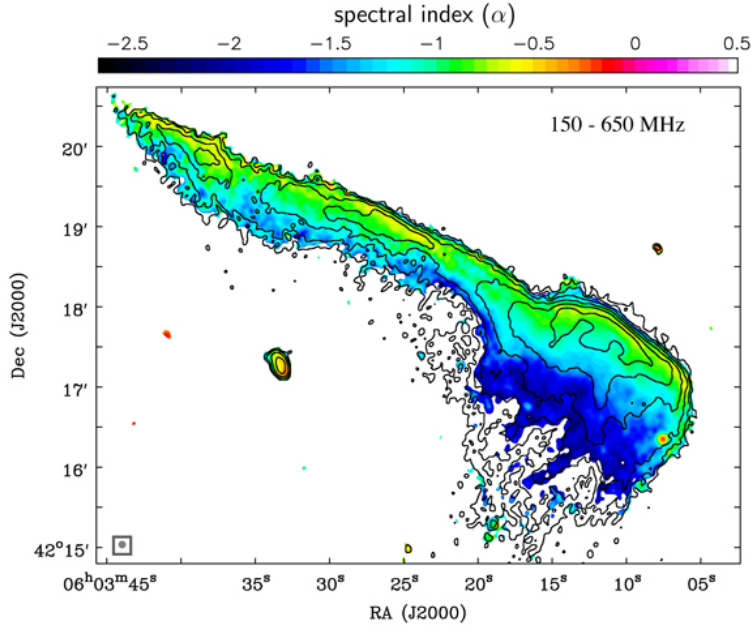
Figure 2.3: Spectral index map of the *Toothbrush* relic between 150 and 650 MHz. *Credits:* Rajpurohit et al. [2020].

Diffuse radio synchrotron emission CR electrons with GeV energies ($\gamma > 10^3$) moving in a magnetized medium with $B \sim \mu$G are able to radiate via synchrotron emission, which can be detected in the radio domain by facilities such as JVLA, GMRT, LOFAR, MWA, ASKAP, MeerKAT, and in the future by SKA. The typical sources that have been observed and associated to shocks are radio relics in merging GCs (see Section 1.2.1). If we assume that the CR energy distribution in the ICM can be described by a power law [Feretti et al., 2012], then the energy flux follows $F_\nu \propto \nu^\alpha$, where $\alpha = (1 - p)/2$ and p is defined in Section 2.3.1. Assuming DSA, the parameter α gives an estimate of the shock's Mach number:

$$M_{\text{s,DSA}} = \sqrt{\frac{2\alpha - 3}{2\alpha + 1}}. \tag{2.20}$$

Figure 2.3 shows an example of spectral number analysis on the radio relic known as *Toothbrush*.

γ-ray hadronic emission CR protons are expected to collide with the thermal ICM and produce γ rays via hadronic interactions. The lack of detection of this kind of emission in GCs [Ackermann et al., 2014] has set upper limits on the abundance of energetic protons that can be accelerated in shocks hosted by these objects, which appear to be inconsistent with the expected γ-ray emission for DSA in relics [Vazza et al., 2016].

Several explanations to solve this tension were proposed.

- CR protons are assumed to have lifetimes of $\sim 1 - 10$ Gyr once injected in GCs due to their trapping into the tangled intraclsuter magnetic field [Berezinsky et al., 1997]: Enßlin et al. [2011] first proposed to relax this assumption by introducing the possibility that CR protons stream out of the innermost cluster regions faster than the medium's Alfvén velocity, thereby lowering the expected hadronic emission. The tangled topology of ICM magnetic fields which can be inferred from rotation measure observations, however, disfavor this scenario.

- If a shock has evidence of accelerated electrons, but not of accelerated protons (e.g. radio relics), it has been proposed [e.g. Pinzke et al., 2013] that the radio emission is actually the outcome of re-accelerated electrons, implying the presence of a pool of fossil electrons. This way, even weak shocks ($M \sim 1.3 - 2.5$) can produce detectable radio emission, while CR proton acceleration is low enough not to violate Fermi's limit.

- The tension could potentially be solved if the shocks' microscopic properties allowed to preferentially accelerate electrons instead of protons: this is expected to be true if the shock obliquity (see Section 2.3.3) is quasi-perpendicular [Wittor et al., 2020]. This issue will be thoroughly addressed in Chapter 5.

X-ray thermal bremsstrahlung emission The presence of shocks linked to radio relics can also be inferred from discontinuities in the X-ray profile: by deprojecting the surface brightness and gas temperature profiles, the shock's Mach number can be estimated [Markevitch and Vikhlinin, 2007] applying the Rankine-Hugoniot jump conditions (see Section 2.2). This method generally obtains lower M values with respect to the radio estimates [e.g. Akamatsu and Kawahara, 2013, Mazzotta et al., 2011, Stuardi et al., 2019], which in principle challenges the assumptions made on DSA. Wittor [2021] investigated this discrepancy by means of mock observations and attributed this effect on the fluctuations of the ICM [Dominguez-Fernandez et al., 2021] which cause a variation of M across the shock front: while X-ray Mach numbers match the peak of the Mach number distribution, radio Mach numbers preferentially probe higher-M regions of the shock front, which tend to be more radio luminous.

Faraday rotation The analysis of Faraday rotation of radio synchrotron emission allows one to estimate the magnetic field strength in GCs. This effect occurs when a linearly polarized radiation crosses a magnetized plasma containing thermal electrons: the right and left-handed circularly polarized components of the wave propagate at different phase velocities, causing a rotation of the polarization angle (rotation measure RM):

$$RM \ [\mathrm{rad/m^2}] = 812 \int \frac{B_{\mathrm{los}}}{\mu \mathrm{G}} \cdot \frac{n_{\mathrm{e}}}{\mathrm{cm^3}} \cdot \frac{\mathrm{d}l}{\mathrm{kpc}}. \tag{2.21}$$

From RM measurements, the strength and structure of the magnetic field can be constrained by means of semi-analytical approaches, numerical techniques or RM synthesis [e.g. Brentjens and de Bruyn, 2005, Murgia et al., 2004, Bonafede et al., 2010, Guidetti et al., 2008].

Inverse-Compton X-ray emission CR electrons in the ICM must scatter photons from the CMB and result in a power-law of X-ray emission, additionally to the thermal bremsstrahlung. The absence of conclusive evidence indicating the presence of this emission allows to infer a lower limit on the ICM magnetic field strength: the ratio of the monochromatic flux of intracluster X-ray and sychrotron radio emission can be written as [Petrosian, 2001]

$$R = \frac{f_{\mathrm{IC}}(k_{\mathrm{B}}T)}{f_{\mathrm{sync}(\nu)}} = 1.86 \times 10^{-8} \left(\frac{\mathrm{photons}}{\mathrm{cm^2 \ s \ keV \ Jy}} \right) \left(\frac{k_{\mathrm{B}}T}{20 \ \mathrm{keV}} \right)^{-\Gamma} \left(\frac{\nu}{\mathrm{GHz}} \right)^{\Gamma-1} \left(\frac{T_{\mathrm{CMB}}}{2.8 \ \mathrm{K}} \right)^{\Gamma+2} \left(\frac{B}{\mu \mathrm{G}} \right)^{-\Gamma} c(p), \tag{2.22}$$

where $\Gamma = (p + 1)/2$, p is the power-law slope of the electron energy distribution, f_{IC} is the intracluster flux density, f_{sync} is the synchrotron flux density, T_{CMB} is the CMB temperature at the object's redshift and $c(p)$ is a normalization factor. Lower limits on the magnetic field intensity in clusters and estimates based on RM are found to be consistent in most cases [e.g. Bonafede et al., 2010, Stuardi et al., 2020].

2.5   Magnetic fields in the cosmic web

Large-scale magnetic fields are ubiquitous throughout the cosmic web: they are believed to be the result of amplification of so-called seed fields, whose origin is still debated. The proposed scenarios for magnetogenesis are essentially two.

1. The *primordial* scenario posits that seed fields were already present at the epoch of the CMB, implying that they have been generated possibly during inflation but they are too weak to be constrained by CMB measurements [e.g. Turner and Widrow, 1988, Grasso and Rubinstein, 2001, Subramanian et al., 2006]. Different mechanisms for primordial magnetic field generation would determine different coherence lengths which would be inherited by voids, possibly providing insights on primordial helicity [e.g. Semikoz and Sokoloff, 2005, Campanelli, 2009, Kahniashvili et al., 2016].

2. In the *astrophysical* scenario, the seed fields are generated at a later stage, during galaxy formation, possibly powered by galactic winds or AGNs [e.g. Völk and Atoyan, 1999, Donnert et al., 2009, Furlanetto and Loeb, 2001]. These processes could have left signatures on the transport of heat, entropy, metal content and CR production in the forming structures [Planelles et al., 2016].

Figure 2.4 shows differences in the magnetic field maps for different initial conditions of the magnetic field in recent magnetohydrodynamics cosmological simulations similar to the ones analyzed in this thesis. Additional processes like the *Biermann battery* [Kulsrud et al., 1997], aperiodic plasma fluctuations [Schlickeiser et al., 2012], resistive mechanisms [Miniati and Bell, 2011] and ionization fronts around the first stars [Langer et al., 2005] may have been able to further amplify these fields. Within the volume of self-gravitating halos, where accretion motions are expected to stir mostly turbulence over the timescale of several Gyr [e.g Miniati, 2014, Vazza et al., 2018a], weak fields can be amplified by the small-scale dynamo mechanism [e.g. Schober et al., 2013, Vazza et al., 2018a, Domínguez-Fernández et al., 2019, Quilis et al., 2020]. Given the plethora of mechanisms potentially contributing to magnetogenesis, the strength of magnetic fields in the cosmic web could in principle span several orders of magnitude: additionally, the efficiency of magnetic field amplification linked to astrophysical processes is strongly affected by the degree of overdensity, making it especially difficult to probe magnetic fields in the most rarefied environments. In the densest structures, like GCs, observational evidence of the presence of $\sim \mu$G magnetic fields coherent on Mpc scales can be inferred from diffuse synchrotron emission, Faraday rotation, ultra-high energy CRs and fast radio bursts (see Section 2.4).
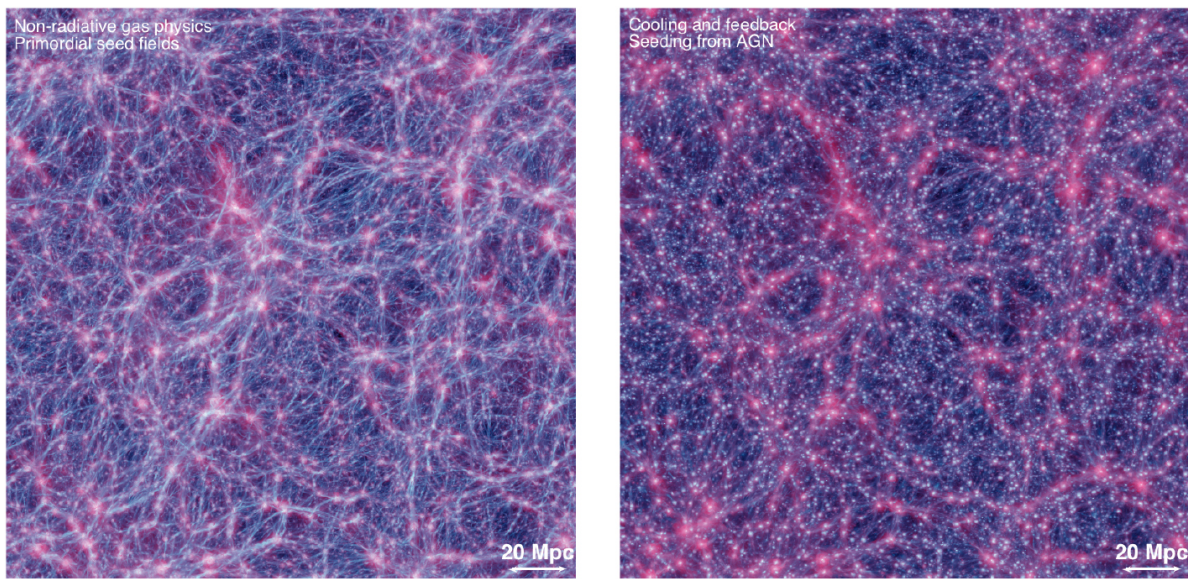
Figure 2.4: Simulated volume rendering of temperature (red) and magnetic field strength (green+blue) for a primordial scenario (*left panel*) and an astrophysical scenario (*right panel*). *Credits:*Vazza et al. [2017]

3. Methods: MHD and PIC simulations

3.1 Magnetohydrodynamic simulations

Magnetohydrodynamics allows us to study electrically conducting fluids by means of a set of differential equations including Navier-Stokes, fluid dynamics and Maxwell equations, which generally requires a numerical approach. This model holds as long as the considered plasma motions are non-relativistic and slowly varying (with respect to the plasma frequency). The equations required for the MHD description of plasmas include the *equation of continuity*:

$$\frac{\partial \rho}{\partial t} + \nabla \cdot (\rho \mathbf{v}) = 0, \tag{3.1}$$

with ρ density and $\mathbf{v}$ velocity; the *equation of motion*:

$$\frac{\partial \mathbf{v}}{\partial t} + (\mathbf{v} \cdot \nabla)\mathbf{v} = -\frac{1}{\rho}\nabla p + \frac{1}{4\pi\rho}(\nabla \times \mathbf{B}) \times \mathbf{B}, \tag{3.2}$$

which takes into account the Lorentz force $(\nabla \times \mathbf{B}) \times \mathbf{B}$, with p gas pressure and $\mathbf{B}$ magnetic field; the *conservation of energy*:

$$\frac{\partial}{\partial t}\left(\frac{1}{2}\rho v^2 + \rho\epsilon + \frac{B^2}{8\pi}\right) = -\nabla\left[\rho\mathbf{v}\left(\frac{1}{2}v^2 + \epsilon + \frac{p}{\rho} + \frac{B^2}{4\pi\rho}\right) + \frac{1}{4\pi}\mathbf{B} \times (\mathbf{v} \times \mathbf{B})\right] \tag{3.3}$$

with ϵ internal energy per unit mass. The conditions on the electromagnetic field also require

$$\nabla \cdot \mathbf{B} = 0 \tag{3.4}$$

and the *induction equation*

$$\frac{\partial \mathbf{B}}{\partial t} = \nabla \times (\mathbf{v} \times \mathbf{B}) + \lambda\nabla^2\mathbf{B}, \tag{3.5}$$

where $\lambda = c^2/(4\pi\sigma)$ is the *magnetic diffusivity* and σ is the electrical conductivity. In the hypothetical limit of infinite conductivity, which is appropriate in most astrophysical systems, this becomes (*ideal MHD*),

$$\frac{\partial \mathbf{B}}{\partial t} = \nabla \times (\mathbf{v} \times \mathbf{B}). \tag{3.6}$$

By combining the equations of continuity and induction equation for ideal MHD, we get

$$\frac{d}{dt}\left(\frac{\mathbf{B}}{\rho}\right) = \left(\frac{\partial}{\partial t} + \mathbf{v} \cdot \nabla\right)\frac{\mathbf{B}}{\rho} = \left(\frac{\mathbf{B}}{\rho} \cdot \nabla\right)\mathbf{v}. \tag{3.7}$$

This formula describes how the magnetic field lines are 'frozen' in the fluid, i.e. the magnetic field can be regarded as a plastic material which can be distorted by making the plasma move accordingly (also known as *Alfvén theorem*).

In general, fluid dynamics equations can be solved using two main numerical approaches, namely Lagrangian and Eulerian: the former consists of studying the fluid motions by following an individual fluid parcel as it moves through space and time, while the latter employs a fixed mesh in which the fluid flows as time evolves. The most popular Lagrangian scheme is *smoothed particle hydrodynamics* (SPH), where the continuous fluid is composed by a discrete set of particles by using a kernel to interpolate the various quantities over a certain smoothing length. The advantages of SPH lie in the very high resolution provided in dense regions with relative low computational cost: however this also implies a worse accuracy in more rarefied regions. Among the most popular SPH codes for cosmological MHD, there is GADGET [Springel et al., 2001]. The main advantages of Eulerian grid-based simulations, in which equations are solved in each grid cell, consist in the ability of capturing the formation of shocks and fluid instabilities, also for very low densities, as the ones involving external shocks (see Section 2.2). Eulerian codes also allow to locally refine the grid in order to increase the resolution of certain regions with the lowest amount of computational cost. For these reasons, the simulations analyzed for this work were performed with the Eulerian code ENZO (see Section 3.1.1). Recently, some codes have implemented a hybrid approach, such as GIZMO [Hopkins, 2014] and AREPO [Springel, 2010]. Several work attempted to compare between the different possible approaches to simulate gas dynamics in cosmological simulations [e.g. Frenk et al., 1999, O'Shea et al., 2004, Tasker et al., 2008, Mitchell et al., 2009, Scannapieco et al., 2012] while a detailed comparison between various codes on their ability to properly characterize shocks in the large-scale structure is provided in Vazza et al. [2011b].

3.1.1 ENZO

ENZO [Bryan et al., 2014] is an open-source, Eulerian grid-based code which provides high spatial and temporal resolution for modelling astrophysical fluid flow, which include an adaptive mesh refinement module. It supports a wide range of physics including ideal and non-ideal MHD, N-body dynamics, gas chemistry, radiation transport, cosmological expansion and models for star formation and feedback. Furthermore, ENZO supports an accurate treatment of the dynamics of supersonic flows and shock waves, which is especially important for this work's purpose. In the cosmological simulations analysed in the following chapters, the Eulerian equations of ideal MHD solved by ENZO must include the cosmological expansion parameter a. Therefore, for instance, Equation 3.1 becomes

$$\frac{\partial \rho}{\partial t} + \frac{1}{a} \nabla \cdot (\rho \mathbf{v}) = 0. \tag{3.8}$$

The evolution of $a(t)$ is governed by the second Friedmann equation for the expansion of a spatially homogeneous and isotropic universe

$$\frac{\ddot{a}}{a} = -\frac{4\pi G}{3a^3} \left(\rho_0 + \frac{3p_0}{c^2} + \Lambda_c \frac{c^2}{3} \right), \tag{3.9}$$

where ρ_0 is the mean comoving mass density, p_0 is the comoving background pressure and Λ_c is the cosmological constant. ENZO combines an N-body particle-mesh solver for dark matter with different MHD methods. The simulations involved in this work were performed adopting the *piecewise linear method*, which uses linear functions to fit the solution in each grid cell [Colella and Woodward, 1984]. In order to maintain the magnetic field divergence free (Equation 3.4), different numerical schemes can

be adopted: the *divergence cleaning* method implemented by Dedner et al. [2002] introduces an arbitrary function to the magnetic induction equation (Equation 3.5), which allows to keep the divergence as low as possible by means of 'cleaning waves'. The Dedner cleaning method is adopted in the simulation used for our works: in Banfi et al. [2020], we go into more detail and provide numerical tests concerning the adoption of this method.

3.2 Particle-in-cell simulations

While on large astrophysical scales, where charge separation is negligible, the dynamics of plasma is well described by MHD laws, on scales smaller than the Debye length one must consider the interaction between the two particle species. Since most of the plasma in the Universe is dilute and hot, particles can be considered to only interact through collective electromagnetic fields. This implies that ions and electrons can have different temperatures and anisotropic distributions, hence different kinds of plasma instabilities can occur. Such a scenario is typical of collisionless shocks, implying a suitable numerical representation that accounts for particle-electromagnetic field interaction is required: the proper instrument to simulate these phenomena is fully kinetic particle-in-cell (PIC) simulations, where individual particles are tracked in a Lagrangian frame, while fields are computed simultaneously on a Eulerian mesh (Figure 3.1).

This method relies on solving the Vlasov-Maxwell equations. A collisionless plasma can be described by the distribution functions $f(\mathbf{x}, \mathbf{u}, t)$ of each species, i.e. the number of particles per unit volume in the phase space of velocities $\mathbf{u}$ and positions $\mathbf{x}$ at time t. For each kind of particle, i.e. ions and protons, the Vlasov equation describes the evolution of f in time (in the non-relativistic case):

$$\frac{\partial f}{\partial t} + \mathbf{u} \cdot \frac{\partial f}{\partial \mathbf{x}} + \frac{q}{m} \left(\mathbf{E} + \frac{\mathbf{u}}{c} \times \mathbf{B} \right) \cdot \frac{\partial f}{\partial \mathbf{u}} = 0 \tag{3.10}$$

where q is the particle charge, m is the particle mass, $\mathbf{E}$ and $\mathbf{B}$ are the electric and magnetic field generated by the plasma. The fields obey Maxwell's equations:

$$\nabla \times \mathbf{B} = \mu_0 \mathbf{J} + \mu_0 \epsilon_0 \frac{\partial \mathbf{E}}{\partial t} \tag{3.11}$$

$$\nabla \times \mathbf{E} = -\frac{1}{c} \frac{\partial B}{\partial t} \tag{3.12}$$

$$\nabla \cdot \mathbf{E} = \frac{1}{\epsilon_0} \rho_c \tag{3.13}$$

$$\nabla \cdot \mathbf{B} = 0 \tag{3.14}$$

with μ_0 vacuum permeability, ϵ_0 vacuum permittivity, ρ_c charge density and $\mathbf{J}$ current density.

3.2.1 TRISTAN-MP

The code used for PIC simulations in Chapter 6 is TRISTAN-MP [TRIdimensional STANford - Massively Parallel, Spitkovsky, 2005], the parallel version of the code originally developed by Buneman [1993]. It is written in a modular format in Fortran 95 which relies on MPI and HDF5 libraries for parallelization. The code allows to initialize different problems, including shocks with arbitrary plasma parameters. Quantities are scaled consistently with $\epsilon_0 = 1$ and $\mu_0 = 1/c^2$. By scaling the magnetic field by a factor c, the equations solved by TRISTAN-MP become

$$\frac{\partial \mathbf{B}}{\partial t} = -c \nabla \times \mathbf{E} \tag{3.15}$$
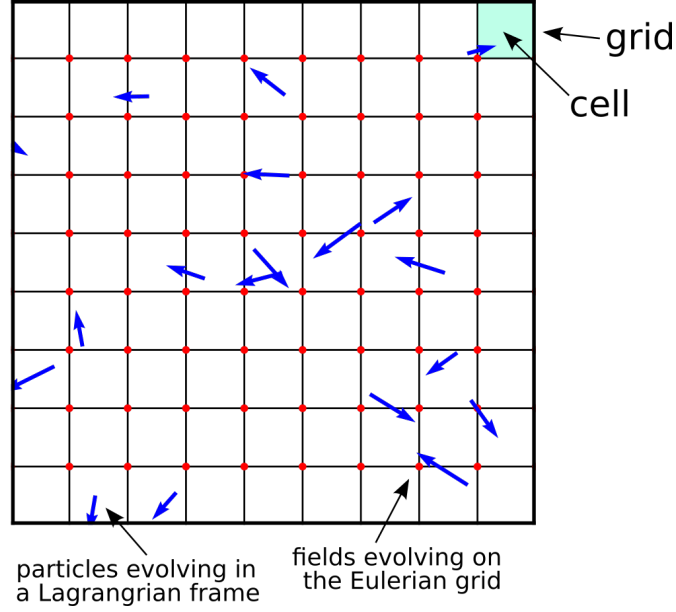
Figure 3.1: Schematic representation of the Eulerian grid partitioning the computational domain of PIC simulations, where particles are free to evolve in a Lagrangian frame.

$$\frac{\partial \mathbf{E}}{\partial t} = c\nabla \times \mathbf{B} - \mathbf{J} \qquad (3.16)$$

for the evolution of the electromagnetic field, and

$$\frac{d\mathbf{p}}{dt} = q\left(\mathbf{E} + \frac{\mathbf{v}}{c} \times \mathbf{B}\right) \qquad (3.17)$$

$$\frac{\partial \mathbf{x}}{\partial t} = \frac{\mathbf{p}}{m} \qquad (3.18)$$

for the particle evolution under the Lorentz force, where $\mathbf{p}$ is the particle's momentum and $\mathbf{x}$ is the particle's position. At the beginning of the simulation, electromagnetic fields are initialized with null divergence by inserting electrons and ions in the same spatial positions. Particles' momenta follow a drifting Maxwell-Jüttner distribution, which takes into account relativistic effects and the plasma bulk velocity $c\beta_0$. The particle energy distribution follows:

$$E_{\mathrm{MJ}}(\gamma) = \frac{1}{\Gamma_0^2 \beta_0 K_2\left(\frac{1}{\theta \Gamma_0}\right)} \exp\left(-\frac{\gamma}{\theta}\right) \gamma \sinh\left(\frac{\beta_0 \sqrt{\gamma^2 - 1}}{\theta}\right), \qquad (3.19)$$

where γ is the particle Lorentz factor, $\Gamma_0 = (1 - \beta_0^2)^{-1/2}$, K_2 is the modified Bessel function of the second kind, $\theta = k_{\mathrm{B}}T/(mc^2)$, k_{B} is the Boltzmann constant, T is the plasma temperature and m is the particle mass. Spatial and temporal derivatives are calculated using space- and time-centered finite difference schemes. Electromagnetic fields are discretized and stored in a staggered grid (Yee lattice, Yee 1966) with electric fields on cell edges and magnetic fields on cell faces, which ensures a divergence-free magnetic field without explicitly solving Equation 3.14. The Lorentz force acting on the particles is obtained with a tri-linear interpolation function on the electromagnetic fields. Particles' momenta and positions are evolved with a leap-frog method: this information is used to calculate the current, which is then used as a the source term in Equation 3.16.

4. Motivation and thesis outline

This work was developed within the aims of an ERC-founded research project called MAGCOW[1] (MAGnetized COsmic Web), whose main goal is to investigate the origin of extragalactic magnetic fields by combining numerical simulations and radio observations. My most important contribution to this project is to address how CRs are accelerated by realistic shock waves in large-scale structures, as a function of the topology and amplitude of cosmic magnetic fields. Differently from other astrophysical environments, such as supernovae, the acceleration of CR protons by structure formation shocks has still to be observed. As explained in Section 2.4, the main open question concerns the lack of evidence of hadronic γ-ray emission in GCs [Ackermann et al., 2010, Arlen et al., 2012, Ackermann et al., 2014], which yields an upper limit on the CR pressure ratio and, as a consequence, on the ability of shocks to accelerate protons. On the other hand, evidence for the acceleration of CR electrons is well established by radio observations, hence many recent works have been dedicated to solve this apparent inconsistency. Some tension has been lifted thanks to PIC simulations [e.g. Caprioli and Spitkovsky, 2014a, Guo et al., 2014b,a], which showed that particle acceleration mechanisms differ for electrons and protons, and, in particular, the relative orientation of the magnetic field with respect to the shock propagation direction (obliquity) heavily affects the acceleration efficiency of either species. With this work, I have examined the interplay between CR acceleration and extragalactic magnetic fields in three main steps, which also correspond to either published or soon-to-be submitted articles:

1. In Chapter 5, I analyzed cosmological MHD simulations of the large-scale structure, with the aim of identifying and characterizing shocks throughout the whole cosmic web. In particular, I studied the typical **shock obliquity** and how this is modified by different assumptions on the origin and evolution of extragalactic magnetic fields. Finally, I tackled the issue of the missing γ-rays by considering the role of obliquity in the acceleration of protons and electrons. This work has been published in MNRAS [Banfi et al., 2020].

2. In Chapter 6, I performed PIC simulations of cosmic shocks, taking advantage of the information gathered from the previous work. In particular, I simulated shocks with characteristics that are expected to be found in filaments and analyzed the mechanisms that foster **electron acceleration**. This work will soon be submitted for publication.

3. In Chapter 7, I focused on the study of the topology of magnetic fields and their evolution in relation to the **cosmic web** components. This analysis is especially useful considering that the orientation of the magnetic field plays a crucial role in most particle acceleration mechanisms, and furthermore that the arrangement of magnetic fields around cosmic structures is found to strongly

---

[1]`https://cosmosimfrazza.myfreesites.net/erc-magcow`

affect the magnetic field estimates obtained with rotation measure observations. This work has been published in MNRAS [Banfi et al., 2021].

In the framework of this project, I also had the chance to contribute to works lead by other members of the MAGCOW group. In particular, I employed some of the algorithms I developed for my analysis in these published articles aimed at constraining magnetic fields in the cosmic web from both observations and simulations: Vazza et al. [2021], Locatelli et al. [2021] and Vazza et al. [submitted]. These works will be briefly discussed in Part IV. Finally, in Part V, I will summarize the results achieved in this Thesis.

Part II

Particle acceleration in cosmic shocks

5. Shock waves in the magnetized cosmic web: the role of obliquity and cosmic-ray acceleration (Banfi et al., 2020)

Abstract   Structure formation shocks are believed to be the largest accelerators of cosmic rays in the Universe. However, little is still known about their efficiency in accelerating relativistic electrons and protons as a function of their magnetization properties, i.e. of their magnetic field strength and topology. In this work, we analyzed both uniform and adaptive mesh resolution simulations of large-scale structures with the magnetohydrodynamical grid code ENZO, studying the dependence of shock obliquity with different realistic scenarios of cosmic magnetism. We found that shock obliquities are more often perpendicular than what would be expected from a random three-dimensional distribution of vectors, and that this effect is particularly prominent in the proximity of filaments, due to the action of local shear motions. By coupling these results to recent works from particle-in-cell simulations, we estimated the flux of cosmic-ray protons in galaxy clusters, and showed that in principle the riddle of the missed detection of hadronic γ-ray emission by the *Fermi*-LAT can be explained if only quasi-parallel shocks accelerate protons. On the other hand, for most of the cosmic web the acceleration of cosmic-ray electrons is still allowed, due to the abundance of quasi-perpendicular shocks. We discuss quantitative differences between the analyzed models of magnetization of cosmic structures, which become more significant at low cosmic overdensities.

5.1   Introduction

Shocks in the large-scale structure of the universe are the natural outcome of the accretion of cold, warm or hot gas onto galaxy clusters or of direct mergers between clusters [e.g. Ryu et al., 2003, Bykov et al., 2008]. These processes convert a fraction of kinetic energy into thermal energy and into the amplification of magnetic fields and acceleration of CR [e.g. Bykov et al., 2019, for a recent review]. Through cosmological numerical simulations, we can estimate the energetics of CR associated to shocks: Miniati et al. [2000] provided the first attempt to simulate shock waves in the large-scale structure with an Eulerian approach and to derive their Mach number from jump conditions. Following works [e.g. Ryu et al., 2003, Pfrommer et al., 2006, Vazza et al., 2009, Planelles and Quilis, 2013] found that, for the majority of shocks in the Universe, the kinetic energy is dissipated in internal shocks with low Mach numbers ($2 \lesssim M \lesssim 4$), while shocks with Mach numbers up to ~ 1000 are found in lower density

environments (like the external accretion regions of structures) but they overall process little energy in the cosmic volume. On the other hand, the acceleration of CRs by first order Fermi acceleration is expected to be mainly driven by strong shocks ($M \gtrsim 5$) [e.g. Ryu et al., 2003, Kang and Jones, 2007, Vazza et al., 2011b].

Radio observations of Mpc-sized synchrotron emission in galaxy clusters confirm the presence of diffuse magnetic fields and relativistic electrons associated with cluster merger shocks [e.g. "radio relics", see Ferrari et al., 2008, Feretti et al., 2012, van Weeren et al., 2019, for reviews], while at the same time the lack of hadronic γ-ray detection by the *Large Area Telescope* (LAT) on board of the *Fermi* satellite [e.g. Ackermann et al., 2010, Arlen et al., 2012, Ackermann et al., 2014] has set stringent upper limits on the content of CR protons in galaxy clusters ($\lesssim 1\%$ of the thermal gas energy), which also can be used to set very low upper limits on the allowed CR acceleration efficiency of structure formation shocks [Vazza and Brüggen, 2014, Brunetti and Jones, 2014].

Several decades of theoretical works suggest that each kind of particles undergoes different levels of acceleration as a function of plasma parameters and of the pre-existing magnetic field topology, but the mechanism that drives this process is still under debate [e.g. Bykov et al., 2019, and references therein]. CRs typically gain energy by crossing the shock front multiple times through a first order Fermi mechanism called diffusive shock acceleration [DSA, Bell, 1978], which produces a power-law distribution of energetic particles. However, unlike protons, electrons need to be pre-accelerated in order for their small gyro-radius to become comparable to the width of the shock front and effectively enter the DSA regime: particle-in-cell (PIC) simulations by [e.g. Caprioli and Spitkovsky, 2014b, Guo et al., 2014b] suggest that shock drift acceleration [SDA, e.g. Matsukiyo et al., 2011, and references therein] could be an efficient way for these particles to be pre-accelerated by drifting along magnetic field lines down the shock front.

A usually underlooked aspect of particle acceleration from cosmic shocks is the role of shock obliquity θ, defined as the angle between the shock normal and the up-stream magnetic field vector (see Figure 5.1). PIC simulations have indeed established the dependence of the acceleration on the shock's Mach number and obliquity: as a consequence CR electrons have been shown to be more easily accelerated by quasi-perpendicular ($45° < \theta < 135°$, Guo et al. 2014b) rather than quasi-parallel ($\theta < 45°$ or $\theta > 135°$) shocks, while the opposite has been found for protons [Caprioli and Spitkovsky, 2014b]. However, magnetohydrodynamical (MHD) simulations are necessary to study the conditions that lead to a certain orientation of the magnetic field where shocks occur and to the possible prevalence of some obliquities over others.

The link between obliquity and acceleration efficiency may also be a viable explanation for the missing γ-ray detection from galaxy clusters, considering that the distribution of random angles in a three-dimensional space is $\propto \sin \theta$, which means that it is peaked at perpendicular shocks. Simulations by Wittor et al. [2017] have shown that the obliquity distribution of shocks in galaxy clusters progressively becomes even more concentrated towards 90° as a result of the passage of several merger shock waves in the lifetime of clusters. They also estimated that, if the acceleration of CR protons is limited to shocks with $\theta < 50°$, the hadronic γ-ray emission produced by DSA gets much reduced and the tension with *Fermi* limits is alleviated, even if not entirely solved. More recent work from Ha et al. [2019] has shown that in simulated galaxy clusters the amount of kinetic energy flux dissipated by quasi-parallel shocks and transferred to CR protons is $\sim 10^{-4}$, assuming a DSA model with more recent efficiencies derived in Ryu et al. [2019]. In this case, the obtained γ-ray emissions are in line with *Fermi*'s constraints. This picture has been recently confirmed by cosmological MHD simulations by Wittor et al. [2020].

However, we notice that Ha et al. [2019] did not use MHD simulations of large-scale structures (but rather a simpler approach involving the evolution of passive magnetic fields via the induction equation),
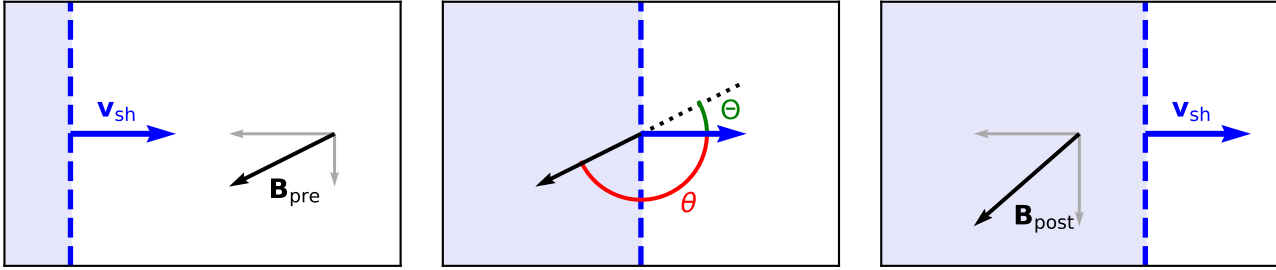
Figure 5.1: The Figure shows the two-dimensional projection of the process of shock crossing on magnetized plasma in the rest frame of the pre-shock. The left panel shows the pre-shock configuration; the central panel represents the obliquity θ, i.e. the angle formed by the shock propagation direction and the pre-shock magnetic field, and $\Theta = 90° - |90° - \theta|$ (for acute angles, $\theta \equiv \Theta$); the right panel shows the magnetic field modification after shock crossing, i.e. the amplification of its perpendicular component.

while Wittor et al. [2017] did not focus on the properties of shock acceleration at the scale of filaments, which are expected to be a major contributor to the total mass content of galaxy clusters. Moreover, the above works were limited to explore the dependence of shock acceleration on the magnetic fields generated by single possible scenarios for the origin of extragalactic magnetic fields, which is still debated [e.g. Donnert et al., 2009, Vazza et al., 2017].

Our work expands on the above points, using new MHD simulations tailored to determine the typical obliquity of cosmic shocks in the acceleration of relativistic particles across the cosmic environment, its potential dependence on magnetogenesis and its effect on the acceleration efficiency of electrons and protons.

The paper is structured as follows. In Section 5.2, we describe the computational setup for the simulations and we outline the approach used to find and characterize shocks. In Section 7.3, we present our results for obliquity and CR acceleration estimates. In Section 5.4, we describe the implications of our results on observations. In Section 5.5, we discuss the validity and limitations of our analysis. Finally, Section 5.6 contains a brief summary and conclusions. In the Appendix, we clarify some details about the analysis.

5.2 Methods

5.2.1 Simulations

We simulated the formation of cosmic structures with the Eulerian cosmological magnetohydrodynamical code ENZO [Bryan et al., 2014], which couples an N-body particle-mesh solver for dark matter (DM) [Hockney and Eastwood, 1988] with an adaptive mesh refinement (AMR) method for the baryonic matter [Berger and Colella, 1989]. We adopted a piecewise linear method (PLM) [Colella and Glaz, 1985], a reconstruction technique in which fluxes are computed using the Harten-Lax-Van Leer (HLL) approximate Riemann solver, and used time integration based on the total variation diminishing (TVD) second-order Runge-Kutta (RK) scheme [Shu and Osher, 1988]. We used the Dedner cleaning MHD solver [Dedner et al., 2002] to keep the divergence of the simulated magnetic field as small as possible. This method has been tested multiple times in the literature, showing that despite the relatively large rate of dissipation introduced by its "cleaning waves", it always converges to the correct solution as resolution is increased, at variance with other possible "divergence cleaning" methods [e.g. Stasyszyn et al., 2013, Hopkins and

Raives, 2016, Tricco et al., 2016]. We refer the reader to more recent reviews for a broader discussion of the resolution and accuracy of different MHD schemes in properly resolving the dynamo in cosmological simulations [Donnert et al., 2018].

In this work, we present the analysis of two kinds of simulations (described in more detail in the next two Sections): a suite of runs employing a fixed spatial/mass resolution ($\approx$ 83 kpc/cell comoving) to simulate the cosmic web on a representative cosmic volume and for different scenarios of the origin of magnetic fields, and single cluster re-simulations using nested initial conditions, which allow us to study magnetic field topology at high resolution ($\approx$ 25 kpc/cell comoving) for a specific scenario of cosmic magnetism.

5.2.2 Static grid simulations

We simulated a volume of $\approx$ (85 Mpc)^3 (comoving) sampled with a static grid of 1024^3 cells: the decision to neglect AMR allows us to maintain a resolved description of magnetic fields even in low-density regions. These datasets are extracted from the "Chronos++" suite[1], which includes a total of 24 simulations aimed at exploring different possible scenarios concerning the origin and evolution of magnetic fields in the cosmic web environment [Vazza et al., 2017]. Here, we focus on four of the most realistic models, characterized by relevant variations of the topology of magnetic fields, which is very interesting for our study:

1. *"baseline"*: non-radiative run with a primordial uniform volume-filling comoving magnetic field $B_0 = 1$ nG at the beginning of the simulation;

2. *"Z"*: non-radiative run with a primordial magnetic field oriented perpendicularly to the velocity vector, as in Vazza et al. [2017]; in order to ensure that $\nabla \cdot \mathbf{B} \equiv 0$ at the beginning, the starting magnetic field vectors were initialized perpendicularly to the three-dimensional gas velocity field computed with the Zel'dovich approximation [e.g. Dolag et al., 2008], so that a purely solenoidal initial field is produced and thus enforce the $\nabla \cdot \mathbf{B} \equiv 0$ condition construction. The r.m.s. values of each component generated with the Zel'dovich approximation are renormalized within the cosmic volume, in order to match the same level of seed magnetic field as in the baseline primordial run, i.e. $\sqrt{\langle B^2 \rangle} = B_0$;

3. *"DYN5"*: non-radiative run with sub-grid dynamo magnetic field amplification. The small-scale dynamo amplification of a weak seed field of primordial origin ($B_0 = 10^{-9}$ nG comoving) is computed at run-time. In this model, the dissipation of solenoidal turbulence into magnetic field amplification is estimated at run-time based on the measured gas velocity vorticity in the cells, with a flow Mach number-dependent efficiency derived from Federrath et al. [2014]. This model attempts to bracket the possible residual amount of dynamo amplification which can be achieved in low density environments as suggested by other works [e.g. Ryu et al., 2008], but is lost due to finite resolution effects [see Vazza et al., 2017, for more details];

4. *"CSFBH2"*: radiative run with an initial background magnetic field $B_0 = 10^{-10}$ nG (comoving) including gas cooling, chemistry, star formation, thermal/magnetic feedback from stellar activity and active galactic nuclei (AGN). In this model, supermassive black hole (SMBH) particles are initially added to the simulation at $z = 4$ at the center of massive halos as "seeds", with an initial mass of $M_{\mathrm{BH},0} = 10^4$ M$_\odot$ [Kim et al., 2011]. From that moment on, they accrete matter from

---

[1]http://cosmosimfrazza.myfreesites.net/the_magnetic_cosmic_web

the gas distribution in the grid based on the spherical Bondi-Hoyle formula, assuming a fixed $\sim 0.01\,M_\odot/\text{yr}$ accretion rate and a "boost" factor to the mass growth rate of SMBH ($\alpha_{\text{Bondi}} = 1000$, calibrated to balance the unresolvable gas clumping in the innermost accretion regions). Star forming particles are also generated on the fly based on the Kravtsov [2003] star formation recipe, which also accounts for the thermal feedback of star formation winds onto the surrounding gas. In this simulation we coupled the ENZO thermal feedback from SMBH and from star forming particles to the injection of additional magnetic energy via bipolar jets, with efficiencies $\epsilon_{\text{SF,b}} = 10\,\%$ and $\epsilon_{\text{BH,b}} = 1\,\%$ for the star formation and SMBH respectively, referred to the corresponding $\dot{M}c^2$ energy accreted in the two processes. While all above prescriptions obviously represent a gross oversimplification of the very complex physics behind star formation and black hole evolution, such ad-hoc models have been calibrated and chosen out of the larger sample of simulations tested in Vazza et al. [2017] as they provide a good match to the observed cosmic average star formation rate as well as to observed galaxy cluster scaling relations. Our main purpose in using this model is to have a realistic representation of the impact of galaxy formation physics on the $\gtrsim 100$ kpc scales which are relevant for our study of cosmic magnetism and structure formation shocks.

The cosmological parameters were chosen accordingly to a ΛCDM cosmology: $H_0 = 67.8\,\text{km s}^{-1}\,\text{Mpc}^{-1}$, $\Omega_b = 0.0468$, $\Omega_m = 0.308$, $\Omega_\Lambda = 0.692$ and $\sigma_8 = 0.815$ [Planck Collaboration et al., 2016]. In the following, we will refer to these simulations as to the "Chronos" runs.

5.2.3 Nested grid simulations

To study the evolution of obliquity and magnetic fields around galaxy clusters at a resolution more comparable to the one of radio observations, we also examined six simulations from the "San Pedro" suite[2] [Wittor et al., 2020]. This set of simulations uses nested grids to assure a uniform resolution even at the most refined level. Each cluster was extracted from the box with a root-grid size of $(207\,\text{Mpc})^3$ sampled with 256^3 cells. A region of $\approx (6.5\,\text{Mpc})^3 - (9.8\,\text{Mpc})^3$ was further refined using five levels, i.e. 2^5 refinements, of nested grids. The procedure guarantees a uniform resolution of ≈ 25 kpc comoving around the clusters, from the beginning to the end of the run. The sizes of the nested regions ensure that their volume is at least 3.5^3 times larger than the volume enclosed in r_{200}^3[3]. The initialization of the nested grids was performed using MUSIC [Hahn and Abel, 2011]. In each simulation, the initial magnetic field is uniform and takes a value of 0.1 nG (comoving) in each direction. The six clusters used in this work are characterised by different evolutionary stages, ranging from pre-merger, over actively merging, to post-merger.

We note that these simulations use slightly different cosmological parameters than the Chronos runs (see Section 5.2.2). The parameters of these runs are based on the latest results from the Planck-collaboration [i.e. Planck Collaboration et al., 2018]: $H_0 = 67.66\,\text{km s}^{-1}\,\text{Mpc}^{-1}$, $\Omega_b = 0.04831914$, $\Omega_m = 0.3111$, $\Omega_\Lambda = 0.6889$ and $\sigma_8 = 0.8102$. Furthermore, for code stability issues at the fixed refinement regions in this case we used the somewhat more diffuse Local Lax-Friedrichs (LLF) Riemann solver to compute the fluxes in the PLM. In the following, we will refer to the set of nested simulations as to the "San Pedro" runs.

---

[2] https://dnswttr.github.io/proj_sanpedro.html

[3] r_{200} is defined as the radial distance from the cluster center inside which the mean density is 200 times the critical density.

5.2.4 Shock finder

The shock finding method is applied in post-processing and it is based on Ryu et al. [2003], with the changes explained in Vazza et al. [2009]. It allows to determine the Mach number M of a shock from the velocity jump $\Delta v \leq 0$ between pre-shock and post-shock cells:

$$\Delta v = \frac{3}{4} v_s \frac{1 - M^2}{M^2}, \tag{5.1}$$

where $v_s = M c_s$ and c_s is the sound speed of the pre-shock cell. The procedure is the following:

1. candidate shocked cells are selected with the constraint on the three-dimensional velocity divergence $\nabla \cdot \mathbf{v} < 0$;

2. for each Cartesian direction, the pre-shock (post-shock) cell is identified as the one with the minimum (maximum) temperature at a distance Δx from the candidate cell. We investigated different values for $\Delta x = 1, 2, 3$, which serves as a stencil for the computation of the Mach number via jump conditions. This is motivated by the fact that numerical shocks (especially if they are oblique with respect to the grid) are not an ideal discontinuity but are typically broadened across a few cells: hence, the jump conditions must be computed over a large enough distance. Our tests have shown that the optimal choice here is $\Delta x = 1$, since larger steps would include the contribution of contaminating flows unrelated to the shock, consistently with previous work [Vazza et al., 2009];

3. the shock Mach number is given by Equation 5.1 for each of the three dimensions, preceded by a sign indicating the orientation of the velocity jump: in case multiple contiguous cells are flagged as shocked along the same direction, those with the lowest absolute Mach number are discarded;

4. the final Mach number is calculated as $M = \sqrt{M_x^2 + M_y^2 + M_z^2}$ and it is assigned to the post-shock cell;

5. only shocks above a certain threshold of Mach number (which we calibrated depending on the resolution of the specific simulation, see Section 5.3.2) are considered in order to prevent spurious identification in the complex gas flows of galaxy clusters [e.g. Vazza et al., 2009].

The three components of the Mach number give the direction along which the shock propagates, i.e. the normal to the shock front.

5.2.5 Shock obliquity

The obliquity is computed as the angle between the propagation direction and the magnetic field $\mathbf{B}$ in the pre-shock cell:

$$\theta = \arccos\left(\frac{M_x \cdot B_x + M_y \cdot B_y + M_z \cdot B_z}{M \, B}\right). \tag{5.2}$$

and it ranges from $0°$ to $180°$. In the following analysis we will mostly refer to the quantity defined as $\Theta = 90° - |90° - \theta|$, which ranges from $0°$ to $90°$: this way, for example, shocks with $\theta = 20°$ and $\theta = 160°$ are considered equivalent in terms of CR acceleration efficiency (see Figure 5.1).

During step (iii) of the shock finding procedure, for each shock we identify three pre-shock cells, one for each direction, in order to compute the Mach number components M_x, M_y and M_z from jump conditions. Knowing the up-stream magnetic field orientation is necessary to measure the shock obliquity,
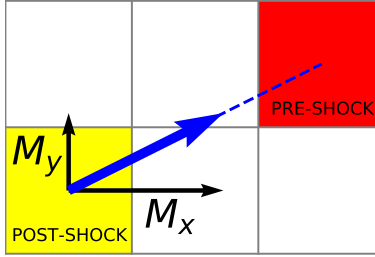
Figure 5.2: Sketch of the adopted procedure to identify the pre-shock region (red) of a post-shock cell (yellow) in our simulation, under the prior that the numerical shock structure is always spread over at least three cells (here a simple two-dimensional case is given for simplicity).

so we need to identify a single cell as the pre-shock. Determining the proper pre-shock cell for each identified shocked cell is not always a trivial operation, as in converging flows or shocks with complex pre-shock conditions this operation is affected by some level of uncertainty, and numerical shocks are typically spread over (at least) three cells. Hence, to locate the pre-shock of a given shocked cell, we have to move two cells away, along the direction suggested by the measured Mach number. Figure 5.2 gives the example of the reconstruction of post-shock and pre-shock cells for an oblique shock (limited to the two-dimensional case for simplicity). In this analysis, we choose the pre-shock cell as the one that is bound to be crossed by the shock at the following timestep in the simulation. In practice, a cell is tagged as a pre-shock cell, if a) it is located in the up-stream of the shock, b) it lies along the shock normal and c) it is located at a distance of two grid cells from the post-shock cell.

This approach has provided reasonable identification of pre-shock cells, which can be we visually checked in the case of large-scale shocks, such as those surrounding cosmic filaments or galaxy clusters. Another way to determine the reliability of this method is to evaluate the conservation of the component of the magnetic field parallel to the putative shock normal, as required by idealized MHD: we discuss this issue in more detail in Appendix 5.7.1.

Figure 5.3 gives an example of the distribution of shocks around a galaxy cluster (and around a zoomed filament) as well as of their obliquity, as measured by our method. Shocks are distributed around the cluster and the filaments with a large range of angles, yet with a clear predominance of quasi-perpendicular geometries ($\Theta > 45°$). A higher resolution view of the distribution of shock obliquities around clusters and during their formation will be given in more detail in Section 5.3.2.

5.3 Results

5.3.1 Analysis of full cosmic volumes

Thermal, magnetic and shock properties at $z = 0$

First, we analyze the final properties of shocks and magnetic fields in our four different Chronos unigrid runs, described in Section 5.2.2. In Figure 5.4, we show the projected maps of gas density, DM density, gas temperature and magnetic field strength integrated along the line of sight, for our baseline simulation at $z = 0$. The maps show the usual clustering of cosmic matter into galaxy groups and galaxy clusters ($\sim 10^6$ K in the projected temperature map), cosmic filaments ($\sim 10^4 - 10^5$ K) and voids. Following from the density contrast formed within structures, as well as partially from the dynamo amplification within the largest halos, the projected magnetic field varies over two orders of magnitude from voids to halos. In
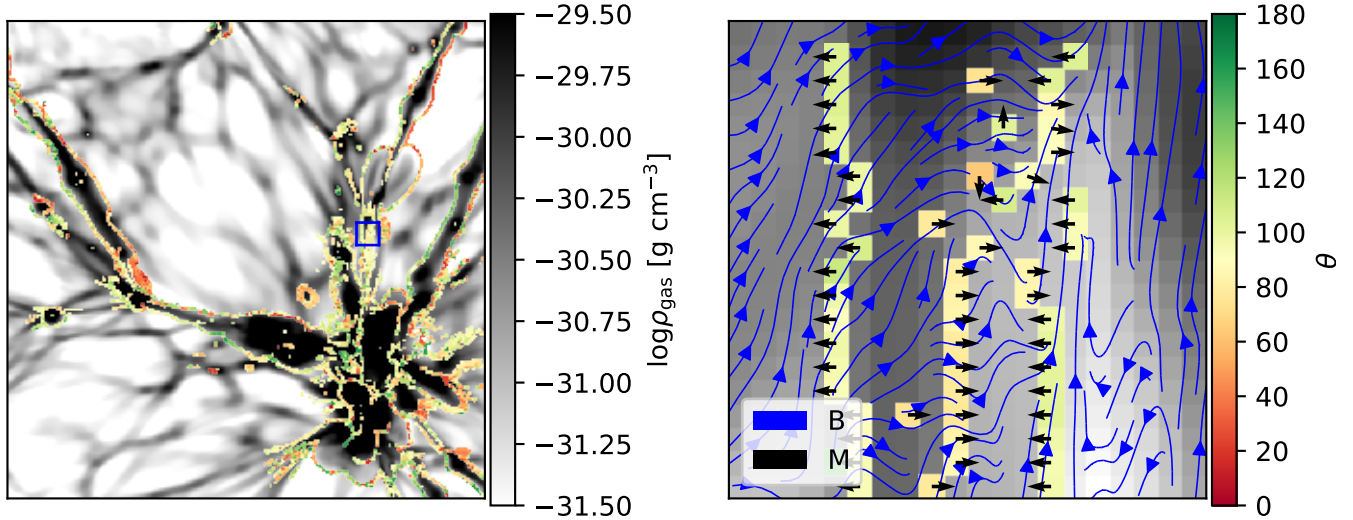
Figure 5.3: Density slice of the baseline simulation at redshift $z = 0$, with shocks color-coded by obliquity: the highlighted square on the left is zoomed on the right, where the arrows represent the projected magnetic field and Mach number. The box length is ≈ 41 Mpc on the left and ≈ 1.6 Mpc on the right.

reality, the range of difference in the three-dimensional grid is even higher, and the magnetic field within halos can reach $\sim 0.1 - 1$ μG (e.g. Figure 5.12 below). For other visualizations of the distribution of magnetic fields in these runs we refer the reader to Vazza et al. [2017] and Gheller and Vazza [2019]. From the combination of the above trends we can expect that the thermal gas energy and the magnetic energy (and possibly their ratio) can vary very significantly across the simulated volume.

In particular, the relative importance of the thermal component with respect to the magnetic component in a magnetized plasma is parametrized by the quantity $\beta = nk_{\mathrm{B}}T/(B^2/8\pi)$, defined as the ratio of the thermal pressure over the magnetic pressure. In Figure 5.5, we show the values of β in the same slice of volume for the four simulations. In all runs, there is a considerable difference between the values of β in virialized structures and in voids, but the trends are opposite for the first two and last two runs, and are mostly driven by the different scenarios for magnetogenesis. The baseline and Z simulations are overall characterized by low values of β, due to their stronger seed magnetic field. In such cases, β is highest in clusters and filaments, owing to the larger value of gas pressure there. On the other hand, in runs with weak seed magnetic fields (DYN5 and CSFBH2) the thermal pressure in voids always dominates over the very weak magnetic pressure ($\beta \gg 1$), while dynamo and stellar evolution amplify magnetic fields to $\beta \sim 1 - 10^2$, only within dense structures. Therefore, in our scenarios there are several environments in which the effect of magnetic pressure is not negligible compared to the thermal pressure. However, it shall also be noticed that even where $\beta \sim 1$, in the cosmic volume the kinetic ram pressure is always dominant, due to the typically large ($\sim 10^2 - 10^3$ km s^{-1}) infall motions induced by accretions: hence, in most cases the magnetic fields are still being passively advected in the cosmic volume.

We analyzed shocked cells in the simulated volume and we selected only shocks with $M > 2$, since weaker shocks are expected to be unable to accelerate CRs [Ha et al., 2018c]: identified shocks in all runs correspond to ≈ 2 % of the total number of cells. In Figure 5.6, we show the distribution of shock Mach numbers in the entire volume. The shape is consistent with previous results from the literature [e.g. Ryu et al., 2003], i.e. cosmological shocks belong to two distinct populations, external and internal
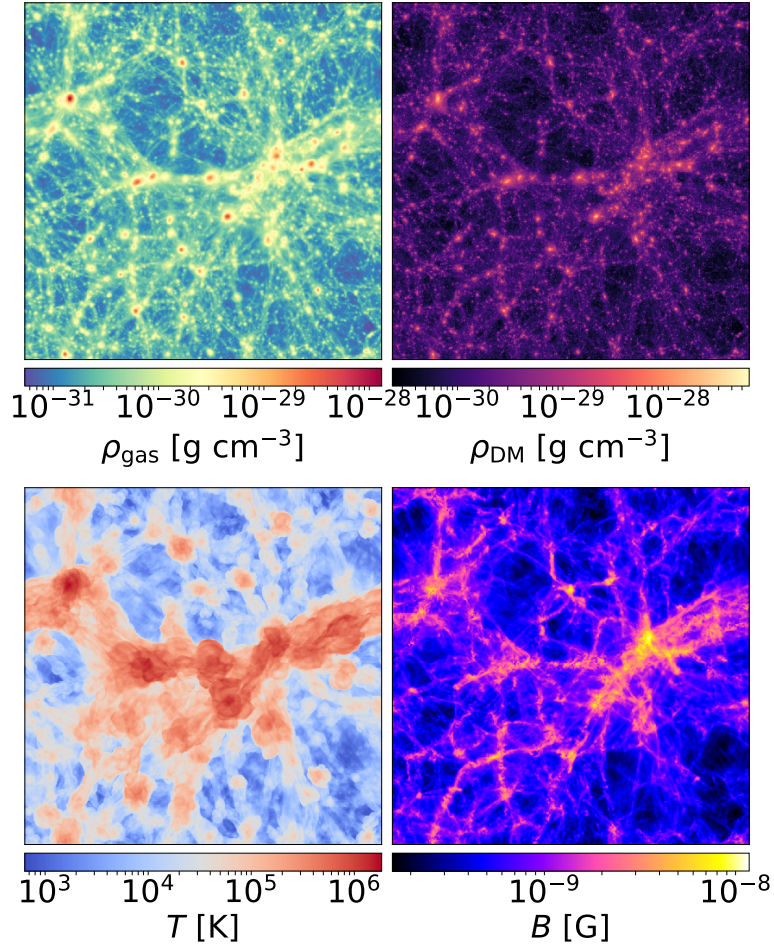
Figure 5.4: Maps of average gas density, DM density, temperature and magnetic field volume-weighted along the line of sight for the baseline simulation at $z = 0$. The box length is ≈ 85 Mpc.
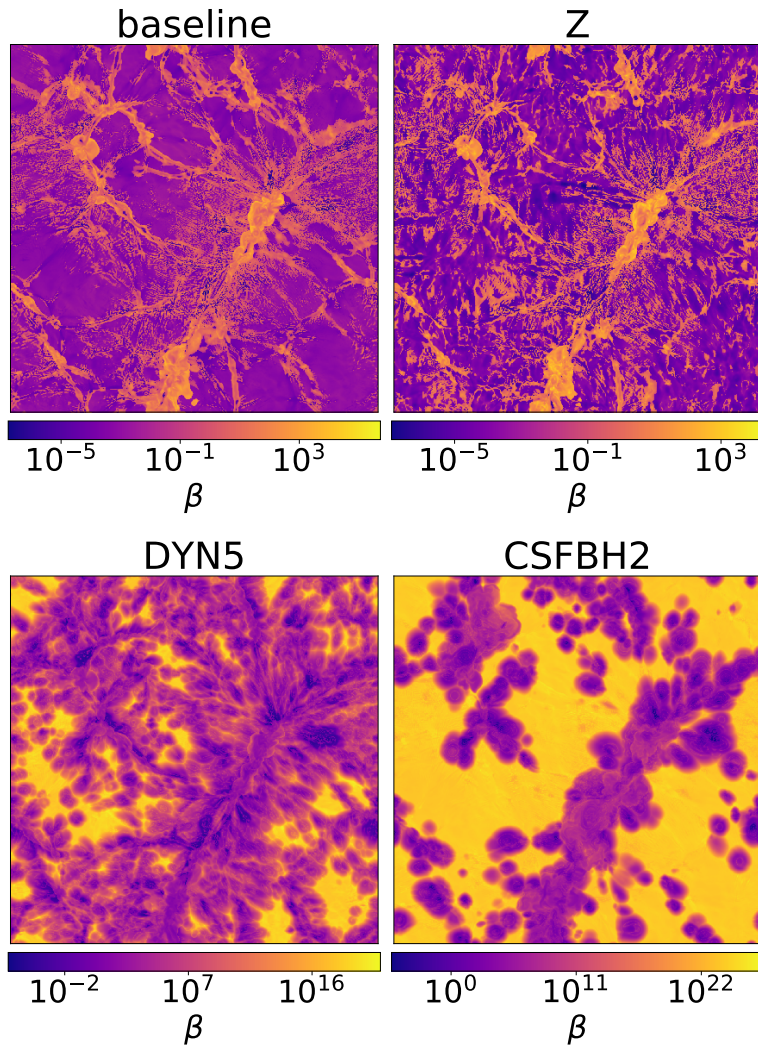
Figure 5.5: Plasma β of a slice of volume with thickness of 83 kpc for the four Chronos simulations at $z = 0$. The box length is ≈ 85 Mpc.
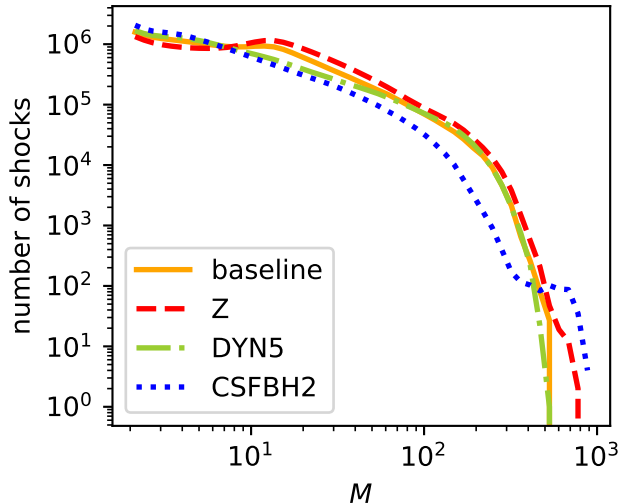
Figure 5.6: Number of occurring shocks per intervals of Mach number for the four Chronos simulations at $z = 0$.

shocks, identifying shocks affecting gas with pre-shock temperature $\lesssim 10^4$ K or $\gtrsim 10^4$ K respectively, the latter meaning that the material had already been previously shocked. This division can be observed in Figure 5.6, where the bump at $M \approx 20$ marks the separation between weaker internal shocks, associated to mergers, from stronger external shocks surrounding filaments. The distribution of CSFBH2 deviates from the others: at low M, a significantly larger number of shocks is generated in high-temperature regions due to AGN feedback, consistently to previous works [e.g. Kang et al., 2007, Vazza et al., 2013]. On the other hand at high M, due to heating effect of reionization modelled in CSFBH2, the gas temperature is increased to $\sim 10^4$ K, preventing the sound speed to be as low as in the other runs.

We computed the obliquity for each shock (as in Section 5.2.5): Figure 5.7, analogously to Figure 5.3, shows the distribution of shocks and the corresponding obliquity for a slice of the simulated volume for the remaining three runs. The density slice remains mostly unvaried from one run to another, as well as the location of the zoomed filament: however, the magnetic field topology differs, thus affecting the obliquity. We then investigated the deviation of obliquity from the distribution of angles expected from random vectors in space, which is $\propto \sin \theta$. Figure 5.8 shows the number of identified shocks per intervals of θ. The curves have a higher peak at perpendicular shocks with respect to the random distribution: previously-shocked gas hosts shocks that are on average more perpendicular than in the random distribution, likely due to the compression of the perpendicular component of the magnetic field after shock crossing, consistently to what Wittor et al. [2017] found. The CSFBH2 run shows a skewed distribution that may be attributed to the few bursts of star and/or AGN feedback which still occur at low redshift, and that can thus vary from snapshot to snapshot.

Figure 5.9 shows the excess of quasi-perpendicular shocks ($\Theta > 45°$, capable of accelerating electrons) with respect to quasi-parallel shocks ($\Theta < 45°$, capable of accelerating protons) as a function of Mach number. As it can be seen in Figure 5.8, for vectors randomly distributed in space a perpendicular configuration is more probable than a parallel one. In particular, a random configuration would return a value of $N_\perp/N_\parallel \approx 2.3$ integrated over the entire distribution of angles. Therefore, for weak shocks, quasi-perpendicular geometries are way more frequent than by chance, and thus the (magneto)hydrodynamics of gas is playing a role in aligning magnetic field vectors with the shock surface. We will discuss on
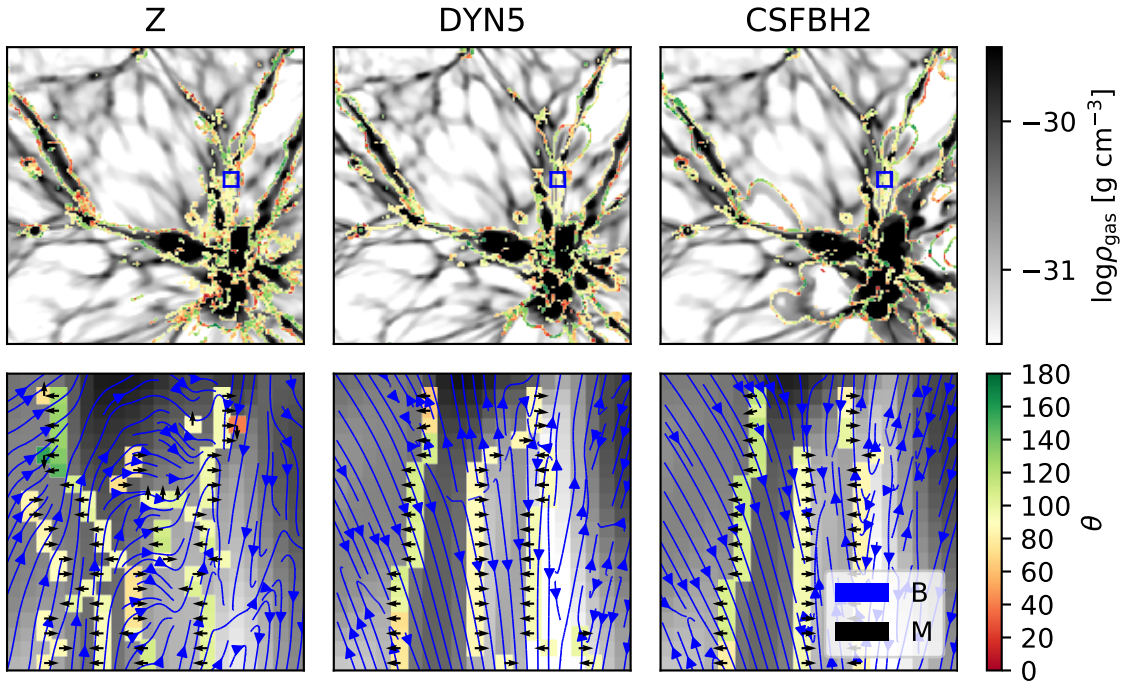
Figure 5.7: Same as Figure 5.3 for the remaining Chronos simulations.
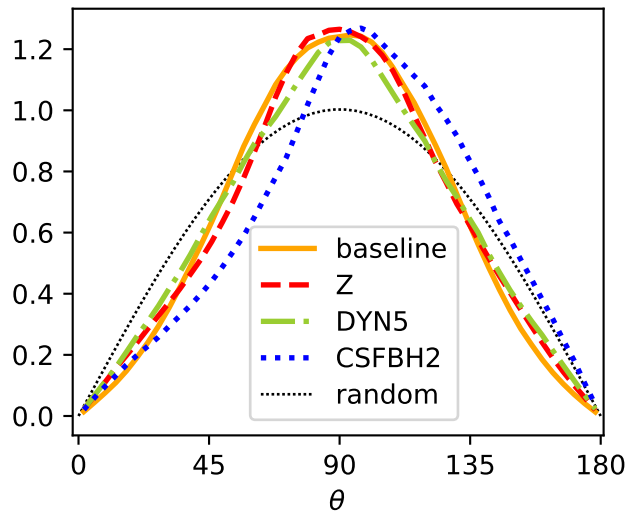

Figure 5.8: Number distribution of shocks per intervals of obliquity for the four Chronos simulations at $z = 0$, normalized to the random distribution.
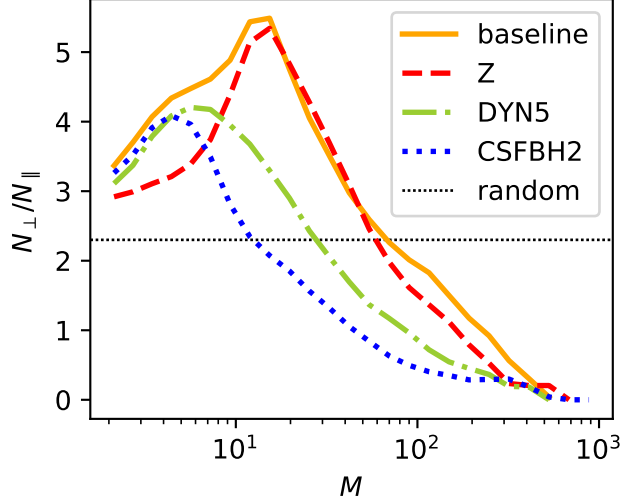
Figure 5.9: Ratio of number of quasi-perpendicular shocks and number of quasi-parallel shocks per Mach number intervals for the four Chronos simulations at $z = 0$, compared to the ratio expected for randomly distributed obliquities.

the physical interpretation of this phenomenon in more detail in Section 5.3.2 (see also Appendix 5.7.4). The opposite trend is found for $M \gtrsim 50$ shocks: at least in part, this can be ascribed to numerical problems. Shocks in this regime are not energetically relevant and are typically confined in very low density environment; the numerical uncertainties related to the modelling of shock obliquity in this regime are discussed in detail in Appendix 5.7.3.

The highest overabundance of perpendicular shocks is found at $M \approx 10$, with the exact location of the peak changing from one run to another. By computing the same ratio as a function of pre-shock density, we constrain the peak to be located at $\rho \approx 10^{-30}$ g cm^{-3}, independently of the specific re-simulation (Figure 5.10). This means that these shocks, which are more perpendicular than average, are likely to be generated in the same cosmic environment, regardless of the specific model for magnetism. Based on the density range, we can constrain these shocks to be associated with filaments of the cosmic web, which is also supported by visual inspection. However, the same density interval does not correspond to the same Mach number interval in the four runs: in CSFBH2 this is explained by the rise in temperature due to reionization, which limits the strength of shocks. Also in DYN5 we measure a larger temperature than in the other non-radiative runs, leading to slightly weaker shocks [Gheller and Vazza, 2019]. Filaments of the cosmic web are thus an environment where the acceleration of CRs mostly happens via quasi-perpendicular shocks, with implications on the injection and evolution of relativistic energy inside cosmic structures.

Energy dissipation

We define the incident kinetic energy flux as in Ryu et al. [2003]:

$$F_{\text{kin}} = \frac{1}{2} \rho_{\text{pre}} v_{\text{sh}}^3. \tag{5.3}$$

The total incident kinetic energy flux is represented in Figure 5.11: the trend, already expected from Figure 5.6, reflects the dual distribution of shocks, i.e. internal (low M), with a monotonic decreasing
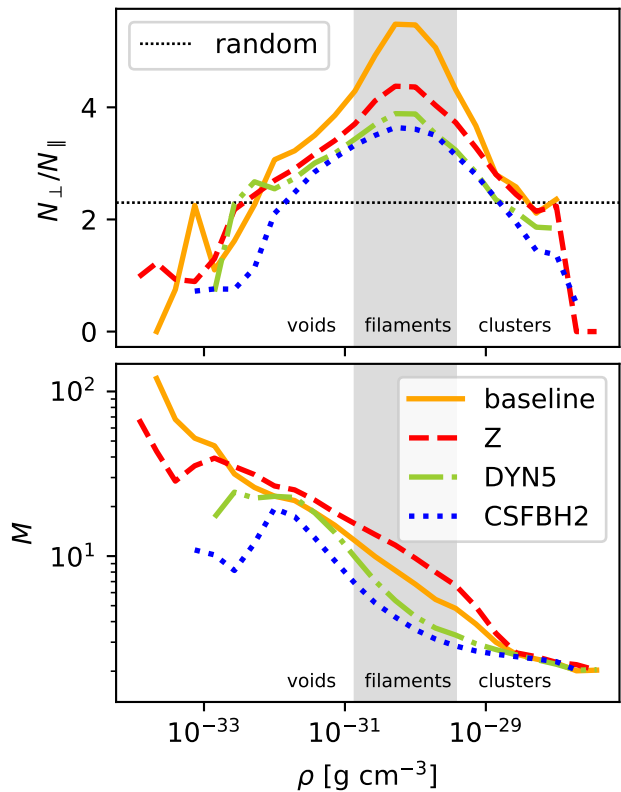
Figure 5.10: Top panel: ratio of number of quasi-perpendicular shocks and number of quasi-parallel shocks per density intervals for the four Chronos simulations at $z = 0$, compared to the ratio expected for randomly distributed obliquities. Bottom panel: mean Mach number per density intervals for the four Chronos simulations. In both panels the range in which the overabundance of perpendicular shocks is largest is highlighted in grey: this corresponds roughly to the regions hosting filaments.

Figure 5.11: Total kinetic flux per intervals of Mach number for the four Chronos simulations. The most energetic shocks ($M < 2$) have been excluded, as explained in 5.3.1.

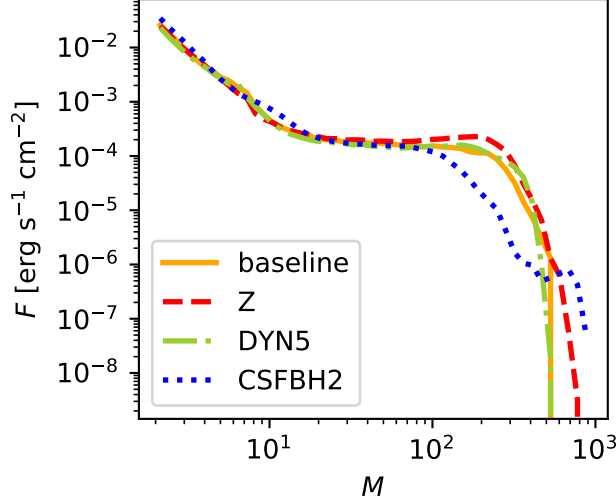flux, and external (high M), with a bump at $M \approx 100$. The behavior of CSFBH2 slightly deviates for $M \lesssim 5$ and $M \gtrsim 100$, for the same effects discussed in the previous Section. The dissipated incident kinetic energy flux which is converted into thermal energy flux F_{th}, or into a CR energy flux F_{CR}, can be parametrized as $\delta(M) = F_{th}/F_{kin}$ and $\eta(M) = F_{CR}/F_{kin}$, i.e. with the thermalization efficiency and with the assumed CR acceleration efficiency respectively. Although more recent works provided updated guesses for the acceleration efficiency by shocks, for the sake of comparison with previous works we based our prescriptions for δ and η on Kang and Ryu [2013], which assumed DSA as the accelerating mechanisms and included the effect of magnetic field amplification by CR streaming instabilities and Alfvénic drift.

The (ρ, T) phase diagrams of the shocked cells indicating the values of pre-shock magnetic field and dissipated flux are given in Figure 5.12. In all the four runs, high-M accretion shocks in low-density and low-temperature areas (see Figure 5.10) are less energetic (as in Figure 5.11) and occur in higher-β plasma. Instead, the most energetically relevant events occur in denser and hotter environments, through low-M internal shocks: ~ 85 % of the total energy flux in the volume is enclosed in the area having approximately pre-shock values of $\rho \gtrsim 10^{-30}$ g cm^{-3} and $T \gtrsim 10^5$ K in all runs. Therefore, without taking into account the effect of shock obliquity on the acceleration of CR, we can expect the bulk of CR acceleration to happen in the same environment in all models, i.e. within and around galaxy clusters/groups of galaxies. On the other hand, the four simulations are characterized by very different pre-shock magnetic field strengths: as a consequence of DYN5 and CSFBH2 having very weak seed fields, shocks in rarefied regions run over magnetic field strengths which are several orders of magnitude below the ones in the baseline and Z run. We remark that the shape of the phase diagram in CSFBH2 differs from the others due to the inclusion of reionization, which increases the temperature of pre-shock regions at low cosmic densities: this delimits a region at the bottom of the diagram (below the sharp discontinuity marked by contours of magnetic field and energy flux) whose combinations of temperature and density are forbidden for the intracluster medium (ICM). Shocks below this line are likely to be related to outflows originated in dense regions, whose temperature has cooled down, while its associated magnetization has only be affected by adiabatic expanse [e.g Vazza et al., 2017]. However, these cells only process a negligible fraction of the total flux. In summary, despite the very dissimilar magnetic

properties of the simulations, we found a consistent trend as regards the thermal characterization of shocks and the energy dissipation.

Figure 5.13 shows the ratio of the total CR energy flux in quasi-perpendicular shocks over the total CR energy flux in quasi-parallel shocks within gas density bins. While in the main paper we adopt the simple approach of setting the flux dissipated by quasi-perpendicular shocks to 0 if $\Theta < 45°$, or vice versa for quasi-parallel shocks, in Appendix 5.7.2 we present tests using smoother transition of efficiencies, which suggest similar outcomes. While the global trends are in line with Figure 5.9, relating the $F_\perp/F_\parallel$ to the random distribution is here made difficult by the weighting for the energy flux, which can span across ~ 10 orders of magnitude in most environment, as shown above (Figure 5.12). As a consequence of this, a few energetic events can introduce large spikes in Figure 5.13, which makes it harder to compare this to the expectation from random models. In general, the predominance of quasi-perpendicular shocks across environment and the relative differences between models are the same already discussed in the previous Section.

Galaxy cluster properties

We identified galaxy clusters in the Chronos simulations using a standard algorithm, which delimits the virial volume of simulated halos based on the total matter overdensity, averaged assuming spherical symmetry with respect to the cluster center of mass [e.g. Gheller et al., 1998]. We performed the following analysis on the ten most massive clusters, which are in the mass range $5 \cdot 10^{13}$ $M_\odot \lesssim M_{100} \lesssim 3 \cdot 10^{14}$ $M_\odot$[4].

We extracted the radial profile of shocked cells inside these clusters for each of the four runs at redshift $z = 0$. In Figure 5.14, we give the median value of shock Mach number as a function of the distance from the cluster, which shows an overall monotonic trend for all runs, in which the median Mach number of shocks increases as the local sound speed decreases following the radial decrease of gas temperature. The combination of the shallower radial trend of gas temperature due to reionization, as well as the integrated effect of shocks previously launched by the past activity of AGN explains the flatter radial behaviour of the Mach number profiles of clusters in the CSFBH2 model. Figure 5.15 shows the flux dissipated by shocks for each radial bin: shocks in CSFBH2 are globally more energetic in the proximity of clusters due to the additional driving of powerful but low-M shocks promoted by AGNs. Even higher fluxes are expected for shocks more internal than 1 r_{virial}, but the averaging procedure blurs them in the simulated dataset, due to limited resolution and to the $M = 2$ lower threshold (see Section 5.3.2 for a more resolved view using nested grids). Finally, in Figure 5.16 we measure the ratio between the CR energy flux in quasi-perpendicular shocks over the CR energy flux in quasi-parallel shocks, as a function of radius from the cluster centers for the four runs. The trend of this ratio as a function of radius is similar to the one obtained as a function of gas density in Figure 5.13, and further confirms the general trend that models with a large primordial seed field have a significantly larger dissipation of shock energy flux through quasi-perpendicular shocks, even at distances of $\sim 3 - 4$ r_{virial} from the center of clusters.

We can recap the main results achieved by the analysis of the low-resolution cosmic volumes by saying that an excess of quasi-perpendicular shocks is widespread in all magnetization scenarios and in most cosmic environments. The extent of this tendency to produce perpendicular shocks has proven to be a function of magnetic properties, gas density, shock strength and distance from the clusters. In particular, we consistently report that in shocks surrounding filaments the excess of quasi-perpendicular shocks is extreme, rather independently on the assumed magnetization scenario.

In order to better assess the significance of such results at higher resolution, as well as to resolve in time the process which brings simulated fields to align with filaments, in the next Section we apply the

---

[4]M_{100} is defined as the total mass enclosed in a spherical volume of radius r_{virial}, i.e. the distance from the cluster center where the average inner matter density is 100 times the cosmological critical density.

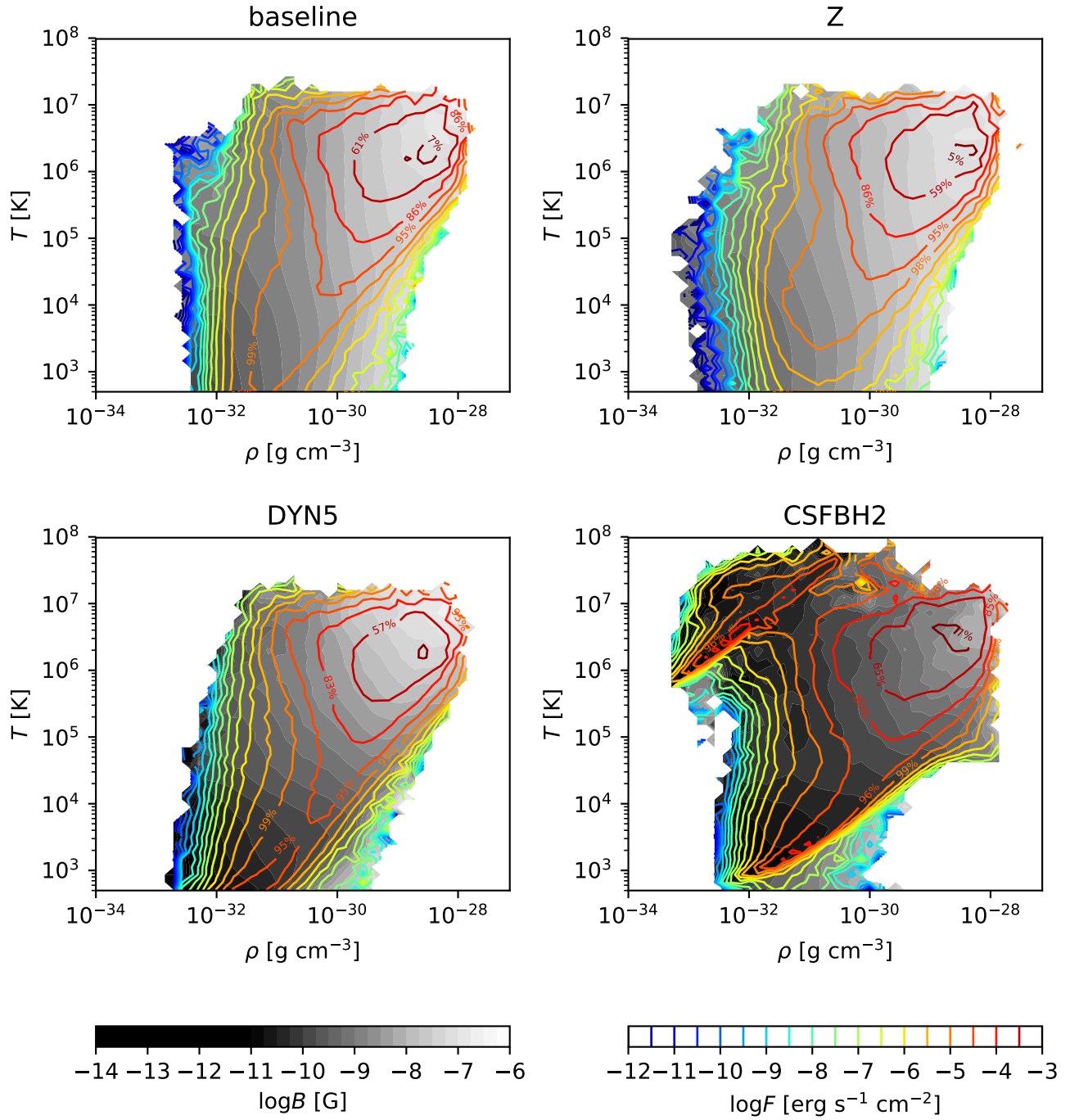Figure 5.12: Phase diagrams of shocked cells showing the pre-shock magnetic field in grey scale per intervals of pre-shock gas density and temperature for the four Chronos simulations at $z = 0$. The colored contour lines show the sum of the dissipated flux in each bin, while the percentages indicate the fraction of the total flux which is dissipated for values of the flux higher than the corresponding one.

Figure 5.13: Ratio of CR flux in quasi-perpendicular shocks and CR flux in quasi-parallel shocks as a function of gas density for the four Chronos simulations at $z = 0$.
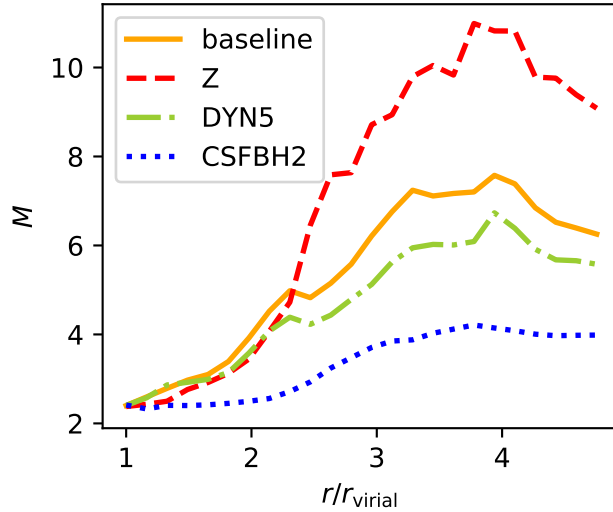
Figure 5.14: Median Mach number as a function of radial distance from the cluster cores in units of virial radius in the range $1 < r/r_{\mathrm{virial}} < 5$. Values of M span from ≈ 2 to ≈ 10: the CSFBH2 run hosts weaker shocks due to the higher temperatures.
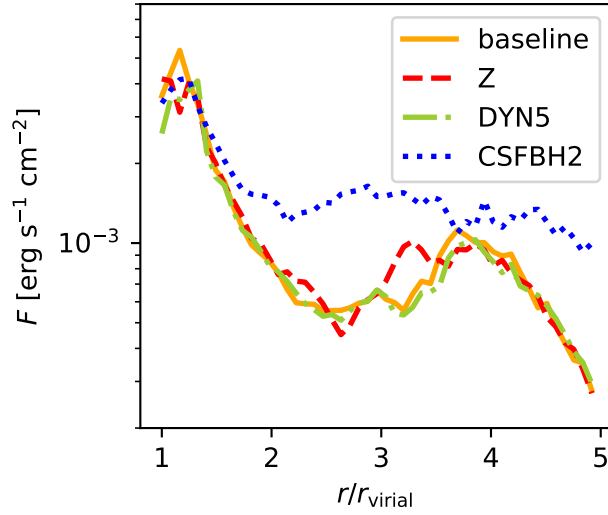
Figure 5.15: Total dissipated kinetic flux as a function of the distance from the centers of the clusters, rescaled to the virial radius of each cluster, for the four Chronos simulations. The most energetic shocks ($M < 2$) have been excluded.
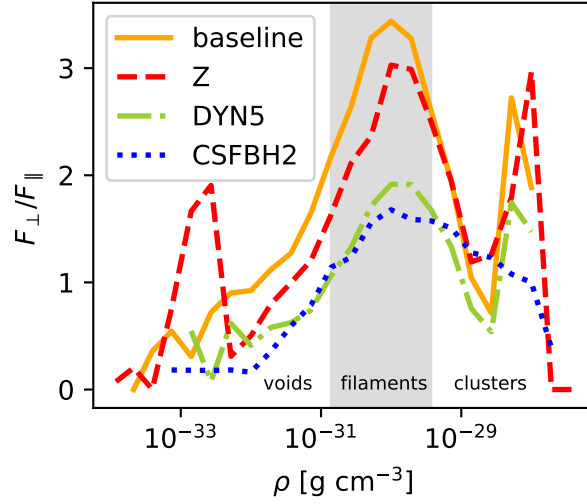

Figure 5.16: Ratio of CR flux in quasi-perpendicular shocks and CR flux in quasi-parallel shocks as a function of the distance from the center of the clusters, rescaled to the virial radius of each cluster, for the four Chronos simulations.
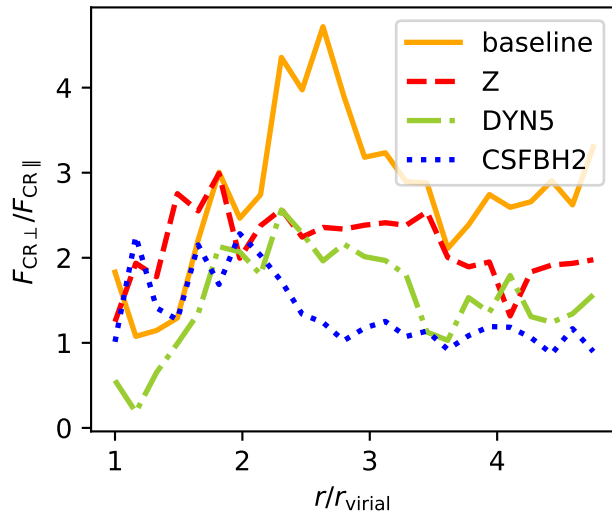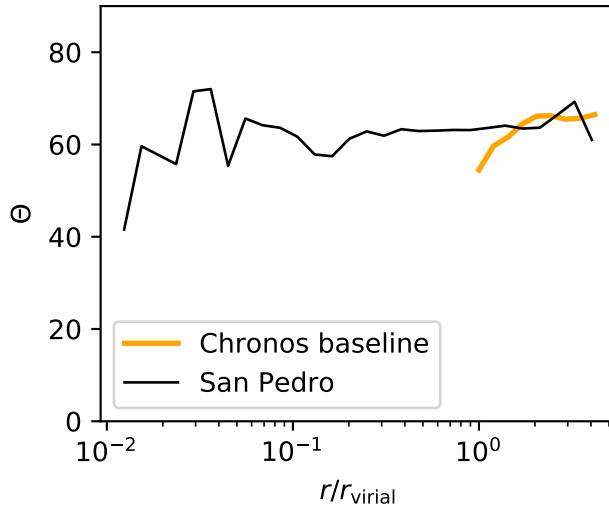
Figure 5.17: Median obliquity as a function of the distance from the centers of the clusters, rescaled to the virial radius of the six San Pedro clusters, compared to the ten clusters extracted from the baseline Chronos run.

same methods to study higher resolution simulations of galaxy clusters.

5.3.2 Temporal and spatially resolved analysis of galaxy clusters: the origin of the excess of quasi-perpendicular shocks

Shocks in the volume of clusters from the San Pedro runs were identified using the same procedure as for Chronos, except for the Mach number threshold: there, we neglected shocks below $M = 2$ for the larger simulations, since they are not expected to be able to accelerate particles [Ha et al., 2018c]. On the other hand, with San Pedro simulations we aim at studying the formation of perpendicular and parallel shocks, regardless of their strength and possibly even in the innermost hot regions of galaxy clusters, so in this case we set the threshold at $M = 1.3$, which gives us a slightly higher statistics of shocks. Probing weaker Mach numbers gets also more accurate at high resolution, while on coarser grids spurious classification can occur.

First, we assess whether there is a regularity between the two sets of simulations, in particular between the San Pedro clusters and the baseline simulation from Chronos, whose initial conditions are similar, and we investigate the reason behind the quasi-perpendicular excess found in Chronos. Figure 5.17 shows the median obliquity of shocks for each bin of radial distance from the cluster centers: we find there is an agreement above 1 r_{virial}, while there are too few identified shocks closer to the cluster cores in Chronos, due both to the lower resolution and to the higher Mach number threshold. The distribution of shocks in the central slice of the high-resolution clusters can be seen in Figure 5.18, along with their color-coded obliquity.

The high-resolution clusters show an excess of quasi-perpendicular shocks, which is visually rendered by the predominance of blue cells in Figure 5.18. Figure 5.19 shows the excess of quasi-perpendicular to quasi-parallel shocks as a function of Mach number for the six clusters, which is mostly prominent in the $5 \lesssim M \lesssim 20$ range, similar to the previous statistics derived for the Chronos suite. The shift in the peak from Chronos to San Pedro simulations is due to the ~ 3 times better resolution of San Pedro runs,

51
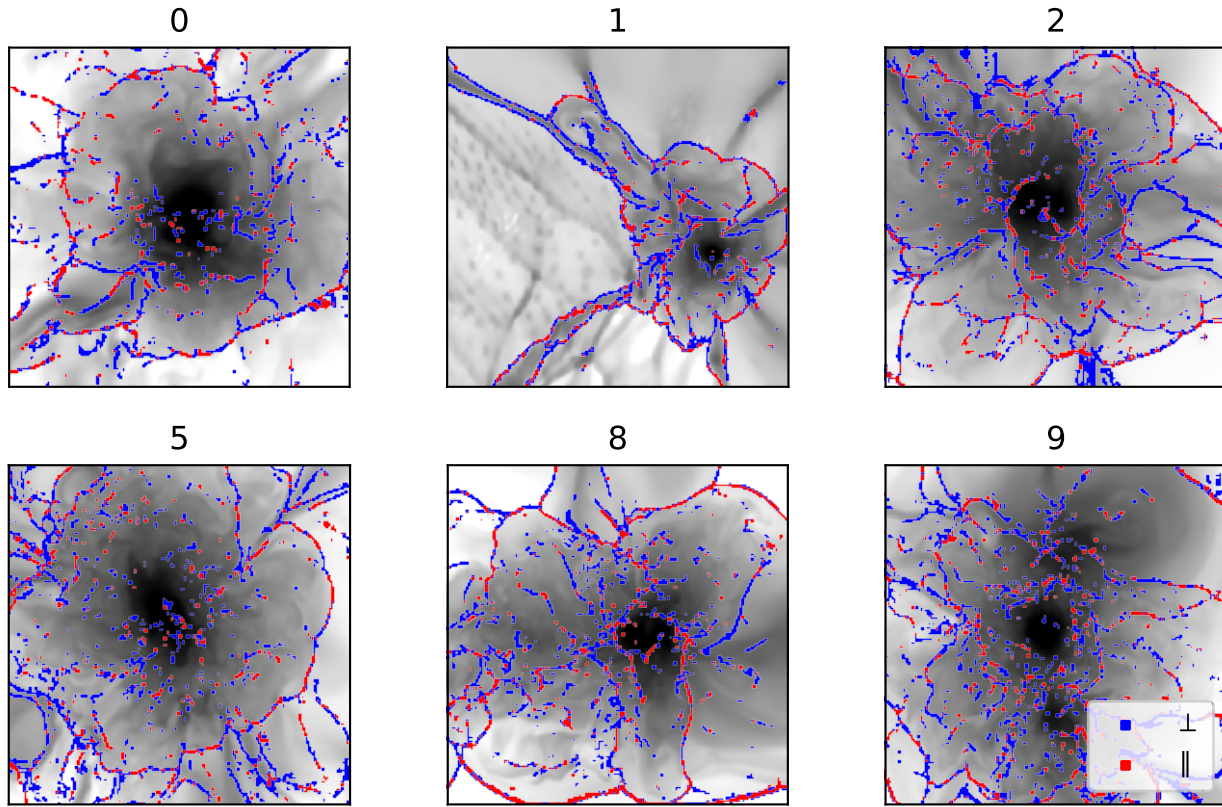
Figure 5.18: Central slice of the San Pedro galaxy clusters. The grey scale measures the gas density, shocked cells are identified in blue (quasi-perpendicular) and red (quasi-parallel). The box length varies from ≈ 6.5 Mpc to ≈ 9.8 Mpc.
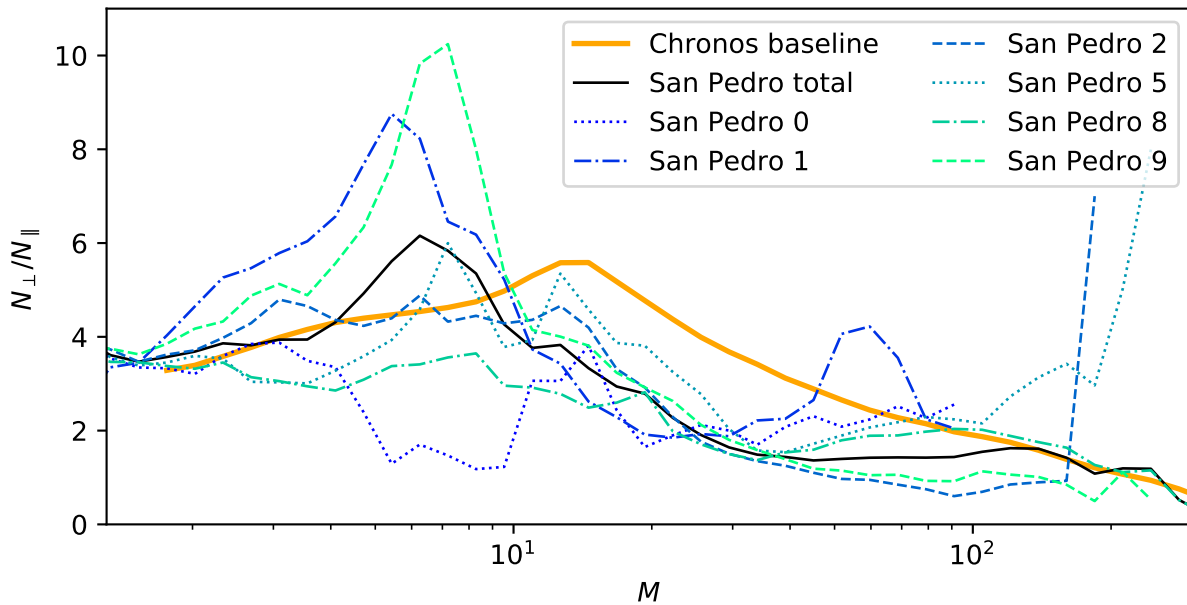

Figure 5.19: Ratio of quasi-perpendicular to quasi-parallel shocks per Mach number intervals for the six San Pedro clusters (both individually and collectively), compared to the baseline Chronos run.

which affects the Mach number estimation (see Section 5.2.4).

Shocks propagating from the clusters outwards are mostly parallel, while quasi-perpendicular shocks are often associated to filaments (Figure 5.18): thanks to the higher resolution we now have a clearer view of what happens in the pre-shock region outside filaments. Due to the shear of the velocity field where filaments form starting from the cosmological initial conditions, derived from the Zel'dovich approximation [Bond et al., 1996], the magnetic field lines are dragged by the gas and tend to align with the leading axis of filaments.

Such large-scale motions, described by the shear velocity tensor, are primordial, in the sense that they are already contained in the initial conditions of cosmological simulations [e.g. Libeskind et al., 2014, Zhu and Feng, 2017]. This leads to the presence of significant alignment of the velocity field and of filaments already very early ($z \gtrsim 20$) as well as to a persistence of the leading orientation of the shear tensor for large, $\gtrsim 10$ Mpc scales. These scales are manifestly larger than the ones involved in the formation of accretion shocks, as well as in the injection of vorticity within filaments [e.g. Ryu et al., 2008]. Simulations have also shown that on such linear scales the dynamics of gas fully follows the one of DM [e.g. Zhu and Feng, 2017]. As a consequence, both pre-shock and post-shock velocity fields are affected by this phenomenon, as well as magnetic field lines, which mostly passively follow the gas velocity due to the large kinematic plasma β in this environment (see Section 5.3.1).

The effect of shear motions which develop in the formation region of filaments can be seen in Figure 5.20, where the streamlines of both velocity[5] and magnetic field tend to self-align with the leading axis of filaments. As this large-scale velocity shear emerges from the cosmological initial conditions and is structured on scales larger than the filament width, the local alignment affects both the pre-shock and the post-shock regions across the filament's edge. This can be observed in Figure 5.21, where the time evolution of the arrangement of the magnetic field around a filament is shown. Therefore, when shocks are formed at the interface between the infalling smooth gas accreted from voids and the filament's region, they often propagate over a magnetic field which was previously aligned with the filament axis by the large-scale shear. This leads to the tendency of forming mostly quasi-perpendicular shocks in the simulated cosmic web. The framework recently developed by Soler and Hennebelle [2017] (and applied to study the effects of MHD turbulence on the distribution of angles formed by density gradients, $\nabla\rho$, and magnetic fields in simulations of the interstellar medium) provides a quantitative explanations for this effect. They found that the alignment of the magnetic field along the direction of low-density structures (e.g. filaments) is spontaneously produced in regions where shear motions dominate over compression. In particular, they demonstrated that the configuration where $\nabla\rho$ and $\mathbf{B}$ are mostly parallel or mostly perpendicular are equilibrium points to which the fluid tends to evolve on hydrodynamical timescales, depending on the local flow conditions. Supported by direct numerical simulations, they reported that for low density, high β and large (negative) velocity divergence the relative orientation of magnetic fields and $\nabla\rho$ becomes preferentially quasi-perpendicular, and this well explains what we also observe in our simulations (see also Appendix 5.7.4). Considering that $\nabla\rho$ is in general a trustworthy tracer of the shock direction, this explains why shocks in our simulated filaments have the tendency of showing quasi-perpendicular geometries.

As a consequence, the excess of perpendicular shocks over parallel shocks (Figure 5.19) varies from cluster to cluster due to their different evolutionary stages, as well as depending on the number of filaments connected to them.

Finally, Figure 5.22 shows the evolution from $z = 10$ to $z = 0.1$ of one of the clusters with streamlines

---

[5]The considered quantity is actually $\mathbf{v} - \langle\mathbf{v}\rangle$, where $\langle\mathbf{v}\rangle$ is the velocity field averaged inside the whole slice. Without this adjustment, the flow motions would be dominated by a bulk displacement towards more massive centers of gravity lying outside the box and the smaller-scale flow around filaments would not be visible.
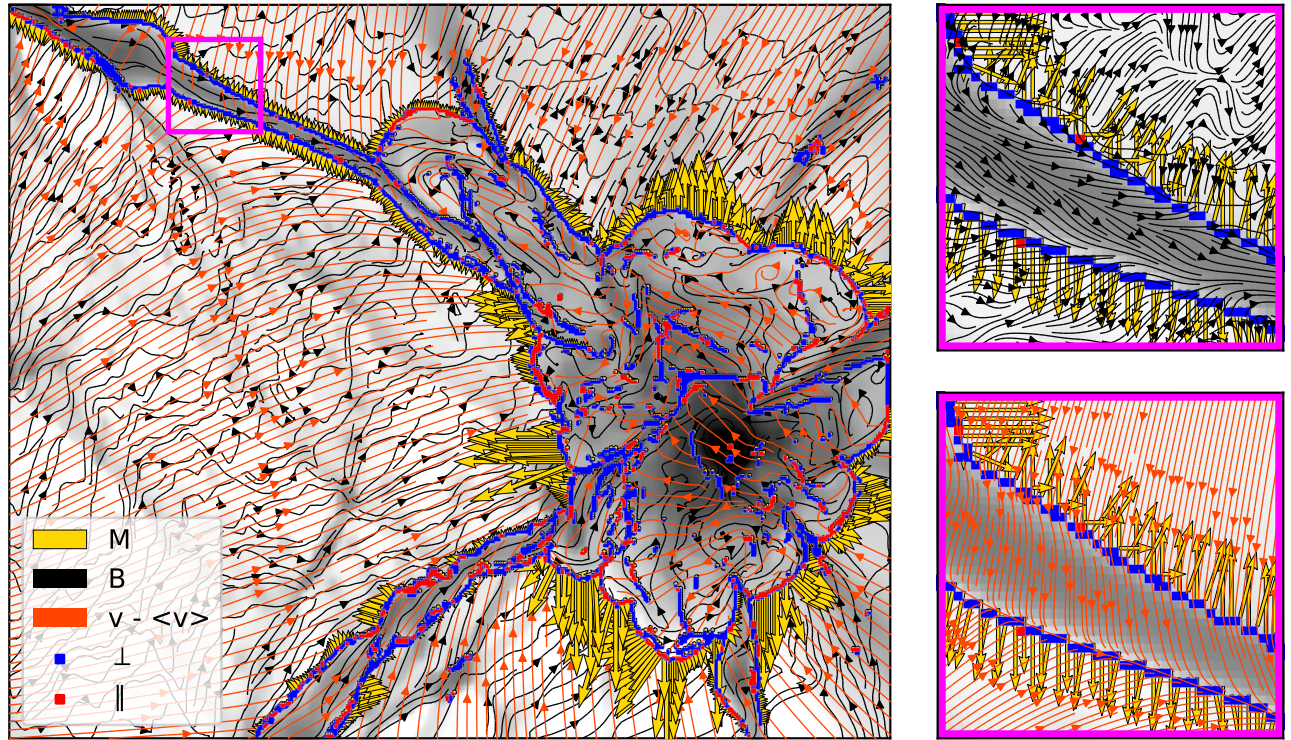
Figure 5.20: Left panel: slice of one of the San Pedro galaxy clusters (number 1). The grey scale measures the gas density, the black arrows trace the projected magnetic field, the orange arrows trace the velocity field. Blue and red cells indicate shocks (respectively quasi-perpendicular and quasi-parallel shocks), the yellow arrows indicate the projected direction of propagation and intensity of the shocks. The box size is $\approx (9.6 \times 8.0)$ Mpc^2. Right panel: zoom on a filaments from the left panel (box length of ≈ 1 Mpc), where the bending of the magnetic field (top) and velocity field (bottom) lines along the filament in the pre-shock region can be seen.

Figure 5.21: Time evolution of a filament near San Pedro cluster number 1, where the represented quantities are the same as Figure 5.20: magnetic field lines start to bend outside the filament before shocks are even generated, thus favoring perpendicular obliquities. The box size is $\approx (1.5 \times 1.8)$ Mpc^2.
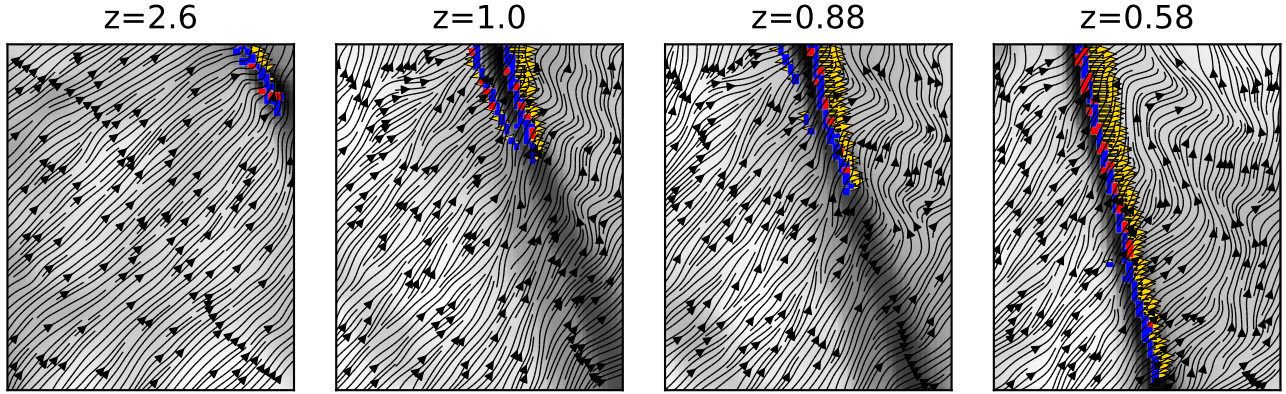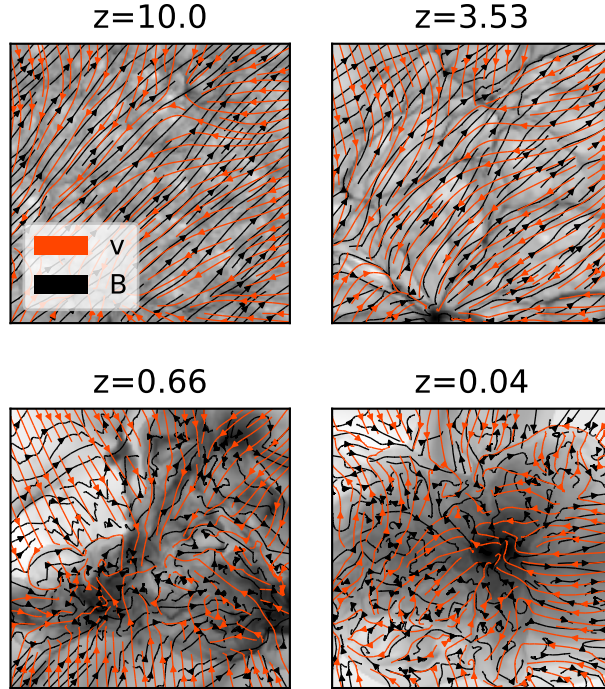
54

Figure 5.22: Central slice of one of the San Pedro galaxy clusters (number 8) at different redshifts z. The grey scale measures the gas density, the black arrows trace the projected magnetic field and the orange arrows trace the projected velocity field (box length of ≈ 9.6 Mpc).

of magnetic field and velocity: at the beginning the orientation is set by the initial conditions, but later on the dynamics begin to dominate and the fields self-arrange in a pattern that favors perpendicular shocks near filaments. The evolution of the quantity $N_\perp/N_\parallel$ is shown in Figure 5.23: higher values of this volume-weighted statistics are typically reached at high redshifts, given that the box includes more filaments before the cluster has grown to its final volume. As z decreases, the excess of perpendicular shocks decreases because the same volume gets increasingly more swept by internal merger shocks running over a typically tangled magnetic field.

In summary, our analysis supports that the circulation of gas falling into filaments, coupled via MHD equations to the evolution of magnetic fields [Soler and Hennebelle, 2017], is responsible for the observed tendency of shocks in filaments to be preferentially perpendicular to the local orientation of the magnetic fields. In retrospective, this model can also explain why the same tendency is somewhat less prominent in the CSFBH2 and in the DYN5 models, as previously outlined in Section 5.3.1. In the latter models, the magnetic field is subject to a more significant build-up over time, due to either the effect of the injection of new magnetic fields via feedback events, or due to the implemented sub-grid dynamo amplification. As a result of this, in these models shocks are typically running over dynamically "young" magnetic structures, in the sense that the alignment mechanisms described by Soler and Hennebelle [2017] is less effective there, because the equilibrium point in the local topology of magnetic fields and density gradient can only be reached after a fraction of the system crossing time. Moreover, the impulsive activity by AGN feedback continuously stirs fluctuations in the surroundings, making it difficult for the fluid to equilibrate. For the above reasons, we can thus conclude that the excess of quasi-perpendicular shock geometries is a tendency found regardless of the model of magnetogenesis, and that the amplitude of this excess is increased in primordial models, or in general in scenarios where magnetic fields have co-evolved with gas matters for longer timescales.
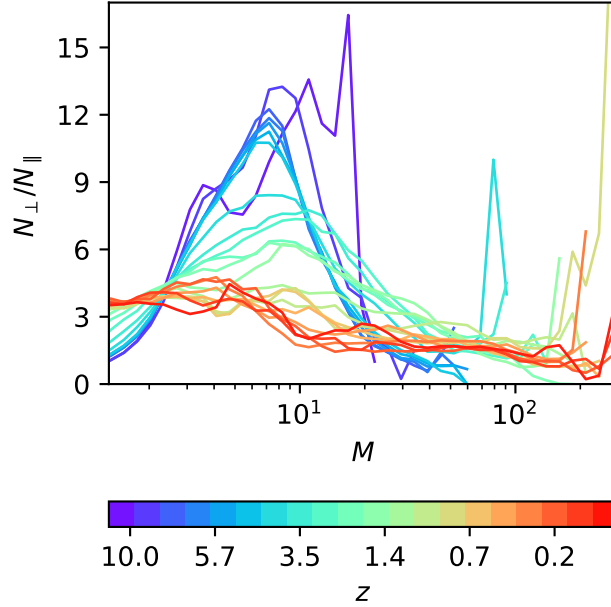
Figure 5.23: Time evolution of the ratio of quasi-perpendicular to quasi-parallel shocks per Mach number intervals for San Pedro cluster number 8 from redshift $z = 10$ to $z = 0.1$.

5.4 Implications for observations

The distribution of shock obliquities in the cosmic environment and in galaxy clusters may have a significant impact on the observed CR signatures, i.e. synchrontron radio emission produced by CR electrons and hadronic γ rays from CR proton interactions. We briefly discuss that the estimates of obliquities found in our work suggest that γ-ray emission may be lower than expected and thus explain the *Fermi*-LAT non-detections.

In Figure 5.24, we compute the differential and cumulative fraction of CR flux dissipated by parallel or perpendicular shocks with respect to the total F_{CR}, as a function of distance from the San Pedro clusters' cores. For the sake of simplicity, we consider here that the impact of obliquity on the acceleration of radio-emitting electrons can be studied with respect to the instantaneous energy dissipation at shocks, while the impact on CR protons is more related to the total energy flux processed by shocks within the cluster volume. Indeed, the characteristic lifetime of the synchrotron emitting electrons ($\sim$ GeV energies) due to energy losses is $\lesssim 10^8$ yr in clusters [van Weeren et al., 2019], which corresponds to a diffusion length-scale in the ICM of 10 kpc [Bagchi et al., 2002]. This implies that $F_{CR\perp}(r)$, i.e. the sum of the CR energy dissipated by quasi-perpendicular shocks within each radial shell, directly relates to the energy dissipation involved in the powering of observable radio relics. On the other hand, CR protons are long-lived (i.e. typically longer than the age of the cluster for energies $\lesssim 2 \cdot 10^7$ GeV, Berezinsky et al. 1997), and thus at a given epoch a better proxy for their level of hadronic γ-ray emission is given by the total integrated amount of CRs within the cluster radius. Figure 5.24 shows the average behavior of all shocks in the San Pedro sample, in which we binned the contribution from all clusters as a function of radius, normalized to the virial radius of each system. The plots show that $F_{CR\parallel}/F_{CR}$ lies mostly below $F_{CR\perp}/F_{CR}$, with a maximum difference at large radii from the cluster center, which based on Section 5.3.2 is largely related to filaments. The total dissipation via quasi-parallel shocks is ~ 40 % of the total CR flux within the virial radius, and only ~ 20 % within the clusters core (dashed line, left panel). The fraction of CR flux linked to perpendicular shocks is, on the other hand, larger than the random

distribution at distances larger than the virial radius (solid line, right panel), and is $\sim 80\,\%$ of the total CR flux in most of the large volume surrounding the clusters virial radius.

Figure 5.25 shows the phase diagrams of the CR flux for quasi-parallel and quasi-perpendicular shocks in all San Pedro clusters. Similar to what found for the Chronos phase diagrams, the most energetic merger shocks are located in the temperature and density range typical of the innermost ICM, i.e. $T \gtrsim 10^7$ K and $\rho \gtrsim 10^{-29}$ g cm^{-3}. Such shocks dissipate $\gtrsim 10^{-4}$ erg s^{-1} cm^{-2} and should be responsible for most of the injection of CRs in the ICM, and are also likely connected with the powering of radio relics, [e.g. van Weeren et al., 2019]. From the phase diagrams, it can clearly be seen that most of their CR flux gets dissipated into quasi-perpendicular shocks, up to $\sim 70 - 80\,\%$. On the other hand, quasi parallel shocks are found to dominate the dissipation of CRs only for low density regions, which are however associated with negligible CR flux levels ($\lesssim 10^{-8}$ erg s^{-1} cm^{-2}).

Fermi observations [Ackermann et al., 2014] constrained the CR proton pressure ratio $X_{\rm CR}$, i.e. the ratio between the total CR proton pressure and the total gas pressure within r_{200} for the observed cluster population at the level of $X_{\rm CR} \lesssim 1.3\,\%$. Under the assumption of a quasi-stationary population of shocks, and considering that the bulk of gas pressure and CR pressure is produced by shock dissipation, here for simplicity we can relate $X_{\rm CR}$ to the ratio of the instantaneous flux of CRs and thermal energy flux at shocks, i.e. $X_{\rm CR} \approx F_{\rm CR}/F_{\rm th}$, similar to other works [e.g. Vazza et al., 2009, Ha et al., 2019]. We thus computed this ratio assuming that all shocks are able to accelerate protons, and compared this to the same quantity restricted to $< 45°$. The two panels in Figure 5.26 compare the CR pressure ratio before and after the obliquity cut: if no distinctions were made in terms of obliquity, at least two of the simulated clusters in our sample would be detected by *Fermi*, while all the curves of $X_{\rm CR}$ are shifted below the *Fermi* detection threshold if only quasi-parallel shocks are considered. This suggests that our assumptions on obliquity could in principle be able to explain the missing detection of hadronic γ rays, even with the CR acceleration efficiency by Kang and Ryu [2013] assumed here.

In Figure 5.27 we show how the CR pressure ratio of the six clusters combined changes for different obliquity distributions. Although globally we obtained more perpendicular shocks than randomly expected, this is mostly relevant around filaments, while near cluster cores the trend is more similar to the random distribution of obliquities: as can be seen in Figure 5.24 as well, shocks occurring inside the cluster virial radius can even have more parallel obliquities than random. As a consequence, the CR pressure ratio which would be obtained from a purely random distribution of shock obliquities (in which $\approx 30\,\%$ of shocks would have $\Theta \lesssim 45°$) lies below the one found in the simulation (see dotted line in Figure 5.27). We also estimated the upper limit of the fraction of shocks able to accelerate protons ($\approx 72\,\%$), such that a higher value would generate a marginally detectable γ-ray emission from our clusters within r_{200} (dash-dotted line).

As a caveat, here we did not apply any temporal integration of the CR energy flux which might vary with time [e.g. see Figure 7 in Wittor et al., 2017]. Furthermore, Ha et al. [2018c] found that in a high-β plasma the Mach number has to be larger than 2.25 for efficient CR proton acceleration. However, although we do not consider a Mach number cut at 2.25 that would further reduce the CR energy flux [Ha et al., 2019], we adopted the values of η from Kang and Ryu [2013], which strongly decrease the contribution of low-M shocks. As a consequence, the estimates of the CR pressure ratio would barely be affected by introducing this cut. Additionally, our findings are in agreement with a more sophisticated modelling of the γ-ray emission in the San Pedro simulations using Lagrangian tracer particles, recently discussed by Wittor et al. [2020].
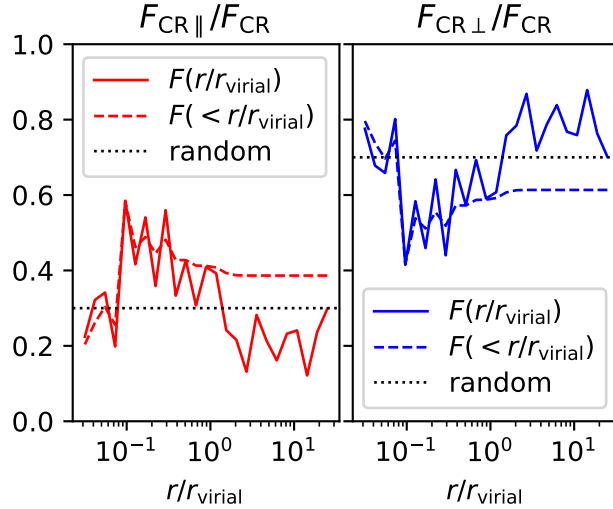
Figure 5.24: Fraction of CR flux dissipated by quasi-parallel (left) and quasi-perpendicular (right) shocks as a function of distance from the San Pedro clusters cores. The solid line represents the total flux dissipated by shocks at a certain r/r_{virial}, while the dashed line represents the integral of the same quantity enclosed inside a certain radius. The dotted line is the trend we would expect if obliquities were randomly distributed.

5.5 Numerical limitations and approximations

We shortly address here (and more in detail in the Appendix) the unavoidable numerical limitations involved in our analysis. First, the adopted spatial resolution somewhat affects the shock finding process, since pre-shock and post-shock conditions are often contaminated by additional flows which blend with the shock. However, although there is a slight discrepancy between the Chronos and San Pedro simulations in the estimate of Mach numbers (e.g. Figure 5.19), we found an agreement for the trends of obliquity between the two sets of simulations (see Figure 5.17). The computation of obliquity itself is still a first attempt: the identification of the pre-shock cell and thus the reliability of the up-stream magnetic field orientation are highly affected by the resolution of the simulation (see Appendix 5.7.1). A close examination of the Chronos simulations exposed an additional issue, most likely of numerical origin, i.e. sequences of wave-like features in the magnetic field orientation in the most rarefied regions of the simulated volume. Low densities are usually critical to handle in simulations, as they are subject to hypersonic flows, for which a "dual energy formalism" is necessary [e.g. Bryan et al., 2014], as well as to the introduction of numerical floor levels of gas temperature. The fact that such patterns change their orientation when a different solver is used, unlike the rest of the simulation (see Appendix 5.7.3), leads us to suspect that these features are driven by numerics and shall not be trusted. However, the impact of such biased obliquities is small in our statistics, as they are limited to very underdense regions and are associated to less than 2 % of the total energy dissipated by shocks in the volume.

There are also physical processes that were not included in these simulations, which give this work room for improvement. In particular, no microphysical processes are implemented: according to DSA, strong shocks may undergo modifications by CRs, as well as magnetic field amplification promoted by CR-driven instabilities, turbulence generation and plasma heating [for a review see Brüggen et al., 2011]. Moreover, in this work (and similarly to previous others in the literature, e.g. Ha et al. 2019) we relied on estimates of the instantaneous energy dissipation into CRs to derive comparisons with the integrated

58
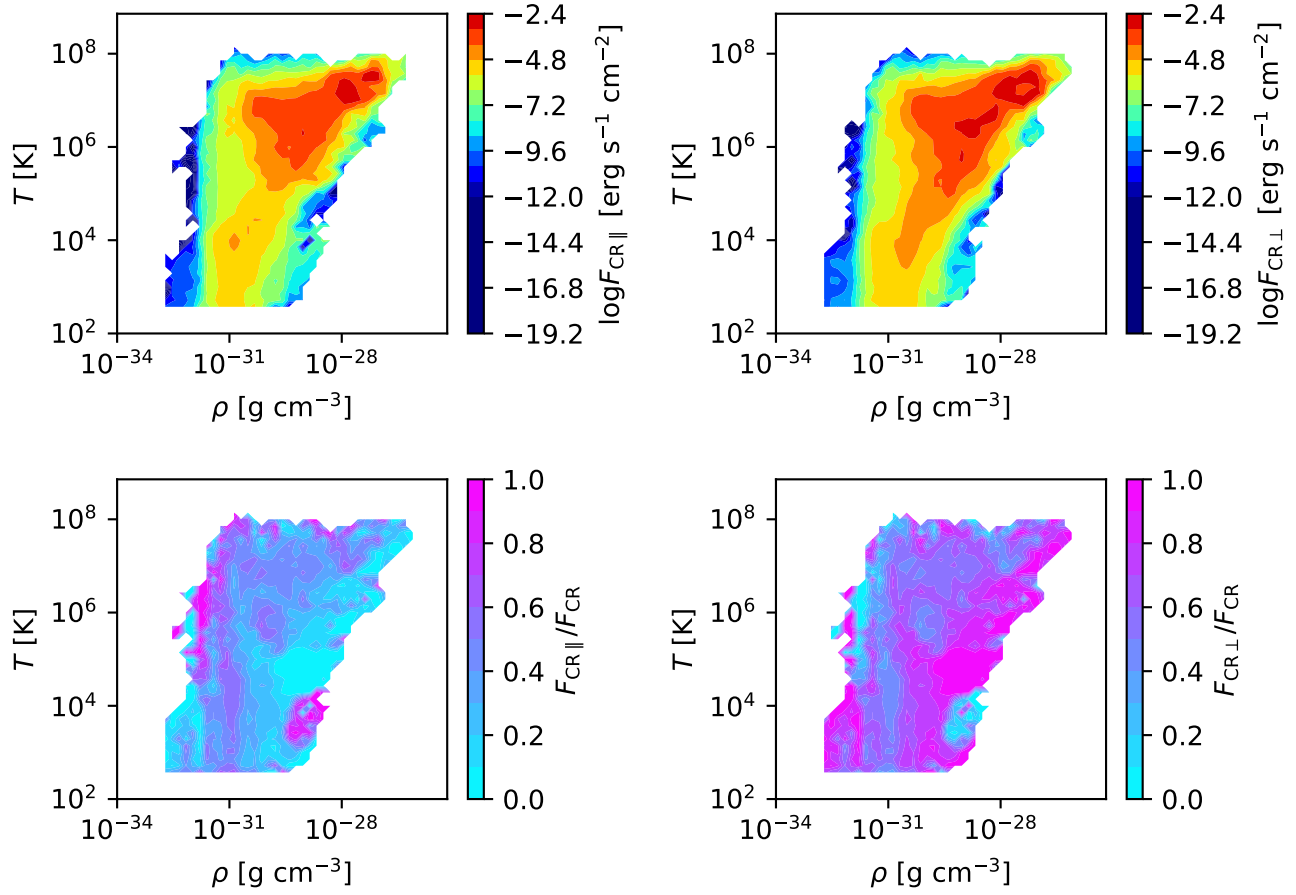
Figure 5.25: Phase diagrams for the San Pedro clusters showing the CR flux dissipated by quasi-parallel and quasi-perpendicular shocks and their fraction with respect to the total as a function of pre-shock density and temperature.
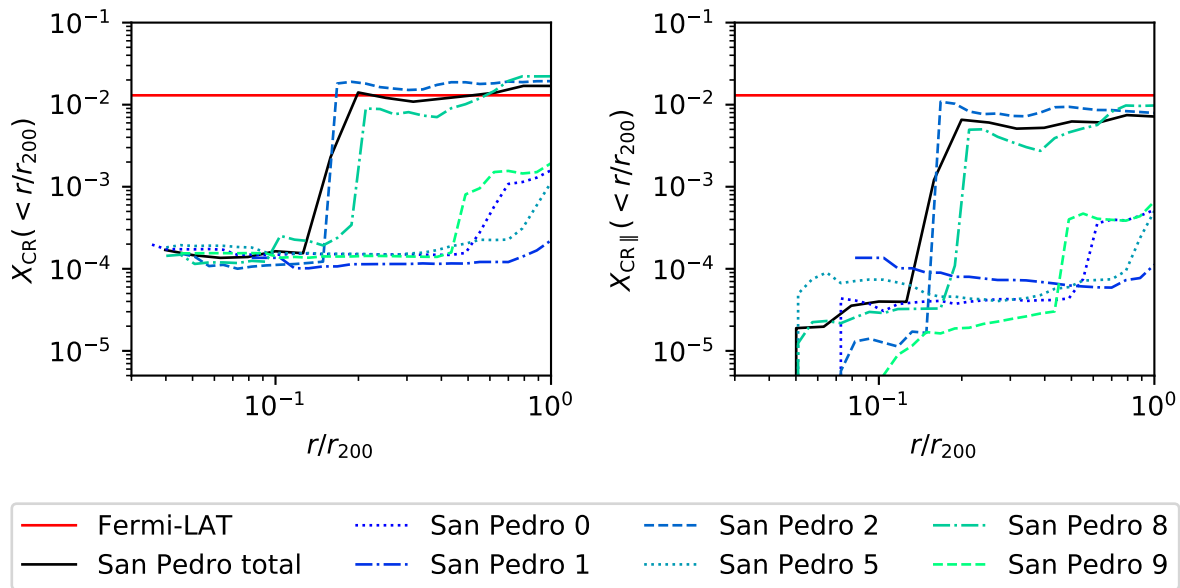
Figure 5.26: CR pressure ratio for all shocks (left) and for parallel shocks only (right), integrated inside a certain radial distance from cluster cores (rescaled to r_{200}), compared to the upper limit imposed by *Fermi* (red line) for the San Pedro clusters both globally (black solid curve) and individually (colored curves).
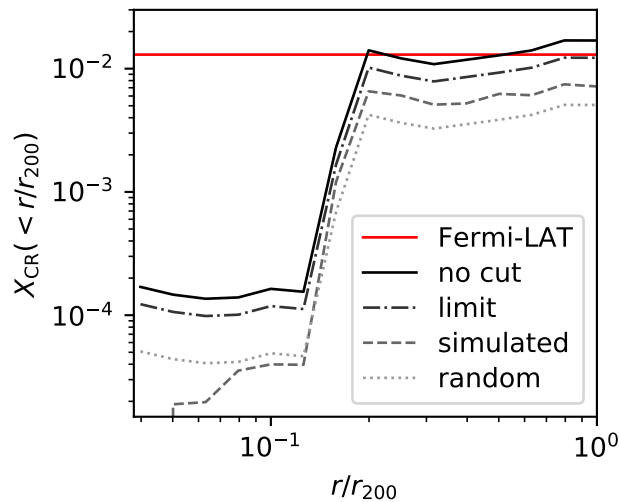
Figure 5.27: CR pressure ratio of the totality of the San Pedro clusters for different obliquity distributions compared to the upper limit imposed by *Fermi* (red line). The grey lines represent the CR pressure ratio for no obliquity cut (solid line), for the simulated obliquity (dashed line), if obliquity were randomly distributed (dotted line) and for the limit obliquity distribution above which γ rays would be detected by *Fermi* (dash-dotted line).

energy budget constrained by *Fermi*-LAT. More sophisticated approaches involving the deployment of "two-fluid models" [e.g. Pfrommer et al., 2007, Vazza et al., 2016] or of passive tracer particles storing the evolution of CRs in time [e.g. Wittor et al., 2017] were beyond the goal of this work, which is just the first step towards future ad-hoc PIC simulations.

5.6   Summary and conclusions

In this work we have considered two sets of grid simulations performed with ENZO: Chronos, which simulates an $\approx (85\ \mathrm{Mpc})^3$ volume, and San Pedro, which zoomes in on six galaxy clusters, ~ 3 times more resolved than Chronos. We evaluated the typical obliquity of cosmic shocks as a function of environment, magnetic field topologies and magnetogenesis scenarios. We then used these results to estimate the observable CR flux for both proton and electron signatures and try to address the issue of the missing γ-ray detection by *Fermi*-LAT. The main conclusions we reached are the following:

1. in the simulated cosmological volume, there is always an excess of quasi-perpendicular shocks over quasi-parallel shocks (up to ~ 5 times) for each of the Chronos runs. This excess is even more significant than the excess expected from a purely random distribution of angles in a three-dimensional space (Section 5.3.1, Figure 5.9);

2. this excess characterizes shocks generated in pre-shock regions with gas density of $\rho \approx 10^{-30}\ \mathrm{g\ cm}^{-3}$. The interval of Mach numbers with the highest percentage of perpendicular shocks is generally in the range $5 \lesssim M \lesssim 20$, but it depends on the typical pre-shock temperatures, e.g. the runs with dynamo and reionization have higher T and thus lower M (Section 5.3.1, Figure 5.10);

3. this effect is maximized around filaments, where the shocks propagate perpendicularly to the filament length and the magnetic field aligns with the filament (Figure 5.18);

4. the physical effect at play here likely is the progressive alignment of the magnetic field with respect to the velocity vector, through the equilibration process described by Soler and Hennebelle [2017], which often arranges the local magnetic field to be quasi-perpendicular to the local direction of the density gradient;

5. the alignment of the magnetic field depends on the plasma β and the magnetic field's origin, as well as its initial topology (Section 5.3.1, Figure 5.9). A recent origin of magnetic field lines is found to slightly reduce the excess of quasi-perpendicular shock geometries;

6. the decreased fraction of proton-accelerating shocks potentially has an effect in reducing the γ emission linked to proton interactions, thus possibly explaining the lack of detection by *Fermi*-LAT, while leaving the acceleration of CR electrons almost unchanged (Section 5.4, Figure 5.26).

To conclude, we have found preliminary results suggesting that the role of obliquity is far from negligible in the process of particle acceleration and signature emission of CRs, and that different cosmic environments may be characterized by systematically different regimes of shock obliquity and local plasma parameters, confirming earlier findings by Wittor et al. [2017].

Our modelling of CR acceleration across cosmic environments has implicitly assumed that the topological properties of magnetic fields resolved by our simulations ($\sim 10^{21}$ cm) remain unvaried down to the scales where DSA and SDA take place ($\sim 10^{16}$ cm). This is certainly a gross oversimplification, which we consider only as first step towards a gradual multi-scale approach for future PIC simulations, which will allow us to bridge the tremendous gap in spatial scales that separate the "micro" scales at which acceleration takes place, to the "macro" scales that radio telescopes can observe.
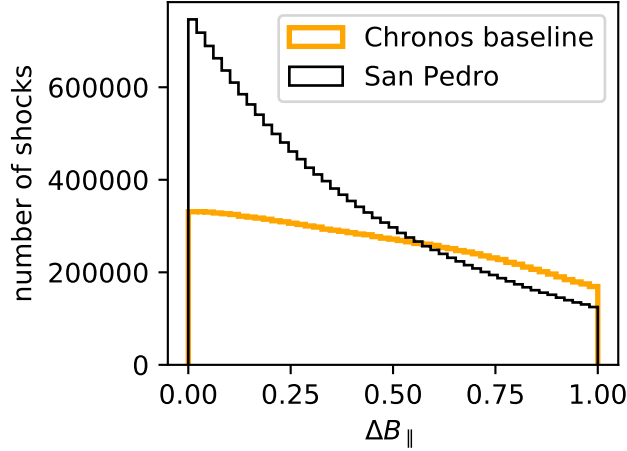
Figure 5.28: The Figure shows the distribution of $\Delta B_\parallel$, i.e. how much the parallel component of magnetic fields is measured to change from pre-shock to post-shock cell for each shock in the Chronos baseline run and in the San Pedro clusters.

5.7   Appendix

5.7.1   On the conservation of B-parallel in MHD shocks

According to the standard shock jump conditions in ideal MHD [see Fitzpatrick, 2014] the regions crossed by shocks experience a modification in the strength of the magnetic field perpendicular to the shock normal ($B_\perp$) due to compression, while the parallel component ($B_\parallel$) is conserved. Therefore, in principle the conservation of $B_\parallel$ going from the up-stream to the down-stream region can be considered as a way to constrain the identification of the propagation direction of numerical shocks. However, we tested that in practice this operation is prone to typically large numerical errors, due to the fact that multiple flows can affect the evolution of cell values over one timesteps, and that in the most general case the change in $B_\parallel$ and $B_\perp$ is not uniquely due to shocks. We estimated the variation in the parallel component of the magnetic field as

$$\Delta B_\parallel = \left| \frac{B_{\parallel \mathrm{post}} - B_{\parallel \mathrm{pre}}}{B_{\parallel \mathrm{pre}}} \right|. \tag{5.4}$$

In Figure 5.28, we show the distribution of $\Delta B_\parallel$ for the two sets of simulations. The lack of conservation in $B_\parallel$ is linked to the resolution of the simulation, since the smaller the cell size the smaller the time interval that separates the pre-shock and post-shock cells. Assuming a typical velocity of $\sim 10^2 - 10^3$ km s^{-1} for accreting matter, for the Chronos simulations (resolution of ≈ 83 kpc) the timescale is of the order of $10^8 - 10^9$ yr; for the higher-resolution simulations (≈ 25 kpc) the timescale is $\sim 5 \cdot 10^7 - 5 \cdot 10^8$ yr. As a consequence, the higher accuracy of the pre-shock cell identification in San Pedro clusters leads to a better conservation of $B_\parallel$, while the values of obliquity obtained with Chronos may not be fully reliable. Nonetheless, we already established that the two sets of simulations are mostly in agreement in terms of obliquity (e.g. Figure 5.19), so we consider our estimates for Chronos to be valid to a first approximation.
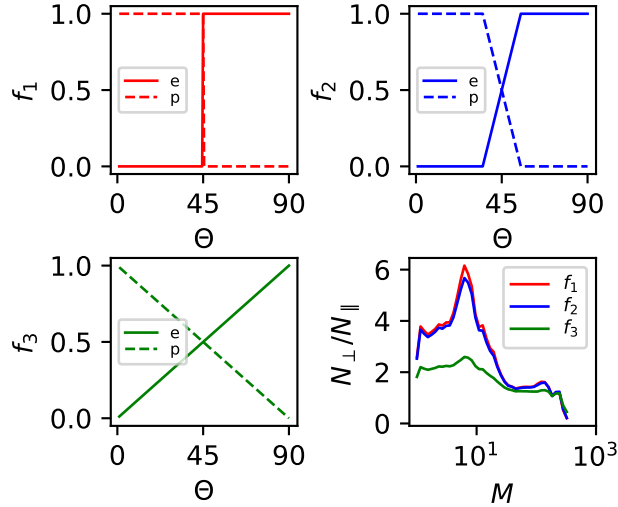
Figure 5.29: Plots of the functions f_1, f_2 and f_3 determining the fraction of electrons (solid lines) and protons (dashed lines) of the total amount of CR that a shock with a certain obliquity can accelerate. The lower-right panel shows the effect of the different functions f on the ratio $N_\perp/N_\parallel$ for shocks in the San Pedro clusters.

5.7.2 On the distinction between perpendicular and parallel shocks

In this analysis we identified as quasi-perpendicular shocks the ones having $\Theta > 45°$, while quasi-parallel shocks are the ones with $\Theta < 45°$. PIC simulations [Guo et al., 2014b, Caprioli and Spitkovsky, 2014b] showed that this transition should be a smoother function of Θ. We show how the ratio of number of perpendicular over parallel shocks in the San Pedro runs varies for three different functions f ranging from 0 to 1 that parametrize the ability of a shock to accelerate electrons and protons. f_1 is the step function adopted for the analysis; f_2 assumes a linear transition from 0 to 1 in the interval $35° < \Theta < 55°$; f_3 assumes a linear transition from 0 to 1 in the interval $0° < \Theta < 90°$. Figure 5.29 shows that there is no significant discrepancy in the trend of the ratio as a function of Mach number from f_1 to f_2, while f_3 would introduce a non-negligible change. However, according to PIC simulations, the most accurate function should be similar to f_2, whose effect on $N_\perp/N_\parallel$ is approximately the same as f_1's.

5.7.3 Spurious small-scale waves

We investigated a quantity which is strictly related to obliquity, but can be defined for each cell, not only for shocked ones: this "pseudo-obliquity" θ' is the angle between the gas velocity and the magnetic field. We found that this quantity behaves peculiarly, i.e. "stripes" of null and straight angles are formed in rarefied regions of the four Chronos runs, similar to waves crossing the ICM. When $\theta' \approx 0°$ or $\theta' \approx 180°$, **v** and **B** are aligned and they assume alternately either concordant or inverted direction: by analysing the orientation of velocity and magnetic field vectors we have determined that this phenomenon is associated to the inversion of the magnetic field. We suspected that these features could be linked to the divergence cleaning method [Dedner et al., 2002], so we analyzed two smaller simulations (400^3 cells, with a 147 kpc resolution and initial conditions similar to the baseline from Chronos), run respectively with Dedner cleaning and constrained transport[6] (CT) [Collins et al., 2010] and otherwise identical. In

---

[6]We remark that in the CT run we encountered some numerical issues of unclear origin in the magnetic field computation by ENZO in high-density regions, which discouraged us from using this solver for the Chronos runs: however, here we want
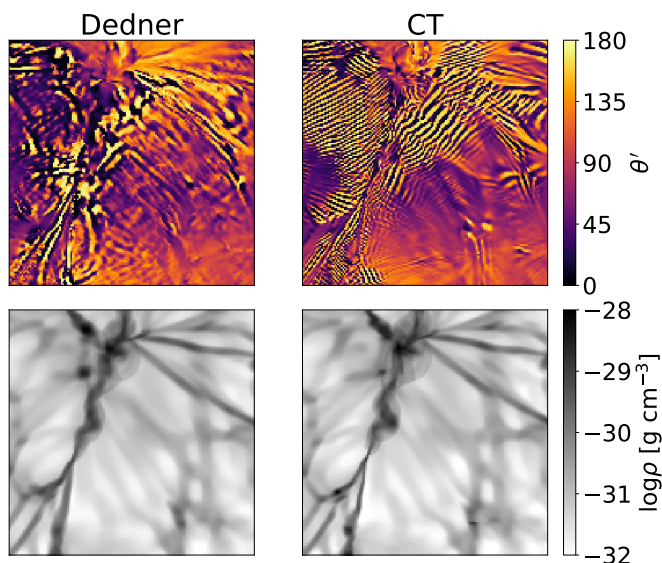
Figure 5.30: Angle formed by velocity and magnetic field ("pseudo-obliquity") in a slice of volume for simulations run with Dedner cleaning and CT in the top panels. Density slice of the corresponding simulations in the bottom panels.

Figure 5.30, we show the values of θ' in a slice of the volume for the two simulations, along with the corresponding density: analogous features are present in both cases, but the morphology of the stripes is quite different. In order to ascertain that the solver does not drastically affect the obliquity estimation, we computed θ for shocks in both cases and verified that the relative abundance of perpendicular and parallel shocks is overall compatible in most environments, as can be seen in Figure 5.31, where the trend of $N_\perp/N_\parallel$ is shown as function of density. Although we do not have a physical or numerical explanation for this phenomenon, this may have repercussion only on low-density regions, which host a very small fraction of the totality of shocks. Given these considerations, the previous analysis should only marginally be affected by this issue: precisely, the obliquity of shocks in rarefied regions (with very high Mach numbers) is not completely reliable.

5.7.4 Comparison with interstellar medium shocks

In this Section, we illustrate the work on simulations of the ISM performed by Soler and Hennebelle [2017] and show how some of the considerations they made applied on our work as well. As anticipated in Section 5.3.2, we found that the magnetic field tends to arrange around low-density structures in a direction which is parallel to the structure itself, due to the action of shear motions. Soler and Hennebelle [2017] encountered this phenomenon while simulating turbulent molecular clouds: they considered the angle ϕ formed by the density gradient $\nabla\rho$ and the magnetic field $\mathbf{B}$ and defined the quantity ξ (relative orientation parameter) as the difference between the number of cells where $|\cos\theta| < 0.125$ and the number of cells where $|\cos\theta| > 0.875$: thus $\xi > 0$ where $\nabla\rho$ is quasi-perpendicular to $\mathbf{B}$ and $\xi < 0$ where they are quasi-parallel[7]. In Figure 5.32, we replicate the plots from Figure 1 and 2 in Soler and Hennebelle [2017] of the relative orientation parameter as a function of the gas density, which identifies the different structures, and as a function of the velocity divergence, which is strictly related to the shock strength. The

---

to compare the behavior of the magnetic field in rarefied environments, which appears to be reliable.

[7]We point out that while for random vectors in space the probability distribution of $0 \leq \phi \leq \pi$ is $\propto \sin\phi$, all values assumed by $-1 \leq \cos\phi \leq 1$ are equiprobable, so a random distribution returns $\xi = 0$.
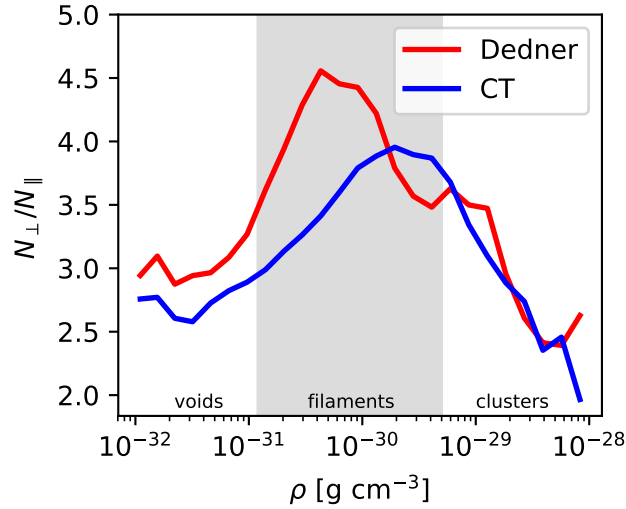
Figure 5.31: Trend of $N_\perp/N_\parallel$ as a function of gas density for the 400^3 simulations, run with Dedner cleaning (in red) and CT (in blue). The ρ-axis is divided into density intervals identifying voids, filaments and clusters.
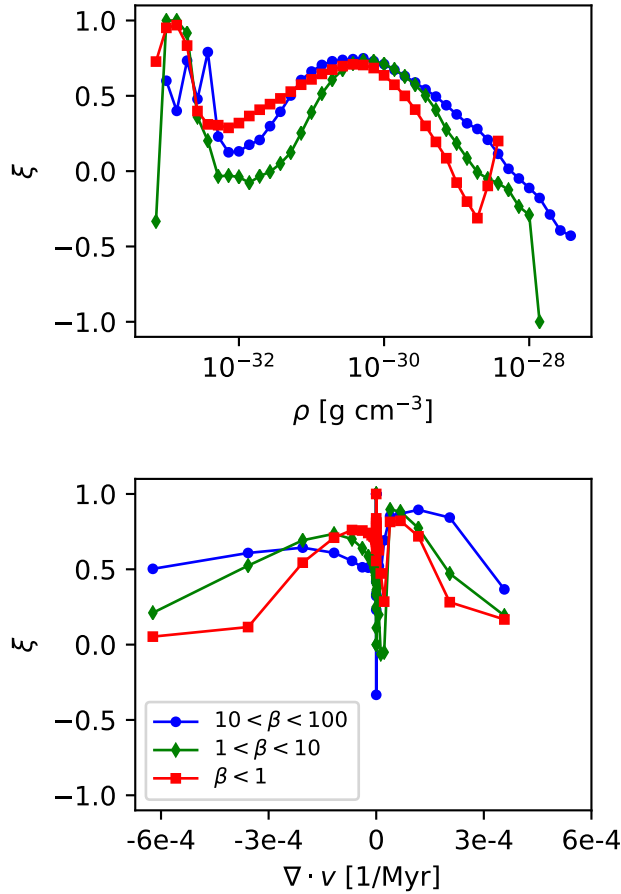
Figure 5.32: Comparison to Figure 1 and 2 in Soler and Hennebelle [2017]: relative orientation parameter ξ as a function of density and velocity divergence for the Chronos baseline simulation for different β intervals.

behavior of ξ is evaluated at varying values of the plasma β. Even though they considered a very different range of densities and velocities, we found similar results in the Chronos baseline simulation. Except for very rarefied regions, possibly affected by numerics, we note the same behavior for ξ, which is positive in most of the volume, i.e. there are more perpendicular configurations with respect to parallel ones, with a decreasing trend towards higher densities, towards more negative values of velocity divergence and towards lower β (i.e. more magnetized plasmas).

6. Electron acceleration efficiency in cosmic collisionless shocks

The material of this chapter is subject of an article in preparation (Banfi et al.), and soon to be submitted.

Abstract Collisionless shocks in the intracluster medium can be responsible for acceleration of electrons and protons to non-thermal energies. Such energetic particles, known as cosmic rays, are responsible for the onset of phenomena that can in principle be observed from Earth, such as synchrotron radiation and hadronic γ-ray emission. Diffusive shock acceleration (or first-order Fermi acceleration) is recognized as the mechanism behind particle acceleration, although other processes need to be invoked to explain how electrons can be pre-accelerated to the supra-thermal energies needed for them to participate in the Fermi process. These mechanisms can be strongly affected by the magnetic properties of the shocked medium: in particular, the angle formed by the shock propagation direction and the magnetic field, known as obliquity θ, determines how efficiently each particle species is accelerated. In this work, we perform particle-in-cell simulations of shocks with typical conditions found in cosmic filaments, which we inferred from previous works: these shocks are characterized by high Mach numbers ($M_s \sim 15$) and a quasi-perpendicular configuration of the magnetic field. We consider different obliquities and evaluate the acceleration efficiency of electrons in each setup. We conclude that for this choice of parameters electrons are pre-accelerated by the motional electric field by drifting along the shock front (shock drift acceleration). This mechanism is especially efficient for less oblique quasi-perpendicular shocks ($\theta = 60°$), which allow more electrons to stream back upstream. We find that a fraction of these electrons eventually takes part to diffusive shock acceleration and becomes strongly relativistic (up to Lorentz factor $\gamma \sim 10$). Finally, we measure the injection efficiency of electrons into diffusive shock acceleration in cosmic environments as a function of obliquity and verify the compatibility of our results to the estimates from previous works: we conclude that, according to our findings, the overall injection of relativistic electrons is a factor $\sim 5 - 10$ higher than previously assumed.

6.1   Introduction

The acceleration of particles up to relativistic energies is believed to be a common process in collisionless shocks, which frequently form in many different astrophysical environment. Among these, cosmic shocks in the large-scale structure of the Universe are predicted to be generated by the accretion of cold gas or merger of subhalos, leading to the production of both cosmic-ray (CR) protons and electrons [e.g. Ryu et al., 2003, Bykov et al., 2019]. Evidence of the presence of electrons with $\sim$ GeV energies is provided by radio observations of the Mpc-size synchrotron emission in clusters of galaxies [e.g. Carilli and Taylor,

2002a, Ferrari et al., 2008, Brunetti and Jones, 2014], while no evidence has been so far reported for diffuse γ-ray hadronic emission from the intracluster medium, which limits the energy of CR protons to be less than a percent of the gas energy in galaxy clusters [e.g. Ackermann et al., 2014].

In principle, particle acceleration by non-relativistic collisionless shocks is well explained by first order Fermi mechanism known as diffusive shock acceleration (DSA) [Bell, 1978, Blandford and Ostriker, 1978, Drury, 1983], in which particles gain energy in the repetitive interaction with the shock front, as they are scattered off plasma magnetohydrodynamic (MHD) waves. While this mechanism is found to be efficient in energizing CR protons [Caprioli and Spitkovsky, 2014a], electrons need to be pre-accelerated before they can be injected into the DSA cycle, due to their gyration radius being much smaller than the shock front: this issue, which has been addressed extensively in literature, is still partially unresolved, and it is known as the 'injection problem'. Different scenarios for electron pre-acceleration have been proposed, depending on the shock strength and plasma characteristics, including the pre-existing magnetic field topology: the relative orientation between the magnetic field and the shock propagation direction (i.e. obliquity) allows to classify shocks as either quasi-parallel or quasi-perpendicular.

Thanks to recent works, we could use state-of-the-art cosmological MHD simulations to study the distribution of shocks across cosmic environment, and quantify the distribution of shock obliquity, for different possible models of cosmic magnetism [Banfi et al., 2020, 2021]. In particular, we looked for common properties in the set of shocks taking place in filaments, elongated structures connecting galaxy clusters in the cosmic web, which are expected to be surrounded by strong (high-Mach number M_s) shocks deriving from the accretion of cold gas [Ryu et al., 2003]: these objects have only been detected a handful of times [e.g. Werner et al., 2008, Farnsworth et al., 2013], hence their features are poorly constrained. In Banfi et al. [2020], we established that quasi-perpendicular configurations make up a significant part of the entire population of high-M_s accretion shocks around filaments, as later explained in Banfi et al. [2021]. Assuming prescriptions for acceleration efficiency from Kang and Ryu [2013], we concluded that proton acceleration should be strongly inhibited by the obliquity distribution, and therefore the constrain imposed by the non-detection of γ emission would be consistent to our inference. These works represent a preliminary and macroscopic inspection of the typical plasma conditions that should be met in cosmic shocks, but in order to reliably predict their CR acceleration efficiency, a different kind of simulations is necessary.

Recent fully-kinetic particle-in-cell (PIC) simulations [e.g. Bohdan et al., 2017] have shown that the physics of strong perpendicular shocks is mostly governed by the instabilities generated by the encounter of incoming plasma and the reflected ion stream. In particular, Buneman instability [Buneman, 1958], resulting from the interaction of cold incoming electrons and reflected ions, allows shock surfing acceleration (SSA) to take place [Shimada and Hoshino, 2000, Hoshino and Shimada, 2002]: in this process, electrons are trapped in potential wells by electrostatic waves and are eventually accelerated by the convective electric field. SSA is found to be less important as ion-to-electron mass ratio is pushed towards larger, more realistic values. On the other hand, the interaction of incoming and reflected ions generates Weibel instability [Kato and Takabe, 2010, Niemiec et al., 2012, Wieland et al., 2016], which causes magnetic fields to acquire a filamentary shape: this configuration is often unstable, thus inducing turbulent magnetic reconnection, which can be responsible for electron pre-acceleration [Matsumoto et al., 2015]. Additionally, the Weibel instability can facilitate electron injection into DSA via stochastic Fermi acceleration [Bohdan et al., 2017] and shock drift acceleration (SDA) [Matsumoto et al., 2017]. SDA consists of electrons gaining energy in the shock transition region due to the electric field generated by the magnetic field gradient across the shock front. While in three-dimensional simulations [e.g. Matsumoto et al., 2017] Buneman waves and Weibel magnetic turbulence co-exist, lower-dimension setups limit the kinds of waves modes that can be included: in two-dimensional simulations the orientation of the magnetic field with respect to the simulation plane plays a fundamental role [e.g. Bohdan et al., 2017]. Xu et al.

[2020], however, have shown that a typical DSA power-law is eventually formed in the electron spectra of strong quasi-perpendicular shocks, even for one-dimensional simulations, thanks to the combination of SSA, SDA and upstream wave scattering.

The aim of this work is to perform a set of PIC simulations of shocks with the typical characteristics of a filament accretion shock and study the dependence of electron (pre-)acceleration mechanisms and efficiency on the variation of both physical (obliquity) and simulation (number of dimensions, ion-to-electron mass ratio, particles per cell) parameters.

6.2 Methods

This work starts by considering the final results of our previous analysis of structure formation shocks, produced by cosmological simulations, which coupled a simple ideal MHD prescription to different models for the origin of magnetic fields in large-scale structures, as presented in Banfi et al. [2020][1]. In this new work, we perform dedicated numerical simulations of cosmological collisionless shocks with the massively parallel electromagnetic PIC code TRISTAN-MP [Spitkovsky, 2005]. We used both 1D and 2D configurations: regardless of the number of dimensions of the computational domain, all three components of particle momenta and electromagnetic field are followed. A shock is generated by reflecting a non-relativistic, super-sonic, super-Alfvénic, electron-ion plasma onto a wall at the edge of the computational box (see Figure 6.1). The domain and the particle injector are set to expand along the shock propagation direction as the shock front approaches. The plasma moves along the x-axis with bulk velocity u_0, which is related to the simulation-frame Mach number as

$$M = \frac{u_0}{c_{\mathrm{s}}} = \frac{u_0}{\sqrt{2\Gamma k_{\mathrm{B}} T_{\mathrm{i}}/m_{\mathrm{i}}}} \tag{6.1}$$

where c_{s} is the upstream sound speed, k_{B} is the Boltzmann constant, $\Gamma = 5/3$ is the adiabatic index, T_{i} is the ion temperature (which is set equal to the electron temperature T_{e}) and m_{i} is the ion mass. This parameter is related to the sonic Mach number:

$$M_{\mathrm{s}} = M \frac{u_{\mathrm{sh}}^{\mathrm{up}}}{u_0} = M \left(1 + \frac{1}{r-1} \right) \tag{6.2}$$

where $u_{\mathrm{sh}}^{\mathrm{up}}$ is the shock velocity in the upstream rest frame and r is the compression ratio, which approaches ≈ 4 for strong shocks, like the ones considered. The plasma initial magnetization is given either by

$$\sigma = \frac{B_0^2/4\pi}{(\gamma_0 - 1)n m_{\mathrm{i}} c^2}, \tag{6.3}$$

or equivalently by

$$\beta_{\mathrm{P}} = \frac{n k_{\mathrm{B}}(T_{\mathrm{i}} + T_{\mathrm{e}})}{B_0^2/8\pi} = \frac{4}{\sigma \Gamma M^2}, \tag{6.4}$$

where B_0 is the (uniform) magnetic field, $\gamma_0 = (1 - \beta_0^2)^{-1/2} = (1 - u_0^2/c^2)^{-1/2}$ and $n = n_{\mathrm{i}} = n_{\mathrm{e}}$ is the plasma number density. The shock Alfvénic Mach number is obtained as $M_{\mathrm{A}} = u_0/v_{\mathrm{A}} = \sqrt{2/\sigma}$. The angle formed by the magnetic field and the shock propagation direction is called obliquity. While in 1D obliquity θ is the only necessary parameter to identify the magnetic field topology at the beginning of the

---

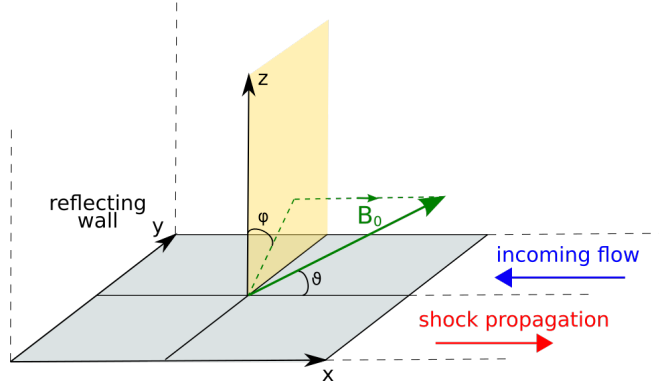[1]In the following, we only consider the run referred to as "baseline".

Figure 6.1: 2D shock simulation setup in TRISTAN-MP.

	θ	mass ratio	particles per cell	β_P	β_0	electron acceleration
1a	78°	300	32	8	0.1	no
1b	78°	100	500	8	0.1	no
1c	60°	300	500	8	0.1	yes
1d	78°	300	500	8	0.1	yes
1e	78°	1000	500	8	0.1	yes

Table 6.1: Simulation initial conditions for the one-dimensional runs. The last column indicates whether or not we observed hints of electron acceleration towards the end of each run.

simulation, for 2D setups another angle, ϕ, needs to be specified: in previous works [e.g. Bohdan et al., 2017], it was shown that the ability of capturing plasma effects by two-dimensional simulations is strictly dependent on the magnetic field orientation with respect to the simulation plane. In our convention, θ is the angle formed by the $\mathbf{B_0}$ vector and the x−axis, while ϕ is the angle formed by the projection of $\mathbf{B_0}$ on the $y - z$ plane and the z−axis, which corresponds to $\phi = 0$ for out-of-plane configurations ($B_y = 0$) and $\phi = 90°$ for in-plane configurations ($B_z = 0$). In this work, both cases are considered. We simulated quasi-perpendicular ($\theta = 60°$ and $\theta = 78°$), super-Alfvénic shocks with $M_s = 15$, $M_A = 39$, $\beta_0 = 0.1$, $k_B T_i/(m_i c^2) = 2.392 \times 10^{-5}$, $\sigma = 0.002392$ ($\beta_P = 8$): the choice of these parameters is explained in Section 6.3.1. We explored different ion-to-electron mass ratios $m_i/m_e = 50, 100, 300$ and 1000 and initial number of particles per cell $ppc_0 = 16, 32, 64$ and 500 (half electrons and half ions). The grid cell size is chosen to be $\Delta x = \Delta y = 0.1 \lambda_e$, where $\lambda_e = c/\omega_{pe}$ is the electron skin depth and $\omega_{p,e} = \sqrt{4\pi n_e e^2/m_e}$ is the electron plasma frequency (the same quantities can be defined for ions by changing the subscript). The timestep is $\Delta t = 0.045\omega_{pe}$, so that $c = 0.45\Delta x/\Delta t$. The characteristics of each run are summarized in Table 6.1 and Table 6.2 for 1D and 2D runs respectively. We point out that, although not all 2D simulations have the same transverse size (i.e. the number of cells which sample the y-direction), we verified that, provided the proper normalization in the number of particles, the particle energy spectra are usually only marginally affected by this parameter.

6.3 Results

6.3.1 Shock initial conditions

In Banfi et al. [2020], we identified shocks throughout the cosmic web and inferred the following main properties: sonic Mach number M_s, magnetization parameter β_P, obliquity θ and dissipated flux F.

	θ	ϕ	transverse size	mass ratio	particles per cell	β_P	β_0	electron acceleration
2a	78°	0° (out-of-plane)	100 λ_e	50	16	8	0.1	yes
2b	78°	90° (in-plane)	100 λ_e	50	16	8	0.1	no
2c	60°	0° (out-of-plane)	5 λ_e	50	16	8	0.1	yes
2d	60°	90° (in-plane)	5 λ_e	50	16	8	0.1	yes
2e	78°	0° (out-of-plane)	5 λ_e	50	64	8	0.1	yes
2f	78°	90° (in-plane)	5 λ_e	50	64	8	0.1	no

Table 6.2: Simulation initial conditions for the two-dimensional runs. The last column indicates whether or not we observed hints of electron acceleration towards the end of each run.
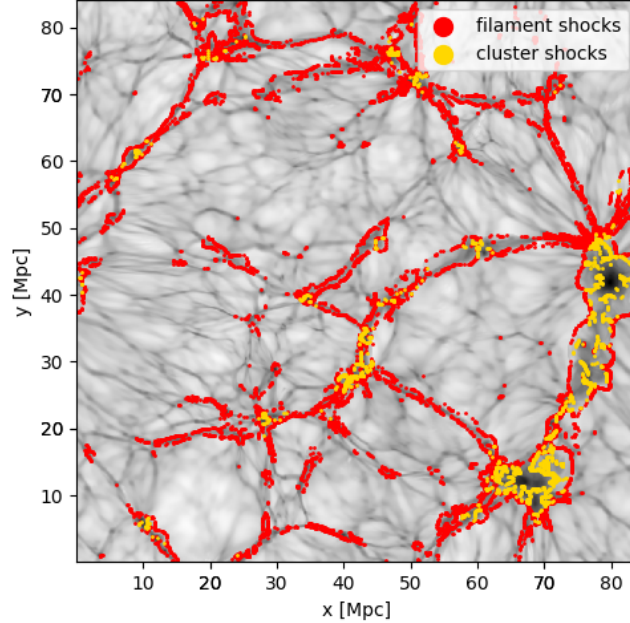

Figure 6.2: Density map of a slice of the cosmological volume simulated. The shocks are marked with either a red dot (if they belong to filaments, i.e. if they fulfil the temperature requirement 5×10^3 K $\leq T \leq 10^5$ K) or a yellow dot (if they belong to clusters, i.e. if $T > 10^5$ K).

Being especially interested in quantifying the acceleration efficiency of electrons in accretion shocks, we selected the shocks having upstream temperatures typical of filaments, i.e. 5×10^3 K $\leq T \leq 10^5$ K (see Figure 6.2). Then, in order to start with the shocks which are most likely to be observable in real radio surveys, we selected the ones which dissipate the largest amount of kinetic energy. To this end, we computed the fraction of kinetic energy flux across shocks, which gets dissipated into the acceleration of CR electrons, based on the expectations from DSA (F_{CRe}, see Banfi et al. 2020 for details). By considering different bins of M_s, β_P and θ we could select the combination of parameters which is found to maximize F_{CRe}. Figure 6.3 shows the overall fraction of F_{CRe} dissipated by all shocks having a certain M_s, β_P or θ. While for M_s and β_P there is a clear peak in the distribution, the values of θ are less strongly constrained (although a modest peak can be identified). Therefore, we decided to maintain fixed $M_s = 15$ and $\beta_P = 8$, while considering two different obliquity values ($\theta = 78°$ and $\theta = 60°$).
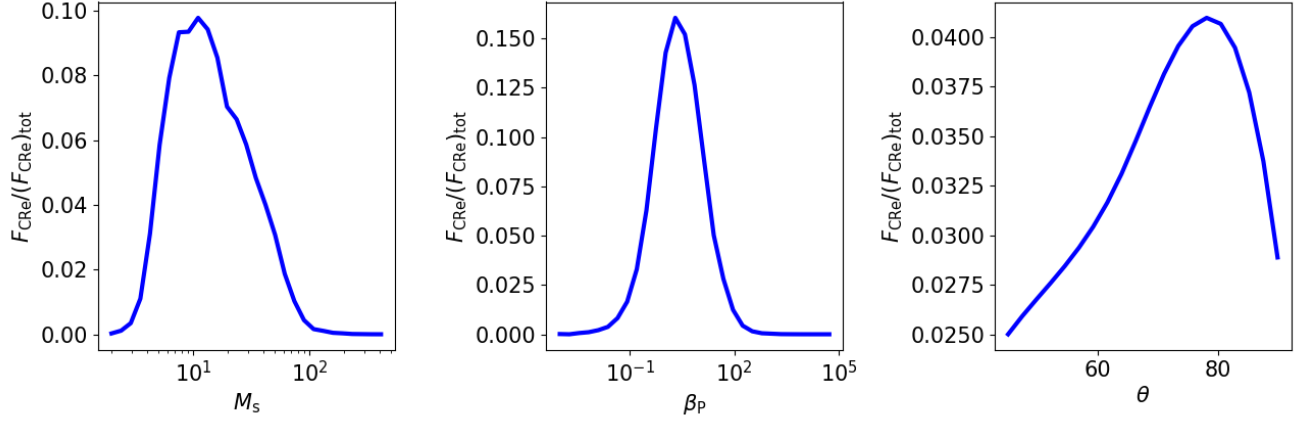
Figure 6.3: Fraction of kinetic energy flux dissipated by shocks into CR electron acceleration as a function of M_s, β_P and θ.

6.3.2 Simulation parameter evaluation

The first part of this work consisted in testing the reliability of the simulation parameters: as for all numerical methods, some compromise between computational resources and physical accuracy is required. For PIC simulations, this mostly translates into 1) choosing the suitable number of particles per cell at the beginning of the simulation (ppc_0, from now on) and 2) adopting a large enough (albeit lower than the real value) mass ratio, i.e. m_i/m_e. As both parameters can directly impact the memory and computing time requirement of the simulation (linearly with ppc_0 and m_i/m_e for 1D simulations), convergence studies are needed in order to determine the minimum suitable numerical configuration to get to a physical solution.

Particles per cell convergence

The parameter ppc_0 indicates the total number of particles per cell when the simulation is initialized (i.e. in the upstream plasma): in our case, half of the particles are ions and the other half electrons. If ppc_0 is too low, the code will develop some effective collisionality (and resulting collisional/numerical heating) due to the noise-level fluctuations arising from coarse graining of the distribution function, which should be avoided in a collisionless code. For 1D simulations, we show the comparison between runs *1a* and *1d*, respectively with $ppc_0 = 32$ and $ppc_0 = 500$ (given a fixed mass ratio of 300). Figure 6.4 shows that pre-acceleration is found in the upstream for $ppc_0 = 500$, while no sign of deviation from the Maxwellian can be identified for low ppc_0.

For 2D simulations, we show the comparison between runs *2a* and *2e*, respectively with $ppc_0 = 16$ and $ppc_0 = 64$ (given a fixed mass ratio of 50). In both these runs, which have an out-of-plane magnetic field configuration, there is evidence of pre-acceleration in the upstream with no particular differences introduced by the ppc_0 increase. Therefore, we can conclude that, for 2D setups, a value of $ppc_0 = 16$ is enough to prevent numerical effects and accurately describe particle evolution. Since the degree of collisionality is controlled by the number of computational particles in a sphere with radius of one skin depth (which is actually a line in 1D and a circle in 2D), it must be noticed that $ppc_0 = 64$ in 2D is roughly equivalent to $ppc_0 = 500$ in 1D.

Figure 6.4: Comparison of runs *1a* and *1d* at $t\omega_{ci} = 19$, which differ in the choice of the parameter ppc_0. *Left and central panel:* spectra of electrons upstream and downstream, rescaled to the number of particles. *Right panels:* density profile normalized to the initial density; the highlighted areas indicate the regions from which electrons are extracted in the upstream ($[x_{shock} + 10\lambda_i, x_{shock} + 50\lambda_i]$) and in the downstream (two different downstream areas are compared: $[x_{shock} - 120\lambda_i, x_{shock} - 80\lambda_i]$, dotted line, and $[x_{shock} - 50\lambda_i, x_{shock} - 10\lambda_i]$, solid line).
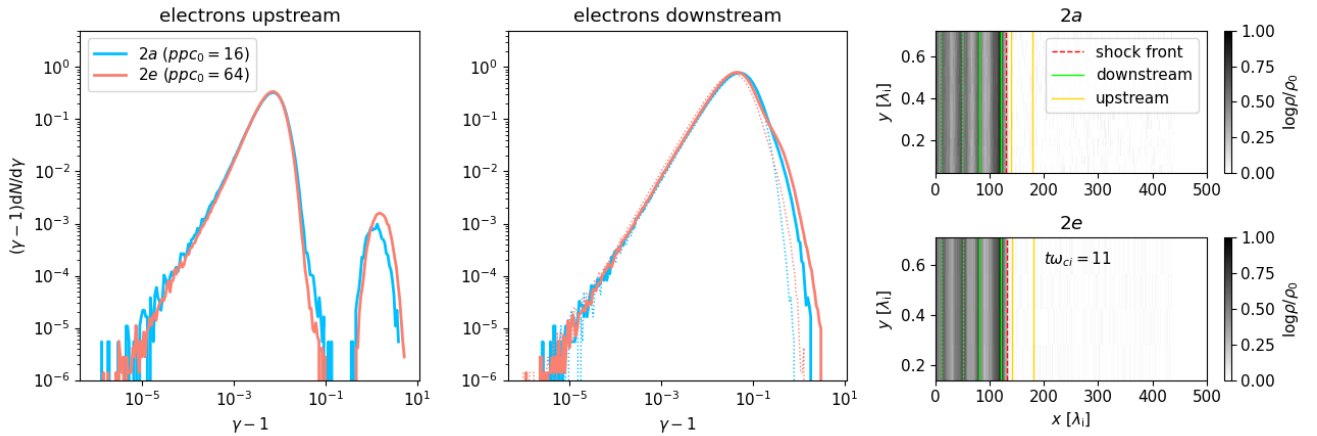
Figure 6.5: Comparison of runs *2a* and *2e* at $t\omega_{ci} = 11$, which differ in the choice of the parameter ppc_0. *Left and central panel:* spectra of electrons upstream and downstream, rescaled to the number of particles. *Right panels:* density map normalized to the initial density; the highlighted areas indicate the regions from which electrons are extracted in the upstream ($[x_{shock} + 10\lambda_i, x_{shock} + 50\lambda_i]$) and in the downstream (two different downstream areas are compared: $[x_{shock} - 120\lambda_i, x_{shock} - 80\lambda_i]$, dotted line, and $[x_{shock} - 50\lambda_i, x_{shock} - 10\lambda_i]$, solid line).
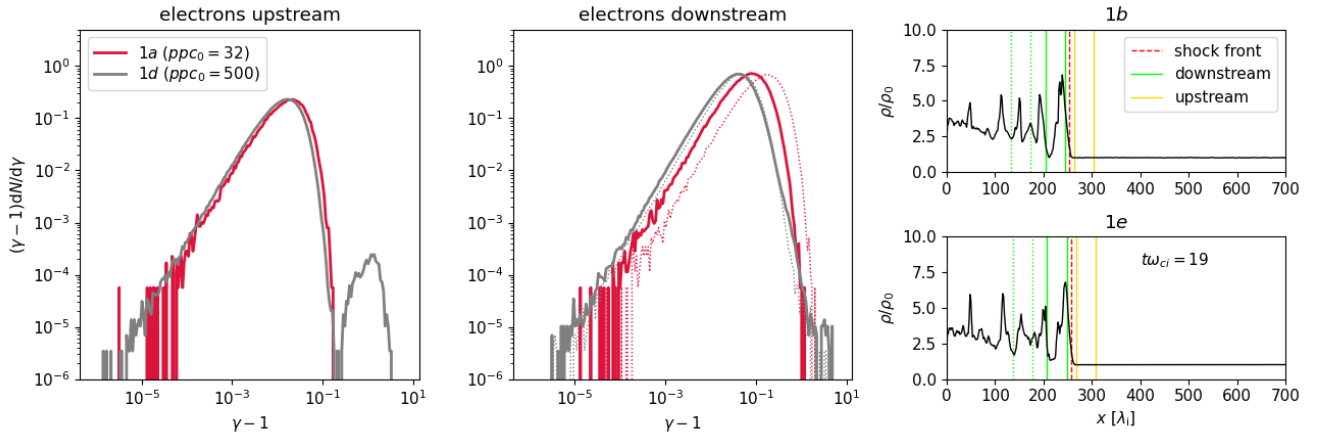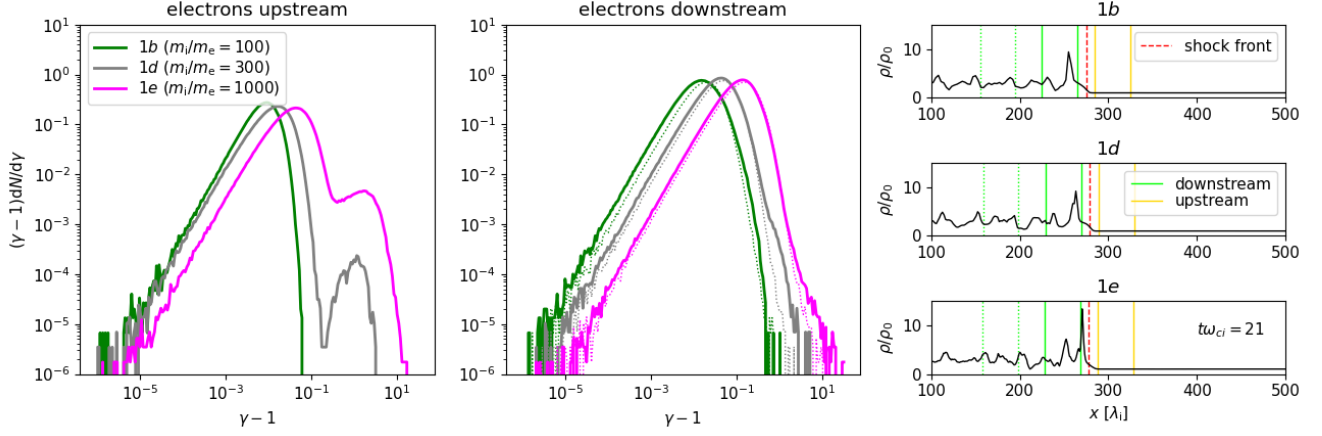
Figure 6.6: Comparison of runs *1b*, *1d* and *1e* at $t\omega_{ci} = 21$, which differ in the choice of the parameter m_i/m_e. *Left and central panel:* spectra of electrons upstream and downstream. *Right panels:* density profile normalized to the initial density; the highlighted areas indicate the regions from which electrons are extracted in the upstream ($[x_{\text{shock}} + 10\lambda_i, x_{\text{shock}} + 50\lambda_i]$) and in the downstream (two different downstream areas are compared: $[x_{\text{shock}} - 120\lambda_i, x_{\text{shock}} - 80\lambda_i]$, dotted line, and $[x_{\text{shock}} - 50\lambda_i, x_{\text{shock}} - 10\lambda_i]$, solid line).

Mass ratio convergence

The parameter m_i/m_e indicates the ratio between the ion and electron mass. The advantage of a non-realistic mass ratio ($m_i/m_e < 1836$) is that, if we fix electron scales, ion scales become smaller, so it is cheaper to run the code for a given number of ion times. However, an arbitrarily small mass ratio is bound to inhibit the interaction of particles with the shock, and therefore particle acceleration is prevented. Following Sironi and Spitkovsky [2009], the minimum velocity required by the particle to escape ahead of the shock and not be advected in the downstream is

$$u_t = u_{\text{sh}}^{\text{up}} \sec\theta = \sqrt{\frac{2\Gamma k_B T_e}{m_e}}\sqrt{\frac{m_e}{m_i}} M_s \sec\theta, \tag{6.5}$$

which implies that u_t will approach the speed of light as the mass ratio m_i/m_e decreases and the obliquity $\theta \to 90°$. Therefore, depending on the choice of obliquity (as will be discussed later in this Section), lower mass ratios can be adopted without compromising the evolution of particles. By comparing runs *1b*, *1d* and *1e*, respectively with $m_i/m_e = 100$, 300 and 1000, we can observe how the mass ratio affects the electron pre-acceleration in the upstream, at fixed value of $ppc_0 = 500$. We observe a gradual increase in the fraction of particles deviating from the Maxwellian in the upstream as the mass ratio becomes larger: specifically, we identify a transition between the complete lack of pre-acceleration for $m_i/m_e = 100$ and a visible bump at large Lorentz factors in the upstream for $m_i/m_e = 300$. This behavior is expected from Equation 6.5, since more particles are able to interact with the shock if the mass ratio is larger. However, we must also take into account another effect: as a consequence of the increased mass ratio, the energy distribution of electrons gets shifted towards higher temperatures, at fixed values of β_0 and $k_B T_i/(m_i c^2)$. Therefore, differences in the electron spectra could also be due to the fact that the mass ratio is increased to an extent which allows thermal electrons to be already relativistic, which would be highly unrealistic in the scenario of shocks occurring in filaments. In order to assess whether this effect is relevant, we performed some tests, which we show in Appendix 6.5.1.
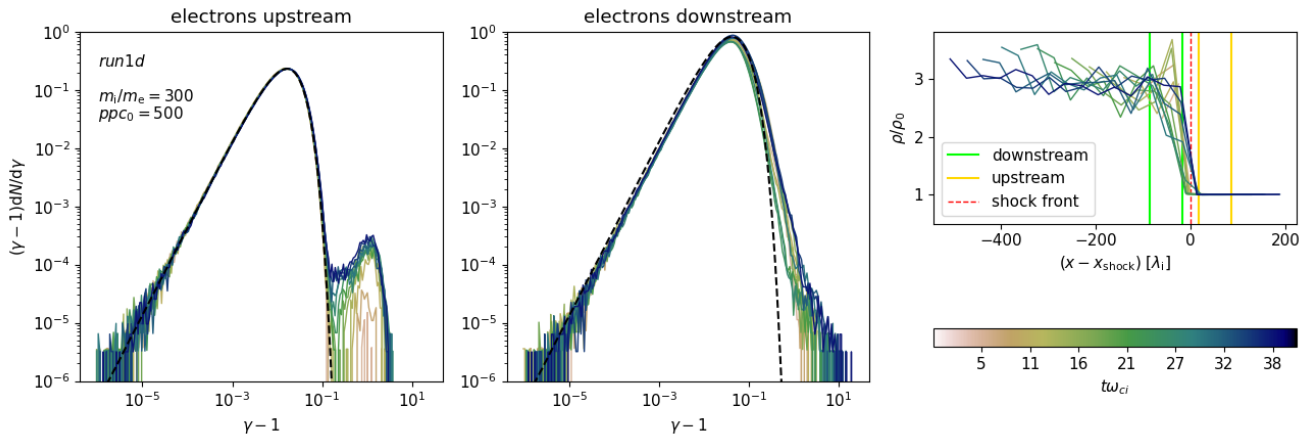
Figure 6.7: Evolution of electron spectra of run *1d* for $5 < t\omega_{ci} < 40$. *Left and central panel:* spectra of electrons upstream and downstream compared to the thermal Maxwellian (dashed line). *Right panel:* density profile normalized to the initial density; the highlighted areas indicate the regions from which electrons are extracted in the upstream ($[x_{\text{shock}} + 10\lambda_i, x_{\text{shock}} + 50\lambda_i]$) and in the downstream ($[x_{\text{shock}} - 50\lambda_i, x_{\text{shock}} - 10\lambda_i]$).

Time convergence

Based on the previous discussion on the simulation parameters in 1D, we assume that the parameter combination $ppc_0 = 500$ and $m_i/m_e = 300$ describes the shock's physical setup in a sufficiently accurate manner. Therefore, we advance run *1d* as long as possible and study the evolution of the spectral properties of electrons. We find that the upstream curve settles at $t\omega_{ci} = 20$, after which an approximately stable fraction of electron gets pre-accelerated and eventually reaches relativistic energies $\gamma \sim 10$ in the downstream, which are suitable for further DSA acceleration. Therefore, we conclude that $t\omega_{ci} \approx 20$ is the required suitable time to observe the features that we identify as pre-acceleration in the upstream: however, we evolved a few significant runs for longer times, in order to also witness the early stages of acceleration in the downstream and to reliably determine the properties of the power law tail.

Dimensionality

In this Section we discuss to which extent the limitation of the computational domain to a single dimension impacts on particle acceleration. In particular, differences are expected to arise due to the ability of higher-dimensional simulations to capture certain kinds of plasma waves and/or instabilities. Furthermore, when moving up from 1D to 2D, the orientation of the magnetic field is not only identified by θ, but also by ϕ (defined in Section 6.2). This choice affects the evolution of the shock under many aspects: Figure 6.8, for instance, shows how both the speed of the shock propagation and the shock front morphology differ. As previously found by Bohdan et al. [2017], in-plane configurations allow the formation of Weibel-like filaments, while an out-of-plane magnetic field generates strong Buneman waves instead, which inevitably affects particle (pre-)acceleration mechanisms. In principle, there is no reason to choose one configuration over the other, since these phenomena actually occur in a 3D space: more time-consuming 3D simulations would be required to asses which scenario is in better agreement to the real one. In Figure 6.9, we show the comparison between electron energy spectra for the 1D run *1d* and the 2D runs *2a* and *2b*, having respectively out-of-plane and in-plane configurations. We observe that while the 2D in-plane configuration does not show signs of electron pre-acceleration, the 2D out-of-plane
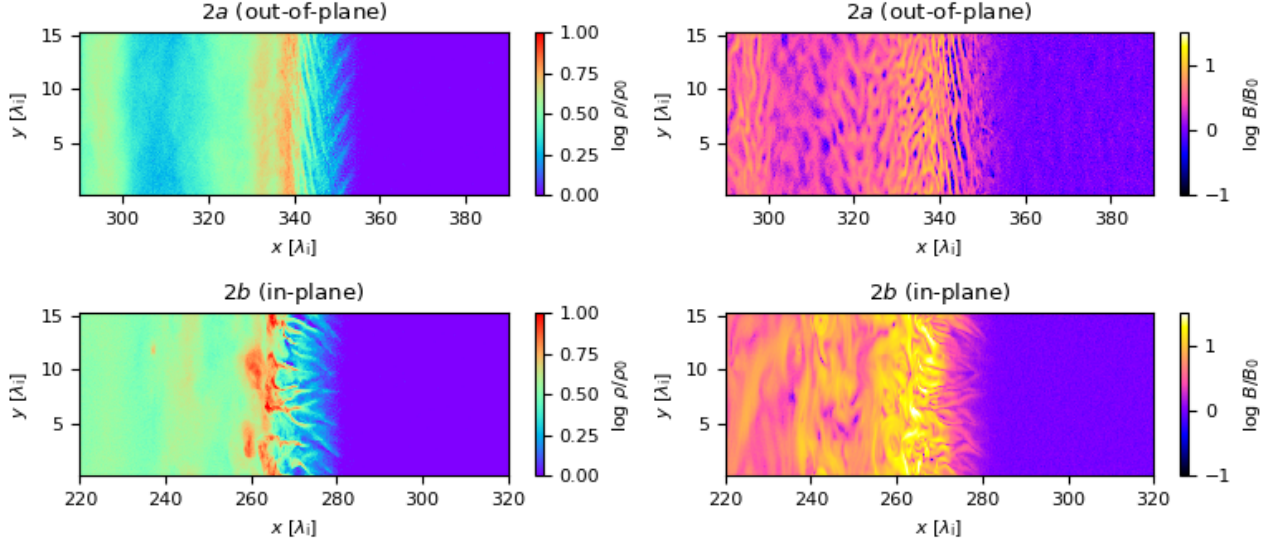
75

Figure 6.8: Comparison of density and magnetic field maps for runs *2a* and *2b*, having same obliquity $\theta = 78°$ but different initial magnetic field orientation with respect to the simulation plane at $t\omega_{ci} = 28$.

and the 1D run have similar features in the upstream. We must take into account the fact that the 1D run requires a higher mass ratio in order to develop a comparable amount of pre-acceleration, so the curve is peaked at higher energies, as explained above.

We conclude that, in 1D simulations, most physical processes present in 2D (out-of-plane) runs are observed as well, so we can consider them accurate enough to study particle acceleration. In these setups, we find that the following parameter combination is the best compromise between reliability and computational cost: $ppc_0 = 500$ and $m_i/m_e = 300$.

The role of obliquity

As discussed in Section 6.3.1, we chose $\theta = 78°$ as the reference obliquity for cosmic shocks in filaments. However, we pointed out that, although corresponding to the peak of the distribution in Figure 6.3, this obliquity does not represent the absolute majority of shocks. In order to provide a broader analysis, we also considered the case of a less oblique shock (albeit still quasi-perpendicular) with an initial obliquity of $\theta = 60°$. We covered both the 1D (run *1c*) and 2D cases (run *2c*, out-of-plane, and run *2d*, in-plane). In Figure 6.10 and Figure 6.11, we compare these runs with their corresponding run having $\theta = 78°$. We notice that some degree of acceleration is present in all runs (except for run *2b*, as previously observed), with a systematic increase at lower obliquities.

It is known that for quasi-perpendicular shocks, electron (pre)-acceleration is more prominent for smaller angles, as a consequence of the presence of a critical angle θ_{crit} [Sironi et al., 2015]. This effect is ascribable to the fact that fewer and fewer electrons can outrun the shock if the obliquity exceeds $\theta > \theta_{crit}$, and particles would need to move along the field faster than the speed of light in order to move back upstream. The value of θ_{crit} is a function of flow velocity, magnetization and mass ratio (see Equation 6.5).

Therefore, as expected, the energy spectra for the two tested obliquities differ due to two main features: 1) more particles deviate from the Maxwellian for $\theta = 60°$ (as will be quantified later), because they are facilitated in outrunning the shock; 2) the Maxwellian peak is shifted towards higher temperatures for $\theta = 60°$: this is ascribable to the higher number of particles that are scattered back and forth upstream
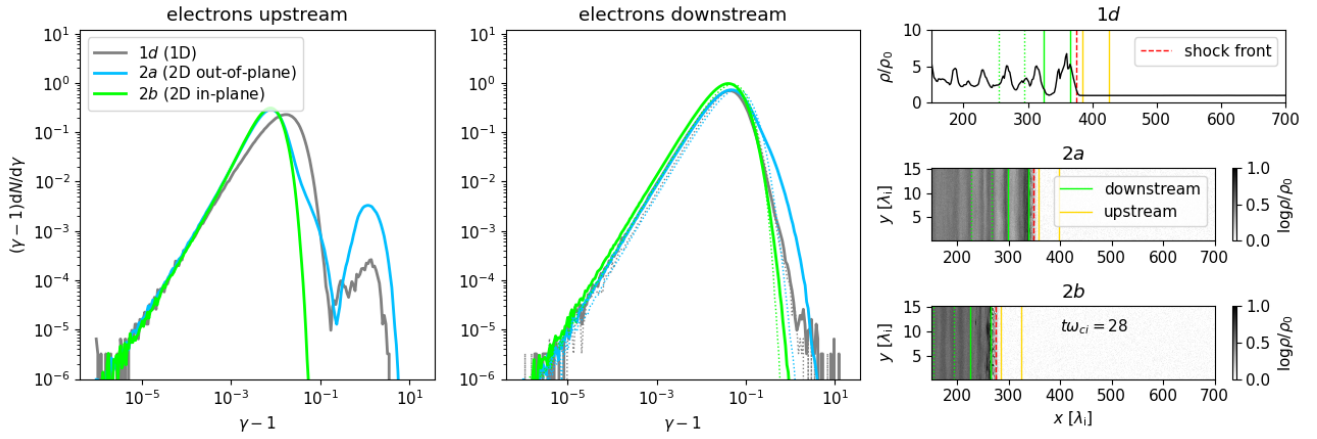
Figure 6.9: Comparison of runs *1d*, *2a* and *2b* at $t\omega_{ci} = 28$, which differ in the number of dimension of the domain and (in the 2D cases) in the angle ϕ. *Left and central panel:* spectra of electrons upstream and downstream. *Right panels:* density profile normalized to the initial density; the highlighted areas indicate the regions from which electrons are extracted in the upstream ($[x_{\text{shock}} + 10\lambda_{\text{i}}, x_{\text{shock}} + 50\lambda_{\text{i}}]$) and in the downstream (two different downstream areas are compared: $[x_{\text{shock}} - 120\lambda_{\text{i}}, x_{\text{shock}} - 80\lambda_{\text{i}}]$, dotted line, and $[x_{\text{shock}} - 50\lambda_{\text{i}}, x_{\text{shock}} - 10\lambda_{\text{i}}]$, solid line).

and downstream after interacting with the shock, which causes heating and therefore a hotter distribution. This is especially evident in the 1D comparison in Figure 6.10.

We point out that even for $\theta = 60°$ there is consistency with our findings about the dependence on dimensionality and ϕ, shown in Section 6.3.2, namely the similarity between the 1D and 2D out-of-plane configurations with respect to the 2D in-plane one, which totally ($\theta = 78°$) or partially ($\theta = 60°$) opposes to particle acceleration (Figure 6.11).

6.3.3 The electron acceleration efficiency

In order to assess the mechanisms behind electron acceleration and its efficiency, we analyse the trajectories of the most energetic electrons found in the downstream for the two values of obliquity in runs *1c* and *1d*. We opt to address this matter for 1D simulations, because we managed to push the mass ratio to more realistic values, which we identified as the most critical parameter determining whether particles are able to outrun the shock or not. Furthermore, an extensive analysis of 2D simulations for both in-plane and out-of-plane configurations was already performed in the work by Bohdan et al. [2019b] (and following papers). In Figure 6.12 we provide an example, taken from run *1d*, of an electron progressively gaining energy through the interaction of the shock front. From this preliminary qualitative analysis, we immediately observe that, every time the particle encounters a density gradient, it gains energy. Although a more rigorous study of the underlying processes is necessary to doubtlessly identify the acceleration mechanism, this kind of behavior strongly points to SDA being the main process involved.

An important outcome of this work is to refine the existing estimates on the (pre-)acceleration efficiency of relativistic electrons by cosmic shocks, especially for the typical accretion shocks surrounding filaments, which have never been subject of PIC simulations. Even if our PIC simulations cannot be run long enough to measure the proper onset of the DSA stage, the measured fraction of pre-accelerated electrons towards the end of our runs can be extrapolated to provide the best estimate ever so far for the acceleration efficiency of shocks in filaments. To a first approximation, we can thus assume that all
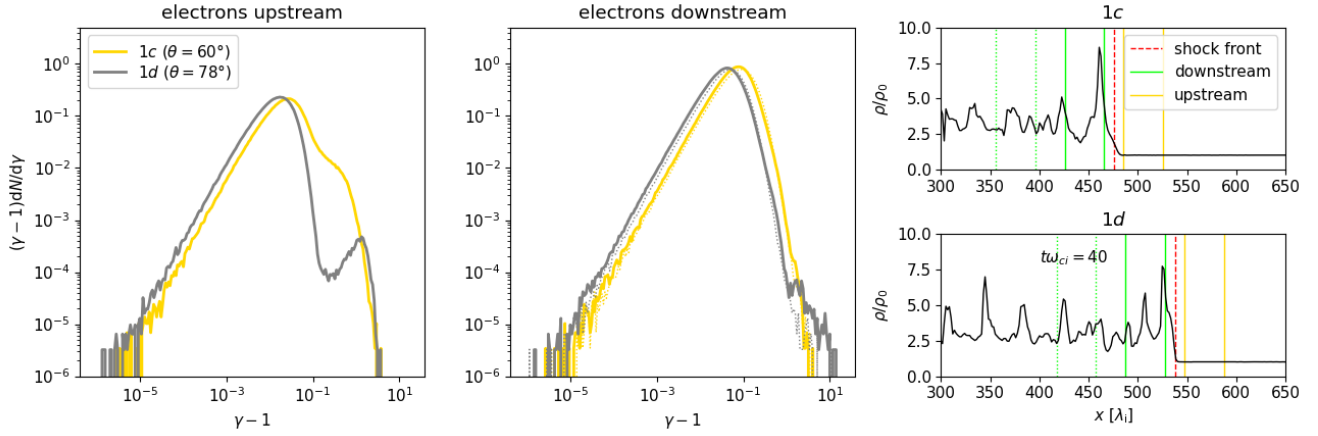
Figure 6.10: Comparison of runs *1c* and *1d* at $t\omega_{ci} = 40$, which differ in the magnetic field obliquity θ. *Left and central panel:* spectra of electrons upstream and downstream. *Right panels:* density profile normalized to the initial density; the highlighted areas indicate the regions from which electrons are extracted in the upstream ($[x_{shock} + 10\lambda_i, x_{shock} + 50\lambda_i]$) and in the downstream (two different downstream areas are compared: $[x_{shock} - 120\lambda_i, x_{shock} - 80\lambda_i]$, dotted line, and $[x_{shock} - 50\lambda_i, x_{shock} - 10\lambda_i]$, solid line).
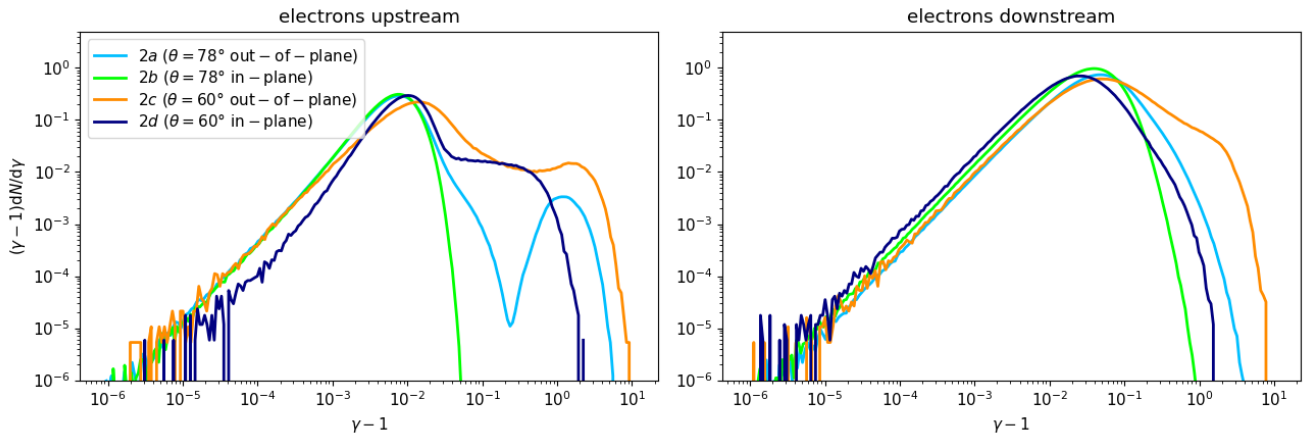
Figure 6.11: Spectra of electrons upstream and downstream for runs *2a*, *2b*, *2c* and *2d* at $t\omega_{ci} = 26$.
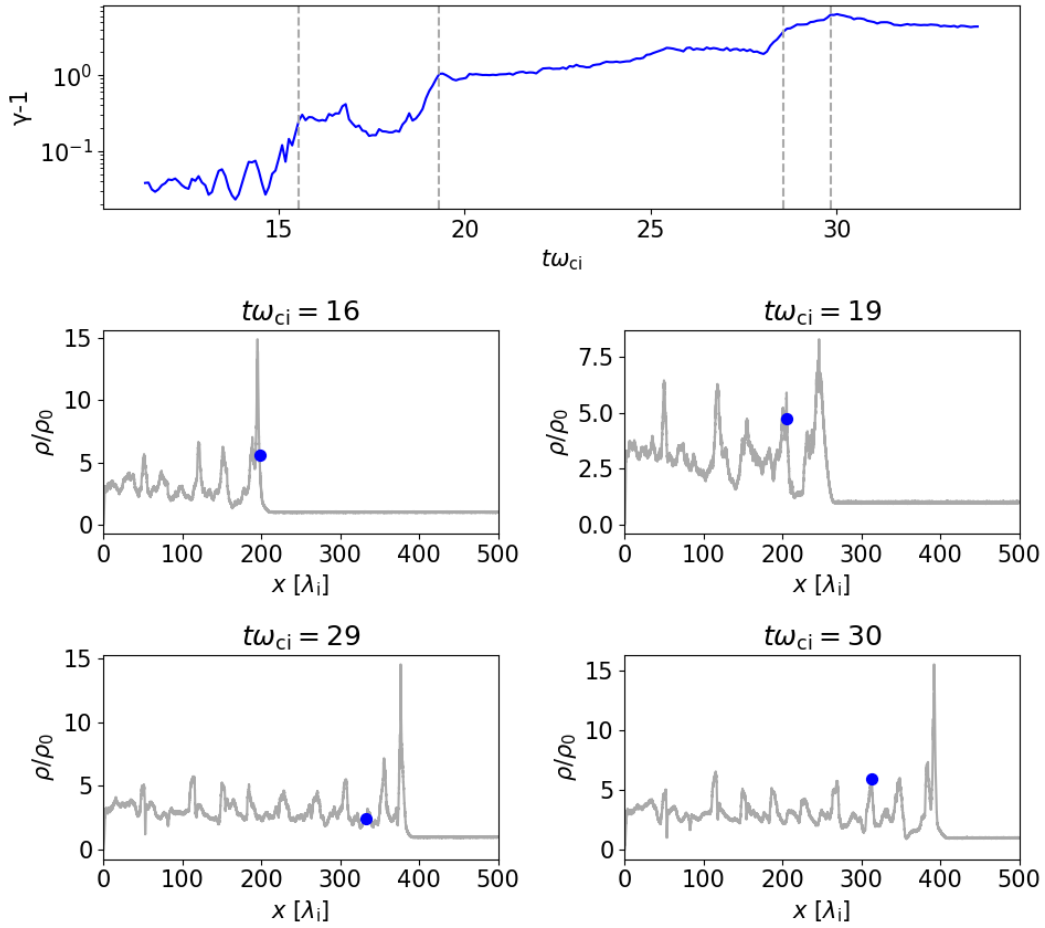
Figure 6.12: Energy evolution of an electron being pre-accelerated by the interaction with density gradients (at four significant points in time).

electrons accelerated above a critical energy will, sooner or later, undergo first-order Fermi acceleration, and eventually develop the classic power-law distribution of momenta produced by DSA. Even if this can be directly tested only with longer and more computationally demanding simulations (owing to the much larger domain we should simulate), our results can be already used for a first order estimate of the injection fraction into DSA.

To this end we computed, both in the upstream (i.e. the area delimited by $[x_{\mathrm{shock}} + 10\lambda_i, x_{\mathrm{shock}} + 50\lambda_i]$) and in the downstream (i.e. the area delimited by $[x_{\mathrm{shock}} - 50\lambda_i, x_{\mathrm{shock}} - 10\lambda_i]$) the fraction of electrons with energies above a critical energy threshold, marking the injection region into the DSA regime. The energy spectra of non-accelerated electrons can be approximated by a Maxwellian: in the upstream, since the fluid is moving with respect to the reference frame, the spectra need to be fitted with a moving Maxwell-Jüttner distribution with temperature $T = 2.392 \times 10^{-5} \, m_i c^2 / k_{\mathrm{B}}$ and velocity $\beta_0 = 0.1$. In the downstream, the plasma is at rest with respect to the reference frame and the Maxwellian is shifted due to heating. We choose a fiducial margin of 3 times the value of the Maxwellian (computed as a function of $\gamma - 1$), and tag all particles in the range above this threshold as pre-accelerated (see Figure 6.13). This way we can paramterize the acceleration efficiency, ξ_{inj}, as the percentage of electrons exceeding the Maxwellian, with respect to all of the electrons in the selected (upstream or downstream) subvolume.

In the example given in Figure 6.13, we find that, at $t\omega_{\mathrm{ci}} = 40$, $\xi_{\mathrm{inj}} \approx 0.017\%$ of electrons in the downstream are pre-accelerated significantly beyond the Maxwellian in run *1d*, and $\xi_{\mathrm{inj}} \approx 0.007\%$ in run *1c* (the above estimates are $\approx 0.002\%$ and $\approx 0.15\%$ if measured in the upstream, respectively.). In the following, we will restrict our analysis to the downstream region, where the acceleration of electrons dominating the radio signal is supposed to take place. We shall notice that an intrinsic limitation of this approach is that a precise measure of ξ_{inj} is prevented by the time variability of our spectra, which causes the fraction to fluctuate from snapshot to snapshot, both in the upstream and in the downstream, as shown in Figure 6.14. If we take the time average and the variance of the recorded injection fraction in the two cases, we get $\xi_{\mathrm{inj},60} = 0.01 \pm 0.004\%$ and $\xi_{\mathrm{inj},78} = 0.007 \pm 0.004\%$ (1σ deviates), respectively.

We can now compare this estimate with previous predictions from fluid simulations of DSA, applied to the intergalactic or intracluster medium, in order to assess to which extent the previous guesses for the radio emission from shocked electrons in the cosmic web are reliable. Here we compare with the results of 1D convection-diffusion simulations by Kang and Ryu [2013], who evolved quasi-parallel shocks with Bohm diffusion coefficient, a self-consistent treatments of thermal leakage injection, the Alfvén wave propagation and the back reaction from the magnetic field amplification by CR instabilities at the shock front. In order to translate the predicted trend for $\xi_{\mathrm{inj}}(M_{\mathrm{s}})$ from these simulations into an electron injection fraction, an additional factor is required to convert from CR protons to electrons. This parameter is usually taken to be $K_{\mathrm{ep}} \approx 10^{-2}$, based on the observed ratio between relativistic electrons and protons in the Milky Way. This is also in line with the injection spectral index of local Galactic supernova remnants [e.g. Uchiyama et al., 2007], even though this value is pretty much unconstrained both from theory and observations in the case of the intergalactic medium, and for the regime of shocks we are concerned with here.

Figure 6.15 shows the comparison of our results for the $M_{\mathrm{s}} = 15$ shock with $\theta = 60°$ and $\theta = 78°$ and the trend of $\xi_{\mathrm{inj}(M)}$ simulated by Kang and Ryu [2013]. Clearly, the DSA prediction for $K_{\mathrm{ep}} = 10^{-2}$ (solid line) underestimates the injection fraction we measure in both runs, and the values of ξ_{inj} measured in the two obliquities are better matched if we rescale the DSA prediction by $K_{\mathrm{ep}} \approx 5 \cdot 10^{-2}$ (dashed, $\theta = 78°$) or $K_{\mathrm{ep}} \approx 10^{-1}$ (dotted, $\theta = 60°$).

This finding is very important, as it implies already that the efficiency typically used to predict the emission from the shocked cosmic web in the radio band may be significantly underestimated. Determining the exact amplitude of this underestimate requires more extended calculations, in order to take into account the full distribution of temperatures, shock strengths and obliquities for the whole
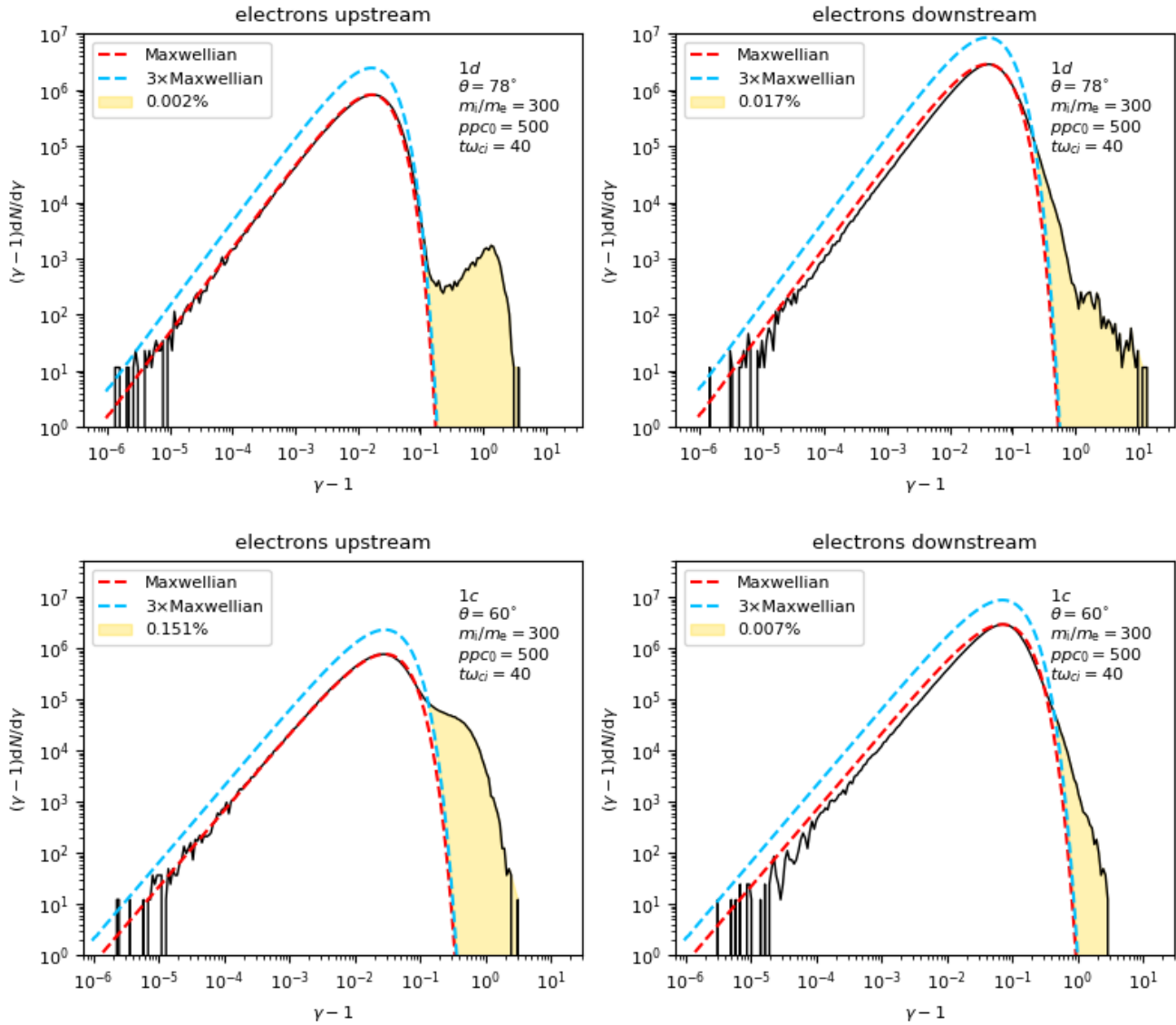
Figure 6.13: Electron energy spectra showing the criterion to estimate (pre-)acceleration efficiency upstream (*left*) and downstream (*right*) for runs *1d* (*top*) and *1c* (*bottom*). The red dashed lines represent the fitted Maxwellian, the light-blue dashed lines are obtained multiplying the Maxwellian times 3 (chosen as the threshold) and the yellow area highlights the particles exceeding this threshold.
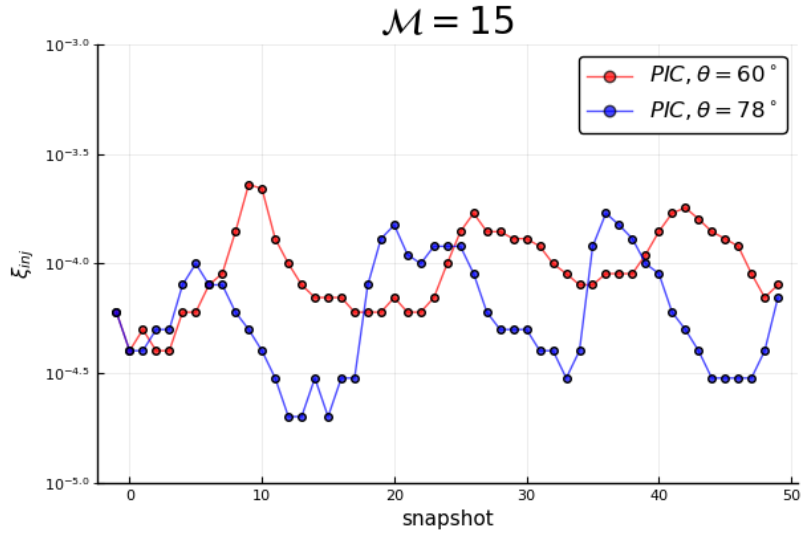
Figure 6.14: Time sequence for the fraction of electrons pre-accelerated in the downstream region of runs *1c* and *1d*, for the last 50 timesteps of each simulation.
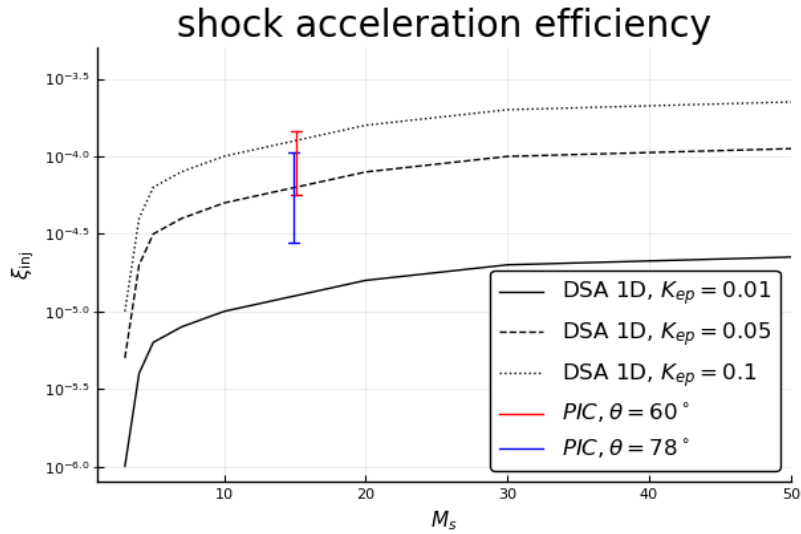
Figure 6.15: Injection fraction of relativistic electrons as measured in our PIC simulation, compared to DSA estimates from Kang and Ryu [2013]. The colors give the values measured for our $M_s = 15$ shock and for the two obliquities of runs *1c* and *1d*. For each run we show the $\pm\sigma$ values around the mean of the acceleration efficiency, measured in the downstream region in the last recorded 50 snapshots of the simulation. For the DSA, we consider two different values of the electron to proton ratio, $K_{ep} = 10^{-2}$, $5 \cdot 10^{-2}$ and 10^{-1}, as a function of the shock Mach number.

simulated population of filaments, and even for different realistic scenarios of magnetogenesis. Moreover, the acceleration efficiency (defined as the ratio between the incoming kinetic energy flux across shocks and the energy flux of accelerated CR electrons) is the fundamental parameter used to link the macroscopic scales of cosmological MHD simulations to the exact prediction on the radio emission [e.g. Hoeft and Brüggen, 2007, Vazza et al., 2015, 2021]. However, this comparison stresses already the relevance of our new campaign of PIC simulations, and it suggests a viable (albeit computing demanding) future approach to improve the existing predictions on the injection efficiency of relativistic electrons, in a regime of cosmic shocks never explored so far.

6.4   Discussion and conclusions

In this work we lay the foundation for a comprehensive study of particle acceleration in shocks typical of cosmic filaments by means of new PIC simulations. We devote a significant part of the analysis to the relevance of the parameter choice for the code TRISTAN-MP and we find that identifying the right combination of mass ratio and number of particles per cell is crucial for an accurate reproduction of the non-thermal processes involved. We also find that, if the minimum requirements for m_i/m_e and ppc_0 are fulfilled, then a 1D setup is enough to provide the same particle energy spectra as 2D simulations, while being much less computationally expensive.

Once established the right parameter combination, we then investigated the role of obliquity (i.e. the angle formed by the magnetic field in the upstream and the shock propagation direction) in the acceleration of electrons. We consider two obliquity options, both in the regime of quasi-perpendicular shocks, which previous works [e.g. Kang and Ryu, 2013] showed to be the most suitable for electron acceleration, and which are also widespread in filaments [Banfi et al., 2020, 2021]: $\theta = 78°$ and $\theta = 60°$. We indeed observe electrons being (pre-)accelerated for both obliquities: by comparing the obtained spectra with previous works and by studying the particles' trajectories at the moment of their maximum energy gain, we ascribe the pre-acceleration (visible as a 'bump' in the upstream) to SDA. SDA allows electrons to gain energy by drifting on the shock front along the motional electric field, up to Lorentz factors $\gamma \sim 3$. We also observe the first stages of the actual acceleration process, i.e. DSA, as a deviation of the spectrum from the Maxwellian in the downstream, which provides electrons with energies of $\gamma \sim 10$ (at the time reached by our simulations, $t\omega_{ci} = 40$). Although a similar trend is found for both magnetic field orientations, the run with the less oblique configuration ($\theta = 60°$) shows a systematic higher degree of electron acceleration, which was also confirmed by a quantitative estimate of the acceleration efficiency. We considered the percentage of (pre-)accelerated particles in the proximity of the shock and concluded that, for 1D simulations, an obliquity of $\theta = 60°$ provides an injection fraction ~ 5 times higher than a configuration with $\theta = 78°$. These new simulations allow us a more precise and physically motivated calibration of the previous acceleration efficiency of electrons in shocks which are and will be targeted by deep radio observations [Locatelli et al., 2021, Vernstrom et al., 2021], with the ambitious goal of detecting the radio cosmic web. Compared to existing predictions on the acceleration of relativistic electrons from shocks surrounding filaments, based on simpler 1D models of DSA usually assumed in cosmological simulations, our new PIC runs suggest an overall injection of relativistic electrons a factor $\sim 5 - 10$ higher (depending on the exact shock obliquity) than what has been usually assumed so far, with important consequences on the future modelling of shocks in this regime.
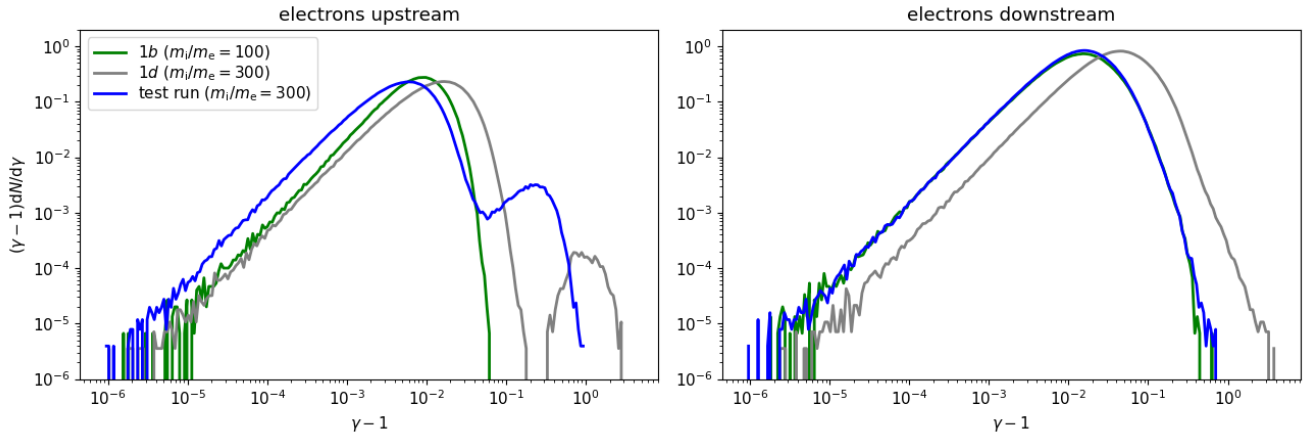
Figure 6.16: Spectra of electrons upstream and downstream for runs *1b*, *1d*, and the test run at $t\omega_{ci} = 15$.

6.5 Appendix

6.5.1 Caveats on mass ratio variation

Since the temperature of ions (which is set equal to the ones of electrons) is regulated by the input parameter $k_B T_i/(m_i c^2)$, which we kept unchanged in all runs, if the mass ratio varies, then the spectrum of electrons will be peaked at different values, as already shown in Figure 6.6. In this Figure, we also notice how an increased mass ratio makes a difference on whether the shock provides acceleration to electrons or not. However, since the spectra of simulations with different m_i/m_e are inevitably shifted with respect to each other, the physics of electrons might introduce some contribution to the occurrence of acceleration by itself. In order to test this, we tried to reproduce a scenario in which we increased the mass ratio by a factor 3 ($m_i/m_e = 300$) , but at the same time we kept the electron's physics similar to the low-mass ratio ($m_i/m_e = 100$) case. To do so, we decreased both the shock velocity and the plasma temperature (by respectively a factor $\sqrt{3}$ and 3), obtaining $\beta_0 = 0.05774$ and $k_B T_i/(m_i c^2) = 7.972 \times 10^{-6}$. In Figure 6.16, we show the spectra of this test simulation compared to the ones of runs *1b* and *1d*: clearly, the electron thermal properties of run *1b* and the test run are similar. However, while no acceleration is provided for the lower mass ratio, the typical pre-acceleration bump can be observed in the upstream for the test run, similarly to what happens in run *1d*, despite the shift of the Maxwellian. This confirms that the pre-acceleration is made easier by the increased mass ratio, regardless of the temperatures reached by the electrons (at least for the values considered here, which are still sufficiently non-relativistic).

Part III

Tracing the magnetized cosmic web

7. On the alignment of halos, filaments and magnetic fields in the simulated cosmic web (Banfi et al., 2021)

Abstract   The continuous flow of gas and dark matter (DM) across scales in the cosmic web can generate correlated dynamical properties of halos and filaments (and the magnetic fields they contain). With this work, we study the halo spin properties and orientation with respect to filaments, and the morphology of the magnetic field around these objects, for halos with masses in the range $\sim 10^8 - 10^{14}$ M$_\odot$ and filaments up to $\sim$ 8 Mpc long. Furthermore, we study how these properties vary in presence, or lack thereof, of different (astro)physical processes and with different magnetic initial conditions. We perform cosmological magnetohydrodynamical simulations with the Eulerian code ENZO and we develop a simple and robust algorithm to study the filamentary connectivity of halos in three dimensions. We investigate the morphological and magnetic properties and focus on the alignment of the magnetic field along filaments: our analysis suggests that the degree of this alignment is partially dependent on the physical processes involved, as well as on magnetic initial conditions. We discuss the contribution of this effect on a potential attempt to detect the magnetic field surrounding these objects: we find that it introduces a bias in the estimation of the magnetic field from Faraday rotation measure techniques. Specifically, given the strong tendency we find for extragalactic magnetic fields to align with the filaments axis, the value of the magnetic field can be underestimated by a factor $\sim$ 3, because this effect contributes to making the line-of-sight magnetic field (for filaments in the plane of the sky) much smaller than the total one.

7.1   Introduction

The evolution of the Universe by hierarchical clustering has led to the assembly of different structures, characterised by being either underdense or overdense to different extents, like voids, walls, filaments and halos. Connected together, all of these elements constitute the so called cosmic web, a network of dark and baryonic matter, which links all kinds of structures in a distinctive, intricate arrangement [Bond et al., 1996]. The pattern of the cosmic web is the manifestation of the tidal field arisen from the inhomogeneous distribution of matter as a result of anisotropic gravitational collapse [Zel'dovich, 1970], leading to the contraction of matter into walls, filaments and fully collapsed entities. The connectivity of these components can be explained by Bond's theory [Bond et al., 1996] as an effect of the tidal shear, which generates the quadrupolar mass distribution leading to a typical cluster-filament-

cluster configuration. Hence, filamentary structures are formed in environments where shear stresses are effective between the overdense matter and voids, thus dragging the gas along the spine of the filament.

The tidal field is also believed to be responsible for the acquisition of angular momentum by these structures, following the Tidal Torque Theory (TTT) [Hoyle, 1949, Peebles, 1969, Doroshkevich, 1970, White, 1984], thus linking the rotation properties of halos to their surroundings' density distribution. According to TTT, the halo spin should initially be correlated with the principal axes of the local tidal tensor, and in particular be perpendicular to the hosting filament orientation. However, many studies showed that there actually is a transition mass below which spins are mostly parallel to the filament, and above which the preferential arrangement is perpendicular: the value of the so called *spin flip mass* is reported to span from ~ 0.5 to $\sim 5 \times 10^{12} \, h^{-1} \, M_\odot$ in different works [e.g. Aragón-Calvo et al., 2007, Hahn et al., 2007, 2010, Codis et al., 2012, Libeskind et al., 2013, Trowland et al., 2013, Dubois et al., 2014, Forero-Romero et al., 2014, Wang and Kang, 2017, Ganeshaiah Veena et al., 2018, 2019, 2021]. This effect is believed to be due to a non-linear phase of TTT, involving mergers or accretion of substructures [Welker et al., 2014, Bett and Frenk, 2012, 2016].

This trend is supported by galaxy observations: spin properties of galaxies can be obtained from their rotation curves, with some assumptions on galaxy morphological properties [e.g. Hernandez and Cervantes-Sodi, 2006]. Observational studies vastly confirm that spins of spiral galaxies (associated to less massive halos) are mostly parallel to the host filament, while elliptical galaxies (associated to more massive halos) tend to spin along the direction normal to the filament [e.g. Tempel et al., 2013, Cervantes-Sodi et al., 2010, Tempel and Libeskind, 2013, Zhang et al., 2013, Pahwa et al., 2016, Hirv et al., 2017].

Among the various large-scale fields that can develop a relevant correlation across scales, are also extragalactic magnetic fields [e.g. Ryu et al., 2008], as we preliminary explored in Banfi et al. [2020]. The formation dynamics of the cosmic web is indeed also found to affect the large-scale topology of magnetic fields, for a variety of possible seeding scenarios. In particular, in Banfi et al. [2020] we studied the angle formed by the propagation direction of cosmic shocks and the up-stream magnetic field (i.e. obliquity), which is believed to be a crucial parameter for cosmic-ray acceleration by shocks [e.g. Bykov et al., 2019, and references therein]: with cosmological simulations we measured that magnetic field lines tend to align to filaments both inside and outside the filament, following the flow direction on the gas, as a consequence of the velocity shear. This effect, which was found to apply to several variations of primordial scenarios of magnetic fields [Vazza et al., 2021] as well as to variations of astrophysical seeding scenarios, albeit in a less prominent way [Banfi et al., 2020], impacts on obliquity and therefore on cosmic-ray acceleration.

The trend outlined above, on one hand being extremely relevant for the study of cosmic-ray acceleration and cosmic magnetism, is also very challenging to detect in observations. In this new work, we seek a way to assess the likely topology of magnetic fields around large-scale structures, based on the local properties of filaments and of the halos they contain. In practice, we want to determine whether morphological and dynamical properties of the cosmic web components are sufficient to adequately predict the characteristics of the magnetic field: in particular, in this work we shall look for a correlation between halos' angular momenta, filament orientation and magnetic field topology. Since in principle such properties may vary for different magnetic models, we also investigate different scenarios for the origin of extragalactic magnetic fields, which is believed to be either primordial or astrophysical: this introduces some degree of uncertainty on its topology, especially around structures like galaxy clusters and filaments [Subramanian, 2016].

This paper is structured as follows. In Section 7.2, we describe the computational setup for the simulations and we outline the network reconstruction method. In Section 5.3, we present our results for spin-filament and filament-magnetic field alignment. In Section 5.5, we describe the possible implications

of our results on observations, as well as the numerical limitations encountered in our analysis. Finally, Section 7.5 contains a brief summary and conclusions.

7.2 Methods

7.2.1 Simulations

The simulations of this work are performed with the Eulerian cosmological magnetohydrodynamical code ENZO [Bryan et al., 2014], which couples an N-body particle-mesh solver for DM [Hockney and Eastwood, 1988] with an adaptive mesh refinement method for the baryonic matter [Berger and Colella, 1989]. We used a piecewise linear method [Colella and Glaz, 1985] with Dedner cleaning MHD solver [Dedner et al., 2002] and time integration based on the total variation diminishing second-order Runge-Kutta scheme [Shu and Osher, 1988]. In this work, we present the analysis of simulations of different volumes, resolutions and scenarios of the origin of magnetic fields. In particular, we analyze two sets of simulations, which will be referred to as *"Roger"* and *"Chronos"* (see Table 7.1). While the first is intended to test the resolution-dependent trends in the properties of the components cosmic web (for a relatively small cosmic volume), the second is designed to allow us to monitor how the properties of large-scale magnetic fields are related to the orientation of cosmic filaments, for a few relevant variations of the assumed origin scenario of cosmic magnetism. For both sets, the cosmological parameters were chosen accordingly to a ΛCDM cosmology: $H_0 = 67.8$ km s^{-1} Mpc^{-1}, $\Omega_b = 0.0468$, $\Omega_m = 0.308$, $\Omega_\Lambda = 0.692$ and $\sigma_8 = 0.815$ [Planck Collaboration et al., 2016].

Roger

We first simulated a small volume of $\approx (19$ Mpc$)^3$ (comoving) sampled with a static grid of 512^3 cells, with the following characteristics:

1. *"NR"*: non-radiative run with a primordial uniform volume-filling comoving magnetic field $B_0 = 0.1$ nG at the beginning of the simulation;

2. *"cool"*: radiative run including cooling, with a primordial uniform volume-filling comoving magnetic field $B_0 = 0.1$ nG at the beginning of the simulation.

Two additional simulations were run, similar to NR, in which the same volume is sampled by 256^3 and 128^3 cells, as a resolution test (see Section 7.3.2). The mass resolution for DM in the three Roger simulations is $6.3 \cdot 10^8$ M$_\odot$, $7.9 \cdot 10^7$ M$_\odot$ and $9.9 \cdot 10^6$ M$_\odot$ for the 128^3, 256^3 and 512^3 runs respectively.

Chronos

We simulated a volume of $\approx (84$ Mpc$)^3$ (comoving) sampled with a static grid of 1024^3 cells. We selected four runs taken from a larger dataset[1] provided by Vazza et al. [2017], which covers different possible scenarios for the origin and evolution of cosmic magnetic fields. The models chosen for this analysis are characterised by the following magnetic properties:

1. *"baseline"*: non-radiative run with a primordial uniform volume-filling comoving magnetic field $B_0 = 1$ nG at the beginning of the simulation;

---

[1] *"Chronos++"* suite: `http://cosmosimfrazza.myfreesites.net/the_magnetic_cosmic_web`

Name	Set	Details	B_0 [nG]	Comoving volume [Mpc^3]	Cells	Spatial resolution [kpc/cell]	DM resolution [M$_\odot$]
NR	Roger	non-radiative	0.1	19^3	512^3	37	$9.9 \cdot 10^6$
NR$_{256}$	Roger	non-radiative	0.1	19^3	256^3	74	$7.9 \cdot 10^7$
NR$_{128}$	Roger	non-radiative	0.1	19^3	128^3	148	$6.3 \cdot 10^8$
cool	Roger	cooling	0.1	19^3	512^3	37	$9.9 \cdot 10^6$
baseline	Chronos	non-radiative	1	84^3	1024^3	82	$8.1 \cdot 10^7$
Z	Chronos	tangled magnetic field	1	84^3	1024^3	82	$8.1 \cdot 10^7$
DYN5	Chronos	subgrid dynamo	10^{-9}	84^3	1024^3	82	$8.1 \cdot 10^7$
CSFBH2	Chronos	cooling + chemistry + star formation + AGNs	10^{-10}	84^3	1024^3	82	$8.1 \cdot 10^7$

Table 7.1: Main parameters of the simulations analyzed in this work.

2. *"Z"*: non-radiative run with a primordial magnetic field oriented perpendicularly to the velocity vector, as in Vazza et al. [2017], accordingly to the Zel'dovich approximation [e.g. Dolag et al., 2008], in such a way to prevent $\nabla \cdot \mathbf{B}$ from deviating from ≈ 0;

3. *"DYN5"*: non-radiative run with an initial seed magnetic field of $B_0 = 10^{-9}$ nG (comoving) and sub-grid dynamo magnetic field amplification computed at run-time, which allows to estimate the hypothetical maximum contribution of dynamo in low density environments [see Ryu et al., 2008], where it would be lost due to finite resolution effects [see Vazza et al., 2017, for more details];

4. *"CSFBH2"*: radiative run with an initial seed magnetic field $B_0 = 10^{-10}$ nG (comoving) including gas cooling, chemistry, star formation, thermal/magnetic feedback from stellar activity and active galactic nuclei (AGN). Supermassive black hole (SMBH) particles with a mass of $M_{\mathrm{BH},0} = 10^4$ M$_\odot$ are inserted at $z = 4$ at the centre of massive halos [Kim et al., 2011] and start accreting matter according to the Bondi-Hoyle formula (with an accretion rate of ~ 0.01 M$_\odot$/yr and a "boost" factor of $\alpha_{\mathrm{Bondi}} = 1000$, to compensate for gas clumping unresolved by the simulation). Star forming particles are generated according to Kravtsov [2003], which includes the contribution of stellar winds to the thermal feedback. Magnetic feedback from bipolar jets is introduced into the system, with efficiencies $\epsilon_{\mathrm{SF,b}} = 10$ % and $\epsilon_{\mathrm{BH,b}} = 1$ % for star formation and SMBH respectively [see Vazza et al., 2017, for more details].

The mass resolution for DM in all Chronos runs is $8.1 \cdot 10^7$ M$_\odot$.

7.2.2 Network reconstruction

The network reconstruction process begins with the identification of halos and it connects them to trace filaments. This simple approach has already been successfully applied to the reconstruction of the network of galaxies in real observations [e.g. de Regt et al., 2018] and also has the potential to allow comparisons with the structural properties of other natural networks [e.g. Vazza and Feletti, 2020]. halos are found with either a halo finding friends-of-friends (FOF) algorithm included in Enzo [Bryan et al., 2014] or using a halo finder developed by our group, which is more suitable to analyse large cosmological simulations [e.g. Gheller and Vazza, 2020, and references therein]. halos in the mass range $\sim 10^8 - 10^{14}$ M$_\odot$ were identified by these methods (see Table in Appendix 7.6.1 for details). Filaments are tentatively found as the line connecting two sufficiently close halos (less than a certain distance l_c apart): if the gas density of each cell encountered by the line is above a certain threshold ρ_t, then the filament is confirmed, meaning that there actually is a significant overdensity even between the two nodes. The values of l_c and ρ_t
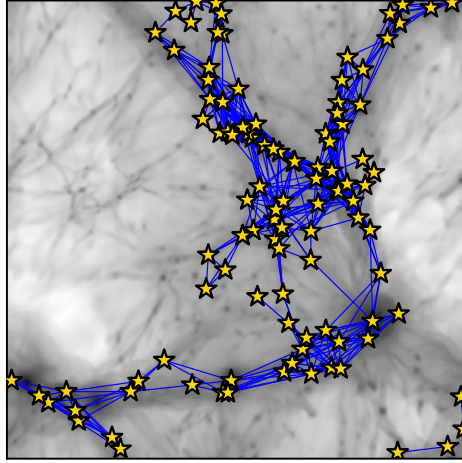
Figure 7.1: Projected density of a slice of 1 Mpc thickness and 19 Mpc side, with halos and filaments obtained by our algorithm inside the selected volume.

used for our network were respectively $\sim$ 4 Mpc and 10^{-30} g cm^{-3} for volumes of the Roger sample and $\sim$ 8 Mpc and 10^{-30} g cm^{-3} for the Chronos suite. Figure 7.1 shows the projection of a portion of the network traced by our algorithm: halos (yellow stars) are connected by filaments (blue lines) if the density requirement is met. The value of the density threshold was chosen by visually inspecting the selected areas for a certain range of values, as in Figure 7.2. Although even longer filaments are expected to be found in the simulated volume, we decided to narrow the sample down to filaments shorter than 4 Mpc or 8 Mpc, since this criterion would allow to obtain a big enough sample, but at the same time limit the computational time required. We comment this choice in Section 7.4.2.

7.2.3 Halo-filament pairing

Determining a correspondence between a halo and a filament is useful to find a relation between their properties, e.g. the alignment of halo spin axis and filament orientation. To assess which filament a certain halo belongs to, we looked for filaments that connect to the halo region[2]: thus, a halo may be associated to multiple filaments, e.g. when it belongs to a cluster which connects two or more filaments. We call this property *multiplicity $\mathcal{M}$*, i.e. the number of filaments corresponding to a halo (see Figure 7.3).

---

[2]We chose a volume of $\approx 400^3$ kpc^3 centred in the halo
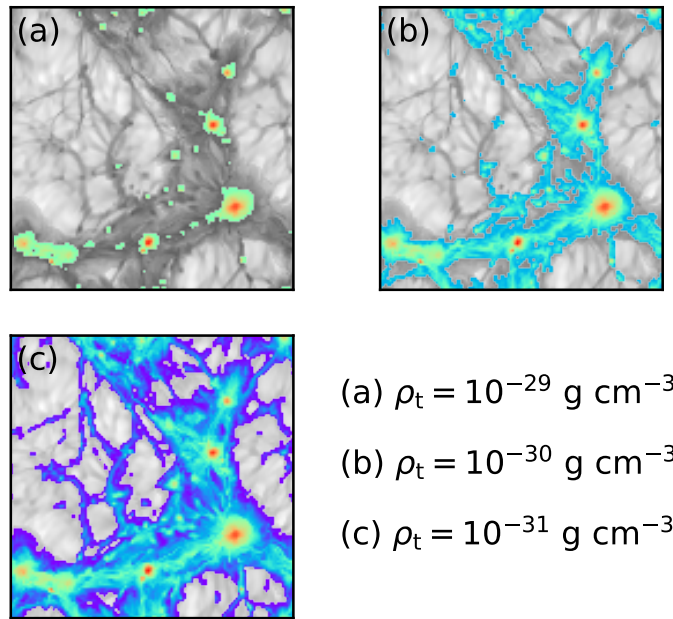
Figure 7.2: Gas density of a slice of 40 kpc thickness and 19 Mpc side, in greyscale (below ρ_t) and in colourscale (above ρ_t), for three different values of density threshold $\rho_t = 10^{-29}$ g cm^{-3}, 10^{-30} g cm^{-3} and 10^{-31} g cm^{-3}. This shows that the best criterion for selecting filaments is requiring $\rho > 10^{-30}$ g cm^{-3}.
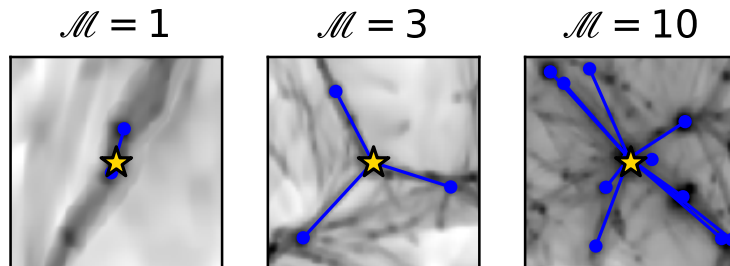
Figure 7.3: Examples of halo-filament(s) pairing for different multiplicities $\mathcal{M} = 1, 3, 10$.

7.3 Results

7.3.1 The alignment of halo spin, filaments and magnetic fields

Network properties

Our network reconstruction algorithm (Section 7.2.2) allows to retrieve each selected filament's endpoints' coordinates inside the grid:

$$\mathbf{P}_1 = \begin{bmatrix} x_1 \\ y_1 \\ z_1 \end{bmatrix} \quad \mathbf{P}_2 = \begin{bmatrix} x_2 \\ y_2 \\ z_2 \end{bmatrix}, \tag{7.1}$$

such that the filament orientation follows the vector $\mathbf{L} = \mathbf{P}_1 - \mathbf{P}_2$ and the filament length is equal to $L = |\mathbf{L}|$. The first panel of Figure 7.4 shows the histograms of filament lengths: the peak is found at ~ 1.5 Mpc and the distribution is mostly unaffected by cooling.

The FOF method that we used allowed to identify halos with a total (gas and DM) mass larger than $\sim 10^8 \, M_\odot$. The trend of the virial mass[3] as a function of the virial radius is shown in the second panel of Figure 7.4: both mass and radius have similar ranges for the two runs, but the run including cooling has a higher mass-to-radius ratio, implying a more concentrated distribution of DM due to baryonic infall [Blumenthal et al., 1986].

The *spin parameter* λ is a measure of the rotation of a halo with respect to its potential energy [Peebles, 1969]. This quantity is automatically computed by ENZO's halo finder according to this formula

$$\lambda = \frac{J \, |E|^{1/2}}{G M^{5/2}}, \tag{7.2}$$

where J, E and M are the halo angular momentum, energy and mass, and G is the gravitational constant. The third panel in Figure 7.4 gives the trend of the spin parameter as a function of halo virial mass: the evident scatter of λ at low masses is likely an effect of the poor accuracy in the determination of the angular momentum of small halos. Thus, in the following, we shall disregard the spin properties of halos with $M_{200} \lesssim 10^9 \, M_\odot$. At larger masses, the curve is mostly flat, meaning that similar values of spin parameters are found in a wide range of masses. This trend in consistent with what Bett et al. [2007] found for the Millennium simulation. We did not find significant changes in spin properties if cooling is turned on: this is in agreement with previous literature [e.g. Bryan et al., 2013]. Finally, in the bottom panel of Figure 7.4 we show that there is a slight correlation between the halo spin parameter (considering only halos with $M_{200} \gtrsim 10^9 \, M_\odot$) and the magnetic field strength at the corresponding location: faster rotating halos tend to be surrounded by stronger magnetic fields, regardless of the presence of cooling mechanisms.

Figure 7.5 illustrates the properties linked to halo multiplicity: the top panel shows that most halos are associated to a limited amount of filaments, but some of them belong to clusters, which are connected to the network through tens of filaments. Overall, cooling is not found to significantly impact on the multiplicity distribution, meaning that the number of halos per filament (at least on the spatial scales probed by this set of simulations) is not affected by the enhanced collapse of gas structures under the effect of radiative gas cooling. In both scenarios, multiplicity correlates with halo mass (bottom panel), i.e. more massive halos are connected to a larger number of filaments. This is consistent to what Colberg et al. [2005] found; also, the very high $\mathcal{M}$ values obtained for some halos could be biased by the fact that spurious filaments are identified in very dense volumes.

---

[3]M_{200} is defined as the total mass enclosed in a spherical volume of radius r_{200}, i.e. the distance from the halo centre where the average inner matter density is 200 times the cosmological critical density.
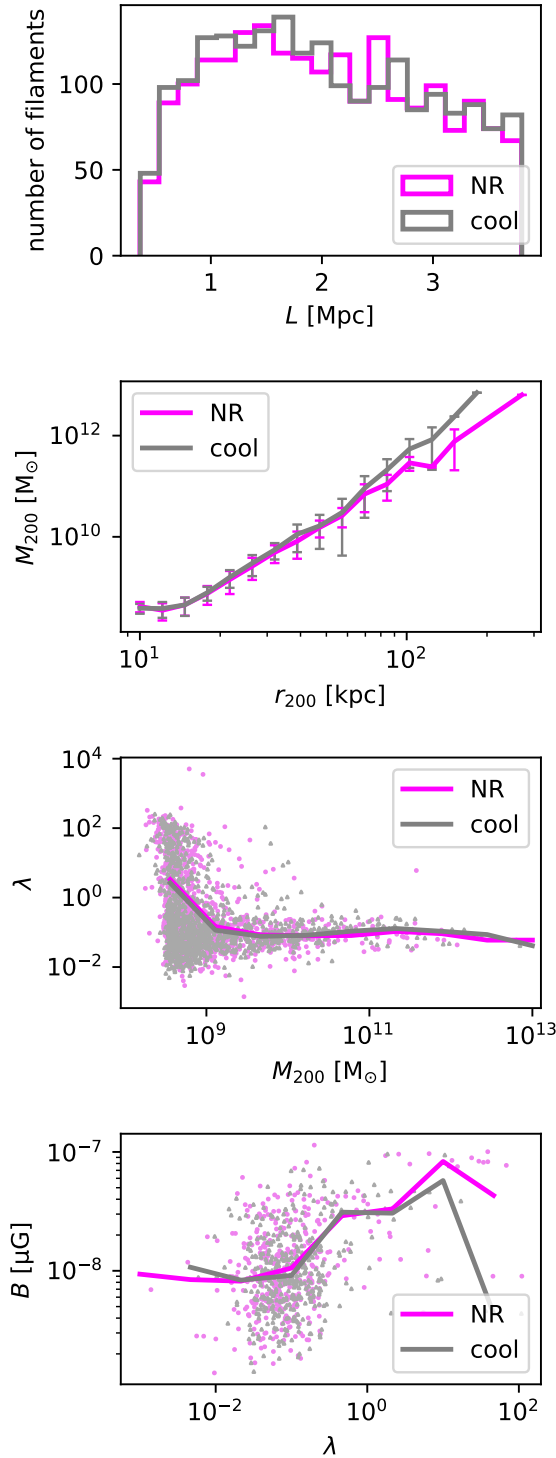
Figure 7.4: Comparison of halo and filament population for the NR and cool runs. First panel: distribution of filament lengths. Second panel: median virial halo mass per virial radius bin with relative error bars corresponding to the standard deviation. Third panel: scatter and median of halo spin parameter as a function of virial mass. Fourth panel: scatter and median of the magnetic field (averaged inside a r_{200}^3 volume around the halo) as a function of halo spin parameter.
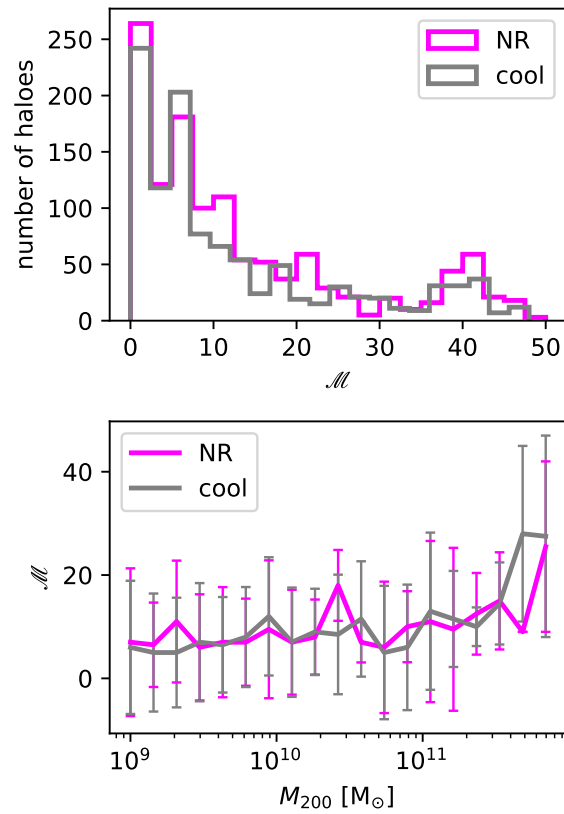
Figure 7.5: Distribution of multiplicity (top) and median multiplicity as a function of virial mass, with relative error bars corresponding to the standard deviation (bottom), for the NR and cool runs.

Spin - filament alignment

The spin axis orientation can be obtained from the angular momentum vector **J** of each halo, i.e. the vector sum of the angular momentum of each DM particle belonging to the halo. Thus, the angle formed by the halo spin axis and the hosting filament is:

$$\theta_{\text{spin--filament}} = \arccos\left(\frac{\mathbf{J} \cdot \mathbf{L}}{J\,L}\right). \tag{7.3}$$

This alignment is best described by the absolute value of the cosine of the angle formed by the two vectors:

$$\psi_{\text{spin}} = \left|\cos\theta_{\text{spin--filament}}\right|, \tag{7.4}$$

since random vectors in space form angles whose ψ_{spin} distribution is flat and averages to 0.5. If a halo corresponds to multiple filaments, a value of ψ_{spin} is computed for each filament, i.e. $\mathcal{M}$ times. The top panel of Figure 7.6 shows the distribution of ψ_{spin}, which is only marginally affected by the contribution of gas cooling. We can notice an excess of quasi-perpendicular configurations in the NR run, which disappears if cooling in included: a possible reason for this is that cooling enhances the accretion of denser material from filaments along more directions, which in turns tends to randomise the spin distribution. The central panel represents the median of ψ_{spin} for bins of increasing multiplicity: the two curves are quite similar and there is no striking trend. In the last panel we restrict the same analysis to halos with $\mathcal{M} = 1$, in order to study the typical behavior of halo spin in the presence of a single filament, as was done in previous works [e.g. the aforementioned Aragón-Calvo et al., 2007]. However, the scarcity of halos with $\mathcal{M} = 1$ makes the distribution too scattered to allow us to constrain any trend, so we were not able to confirm the spin flip found in literature.

Magnetic field - filament alignment

In a scenario in which cosmic magnetism is the product of primordial seed fields, cosmic structures and filaments form in a volume which is already filled by large-scale magnetic field lines. At some degree, this is also true if magnetic fields were seeded early enough for the local dynamics to rearrange the field topology. In Banfi et al. [2020], we studied the tendency of magnetic field lines to arrange parallel to filaments' external surface during filament formation, as a consequence of shear stresses. However, while in this first work we only gave a qualitative insight of this process, here we can perform a quantitative analysis, thanks to the additional information provided by our filament reconstruction algorithm. In order to better analyze the alignment of a filament to the surrounding magnetic field, we first need to establish a way to trace the filaments which is more accurate than a simple straight line between two halos: in many cases, the filament may be curved due to the presence of small halos. Thus, the procedure to trace the actual shape of the filament is the following:

1. the filament is divided into $N_r = 10$ regions, whose centres are equally spaced along the filament line and whose thickness is ~ 700 kpc;

2. for each of these regions, we compute the *centres of mass* for the gas and use them to mark the endpoints of the $N_r - 1 = 9$ *segments* that trace each filament;

3. the magnetic field vectors in the $N_r - 1$ cells corresponding to the segments' midpoints are then compared to the orientation of the $N_r - 1$ segments.
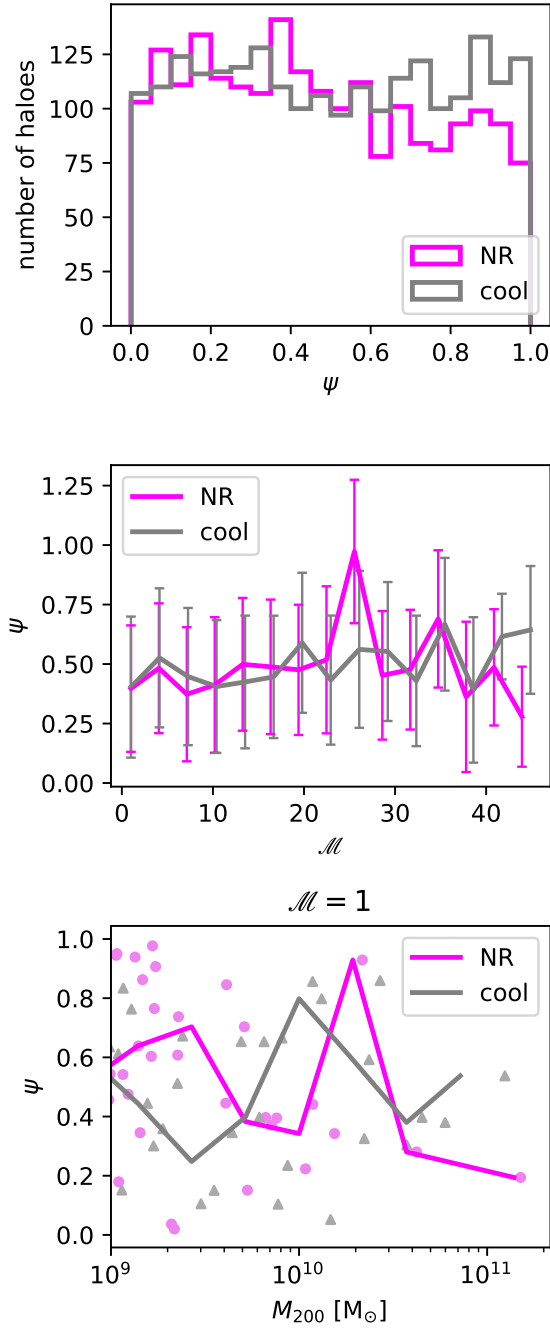
Figure 7.6: Comparison of halo spin behavior for the NR and cool runs. Top panel: histogram of the absolute value of the cosine of the angle between the spin direction and the host filament (if $\mathcal{M} > 1$ each of the angles is included in the statistic). Central panel: median and standard deviation of the cosine of the angle between the spin direction and the host filament for multiplicity bins (if $\mathcal{M} > 1$ each of the angles is included in the statistic), with relative error bars corresponding to the standard deviation. Bottom panel: scatter and median of the cosine of the angle between the spin direction and the host filament for halo mass bins if $\mathcal{M} = 1$.
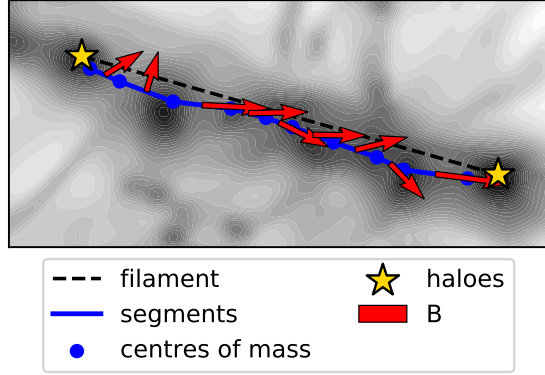
Figure 7.7: Projected density of a filament with local centres of mass, segments and corresponding magnetic field orientation.

Figure 7.7 shows a filament as an example of how the initial straight line differs from the final polygonal chain.

The alignment of the magnetic field and the filament is parametrised by the absolute value of the cosine of the angle formed by each segment and the corresponding **B** orientation at its midpoint[4]:

$$\xi_{\text{seg}} = \left|\cos\theta_{\text{B,midpoint−segment}}\right|. \tag{7.5}$$

The top panel of Figure 7.8 shows that the distribution is largely peaked at high values of ξ_{seg}, quite distinct from the flat distribution expected for random vectors. No relevant changes are introduced by the presence of cooling mechanisms, confirming once again that the density distribution is only slightly affected.

Although the procedure involving segments is a more meticulous way to study the **B**-filament alignment, we found that the initial approximation of the filament (i.e. the line connecting two halos) is not that far from the more accurate tracing of the filament: the bottom panel of Figure 7.8 shows the distribution of the cosine of the angle formed by the initial straight line and each one of the segments composing the polygonal chain. Based on this, we can reasonably consider that the global filament orientation (at least for straight enough filaments) is sufficiently well described by the line traced by connected halos.

Next, we want to determine the characteristic spatial scales at which the alignment develops, i.e. how far from the filament the **B**-filament alignment is still more significant than by random chance. To do so, we consider ellipsoidal shells of gas at increasing distance from the spine of filaments, as in Figure 7.9, and for each region we compute the angle formed by the magnetic field of every cell and the filament orientation. In detail, the procedure is the following:

1. for each filament, we consider a box-shaped subvolume containing it[5];

2. we identify *filament cells* as the ones that are intersected by the line connecting the pair of halos (i.e. filament endpoints);

---

[4]Although the value of the magnetic field at the midpoint may be subject to random fluctuations, the structures that we deal with are regular enough to ensure that no significant error is introduced, e.g. Figures 7.7, 7.9,7.12.

[5]For a filament delimited by two halos having coordinates (x_1, y_1, z_1) and (x_2, y_2, z_2), the box contains all the cells that satisfy $\min(x_1, x_2) − 500$ kpc $< x < \max(x_1, x_2) + 500$ kpc, $\min(y_1, y_2) − 500$ kpc $< y < \max(y_1, y_2) + 500$ kpc and $\min(z_1, z_2) − 500$ kpc $< z < \max(z_1, z_2) + 500$ kpc.
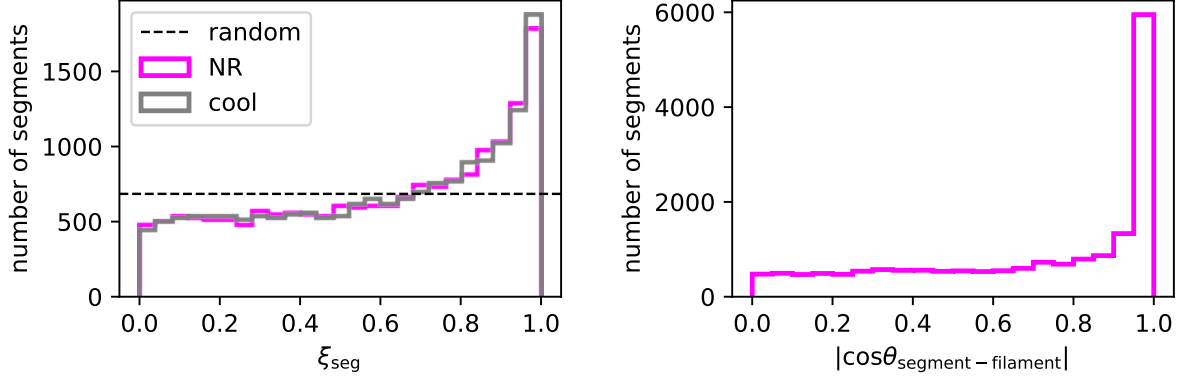
Figure 7.8: Top panel: histogram of the cosine of the angles formed by the magnetic field and the filaments' segments, compared to the random distribution. Bottom panel: histogram of the cosine of the angles formed by the line connecting the halos and the segments identified by the local centres of mass.

3. for every cell in the subvolume (*field cell*), the distance from each of the filament cells d_{fil} is computed;

4. for each field cell, we consider the smallest distance d_{min} among the ones just found;

5. we then bin the values of d_{min} for all the field cells, in such a way to define 5 ellipsoidal shells and the corresponding *shell cells*;

6. for each shell cell, the angle formed by the magnetic field and the filament line is parametrised by

$$\xi_{fil} = \left|\cos\theta_{B,cell-filament}\right|; \tag{7.6}$$

7. the average of ξ_{fil} is computed for each shell: higher values imply a better alignment.

Figure 7.10 shows the median value of ξ_{fil} in each of the five ellipsoidal shells considered, averaged over all filaments: the magnetic field starts to align to the leading direction of filaments already at a distance of ~ 800 kpc away, and it becomes increasingly more aligned approaching the filament spine. The presence of radiative gas cooling only moderately reduces the values of ξ_{fil} as a function of distance but otherwise preserves exactly the same trend: this can be ascribed to the effect of gas cooling, which tends to compress filaments towards their main axis [Gheller et al., 2015], hence a $\sim 10\,\%$ shift of the curve towards smaller distances.

We also noticed that filaments with poor **B**-filament alignment typically have more halos around them. We quantify this property by considering the amount of halos identified by the halo finder in the volume surrounding the filament, defined as above, weighted by their mass. In fact, a relation is found between the total mass of all nearby halos M_{nh} and **B**-filament alignment (Figure 7.11): the degree of alignment is significantly increased when the filament is surrounded by fewer halos.

Incidentally, this also implies that the mass resolution of our simulations (which may affect the number of small mass halos that can be formed in the volume) can slightly impact on the exact values of ξ_{fil}, since more halos are formed for increasing resolution and thus can "perturb" the shape of filaments and their local alignment with magnetic fields (see Section 7.3.2).

In summary, our preliminary analysis with a small cosmological volume, with and without the inclusion of radiative cooling, has shown that most filaments below a certain length can be described
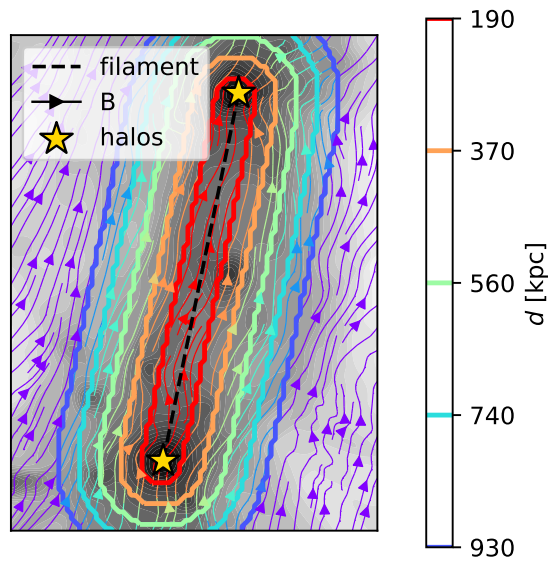
Figure 7.9: Projected density of a filament with contours indicating the distance from the filament with streamlines of integrated magnetic field.
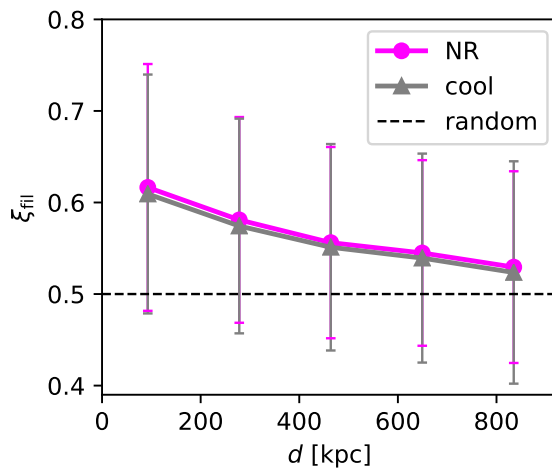
Figure 7.10: Median of the cosine of the angle formed by the magnetic field and the filament as a function of distance from the filament, with relative error bars corresponding to the standard deviation, for the NR and cool runs.
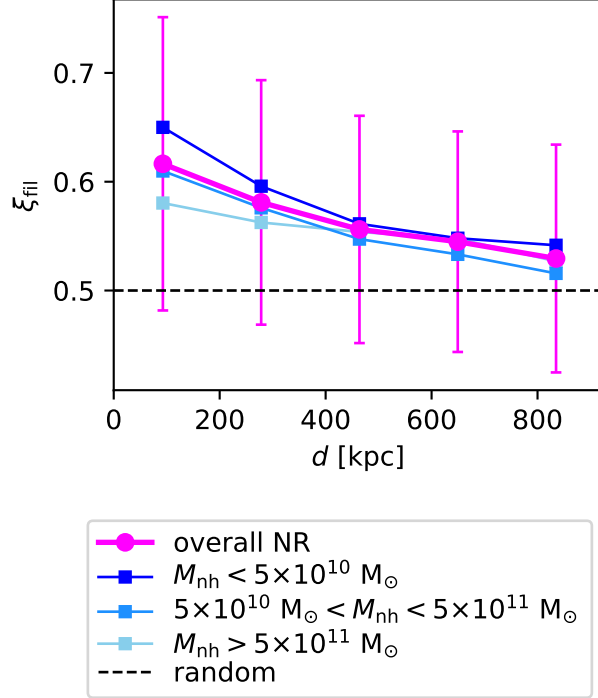
Figure 7.11: Median of the cosine of the angle formed by the magnetic field and the filament as a function of distance from the filament for different nearby halo masses in the NR run, with relative error bars corresponding to the standard deviation.

by straight lines connecting massive matter halos, and that their shape well correlates with the topology of magnetic fields around them. In particular, we found that the magnetic field lines are well aligned to the filament both inside and outside of the overdensity, meaning that shear forces effectively drag the magnetic field, even several hundreds of kpc away from the accretion shocks that surrounds filaments. This means that (as extensively discussed in Banfi et al. 2020) the alignment is not due the passage of shocks, bur rather to the global structure of the (shear) velocity field in the regions where filaments form in the hierarchical scenario. This effect is only marginally affected by non-gravitational effects, like gas cooling. On the other hand, the analysis of halo spin does not suggest any strong relation with the magnetic properties of the cosmic web, except for a slight tendency of magnetic fields to be stronger around halos with higher spin parameters. Furthermore, no significant correlation between spin orientation and filamentary structures is found, unlike what previous literature suggests: this is possibly to ascribe to the limited simulated volume and resolution, and thus the small amount of halos with reliable measures of angular momentum in our sample.

7.3.2 Resolution tests

In this Section, we show the results of a resolution test on the Roger run concerning the **B**-filament alignment. We ran simulations identical to NR, except for the number of cells (256^3 and 128^3, instead of the original 512^3), so that we could compare the same simulated volume (19^3 Mpc^3 comoving) at different resolutions: 37 kpc/cell, 74 kpc/cell and 148 kpc/cell. The three simulated volumes are fairly similar, so we can use the same network that we computed in the 512^3 run: this way, filaments can be found approximately at the same location, so we can estimate the **B**-filament alignment with the new

simulated magnetic field orientation and compare it to the 512^3 run. In particular, if we replicate Figure 7.10 for this set of simulations, we find higher values of $\xi_{\rm fil}$ for decreasing number of cells, i.e. better resolutions imply a slightly smaller **B**-filament alignment (see top left panel of Figure 7.12). We notice that the difference is mainly relevant in the proximity of the filament, so we now focus only on the area which is less than ~ 150 kpc away from the filament.

By visually inspecting some of the filaments, we observe that the variation of $\xi_{\rm fil}$ from the higher to lower-resolution runs is more significant if halos are found along the filament: the presence of massive structures curve the path of the magnetic field lines, lowering the $\xi_{\rm fil}$ value. This effect, however, becomes less important as the resolution worsens, since halos are less easily formed and are blurred into the filament, thus allowing the magnetic field to proceed straight undisturbed, as in Figure 7.12 (bottom right panel).

To further confirm this trend, we compute, for each filament of the original 512^3 run, the total mass of the identified halos which can be found in the filament's surroundings, thus potentially interfering with $\xi_{\rm fil}$. We then consider the average **B**-filament alignment inside the ~ 150 kpc shell and plot it as a function of the nearby halos' total mass $M_{\rm nh}$ in the upper-right panel of Figure 7.12: as expected, a better **B**-filament alignment is found where fewer halos surround the filament. Moreover, the lower-left panel of Figure 7.12 shows that, if many halos are found in the proximity of a filament in the more resolved simulation, then the difference of $\xi_{\rm fil}$ between the 512^3 and 128^3 run for the corresponding filament is considerable.

Nonetheless, the impact of resolution on $\xi_{\rm fil}$ is not dramatic, so we can conclude that our previous analysis is only marginally biased by our simulation's resolution. More importantly, although mass and spatial resolution may affect the absolute amplitude of the alignment in some cases, our analysis shows that the trend of $\xi_{\rm fil}$ with distance from the filament and mass of halos are fairly robust against changes in the resolution of the simulation.

7.3.3 The alignment between filaments and magnetic fields for different scenarios of magnetogenesis

With a second set of runs probing a much larger cosmic volume, Chronos, we tested to which extent the findings above apply to different realistic models for the origin of extragalactic magnetic fields. Due to the significantly larger volume and number of cells of these simulations, we perform in this case a slightly simplified analysis with respect to the one described in Section 7.3.1, i.e. we select only the most massive halos to build the network (see the Table in Appendix 7.6.1 in the for details) as they are the ones connected to the most prominent filaments in the simulated volume, for which we wish also to derive observational implications (Section 5.5). In any case, we present tests for the statistical consistency between Roger and Chronos sets, when analyzed in a similar way, in Appendix 7.6.2. In this Section, we focus in particular on the alignment of the magnetic field up to larger distances from filaments (Figure 7.13). We remind the reader that we are now considering volumes ~ 100 times larger than we did in the previous Section: thus, working on Chronos runs, we manage to perform the analysis concerning magnetic field and filament alignment on a wider range of filament lengths (up to ~ 8 Mpc).

Analogously to Figure 7.10, the values of $\xi_{\rm fil}$ are computed for each shell, whose typical density is indicated in grey, then averaged over all filament. The trends imply that, in runs with a strong primordial magnetic field, the alignment is enhanced and is not affected by its initial topology. On the other hand, in the simulations where no strong primordial field is present (DYN5 and CSFBH2), the alignment is less prominent, although present, especially within a few hundreds kpc. This confirms the scenario at which we previously hinted in Banfi et al. [2020]: in DYN5 and CSFBH2 the magnetic field undergoes
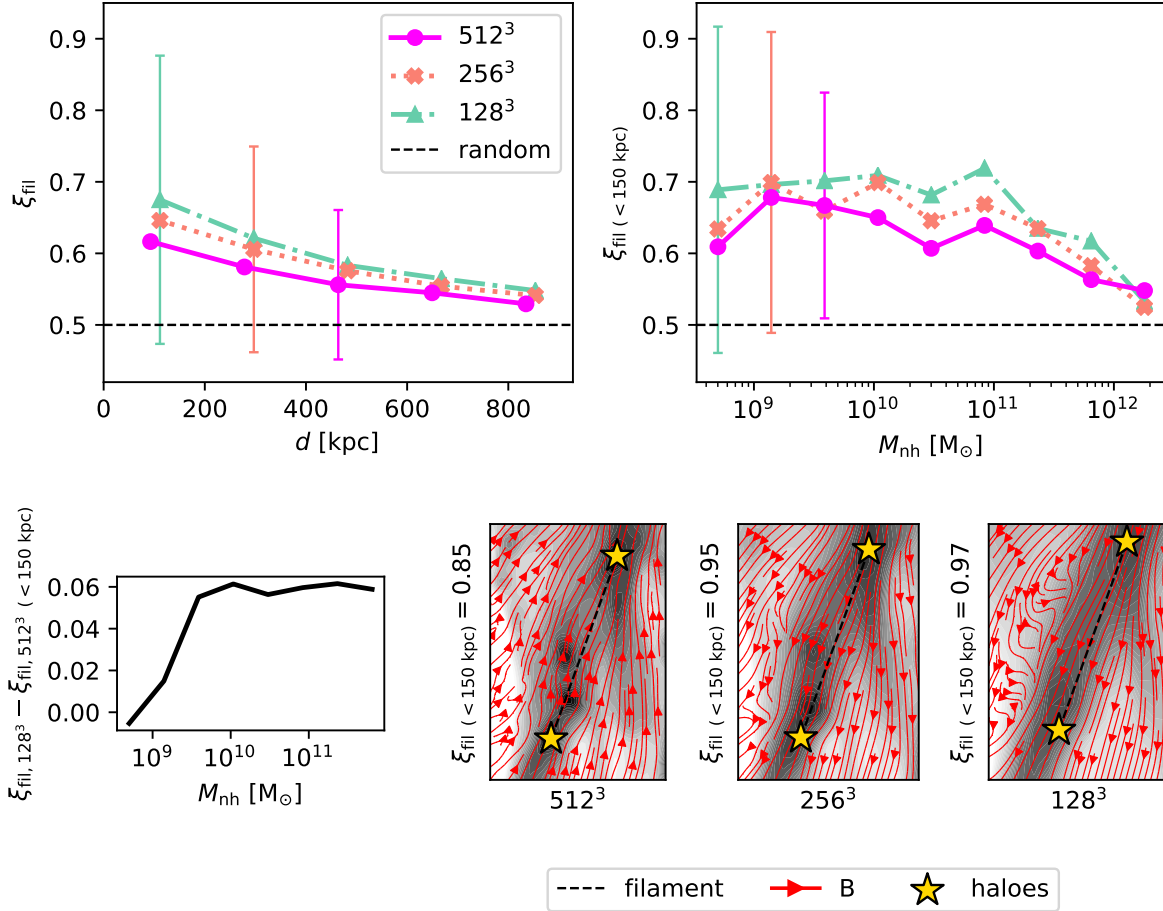
Figure 7.12: Top left panel: median of **B**-filament alignment as a function of distance from the filament for different resolutions of the NR run, with relative error bars corresponding to the standard deviation. Top right panel: median of **B**-filament alignment in cells closer than ~ 150 kpc as a function of the mass of nearby halos for different resolutions of the NR run, with relative error bars corresponding to the standard deviation. Bottom left panel: difference of the median of **B**-filament alignment in cells closer than ~ 150 kpc in the 128^3 and 512^3 NR runs as a function of the mass of nearby halos. Bottom right panel: projected density of a filament with integrated magnetic field streamlines for different resolutions of the NR run: at coarser resolutions smaller halos blend with the background and the magnetic field is better aligned to the filament
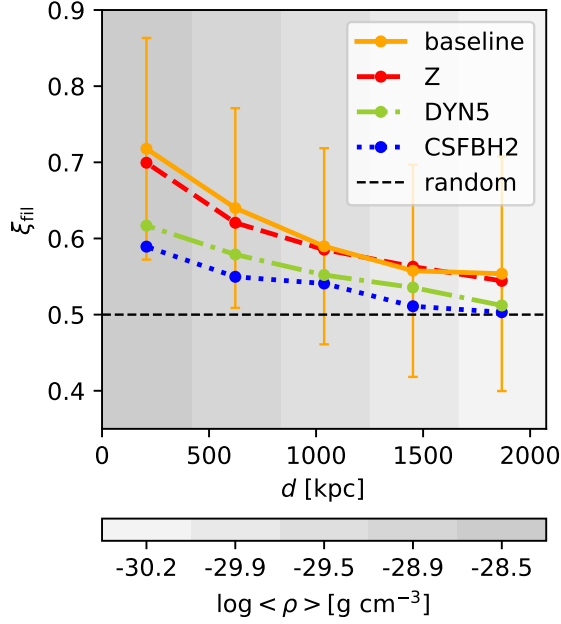
Figure 7.13: Median of **B**-filament alignment as a function of distance from the filament for the four Chronos runs, with relative error bars corresponding to the standard deviation. The greyscale background indicates the averaged gas density of each shell over all filaments.

processes of either dynamo or magnetic feedback, which implies that it experiences a build-up over time and has not had the chance to fully align to the structures yet. On the other hand, primordial fields in the baseline and Z runs are able to adjust their orientation, following the shear motions, for a longer span of time.

To make sure that the results obtained from Roger and Chronos datasets are compatible, we must compare the non-radiative runs (Roger NR and Chronos baseline). Although they have similar initial conditions, there are two aspects which may cause some discrepancy in the final results: 1) the spatial resolution in the Chronos set is ~ 2.5 times worse than the Roger set, which would shift the curve towards higher ξ_{fil} with respect to the more resolved runs: however, the implications are not drastic, so this effect has a marginal impact (see Section 7.3.2); 2) the volume simulated in Chronos is ~ 100 times larger, which means that there is a significantly larger population of longer filaments, which is more prone to having a better aligned magnetic field. This effect is likely to be linked to the fact that the environment around longer filaments is less perturbed by halos at the filament endpoints, which would easily prevent the magnetic field lines from following a straight line. In Figure 7.14 we show how filament length is strictly related to **B**-filament alignment: that is why Chronos has, on average, higher values of ξ_{fil}. This can be verified by comparing the ξ_{fil} trend as a function of distance for the same filament length range in both simulations, as in Figure 7.15.

To summarise, this analysis, extended to simulations of larger volumes which covered a spectrum of magnetic properites, established the role of magnetic field topology and magnetogenesis on the ability of **B** to align to filaments, due to shear motions surrounding these structures. We can infer that this alignment is partially attenuated by the ongoing modification of magnetic fields by means of either dynamo amplification or AGN and star formation feedback.
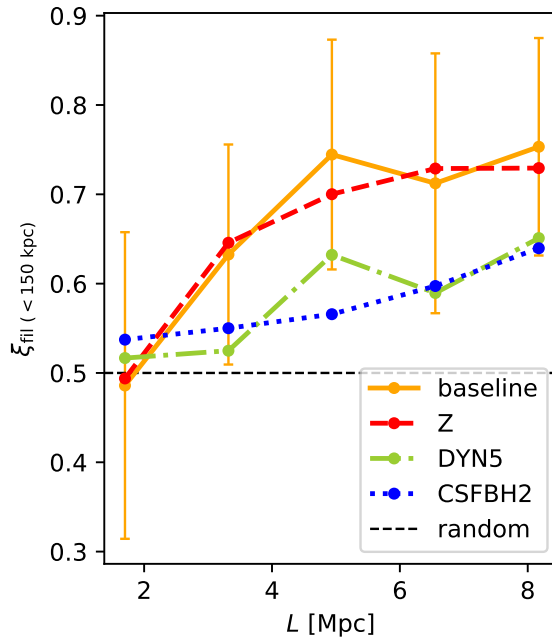
Figure 7.14: Median of **B**-filament alignment in the proximity of the filament (inside a 150 kpc shell) as a function of filament length for the four Chronos runs, with relative error bars corresponding to the standard deviation.
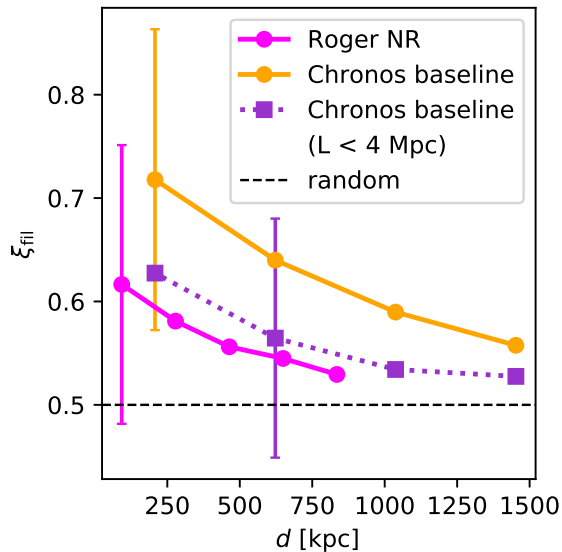
Figure 7.15: Median of **B**-filament alignment as a function of distance from the filament for Roger NR, Chronos baseline (for all filament lengths) and Chronos baseline's shortest filaments, with relative error bars corresponding to the standard deviation.

7.4 Discussion

7.4.1 Observational implications

The detection of magnetic field in filaments can in principle be accomplished in two ways: through the synchrotron emission due to electrons being accelerated by magnetic fields, linked to observable radio emission [e.g. Vernstrom et al., 2017, 2021], and through Faraday rotation, which rotates the linear polarization angle of the radio emission in the background, as a function of wavelength [e.g. Akahori et al., 2018]. This latter method requires the measurement of the so called rotation measure (RM), which is a function of the magnetic field and thermal electron density, both integrated along the line of sight [e.g. Carilli and Taylor, 2002b]:

$$RM \ [\text{rad/m}^2] = 812 \int \frac{B_{\text{los}}}{\mu G} \cdot \frac{n_e}{\text{cm}^3} \cdot \frac{dl}{\text{kpc}}. \tag{7.7}$$

Our work, having showed a certain tendency of magnetic field to align to filaments, suggests that it may be possible to estimate the intensity of magnetic field around filaments, starting from its line-of-sight component: in particular, if the magnetic field lines are indeed parallel to the filament, RM values measured for filaments in the sky plane should highly underestimate the magnetic field intensity in that volume. The existence of a systematic bias in the measurement of magnetic field from RM implies that this technique should yield a different estimate with respect to the one inferred from radio synchrotron detection, which instead depends on the total magnetic field. As of today, no filaments have been detected thanks to RM measurements, with the exception of some excess of RM signal, possibly linked to intergalactic medium [O'Sullivan et al., 2019].

We measure this effect by defining the *magnetic bias factor ε* as

$$\varepsilon = \frac{|\sum (B_{\text{los}} \cdot \rho)|}{\sum (B_{\text{tot}} \cdot \rho)}, \tag{7.8}$$

where the numerator contains the absolute value of the sum of the line-of-sight component of the magnetic field, weighted by each cell's density, and the denominator is the density-weighted total magnetic field. Figure 7.16 illustrates three examples in which a filament is observed with an inclination of 0°, 45° and 90° with respect to the line of sight, for the simplest scenario in which the magnetic field is perfectly aligned to the filament direction throughout the whole volume. Thus, if a uniform distribution of the magnetic field were always the case, ε would assume values equal to the cosine of the angle formed by the magnetic field vector and the line of sight: this distribution is flat for a random distribution of angles in space, i.e. values from 0 to 1 are all equiprobable, meaning that ε computed for a sufficiently large sample of object would average to $\varepsilon_{\text{rand}} = 0.5$. However, it shall be remarked that in reality no line of sight can perfectly probe 100 % of the magnetic field, because in practice the three-dimensional distribution of magnetic fields will always fluctuate within some scale (which can change from scenario to scenario and across the variety of cosmic objects).

We computed this value for every filament in the Chronos simulations, by considering a small volume, defined as in Section 7.3.1, around each of them, as if they were isolated. In order to extract the contribution of filaments alone, we computed the bias factor excluding the highest-density cells ($\rho > 10^{-29}$ g cm^{-3}, see Figure 7.2), typically corresponding to clusters. First, we measured the bias factor as a function of the angle formed by the filament and the line of sight, for the three spatial directions (Figure 7.17). To better understand this plot, we note that the horizontal axis indicates the orientation of the filament with respect to the line of sight (parallel on the left-hand side, i.e. edge on, and perpendicular on the right-hand side,
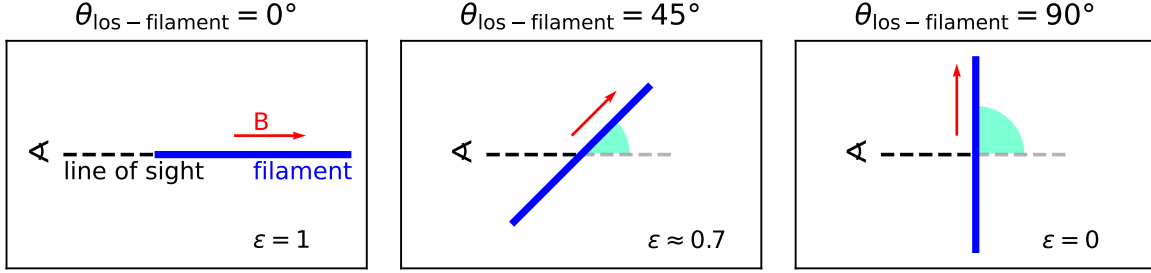
Figure 7.16: Schematic representation of three possible orientations of an observed filament with respect to the line of sight: $\theta_{\mathrm{los-filament}} = 0°$, $45°$ and $90°$. Then, assuming a uniform magnetic field perfectly aligned to the filament, the corresponding values of $\varepsilon = \left|\sum \left(B_{\mathrm{los}} \cdot \rho\right)\right| / \sum \left(B_{\mathrm{tot}} \cdot \rho\right)$ are 1, ≈ 0.7 and 0.

i.e. in the sky plane). The vertical axis contains the bias factor: lower values of ε imply that the magnetic field is highly underestimated, while higher values imply that the magnetic field is less underestimated. The following particular cases correspond to specific limiting values of ε:

- if the distribution of the magnetic field in the selected volume is completely random, then $\varepsilon = 0$, since the algebraic sum of the magnetic field cancels out;

- if the distribution of the magnetic field is uniform in all the selected volumes, then the average over multiple objects returns $\varepsilon = \varepsilon_{\mathrm{rand}} = 0.5$.

In Figure 7.17, simulations with a primordial magnetic field (baseline and Z), or with a dynamo-amplified magnetic field (DYN5) show a clear growing trend, compatible to a configuration in which magnetic fields tend to align to filaments. The values of ε in CSFBH2 run, on the other hand, settle around $\sim 0.3 - 0.4$, meaning that the **B**-filament alignment is much more reduced in amplitude, while the randomizing effect of AGN feedback on magnetic field, around galaxies in filaments, generally decreases the average bias factor values along most lines of sight.

We then focus on a subset of filaments roughly aligned to the plane of the sky, which are objects most suitable for observations [e.g. Tanimura et al., 2019b, Govoni et al., 2019] or stacking analysis [e.g. Vernstrom et al., 2021]. The criterion we chose for the position of the filament is that $\left|\cos\theta_{\mathrm{los-filament}}\right| < 0.3$. Figure 7.18 shows the trend of the bias factor along the filament length, as a function of the distance from its midpoint. In all four simulations, ε is smaller closest to the filament's midpoint and grows as the distance increases, compatibly to the fact that, especially for the baseline and Z runs, the **B**-filament alignment is best where the filament is least affected by the clusters at the endpoints.

Then, we estimated the dependence of this trend as a function of the filament length: Figure 7.19 replicates Figure 7.17 for the ~ 50 longest and ~ 50 shortest filaments. The difference between the two cases is not large, but we notice a clearer increasing trend for the selection of longer filaments, even for the CSFBH2 run. This is reflected by a better **B**-filament alignment for longer filaments, as previously found (see Figure 7.14).

In Figure 7.20 we show two volumes containing filaments which are almost aligned to the sky plane, as an example to illustrate the implications of this effect on the rotation measurement of such objects. The top panels show the projected maps of density, *RM* and ε for the four Chronos simulations. In
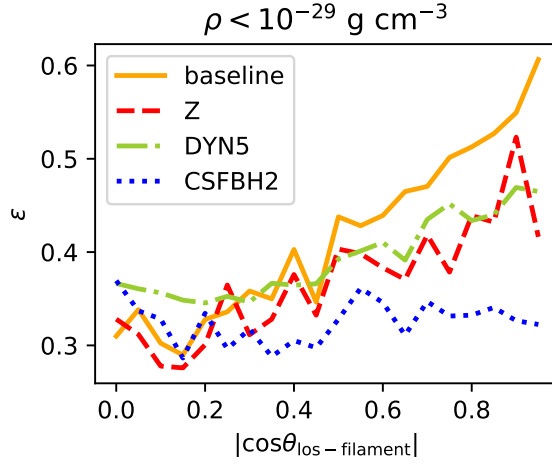
Figure 7.17: Median of the bias factor over all filaments as a function of the alignment between the filament and the line of sight for the four Chronos runs. The bias factor corresponding to a filament is found by performing a mass-weighted mean over the two-dimensional sky projection. Each filament is included three times, since the line of sight can be directed along any of the three coordinates. We excluded from the statistics cells in which $\rho > 10^{-29}$ g cm^{-3}, which we assume to belong to clusters.
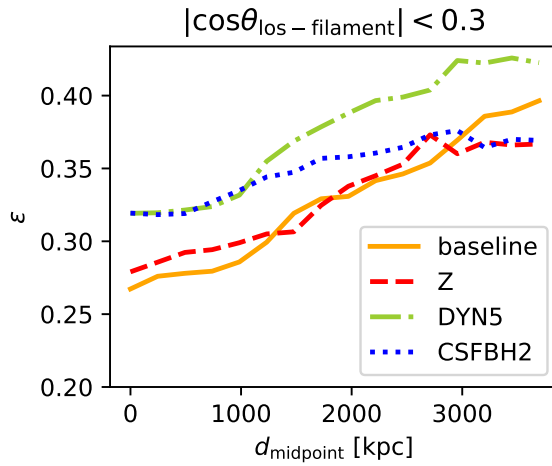
Figure 7.18: Median of the bias factor in the proximity of the filament (distance from the filament axis $\lesssim 400$ kpc), as a function of the distance from the filament's midpoint for the four Chronos runs. Only filaments on the sky plane, i.e. $|\cos\theta_{\text{los}-\text{filament}}| < 0.3$ for any of the three lines of sights, are considered. We excluded from the statistics cells in which $\rho > 10^{-29}$ g cm^{-3}, which we assume to belong to clusters.
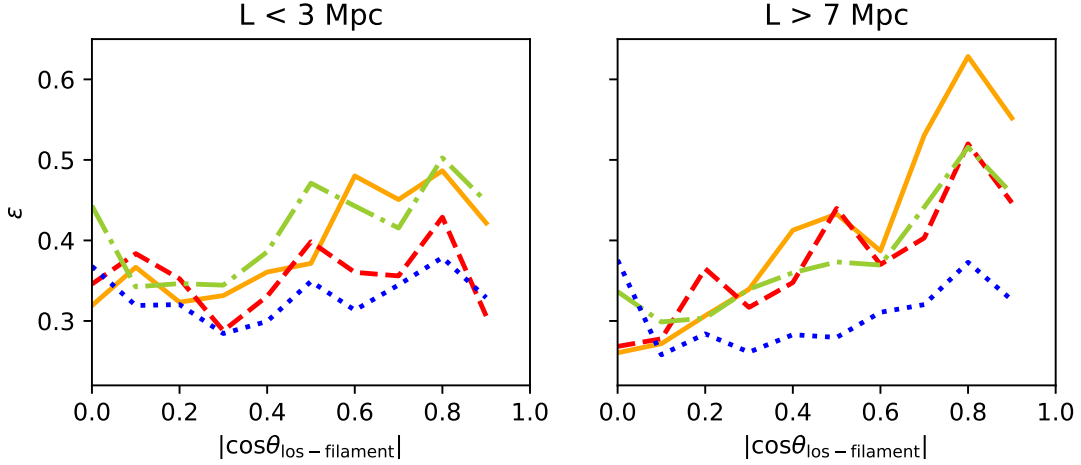
Figure 7.19: Same as Figure 7.17, with the additional distinction between filaments shorter than 3 Mpc and longer than 7 Mpc.

presence of a large degree of alignment between magnetic fields and filaments, we therefore expect the magnetic field to mostly lie in the sky plane as well, with a very small line-of-sight component, thereby reducing the observable $|RM|$ towards the observer. Current instruments (e.g. VLA and LOFAR) are able to detect values of $|RM| \gtrsim 5$ rad/m^2 [e.g. Bonafede et al., 2013, O'Sullivan et al., 2019, Locatelli et al., 2018]. The Figure suggests that, on one hand, clusters easily meet this requirement, while filaments would only be marginally detected, even for the runs in which the magnetic field is stronger (baseline and Z), due to the large degree of **B**-filament alignment, which implies low values of ε, as can be seen in the third column. Therefore, the small line-of-sight component yields only little $|RM|$, typically below the detection threshold of present instruments, especially for runs in which the magnetization is weak already (DYN5 and CSFBH2). On the bottom panels we give, for each of the two selected areas, the median value of ε as a function of the rotation measure (in absolute value). The highest values of $|RM|$, mostly associated to clusters, correspond to higher values of ε, although never approaching $\varepsilon \approx 1$; at the lower side of $|RM|$, corresponding to the areas populated by filaments, lower values of ε are found, as expected from our previous considerations. The simulations are in overall agreement, except for CSFBH2, where AGN and star formation feedback introduces additional effects: although the impact of a quasi-parallel **B**-filament configuration is noticeable for a larger sample of objects (e.g. see Figure 7.18), the bursty and random occurrence of star forming/AGN events may strongly affect the local magnetic field topology and cause the statistic over a small volume to deviate from the expected trend.

The bias in the line-of-sight component typically amounts to a factor ~ 3 lower than the total magnetic field (corresponding to ε values of ~ 0.3).

7.4.2 Numerical limitations

The main numerical limitations that we encountered in this work involve the limited resolution of the simulations: we already quantified the relevance of this effect on our analysis in Section 7.3.2 and concluded that most results should be reliable and independent of resolution. On the other hand, even our post-processing algorithm for network construction is subject to limitations. For example, we restricted our analysis to filaments less than ~ 4 Mpc (for the 19^3 Mpc^3 volumes) or ~ 8 Mpc (for the 84^3 Mpc^3 volumes) long. This may seem to clash with the estimates obtained with more sophisticated network

Figure 7.20: Top panels: projected maps of the two selected volumes containing filaments (left-hand and right-hand side) of gas density, unsigned rotation measure, and ε, for all Chronos simulations. Bottom panels: median values of ε for bins of $|RM|$ over all cells of the two-dimensional projection for the range in which rotation measure can be detected, for the two areas represented above.

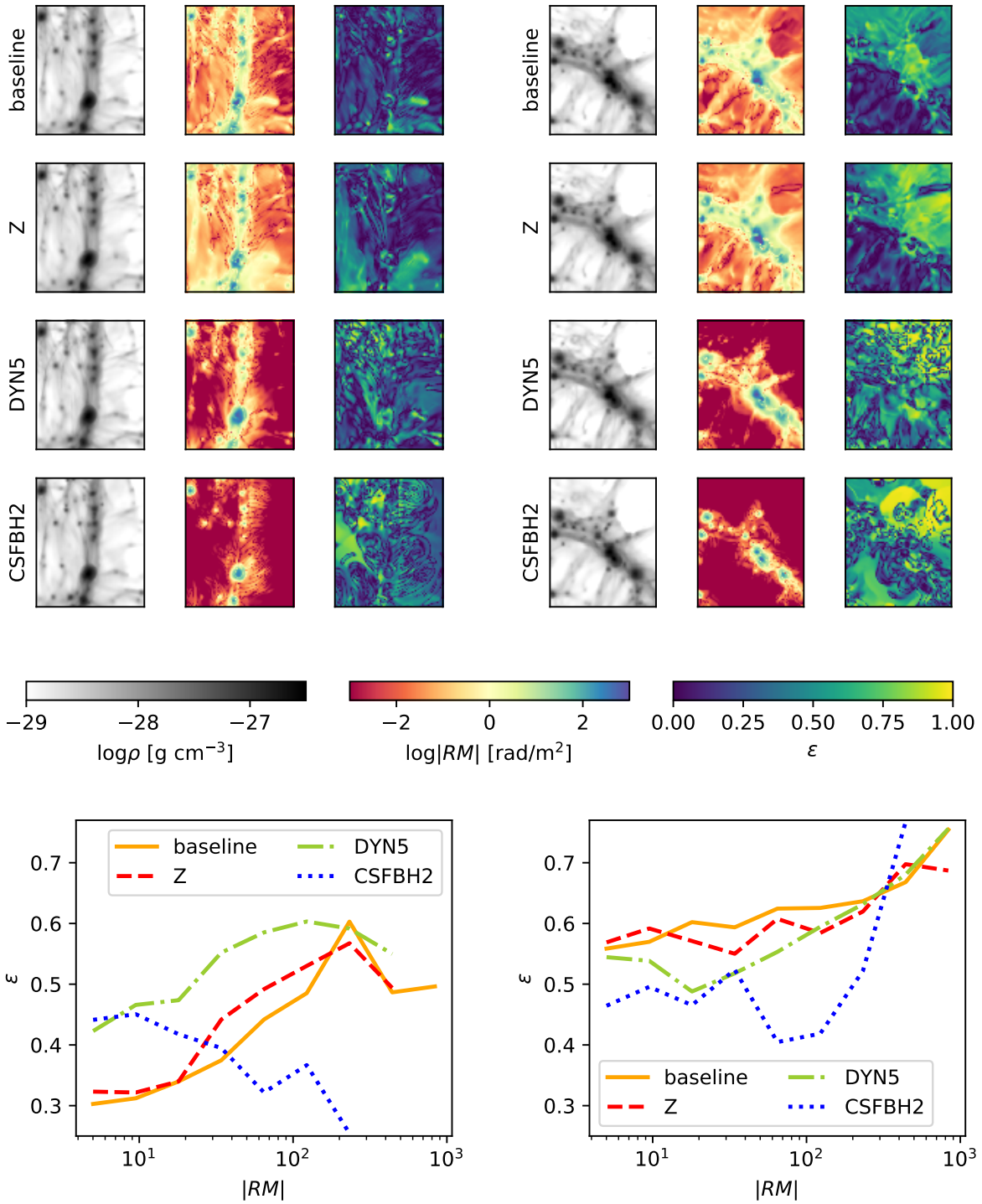finding methods [e.g. Cautun et al., 2013, Gheller et al., 2015], which, applied to cosmological simulations, suggest that filamentary structures up to ~ 100 Mpc can form in a big enough volume. However, Gheller et al. [2015], in particular, showed that most filaments have lengths $\lesssim 10$ % of the box's side length, which is compatible with our cut. On the other hand, if longer filaments were present, these would most likely be characterised by a complex morphology that would not be identified by our algorithm, and which would make it difficult to study alignments with the surrounding halos. In conclusion – bearing in mind that our goal here is manifestly not that of building a complete sample of filaments on all scales and of all possible geometries – our method allows us to speed-up the analysis process and prevent the contamination of the sample by spurious effects, without overly limiting the statistics. Conversely, this might affect the reliability of certain inferred quantities: for example, multiplicity (Section 7.2.3) may be underestimated, since some fraction of filaments are left out.

7.5   Conclusions

With this work we present a simple algorithm which builds the network of filaments in the cosmic web in cosmological simulations, starting from the location of DM halos in the cosmic volume, with the aim of producing a catalog of filaments and studying their physical properties and influence on the surrounding gas flows and magnetic fields. In particular, we looked for a relation between halo spin, filaments and magnetic field, as a function of different simulation properties, such as magnetic field initialization, presence of different astrophysical processes, and resolution. The following are our main findings:

1. morphological and dynamical features of halos in the mass range $\sim 10^8 - 10^{14}$ $M_\odot$ (e.g. mass, spin) and filaments (e.g. length, multiplicity) are only moderately dependent on non-gravitational physics (e.g. gas cooling);

2. in the range of lengths we considered, i.e. $\lesssim 4$ Mpc (for the 19^3 Mpc^3 volumes) and $\lesssim 8$ Mpc (for the 84^3 Mpc^3 volumes), most filaments can reasonably be described by a straight line connecting halos;

3. the distribution of angles formed by magnetic field and the filament orientation in the proximity of filaments is concentrated towards quasi-parallel angles, much more than for a random three-dimensional distribution;

4. filaments affect the shape of magnetic field lines, through the velocity shear they impose to large-scale gas flows: this effect is strongest within a few hundreds kpc, but is still measurable down to ~ 2 Mpc from the filaments' spine;

5. the alignment between magnetic fields and filaments is particularly significant for longer filaments, which typically host fewer halos per unit of volume;

6. physical models with a strong primordial magnetic field show an increased alignment between magnetic field and filaments at $z = 0$, regardless of its initial topology;

7. weak primordial magnetic fields, later amplified by dynamo or by astrophysical processes, show less pronounced alignment, albeit still larger than in a purely random distribution;

8. the alignment between magnetic fields and filaments is generally found to reduce the amplitude of the observable rotation measure (by a factor ~ 3) for filaments observed close to the plane of the

Run	Number of halos	Number of filaments	Maximum halo mass	Maximum filament length
NR	1224	1978	$6 \cdot 10^{13}$ M$_\odot$	4 Mpc
cool	1076	2044	$7 \cdot 10^{13}$ M$_\odot$	4 Mpc
baseline	662	226	$5 \cdot 10^{14}$ M$_\odot$	4 Mpc
Z	662	225	$5 \cdot 10^{14}$ M$_\odot$	8 Mpc
DYN5	662	223	$4 \cdot 10^{14}$ M$_\odot$	8 Mpc
CSFBH2	662	207	$4 \cdot 10^{14}$ M$_\odot$	8 Mpc

Table 7.2: Network properties in the Roger and Chronos simulations.

sky, and it introduces a bias in the normalization of the magnetic field that can be derived from this technique.

To conclude, we remark that the effects above are so general (and independent on physical/numerical variations in the model) that they should also be relevant for other observational techniques probing the cosmic web, also in statistical ways [Vernstrom et al., 2021]. For example, attempts of measuring the magnetization of the intergalactic medium using fast radio bursts, which would require the combination of rotation measure and dispersion measure for the derivation of the magnetic field [see Akahori et al., 2016, Vazza et al., 2018b, Hackstein et al., 2020], will also be subject to a similar bias.

7.6 Appendix

7.6.1 Network details

In Table 7.2 we indicate the details of the halo-filament network found by our algorithm in the analyzed simulations. Although the reconstruction method is essentially the same for both Roger and Chronos runs, we adjusted it before applying it to the much larger volumes involved in Chronos. This was possible due to the fact that we were no longer interested in analyzing the properties of as many halos as possible, as we did for the Roger set in Section 7.3.1. The simplification consists of only selecting very massive halos in Chronos runs with an overdensity algorithm and thus retrieving fewer, longer filaments. This choice allowed us to speed up the whole process on such big volumes, as well as to focus on the differences introduced by different magnetogenesis scenarios (see Section 7.2.1). A more accurate network analysis of Chronos runs starting from the whole catalogue of halos was performed on a small subvolume, as explained in Appendix 7.6.2.

7.6.2 Comparison between Roger and Chronos simulations

Unlike in the main paper, for testing purposes here we apply the same network reconstruction algorithm to the cosmic web simulated in Roger and Chronos simulations (even if, in the latter case, we restrict to a $\approx 20^3$ Mpc^3 subvolume to save computing resources). In the following, we compare our most resolved 512^3 Roger run (as in Section 7.3.1) with the baseline (non-radiative) and CSFBH2 runs of Chronos (Section 7.2.1). In Figure 7.21 we reproduce some of the panels in Figures 7.4, 7.5 and 7.6: the observed trends show that, albeit with some variance related to the small volumes considered here, all main properties of halos and filaments discussed in Section 7.3.1 are also found in the considerably less resolved runs from the Chronos suite, if an identical network reconstruction is used. In any case, it shall be noticed that even if a similar mass cut in the halos used to reconstruct the network is adopted in this case ($M \gtrsim 10^9 M_\odot$), the intrinsic coarser force resolution of Chronos runs leads to a $\sim 50\%$

reduced amount of filaments (especially shorter ones, connecting on average less massive halos) per unit of volume. However, the dynamical correlations (or absence thereof) of gas velocity fields and the spin and multiplicity of nodes and filaments of the network, discussed in the main paper, are also confirmed by the consistent comparison of Roger and Chronos simulated volumes. In the latter case, we notice again that no relevant differences can be appreciated if radiative cooling, star formation and AGN feedback are included, once more enforcing that the main parameters of the network are not affected by these non-gravitational mechanisms.
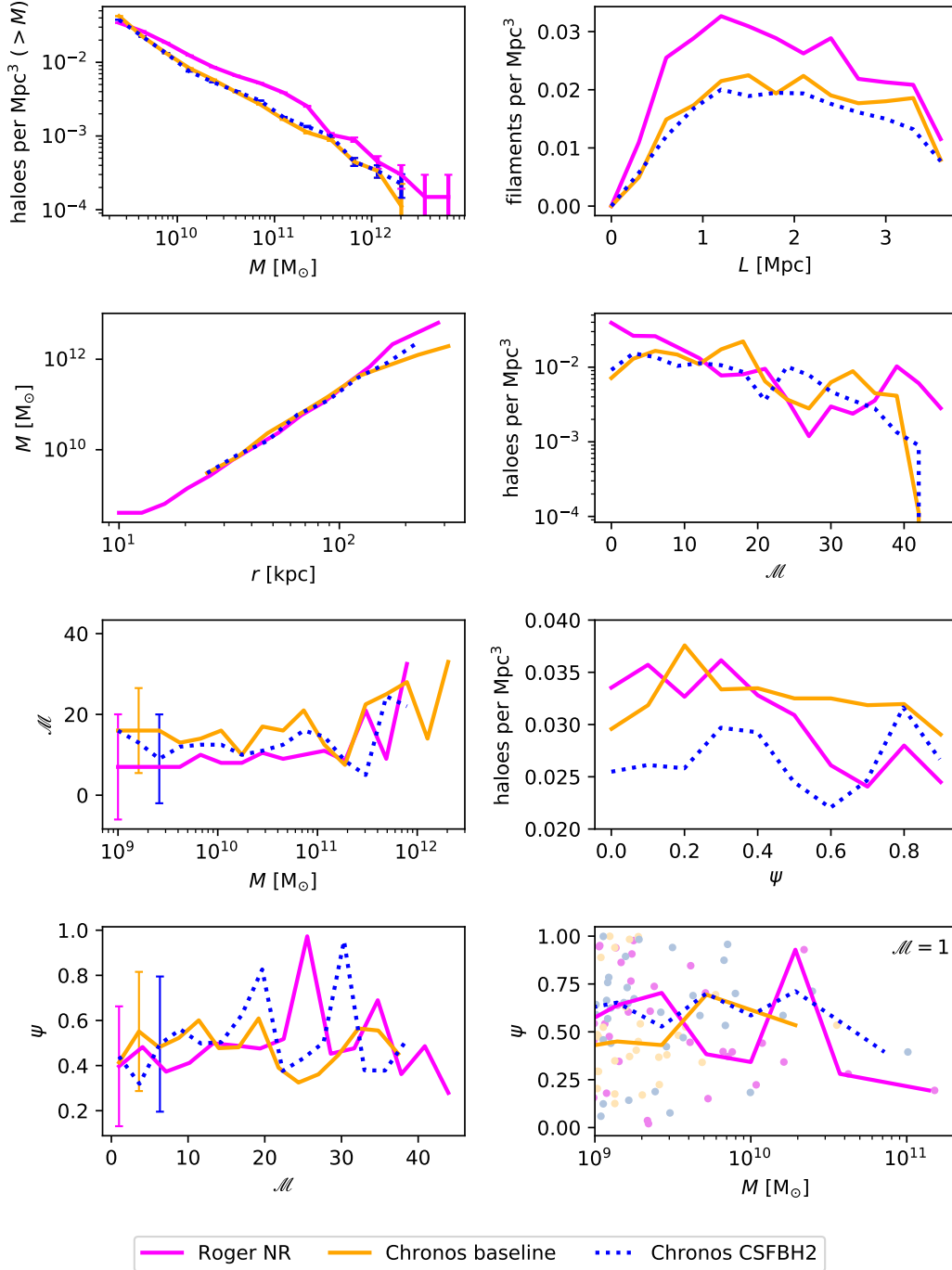
Figure 7.21: Properties of halos and filaments in the Roger non-radiative simulation and in two of the Chronos runs' subvolumes, the baseline and CSFBH2, which includes the feedback from astrophysical phenomena. From top left to bottom right: number of halos per Mpc^3 above a certain mass; number of filaments per Mpc^3 as a function of filament length; median of halo mass as a function of halo radius; number of halos per Mpc^3 with a certain multiplicity; median of halo multiplicity as a function of halo mass; number of halos per Mpc^3 forming a certain spin-filament angle; median of spin-filament alignment as a function of halo multiplicity; median of spin-filament alignment as a function of halo mass for halos with unitary multiplicity.

Part IV

Constraining cosmic web magnetic fields

8. Co-authored works

8.1 Simulations and observational tests of primordial magnetic fields from cosmic microwave background constraints (Vazza et al., 2021)

Abstract We present the first cosmological simulations of primordial magnetic fields derived from the constraints by the cosmic microwave background observations, based on the fields' gravitational effect on cosmological perturbations. We evolved different primordial magnetic field models with the ENZO code and compared their observable signatures (and relative differences) in galaxy clusters, filaments and voids. The differences in synchrotron radio powers and Faraday Rotation measure from galaxy clusters are generally too small to be detected, whereas differences present in filaments will be testable with the higher sensitivity of the Square Kilometre Array. However, several statistical full-sky analyses, such as the cross-correlation between galaxies and diffuse synchrotron power, the Faraday Rotation structure functions from background radio galaxies, or the analysis of arrival direction of Ultra-High-Energy Cosmic Rays, can already be used to constrain these primordial field models.

I contributed to this work by analyzing cosmological simulations in which primordial magnetic fields' power spectra are initialized accordingly to constraints from the CMB. Each run differs in the choice of spectral index α for the primordial magnetic field power spectrum (see Table 8.1). Figure 8.1 shows the topology of the magnetic fields initialized with different power spectra. I performed the shock analysis of the entire sample, following a similar procedure to that described in Section 5.2.4, with particular focus on the topological properties of the magnetic field in the proximity of shocks, namely on obliquity. This allowed us to measure that all of the simulated volumes host a higher fraction of quasi-perpendicular shocks, with respect to the random distribution, consistently to what previously shown in Banfi et al. [2020] (Chapter 5). However, we observe that the highest excess is found in the uniform B0 model: once again, this is in agreement with the explanation we provided in Banfi et al. [2021] (Chapter 7) regarding the alignment between magnetic fields and filaments. The ability of the gas flow to bend magnetic fields can be explained in terms of magnetic tension: if the field curvature increases, the magnetic field is less easily bent, and we thus expect the B5 model to provide the least suitable environment for the formation of perpendicular shocks (see Figure 8.2).

For the complete analysis, see Vazza et al. [2021].

Run ID	Description
B0	homogeneous
B1	$\alpha = -2.9$
B2	$\alpha = -1.0$
B3	$\alpha = 0.0$
B4	$\alpha = 1.0$
B5	$\alpha = 2.0$

Table 8.1: List of cosmological ENZO simulations produced for this work.
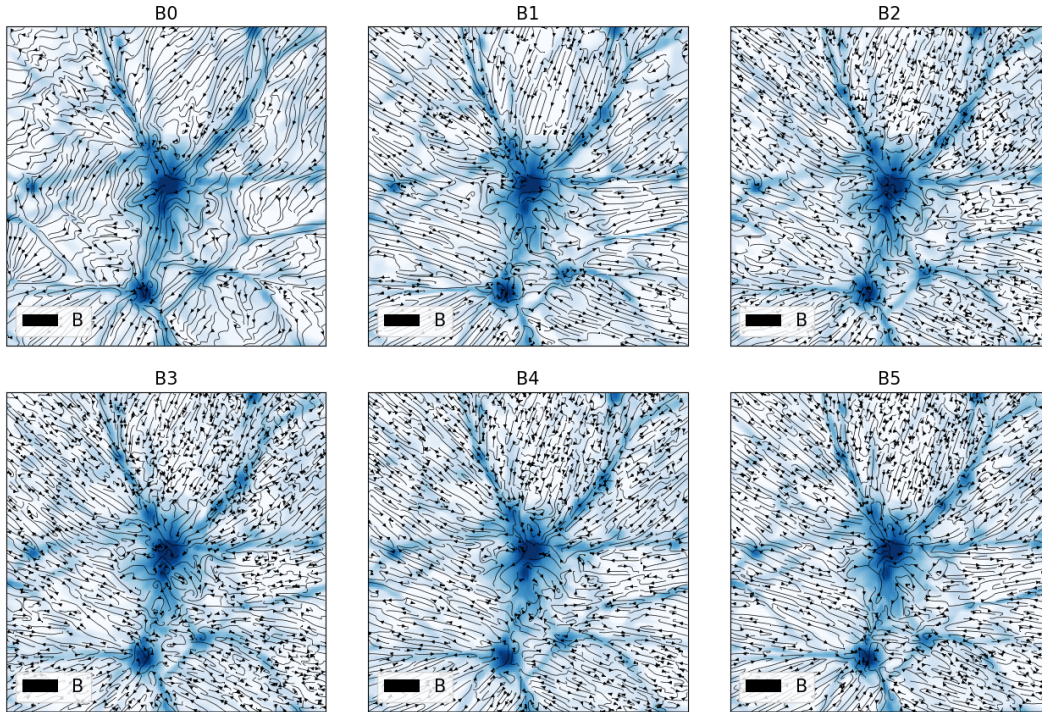
Figure 8.1: Volume slices showing the gas density (blue) and the magnetic field lines (black) around the most massive cluster in our simulated volume.
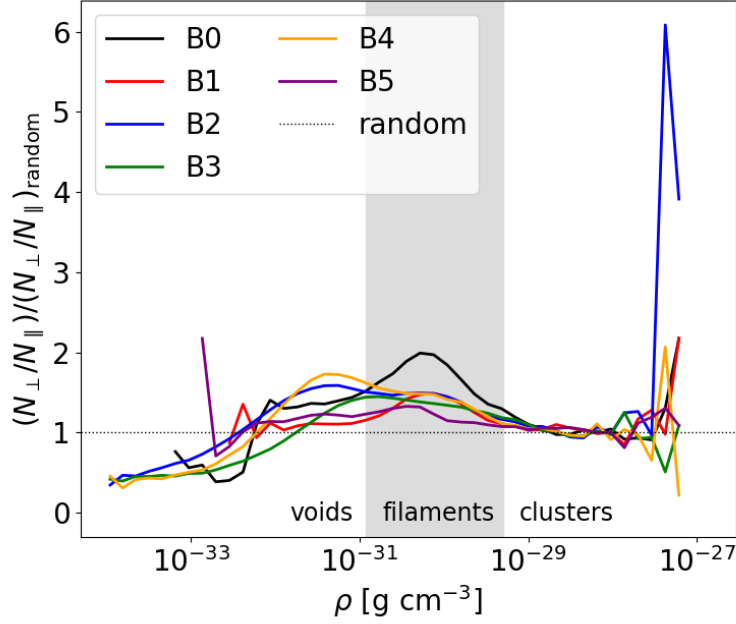
Figure 8.2: Distribution of the ratio quasi-perpendicular to quasi-parallel shocks, normalized to the expected ratio in a random three-dimensional distribution, as a function of gas density.

8.2 New constraints on the magnetic field in filaments of the cosmic web (Locatelli et al., 2020)

Abstract Strong accretion shocks are expected to illuminate the warm-hot inter-galactic medium encompassed by the filaments of the cosmic web, through synchrotron radio emission. Given their high sensitivity, low-frequency large radio facilities may already be able to detect signatures of this extended radio emission from the region in between two close and massive galaxy clusters. In this work we exploit the non-detection of such diffuse emission by deep observations of two pairs of relatively close ($\simeq 10$ Mpc) and massive ($M_{500} \geq 10^{14} M_{\odot}$) galaxy clusters using the LOw-Frequency ARray (LOFAR). By combining the results from the two putative inter-cluster filaments, we derive new independent constraints on the median strength of inter-galactic magnetic fields: $B_{\mathrm{Mpc}} < 2.5 \times 10^2$ nG (95% CL). Based on cosmological simulations and assuming a primordial origin of the B-fields, these estimates can be used to limit the amplitude of primordial seed magnetic fields: $B_0 \leq 10$ nG. We advise the observation of similar cluster pairs as a powerful tool to set tight constraints on the amplitude of extragalactic magnetic fields.

In this work, we combined LOFAR observations to numerical simulations, with the aim of putting constraints of the inter-cluster filaments magnetic field. By using the algorithm outlined in Section 7.2.2, I reconstructed the cosmic web inside a simulated cosmological volume and provided the coordinates for a set of cluster pairs (see Figure 8.3), similar to the ones observed for this work. My network-tracing algorithm allowed to determine the probability of having a filament connecting two observed clusters and therefore to assess the level of diffuse radio emission from filaments.

117
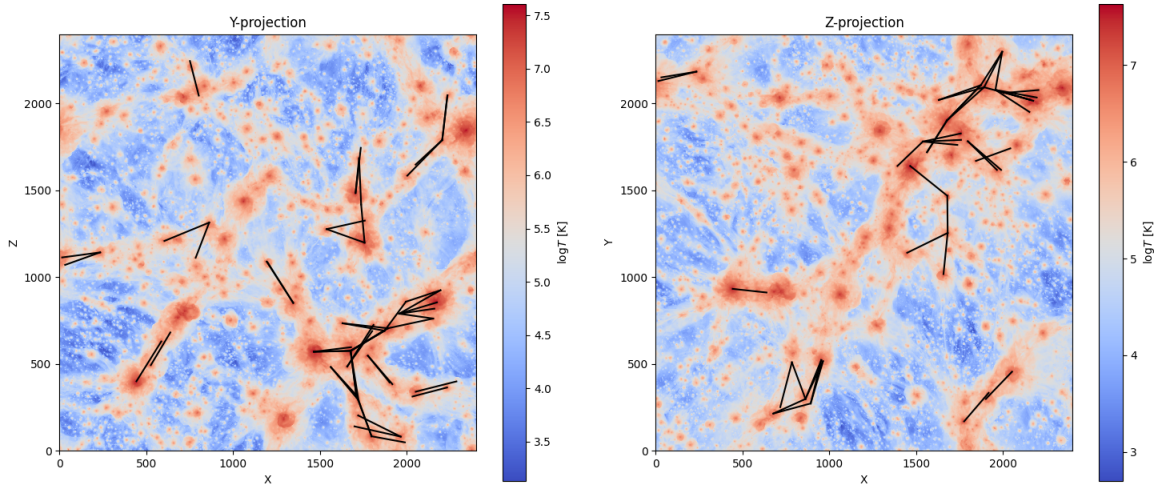
Figure 8.3: Cluster pairs identified in the projected temperature maps which fulfil the requirements of the network-tracing algorithm for the identification of filaments.

For the complete analysis, see Locatelli et al. [2021].

8.3 Magnetogenesis and the cosmic web: a joint challenge for radio observations and numerical simulations (Vazza et al., submitted to MDPI)

Abstract The detection of the radio signal from filaments in the cosmic web is crucial to distinguish between possible magnetogenesis scenarios. We review the status of the different attempts to detect the cosmic web at radio wavelengths, and put them into the context of the advanced numerical simulations of cosmic magnetism carried out in the last few years by our MAGCOW project. While the challenge of imaging the cosmic web in the radio domain has already begun, thanks to pivotal results with MWA and LOFAR, the complexity behind such observations makes a definitive answer still uncertain, albeit many alternative models can be discarded already. A combination of total intensity and polarimetric data at low frequency (that the SKA, as well as LOFAR2.0, will hopefully produce in large amount), appears the key to remove the existing uncertainties related to the contribution of many possible sources of signal along deep cosmic lines of sight. This will make it possible to isolate the contribution from filaments, and expose its deep physical connection with the origin of extragalactic magnetism.

In this review, the main results obtained in the framework of the MAGCOW project are described. In particular, the work that I carried out for Banfi et al. [2020] and Banfi et al. [2021] is used to perform a network reconstruction and produce the statistics of average RM and synchrotron emission from the cosmic web, like the ones in Figure 8.4.
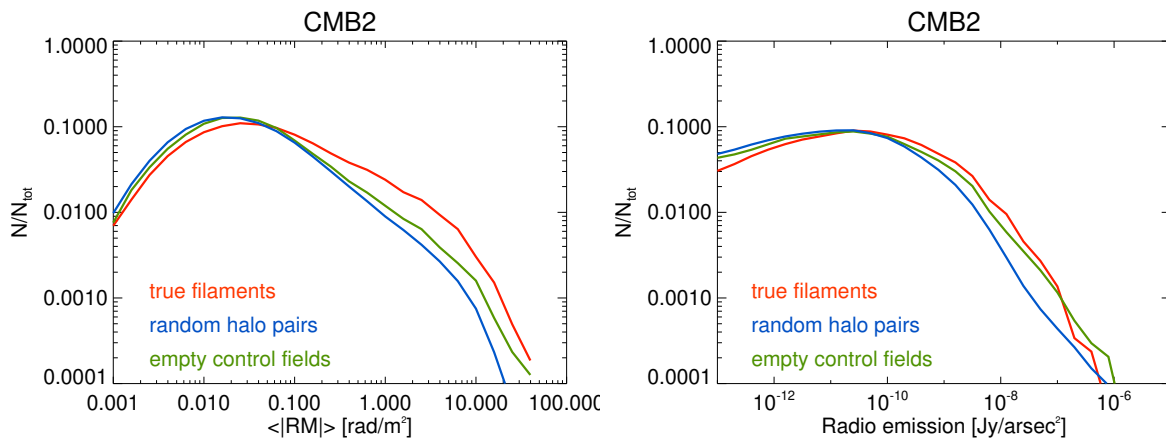
Figure 8.4: Distribution of the Faraday rotation and radio emission for a selection of filaments extracted from one of the simulations.

Part V

Thesis conclusions

9. Summary and conclusions

The formation of collisionless shocks is an ubiquitous process in space, leading to a plethora of non-thermal features and observational signatures. Shocks are found in several astrophysical environments, such as the Earth's magnetosphere, supernova remnants and the intracluster medium: since they form in very different physical conditions, we can expect their acceleration efficiency to be a function of multiple factors too [e.g. Bykov et al., 2019].

In the course of this PhD project, I have focused on cosmic shocks and, in particular, on their relation with the surrounding magnetic field. These shocks are generated either by the accretion of cold gas onto the cosmic web (e.g. accretion shocks around filaments), or during the encounter of hotter matter (e.g. merger shocks in galaxy clusters) [e.g. Ryu et al., 2003]. The latter are believed to be responsible for the diffuse emission observable in radio relics, which can be traced back to the synchrotron radiation produced by cosmic-ray electrons. The mechanism governing the production of cosmic rays is likely to be diffusive shock acceleration, whose efficiency depends on the shock characteristics, such as the Mach number and the orientation of the magnetic field. In particular, the ability of a shock to accelerate either electrons or ions is affected by obliquity, i.e. the angle formed by the shock propagation direction and the underlying magnetic field [e.g. Caprioli and Spitkovsky, 2014a]. Assessing the specific role of magnetic fields, from 'macro' to 'micro' astrophysical scales, has been the main focus of this work, also motivated by the fact that no evidence of cosmic-ray ions has been reported for the case of galaxy clusters and the (weak) shocks they process. Indeed the non-detection of γ-rays by the *Fermi*-LAT satellite [e.g. Ackermann et al., 2010] seems to imply that nearly no hadronic collision between energetic protons and thermal protons of the intracluster medium occur, which sets an upper limit on the total amount of cosmic-ray ions which can be accelerated by structure formation shocks.

My thesis explored these issues by producing and analysing new numerical simulations, both on cosmological scales and on the scales where collisionless shocks form, and investigated the correlation between the magnetic properties of cosmic shocks and their particle acceleration efficiency.

In Chapter 5 [Banfi et al., 2020], I have presented cosmological magnetohydrodynamics simulations of the large-scale structure and studied the typical obliquity of cosmic shocks as a function of their environment, their magnetic field topologies and in the case of different magnetogenesis scenarios. This allowed me to estimate the observable cosmic-ray flux for both ions and electrons, with the final goal of understanding the discrepancy between the observational evidence of the two species. I found that in **shocks surrounding simulated large-scale structures, there always is an excess of quasi-perpendicular shocks over quasi-parallel shocks**, which is maximized around filaments. There, shocks propagate perpendicularly to the filament length, and the (upstream) magnetic field tends to align with filaments. Considering the prescription from Kang and Ryu [2013], which indicates that electrons are accelerated by quasi-perpendicular shocks, while ions are accelerated by quasi-parallel shocks, I conclude

that **the decreased fraction of ion-accelerating shocks may well explain the reduced γ-ray emission below the available *Fermi* limits**, while instead leaving the acceleration of cosmic-ray electrons almost unchanged and compatible with observed level of diffuse radio emission from radio relics.

Although promising, these results are limited by the implicit assumptions that the topological properties of magnetic fields resolved by our cosmological simulations remain constant down to the scales where diffusive shock acceleration actually takes place. To expand on this interesting topic and better connect to different scales, in Chapter 6, I presented new particle-in-cell simulations produced, with the goal of studying the acceleration process on 'microscopic' astrophysical scales. Thanks to the information gathered from the previous work, I could start from a prescription for the realistic initial condition of accretion shocks, which was found to be the statistically more frequent in our cosmological simulations: in particular, I simulated typical filament shocks, characterized by a high Mach number and a magnetic field oriented quasi-perpendicularly to the shock normal. I concluded that **shocks in filaments are indeed able to produce cosmic-ray electrons**, by first pre-accelerating them through shock drift acceleration, and then eventually injecting them in the diffusive shock acceleration regime, to reach relativistic energies. I found a significant dependence of the efficiency of these processes on the initial obliquity: in slightly less oblique shocks, a larger fraction of electrons is accelerated, due to the magnetic field orientation allowing them to more easily interact with the shock multiple times. The measured injection efficiency of relativistic electrons in the shock downstream gives values which are a factor $\sim 5-10$ higher than the available predictions from simpler 1D models of diffusive shock acceleration, with important consequences on the future modelling of the radio signal from shocks surrounding filaments.

I devoted Chapter 7 [Banfi et al., 2021] to better explore the physical connection between filaments and magnetic fields around and within them. I have measured that most shocks in the proximity of filaments have a quasi-perpendicular configuration, which stems from the alignment of the magnetic field to the filament spine. In order to examine the dynamics of this phenomenon, I performed a quantitative analysis of the relative orientation of the magnetic field with respect to the components of the cosmic web. For this purpose, I developed a simple yet efficient algorithm which builds the network of filaments and halos in the cosmic web in cosmological simulations. In particular, I computed the angle formed by filaments and magnetic fields as a function of the distance from the filament spine and concluded that the arrangement is indeed parallel around most filaments, and becomes gradually random as the distance increases. It is possible to attribute this effect on the contribution of the velocity shear that filaments impose to large-scale gas flows [Bond et al., 1996]. The main consequences of this finding are twofold: first, as confirmed by the previous work, perpendicular shocks are more easily formed in the cosmic web, since they typically propagate perpendicularly to the filament spine. Secondly, **the alignment between magnetic fields and filaments is bound to reduce the amplitude of the observable rotation measure for filaments approximately lying in the sky plane**.

In summary, my work has shown how, through the combination of different numerical methods of increasing complexity, it is now possible to achieve a global understanding of magnetic fields and particle acceleration in cosmic structures by means of reliable physical models, with the ultimate hope of them being validated by (soon-to-be) available radio observations.

Thank you to my supervisors, Franco and Lorenzo, for believing in me until the very end.

Bibliography

J. Richard Bond, Lev Kofman, and Dmitry Pogosyan. How filaments of galaxies are woven into the cosmic web. Nature, 380(6575):603–606, April 1996. doi: 10.1038/380603a0.

Y. B. Zel'dovich. The Hypothesis of Cosmological Magnetic Inhomogeneity. Soviet Ast., 13:608, February 1970.

W.H. Press and P. Schechter. Formation of galaxies and clusters of galaxies by self-similar gravitational condensation. *ApJ*, 187:425, 1974.

V. Springel. The cosmological simulation code GADGET-2. MNRAS, 364:1105–1134, December 2005. doi: 10.1111/j.1365-2966.2005.09655.x.

Volker Springel, Carlos S. Frenk, and Simon D. M. White. The large-scale structure of the universe. *Nature*, 440(7088):1137–1144, Apr 2006. ISSN 1476-4687. doi: 10.1038/nature04805. URL `http://dx.doi.org/10.1038/nature04805`.

Y.P. Jing and Y. Suto. The density profiles of the dark matter halo are not universal. *ApJL*, 529:L69, 2000.

Jiajian Shen, Tom Abel, H. J. Mo, and Ravi K. Sheth. An Excursion Set Model of the Cosmic Web: The Abundance of Sheets, Filaments, and Halos. ApJ, 645(2):783–791, July 2006. doi: 10.1086/504513.

R.K. Sheth and G. Tormen. *MNRAS*, 308:119, 1999.

J.F. Navarro, C.S. Frenk, and S.D.M. White. A universal density profile from hierarchical clustering. *ApJ*, 490:493, 1997.

F. Hoyle. Problems of cosmical aerodynamics. *Central Air Documents Office, Dayton, OH*, page 195, 1949.

P. J. E. Peebles. Origin of the Angular Momentum of Galaxies. ApJ, 155:393, February 1969. doi: 10.1086/149876.

A. G. Doroshkevich. The space structure of perturbations and the origin of rotation of galaxies in the theory of fluctuation. *Astrofizika*, 6:581–600, January 1970.

S. D. M. White. Angular momentum growth in protogalaxies. ApJ, 286:38–41, November 1984. doi: 10.1086/162573.

Cristiano Porciani, Avishai Dekel, and Yehuda Hoffman. Testing tidal-torque theory - II. Alignment of inertia and shear and the characteristics of protohaloes. MNRAS, 332(2):339–351, May 2002. doi: 10.1046/j.1365-8711.2002.05306.x.

Sandrine Codis, Christophe Pichon, Julien Devriendt, Adrianne Slyz, Dmitry Pogosyan, Yohan Dubois, and Thierry Sousbie. Connecting the cosmic web to the spin of dark haloes: implications for galaxy formation. MNRAS, 427(4):3320–3336, December 2012. doi: 10.1111/j.1365-2966.2012.21636.x.

C. Pichon, D. Pogosyan, T. Kimm, A. Slyz, J. Devriendt, and Y. Dubois. Rigging dark haloes: why is hierarchical galaxy formation consistent with the inside-out build-up of thin discs? MNRAS, 418(4): 2493–2507, December 2011. doi: 10.1111/j.1365-2966.2011.19640.x.

M. A. Aragón-Calvo, B. J. T. Jones, R. van de Weygaert, and J. M. van der Hulst. The multiscale morphology filter: identifying and extracting spatial patterns in the galaxy distribution. A&A, 474(1): 315–338, October 2007. doi: 10.1051/0004-6361:20077880.

S. D. M. White and M. J. Rees. Core condensation in heavy halos: a two-stage theory for galaxy formation and clustering. MNRAS, 183:341–358, May 1978. doi: 10.1093/mnras/183.3.341.

G. O. Abell. The distribution of rich clusters of galaxies. *ApJS*, 3:211, 1958.

C. L. Sarazin. *The Physics of Cluster Mergers*, pages 1–38. ASSL Vol. 272: Merging Processes in Galaxy Clusters, June 2002.

A. Cavaliere and R. Fusco-Femiano. Reprint of 1976A&A....49..137C. X-rays from hot plasma in clusters of galaxies. A&A, 500:95–102, May 1976.

R. N. Proctor, C. Mendes de Oliveira, L. Azanha, R. Dupke, and R. Overzier. VizieR Online Data Catalog: Mass and luminosity of maxBCG galaxies groups (Proctor+, 2015). *VizieR Online Data Catalog*, art. J/MNRAS/449/2345, November 2015.

Yutong Shan, Michael McDonald, and Stéphane Courteau. Revised Mass-to-light Ratios for Nearby Galaxy Groups and Clusters. ApJ, 800(2):122, February 2015. doi: 10.1088/0004-637X/800/2/122.

C. L. Sarazin and R. E. White, III. Steady state cooling flow models for normal elliptical galaxies. ApJ, 320:32–48, September 1987. doi: 10.1086/165522.

S. Ettori, A. Morandi, P. Tozzi, I. Balestra, S. Borgani, P. Rosati, L. Lovisari, and F. Terenziani. The cluster gas mass fraction as a cosmological probe: a revised study. A&A, 501:61–73, July 2009. doi: 10.1051/0004-6361/200810878.

D. Ryu, H. Kang, J. Cho, and S. Das. Turbulence and Magnetic Fields in the Large-Scale Structure of the Universe. *Science*, 320:909–, May 2008. doi: 10.1126/science.1154923.

F. Vazza, G. Brunetti, C. Gheller, R. Brunino, and M. Brüggen. Massive and refined. II. The statistical properties of turbulent motions in massive galaxy clusters with high spatial resolution. A&A, 529: A17+, May 2011a. doi: 10.1051/0004-6361/201016015.

David Vallés-Pérez, Susana Planelles, and Vicent Quilis. Troubled cosmic flows: turbulence, enstrophy, and helicity from the assembly history of the intracluster medium. MNRAS, 504(1):510–527, June 2021. doi: 10.1093/mnras/stab880.

J. Cho. Origin of Magnetic Field in the Intracluster Medium: Primordial or Astrophysical? ApJ, 797:
133, December 2014. doi: 10.1088/0004-637X/797/2/133.

C. L. Sarazin. X-ray emission from clusters of galaxies. *RvMP*, 58:1, 1986.

Hans Böhringer and Norbert Werner. X-ray spectroscopy of galaxy clusters: studying astrophysical
processes in the largest celestial laboratories. A&A Rev., 18(1-2):127–196, February 2010. doi:
10.1007/s00159-009-0023-3.

Silvano Molendi and Fabio Pizzolato. Is the Gas in Cooling Flows Multiphase? ApJ, 560(1):194–200,
October 2001. doi: 10.1086/322387.

Alastair J. R. Sanderson, Ewan O'Sullivan, and Trevor J. Ponman. A statistically selected Chandra sample
of 20 galaxy clusters - II. Gas properties and cool core/non-cool core bimodality. MNRAS, 395(2):
764–776, May 2009. doi: 10.1111/j.1365-2966.2009.14613.x.

J. R. Peterson and A. C. Fabian. X-ray spectroscopy of cooling clusters. Phys. Rep., 427(1):1–39, April
2006. doi: 10.1016/j.physrep.2005.12.007.

B. R. McNamara and P. E. J. Nulsen. Heating Hot Atmospheres with Active Galactic Nuclei. ARA&A,
45:117–175, September 2007. doi: 10.1146/annurev.astro.45.051806.110625.

A. Leccardi, M. Rossetti, and S. Molendi. Thermo-dynamic and chemical properties of the intra-cluster
medium. A&A, 510:A82, February 2010. doi: 10.1051/0004-6361/200913094.

C. Ferrari, F. Govoni, S. Schindler, A. M. Bykov, and Y. Rephaeli. Observations of Extended Radio
Emission in Clusters. Space Sci. Rev., 134:93–118, February 2008. doi: 10.1007/s11214-008-9311-x.

R. J. van Weeren, F. de Gasperin, H. Akamatsu, M. Brüggen, L. Feretti, H. Kang, A. Stroe, and
F. Zandanel. Diffuse Radio Emission from Galaxy Clusters. Space Sci. Rev., 215(1):16, Feb 2019.
doi: 10.1007/s11214-019-0584-z.

L. Feretti and G. Giovannini. Diffuse Cluster Radio Sources (Review). In Ron D. Ekers, C. Fanti, and
L. Padrielli, editors, *Extragalactic Radio Sources*, volume 175, page 333, January 1996.

C. J. J. Pearce, R. J. van Weeren, F. Andrade-Santos, C. Jones, W. R. Forman, M. Brüggen, E. Bulbul,
T. E. Clarke, R. P. Kraft, E. Medezinski, T. Mroczkowski, M. Nonino, P. E. J. Nulsen, S. W. Randall,
and K. Umetsu. VLA radio observations of theHSTFrontier fields cluster abell 2744: The discovery of
new radio relics. *The Astrophysical Journal*, 845(1):81, aug 2017. doi: 10.3847/1538-4357/aa7e2f.
URL https://doi.org/10.3847/1538-4357/aa7e2f.

D. Eckert, M. Jauzac, H. Shan, J.-P. Kneib, T. Erben, H. Israel, E. Jullo, M. Klein, R. Massey, J. Richard,
and C. Tchernin. Warm-hot baryons comprise 5-10 per cent of filaments in the cosmic web. Nature,
528:105–107, December 2015. doi: 10.1038/nature16058.

R. Cen and J. P. Ostriker. Where Are the Baryons? ApJ, 514:1–6, March 1999. doi: 10.1086/306949.

R. Davé, R. Cen, J. P. Ostriker, G. L. Bryan, L. Hernquist, N. Katz, D. H. Weinberg, M. L. Norman,
and B. O'Shea. Baryons in the Warm-Hot Intergalactic Medium. ApJ, 552:473–483, May 2001. doi:
10.1086/320548.

C. Gheller, F. Vazza, J. Favre, and M. Brüggen. Properties of cosmological filaments extracted from Eulerian simulations. MNRAS, 453(2):1164–1185, October 2015. doi: 10.1093/mnras/stv1646.

N. Werner, A. Finoguenov, J. S. Kaastra, A. Simionescu, J. P. Dietrich, J. Vink, and H. Böhringer. Detection of hot gas in the filament connecting the clusters of galaxies Abell 222 and Abell 223. A&A, 482:L29–L33, May 2008. doi: 10.1051/0004-6361:200809599.

D. Farnsworth, L. Rudnick, S. Brown, and G. Brunetti. Discovery of Megaparsec-scale, Low Surface Brightness Nonthermal Emission in Merging Galaxy Clusters Using the Green Bank Telescope. ApJ, 779:189, December 2013. doi: 10.1088/0004-637X/779/2/189.

Tessa Vernstrom, George Heald, Franco Vazza, Tim Galvin, Jennifer West, Nicola Locatelli, Nicolao Fornengo, and Elena Pinetti. Discovery of Magnetic Fields Along Stacked Cosmic Filaments as Revealed by Radio and X-Ray Emission. *arXiv e-prints*, art. arXiv:2101.09331, January 2021.

H. Tanimura, N. Aghanim, A. Kolodzig, M. Douspis, and N. Malavasi. First detection of stacked X-ray emission from cosmic web filaments. A&A, 643:L2, November 2020. doi: 10.1051/0004-6361/202038521.

Planck Collaboration, P. A. R. Ade, N. Aghanim, M. Arnaud, M. Ashdown, F. Atrio-Barandela, J. Aumont, C. Baccigalupi, A. Balbi, A. J. Banday, and et al. Planck intermediate results. V. Pressure profiles of galaxy clusters from the Sunyaev-Zeldovich effect. A&A, 550:A131, February 2013. doi: 10.1051/0004-6361/201220040.

H. Tanimura, N. Aghanim, V. Bonjean, N. Malavasi, and M. Douspis. Density and temperature of cosmic-web filaments on scales of tens of megaparsecs. *arXiv e-prints*, art. arXiv:1911.09706, Nov 2019a.

Anna de Graaff, Yan-Chuan Cai, Catherine Heymans, and John A. Peacock. Probing the missing baryons with the Sunyaev-Zel'dovich effect from filaments. A&A, 624:A48, April 2019. doi: 10.1051/0004-6361/201935159.

D. Ryu, H. Kang, E. Hallman, and T. W. Jones. ApJ, 593:599–610, August 2003. doi: 10.1086/376723.

Damiano Caprioli, Gianfranco Brunetti, Thomas W. Jones, Hyesung Kang, Matthew Kunz, S. Peng Oh, Dongsu Ryu, Irina Zhuravleva, and Ellen Zweibel. Plasma 2020 - Intracluster Medium Plasmas. *arXiv e-prints*, art. arXiv:1903.08751, March 2019.

O. Buneman. Instability, turbulence, and conductivity in current-carrying plasma. *Phys. Rev. Lett.*, 1:8–9, Jul 1958. doi: 10.1103/PhysRevLett.1.8. URL https://link.aps.org/doi/10.1103/PhysRevLett.1.8.

Y. Matsumoto, T. Amano, T. N. Kato, and M. Hoshino. Stochastic electron acceleration during spontaneous turbulent reconnection in a strong shock wave. *Science*, 347(6225):974–978, February 2015. doi: 10.1126/science.1260168.

X. Guo, L. Sironi, and R. Narayan. Non-thermal Electron Acceleration in Low Mach Number Collisionless Shocks. II. Firehose-mediated Fermi Acceleration and its Dependence on Pre-shock Conditions. ApJ, 797:47, December 2014a. doi: 10.1088/0004-637X/797/1/47.

Vicent Quilis, José M, . Ibáñez, and Diego Sáez. On the Role of Shock Waves in Galaxy Cluster Evolution. ApJ, 502(2):518–530, August 1998a. doi: 10.1086/305932.

A. M. Bykov, K. Dolag, and F. Durret. Cosmological Shock Waves. Space Sci. Rev., 134:119–140, February 2008. doi: 10.1007/s11214-008-9312-9.

V. Quilis, J. M. A. Ibanez, and D. Saez. On the Role of Shock Waves in Galaxy Cluster Evolution. ApJ, 502:518, August 1998b. doi: 10.1086/305932.

Ji-Hoon Ha, Dongsu Ryu, Hyesung Kang, and Allard Jan van Marle. Proton Acceleration in Weak Quasi-parallel Intracluster Shocks: Injection and Early Acceleration. ApJ, 864(2):105, September 2018a. doi: 10.3847/1538-4357/aad634.

Ji-Hoon Ha, Dongsu Ryu, and Hyesung Kang. Properties of Merger Shocks in Merging Galaxy Clusters. ApJ, 857(1):26, April 2018b. doi: 10.3847/1538-4357/aab4a2.

Congyao Zhang, Eugene Churazov, Klaus Dolag, William R. Forman, and Irina Zhuravleva. Encounters of merger and accretion shocks in galaxy clusters and their effects on intracluster medium. MNRAS, 494(3):4539–4547, May 2020. doi: 10.1093/mnras/staa1013.

F. De Hoffmann and E. Teller. Magneto-hydrodynamic shocks. *Phys. Rev.*, 80:692–703, Nov 1950. doi: 10.1103/PhysRev.80.692. URL `https://link.aps.org/doi/10.1103/PhysRev.80.692`.

L.D. Landau and E.M. Lifshitz. Chapter viii - magnetohydrodynamics. In L.D. LANDAU and E.M. LIFSHITZ, editors, *Electrodynamics of Continuous Media (Second Edition)*, volume 8 of *Course of Theoretical Physics*, pages 225–256. Pergamon, Amsterdam, second edition edition, 1984. ISBN 978-0-08-030275-1. doi: https://doi.org/10.1016/B978-0-08-030275-1.50014-X. URL `https://www.sciencedirect.com/science/article/pii/B978008030275150014X`.

R. D. Blandford and J. P. Ostriker. ApJ, 221:L29–L32, April 1978. doi: 10.1086/182658.

ENRICO Fermi. On the origin of the cosmic radiation. *Phys. Rev.*, 75:1169–1174, Apr 1949. doi: 10.1103/PhysRev.75.1169. URL `https://link.aps.org/doi/10.1103/PhysRev.75.1169`.

D. Caprioli, H. Kang, A. E. Vladimirov, and T. W. Jones. Comparison of different methods for non-linear diffusive shock acceleration. MNRAS, 407:1773–1783, September 2010. doi: 10.1111/j.1365-2966.2010.17013.x.

Elena Amato. The origin of galactic cosmic rays. *International Journal of Modern Physics D*, 23(07): 1430013, Jun 2014. ISSN 1793-6594. doi: 10.1142/s0218271814300134. URL `http://dx.doi.org/10.1142/S0218271814300134`.

Bojan Arbutina and Vladimir Zeković. Non-linear diffusive shock acceleration: A recipe for injection of electrons. *Astroparticle Physics*, 127, 1 2021. ISSN 09276505. doi: 10.1016/j.astropartphys.2020.102546.

X. Guo, L. Sironi, and R. Narayan. Non-thermal Electron Acceleration in Low Mach Number Collisionless Shocks. I. Particle Energy Spectra and Acceleration Mechanism. ApJ, 794:153, October 2014b. doi: 10.1088/0004-637X/794/2/153.

Jaehong Park, Damiano Caprioli, and Anatoly Spitkovsky. Simultaneous acceleration of protons and electrons at nonrelativistic quasiparallel collisionless shocks. *Physical Review Letters*, 114, 2 2015. ISSN 10797114. doi: 10.1103/PhysRevLett.114.085003.

Yosuke Matsumoto, Takanobu Amano, Tsunehiko N. Kato, and Masahiro Hoshino. Electron surfing and drift accelerations in a weibel-dominated high-mach-number shock. *Physical Review Letters*, 119, 9 2017. ISSN 10797114. doi: 10.1103/PhysRevLett.119.105101.

Artem Bohdan, Jacek Niemiec, Oleh Kobzar, and Martin Pohl. Electron pre-acceleration at nonrelativistic high-mach-number perpendicular shocks. 8 2017. doi: 10.3847/1538-4357/aa872a. URL `http://arxiv.org/abs/1708.05528http://dx.doi.org/10.3847/1538-4357/aa872a`.

Artem Bohdan, Jacek Niemiec, Martin Pohl, Yosuke Matsumoto, Takanobu Amano, and Masahiro Hoshino. Kinetic simulations of nonrelativistic perpendicular shocks of young supernova remnants. ii. influence of shock-surfing acceleration on downstream electron spectra. 9 2019a. doi: 10.3847/1538-4357/ab43cf. URL `http://arxiv.org/abs/1909.05294http://dx.doi.org/10.3847/1538-4357/ab43cf`.

Bojan Arbutina and Vladimir Zeković. Non-linear diffusive shock acceleration: A recipe for injection of electrons. 12 2020. doi: 10.1016/j.astropartphys.2020.102546. URL `http://arxiv.org/abs/2012.15117http://dx.doi.org/10.1016/j.astropartphys.2020.102546`.

Rui Xu, Anatoly Spitkovsky, and Damiano Caprioli. Electron acceleration in one-dimensional nonrelativistic quasi-perpendicular collisionless shocks. *The Astrophysical Journal*, 897:L41, 7 2020. ISSN 2041-8205. doi: 10.3847/2041-8213/aba11e.

P. A. Sweet. The Neutral Point Theory of Solar Flares. In B. Lehnert, editor, *Electromagnetic Phenomena in Cosmical Physics*, volume 6, page 123, January 1958.

E. N. Parker. Sweet's Mechanism for Merging Magnetic Fields in Conducting Fluids. J. Geophys. Res., 62(4):509–520, December 1957. doi: 10.1029/JZ062i004p00509.

Chunming Zhu, Rui Liu, David Alexander, and R. T. James McAteer. Observation of the evolution of a current sheet in a solar flare. *The Astrophysical Journal*, 821(2):L29, Apr 2016. ISSN 2041-8213. doi: 10.3847/2041-8205/821/2/l29. URL `http://dx.doi.org/10.3847/2041-8205/821/2/L29`.

P. Goldreich and S. Sridhar. Toward a Theory of Interstellar Turbulence. II. Strong Alfvenic Turbulence. ApJ, 438:763, January 1995. doi: 10.1086/175121.

Masahiro Hoshino. Stochastic particle acceleration in multiple magnetic islands during reconnection. *Phys. Rev. Lett.*, 108:135003, Mar 2012. doi: 10.1103/PhysRevLett.108.135003. URL `https://link.aps.org/doi/10.1103/PhysRevLett.108.135003`.

Gianfranco Brunetti and Franco Vazza. Second-order Fermi Reacceleration Mechanisms and Large-Scale Synchrotron Radio Emission in Intracluster Bridges. Phys. Rev. Lett., 124(5):051101, February 2020. doi: 10.1103/PhysRevLett.124.051101.

D. Caprioli and A. Spitkovsky. Simulations of Ion Acceleration at Non-relativistic Shocks. I. Acceleration Efficiency. ApJ, 783(2):91, March 2014a. doi: 10.1088/0004-637X/783/2/91.

J. Giacalone, J. R. Jokipii, and J. Kota. Ion injection and acceleration at quasi-perpendicular shocks. J. Geophys. Res., 99(A10):19351–19358, October 1994. doi: 10.1029/94JA01213.

L. Feretti, G. Giovannini, F. Govoni, and M. Murgia. Clusters of galaxies: observational properties of the diffuse radio emission. A&A Rev., 20:54, May 2012. doi: 10.1007/s00159-012-0054-z.

K. Rajpurohit, M. Hoeft, F. Vazza, L. Rudnick, R. J. van Weeren, D. Wittor, A. Drabent, M. Brienza, E. Bonnassieux, N. Locatelli, R. Kale, and C. Dumba. New mysteries and challenges from the Toothbrush relic: wideband observations from 550 MHz to 8 GHz. A&A, 636:A30, April 2020. doi: 10.1051/0004-6361/201937139.

M. Ackermann, M. Ajello, A. Albert, A. Allafort, W. B. Atwood, L. Baldini, J. Ballet, G. Barbiellini, D. Bastieri, K. Bechtol, R. Bellazzini, E. D. Bloom, E. Bonamente, E. Bottacini, T. J. Brandt, J. Bregeon, M. Brigida, P. Bruel, R. Buehler, S. Buson, G. A. Caliandro, R. A. Cameron, P. A. Caraveo, E. Cavazzuti, R. C. G. Chaves, J. Chiang, G. Chiaro, S. Ciprini, R. Claus, J. Cohen-Tanugi, J. Conrad, F. D'Ammando, A. de Angelis, F. de Palma, C. D. Dermer, S. W. Digel, P. S. Drell, A. Drlica-Wagner, C. Favuzzi, A. Franckowiak, S. Funk, P. Fusco, F. Gargano, D. Gasparrini, S. Germani, N. Giglietto, F. Giordano, M. Giroletti, G. Godfrey, G. A. Gomez-Vargas, I. A. Grenier, S. Guiriec, M. Gustafsson, D. Hadasch, M. Hayashida, J. Hewitt, R. E. Hughes, T. E. Jeltema, G. Jóhannesson, A. S. Johnson, T. Kamae, J. Kataoka, J. Knödlseder, M. Kuss, J. Lande, S. Larsson, L. Latronico, M. Llena Garde, F. Longo, F. Loparco, M. N. Lovellette, P. Lubrano, M. Mayer, M. N. Mazziotta, J. E. McEnery, P. F. Michelson, W. Mitthumsiri, T. Mizuno, M. E. Monzani, A. Morselli, I. V. Moskalenko, S. Murgia, R. Nemmen, E. Nuss, T. Ohsugi, M. Orienti, E. Orlando, J. F. Ormes, J. S. Perkins, M. Pesce-Rollins, F. Piron, G. Pivato, S. Rainò, R. Rando, M. Razzano, S. Razzaque, A. Reimer, O. Reimer, J. Ruan, M. Sánchez-Conde, A. Schulz, C. Sgrò, E. J. Siskind, G. Spandre, P. Spinelli, E. Storm, A. W. Strong, D. J. Suson, H. Takahashi, J. G. Thayer, J. B. Thayer, D. J. Thompson, L. Tibaldo, M. Tinivella, D. F. Torres, E. Troja, Y. Uchiyama, T. L. Usher, J. Vandenbroucke, G. Vianello, V. Vitale, B. L. Winer, K. S. Wood, S. Zimmer, Fermi-LAT Collaboration, A. Pinzke, and C. Pfrommer. Search for Cosmic-Ray-induced Gamma-Ray Emission in Galaxy Clusters. ApJ, 787:18, May 2014. doi: 10.1088/0004-637X/787/1/18.

F. Vazza, M. Brüggen, D. Wittor, C. Gheller, D. Eckert, and M. Stubbe. Constraining the efficiency of cosmic ray acceleration by cluster shocks. MNRAS, 459:70–83, June 2016. doi: 10.1093/mnras/stw584.

V. S. Berezinsky, P. Blasi, and V. S. Ptuskin. Clusters of Galaxies as Storage Room for Cosmic Rays. ApJ, 487:529–+, October 1997. doi: 10.1086/304622.

T. Enßlin, C. Pfrommer, F. Miniati, and K. Subramanian. Cosmic ray transport in galaxy clusters: implications for radio halos, gamma-ray signatures, and cool core heating. A&A, 527:A99, March 2011. doi: 10.1051/0004-6361/201015652.

A. Pinzke, S. P. Oh, and C. Pfrommer. Giant radio relics in galaxy clusters: reacceleration of fossil relativistic electrons? MNRAS, 435:1061–1082, October 2013. doi: 10.1093/mnras/stt1308.

D. Wittor, F. Vazza, D. Ryu, and H. Kang. Limiting the shock acceleration of cosmic ray protons in the ICM. MNRAS, 495(1):L112–L117, April 2020. doi: 10.1093/mnrasl/slaa066.

M. Markevitch and A. Vikhlinin. Phys. Rep., 443:1–53, May 2007. doi: 10.1016/j.physrep.2007.01.001.

H. Akamatsu and H. Kawahara. Systematic X-Ray Analysis of Radio Relic Clusters with Suzaku. PASJ, 65:16, February 2013. doi: 10.1093/pasj/65.1.16.

P. Mazzotta, H. Bourdin, S. Giacintucci, M. Markevitch, and T. Venturi. Study of the M shock wave propagation in RXJ1314.4-2515. Mem. Soc. Astron. Italiana, 82:495, January 2011.

C. Stuardi, A. Bonafede, D. Wittor, F. Vazza, A. Botteon, N. Locatelli, D. Dallacasa, N. Golovich, M. Hoeft, R. J. van Weeren, M. Brüggen, and F. de Gasperin. Particle re-acceleration and Faraday-complex structures in the RXC J1314.4-2515 galaxy cluster. MNRAS, 489(3):3905–3926, November 2019. doi: 10.1093/mnras/stz2408.

Denis Wittor. On the Challenges of Cosmic-Ray Proton Shock Acceleration in the Intracluster Medium. New A, 85:101550, May 2021. doi: 10.1016/j.newast.2020.101550.

P. Dominguez-Fernandez, M. Bruggen, F. Vazza, W. E. Banda-Barragan, K. Rajpurohit, A. Mignone, D. Mukherjee, and B. Vaidya. Morphology of radio relics - I. What causes the substructure of synchrotron emission? MNRAS, 500:795–816, January 2021.

M. A. Brentjens and A. G. de Bruyn. Faraday rotation measure synthesis. A&A, 441(3):1217–1228, October 2005. doi: 10.1051/0004-6361:20052990.

M. Murgia, F. Govoni, L. Feretti, G. Giovannini, D. Dallacasa, R. Fanti, G. B. Taylor, and K. Dolag. Magnetic fields and Faraday rotation in clusters of galaxies. A&A, 424:429–446, September 2004. doi: 10.1051/0004-6361:20040191.

A. Bonafede, L. Feretti, M. Murgia, F. Govoni, G. Giovannini, D. Dallacasa, K. Dolag, and G. B. Taylor. The Coma cluster magnetic field from Faraday rotation measures. A&A, 513:A30+, April 2010. doi: 10.1051/0004-6361/200913696.

D. Guidetti, M. Murgia, F. Govoni, P. Parma, L. Gregorini, H. R. de Ruiter, R. A. Cameron, and R. Fanti. The intracluster magnetic field power spectrum in Abell 2382. A&A, 483:699–713, June 2008. doi: 10.1051/0004-6361:20078576.

Vahé Petrosian. On the Nonthermal Emission and Acceleration of Electrons in Coma and Other Clusters of Galaxies. ApJ, 557(2):560–572, August 2001. doi: 10.1086/321557.

C. Stuardi, S. P. O'Sullivan, A. Bonafede, M. Brüggen, P. Dabhade, C. Horellou, R. Morganti, E. Carretti, G. Heald, M. Iacobelli, and V. Vacca. The LOFAR view of intergalactic magnetic fields with giant radio galaxies. A&A, 638:A48, June 2020. doi: 10.1051/0004-6361/202037635.

M. S. Turner and L. M. Widrow. Inflation-produced, large-scale magnetic fields. Phys. Rev. D, 37: 2743–2754, May 1988. doi: 10.1103/PhysRevD.37.2743.

Dario Grasso and Hector R. Rubinstein. Magnetic fields in the early universe. *Phys. Rept.*, 348:163–266, 2001.

K. Subramanian, A. Shukurov, and N. E. L. Haugen. Evolving turbulence and magnetic fields in galaxy clusters. MNRAS, 366:1437–1454, March 2006. doi: 10.1111/j.1365-2966.2006.09918.x.

V. B. Semikoz and D. Sokoloff. Magnetic helicity and cosmological magnetic field. A&A, 433:L53–L56, April 2005. doi: 10.1051/0004-6361:200500094.

L. Campanelli. Helical Magnetic Fields from Inflation. *International Journal of Modern Physics D*, 18: 1395–1411, 2009. doi: 10.1142/S0218271809015175.

T. Kahniashvili, A. Brandenburg, and A. G. Tevzadze. The evolution of primordial magnetic fields since their generation. Phys. Scr, 91(10):104008, October 2016. doi: 10.1088/0031-8949/91/10/104008.

H. J. Völk and A. M. Atoyan. Clusters of galaxies: magnetic fields and nonthermal emission. *Astroparticle Physics*, 11:73–82, June 1999. doi: 10.1016/S0927-6505(99)00029-8.

J. Donnert, K. Dolag, H. Lesch, and E. Müller. Cluster magnetic fields from galactic outflows. MNRAS, 392:1008–1021, January 2009. doi: 10.1111/j.1365-2966.2008.14132.x.

S. R. Furlanetto and A. Loeb. Intergalactic Magnetic Fields from Quasar Outflows. ApJ, 556:619–634, August 2001. doi: 10.1086/321630.

S. Planelles, D. R. G. Schleicher, and A. M. Bykov. *Large-Scale Structure Formation: From the First Nonlinear Objects to Massive Galaxy Clusters*, pages 93–139. 2016. doi: 10.1007/978-1-4939-3547-5_4.

R. M. Kulsrud, R. Cen, J. P. Ostriker, and D. Ryu. The Protogalactic Origin for Cosmic Magnetic Fields. ApJ, 480:481–491, May 1997. doi: 10.1086/303987.

R. Schlickeiser, D. Ibscher, and M. Supsar. Plasma Effects on Fast Pair Beams in Cosmic Voids. ApJ, 758:102, October 2012. doi: 10.1088/0004-637X/758/2/102.

F. Miniati and A. R. Bell. Resistive Magnetic Field Generation at Cosmic Dawn. ApJ, 729:73–+, March 2011. doi: 10.1088/0004-637X/729/1/73.

M. Langer, N. Aghanim, and J.-L. Puget. Magnetic fields from reionisation. A&A, 443:367–372, November 2005. doi: 10.1051/0004-6361:20053372.

F. Miniati. The Matryoshka Run: A Eulerian Refinement Strategy to Study the Statistics of Turbulence in Virialized Cosmic Structures. ApJ, 782:21, February 2014. doi: 10.1088/0004-637X/782/1/21.

F. Vazza, G. Brunetti, M. Brüggen, and A. Bonafede. Resolved magnetic dynamo action in the simulated intracluster medium. MNRAS, 474:1672–1687, February 2018a. doi: 10.1093/mnras/stx2830.

J. Schober, D. R. G. Schleicher, and R. S. Klessen. Magnetic field amplification in young galaxies. A&A, 560:A87, December 2013. doi: 10.1051/0004-6361/201322185.

P. Domínguez-Fernández, F. Vazza, M. Brüggen, and G. Brunetti. Dynamical evolution of magnetic fields in the intracluster medium. MNRAS, 486(1):623–638, June 2019. doi: 10.1093/mnras/stz877.

Vicent Quilis, José-María Martí, and Susana Planelles. Cosmic magnetic fields with masclet: an application to galaxy clusters. MNRAS, 494(2):2706–2717, May 2020. doi: 10.1093/mnras/staa877.

Franco Vazza, Marcus Brueggen, Claudio Gheller, Stefan Hackstein, Denis Wittor, and Paul Marten Hinz. Simulations of extragalactic magnetic fields and of their observables. *Classical and Quantum Gravity*, 2017. URL `http://iopscience.iop.org/10.1088/1361-6382/aa8e60`.

V. Springel, N. Yoshida, and S.D.M. White. Gadget: a code for collisionless and gasdynamical cosmological simulations. *New Astronomy*, 6:79, 2001.

Philip F. Hopkins. GIZMO: Multi-method magneto-hydrodynamics+gravity code, October 2014.

Volker Springel. E pur si muove: Galilean-invariant cosmological hydrodynamical simulations on a moving mesh. MNRAS, 401(2):791–851, January 2010. doi: 10.1111/j.1365-2966.2009.15715.x.

C. S. Frenk, S. D. M. White, P. Bode, J. R. Bond, G. L. Bryan, R. Cen, H. M. P. Couchman, A. E. Evrard, N. Gnedin, A. Jenkins, A. M. Khokhlov, A. Klypin, J. F. Navarro, M. L. Norman, J. P. Ostriker, J. M. Owen, F. R. Pearce, U. L. Pen, M. Steinmetz, P. A. Thomas, J. V. Villumsen, J. W. Wadsley, M. S. Warren, G. Xu, and G. Yepes. The Santa Barbara Cluster Comparison Project: A Comparison of Cosmological Hydrodynamics Solutions. ApJ, 525(2):554–582, November 1999. doi: 10.1086/307908.

B. W. O'Shea, G. Bryan, J. Bordner, M. L. Norman, T. Abel, R. Harkness, and A. Kritsuk. Introducing Enzo, an AMR Cosmology Application. *ArXiv Astrophysics e-prints*, March 2004.

Elizabeth J. Tasker, Riccardo Brunino, Nigel L. Mitchell, Dolf Michielsen, Stephen Hopton, Frazer R. Pearce, Greg L. Bryan, and Tom Theuns. A test suite for quantitative comparison of hydrodynamic codes in astrophysics. MNRAS, 390(3):1267–1281, November 2008. doi: 10.1111/j.1365-2966.2008. 13836.x.

N. L. Mitchell, I. G. McCarthy, R. G. Bower, T. Theuns, and R. A. Crain. On the origin of cores in simulated galaxy clusters. MNRAS, 395:180–196, May 2009. doi: 10.1111/j.1365-2966.2009.14550.x.

C. Scannapieco, M. Wadepuhl, O. H. Parry, J. F. Navarro, A. Jenkins, V. Springel, R. Teyssier, E. Carlson, H. M. P. Couchman, R. A. Crain, C. Dalla Vecchia, C. S. Frenk, C. Kobayashi, P. Monaco, G. Murante, T. Okamoto, T. Quinn, J. Schaye, G. S. Stinson, T. Theuns, J. Wadsley, S. D. M. White, and R. Woods. The Aquila comparison project: the effects of feedback and numerical methods on simulations of galaxy formation. MNRAS, 423:1726–1749, June 2012. doi: 10.1111/j.1365-2966.2012.20993.x.

F. Vazza, K. Dolag, D. Ryu, G. Brunetti, C. Gheller, H. Kang, and C. Pfrommer. A comparison of cosmological codes: properties of thermal gas and shock waves in large-scale structures. MNRAS, 418:960–985, December 2011b. doi: 10.1111/j.1365-2966.2011.19546.x.

G. L. Bryan, M. L. Norman, B. W. O'Shea, T. Abel, J. H. Wise, M. J. Turk, D. R. Reynolds, D. C. Collins, P. Wang, S. W. Skillman, B. Smith, R. P. Harkness, J. Bordner, J.-h. Kim, M. Kuhlen, H. Xu, N. Goldbaum, C. Hummels, A. G. Kritsuk, E. Tasker, S. Skory, C. M. Simpson, O. Hahn, J. S. Oishi, G. C. So, F. Zhao, R. Cen, Y. Li, and Enzo Collaboration. ENZO: An Adaptive Mesh Refinement Code for Astrophysics. ApJS, 211:19, April 2014. doi: 10.1088/0067-0049/211/2/19.

P. Colella and P. R. Woodward. *Journal of Computational Physics*, 54:174–201, September 1984.

A. Dedner, F. Kemm, D. Kröner, C.-D. Munz, T. Schnitzer, and M. Wesenberg. Hyperbolic Divergence Cleaning for the MHD Equations. *Journal of Computational Physics*, 175:645–673, January 2002. doi: 10.1006/jcph.2001.6961.

S. Banfi, F. Vazza, and D. Wittor. Shock waves in the magnetized cosmic web: the role of obliquity and cosmic ray acceleration. MNRAS, 496(3):3648–3667, June 2020. doi: 10.1093/mnras/staa1810.

Anatoly Spitkovsky. Simulations of relativistic collisionless shocks: shock structure and particle acceleration. In Tomasz Bulik, Bronislaw Rudak, and Grzegorz Madejski, editors, *Astrophysical Sources of High Energy Particles and Radiation*, volume 801 of *American Institute of Physics Conference Series*, pages 345–350, November 2005. doi: 10.1063/1.2141897.

Oscar Buneman. The 3-d electromagnetic particle code. *Computer space plasma physics*, pages 67–84, 1993.

Kane Yee. Numerical solution of inital boundary value problems involving maxwell's equations in isotropic media. *IEEE Transactions on Antennas and Propagation*, 14(3):302–307, May 1966. doi: 10.1109/TAP.1966.1138693.

M. Ackermann, M. Ajello, A. Allafort, L. Baldini, J. Ballet, G. Barbiellini, D. Bastieri, K. Bechtol, R. Bellazzini, R. D. Blandford, P. Blasi, E. D. Bloom, E. Bonamente, A. W. Borgland, A. Bouvier, T. J. Brandt, J. Bregeon, M. Brigida, P. Bruel, R. Buehler, S. Buson, G. A. Caliandro, R. A. Cameron, P. A. Caraveo, S. Carrigan, J. M. Casandjian, E. Cavazzuti, C. Cecchi, Ö. Çelik, E. Charles, A. Chekhtman, C. C. Cheung, J. Chiang, S. Ciprini, R. Claus, J. Cohen-Tanugi, S. Colafrancesco, L. R. Cominsky, J. Conrad, C. D. Dermer, F. de Palma, E. d. C. e. Silva, P. S. Drell, R. Dubois, D. Dumora, Y. Edmonds, C. Farnier, C. Favuzzi, M. Frailis, Y. Fukazawa, S. Funk, P. Fusco, F. Gargano, D. Gasparrini, N. Gehrels, S. Germani, N. Giglietto, F. Giordano, M. Giroletti, T. Glanzman, G. Godfrey, I. A. Grenier, M.-H. Grondin, S. Guiriec, D. Hadasch, A. K. Harding, M. Hayashida, E. Hays, D. Horan, R. E. Hughes, T. E. Jeltema, G. Jóhannesson, A. S. Johnson, T. J. Johnson, W. N. Johnson, T. Kamae, H. Katagiri, J. Kataoka, M. Kerr, J. Knödlseder, M. Kuss, J. Lande, L. Latronico, S.-H. Lee, M. Lemoine-Goumard, F. Longo, F. Loparco, B. Lott, M. N. Lovellette, P. Lubrano, G. M. Madejski, A. Makeev, M. N. Mazziotta, P. F. Michelson, W. Mitthumsiri, T. Mizuno, A. A. Moiseev, C. Monte, M. E. Monzani, A. Morselli, I. V. Moskalenko, S. Murgia, M. Naumann-Godo, P. L. Nolan, J. P. Norris, E. Nuss, T. Ohsugi, N. Omodei, E. Orlando, J. F. Ormes, M. Ozaki, D. Paneque, J. H. Panetta, M. Pepe, M. Pesce-Rollins, V. Petrosian, C. Pfrommer, F. Piron, T. A. Porter, S. Profumo, S. Rainò, R. Rando, M. Razzano, A. Reimer, O. Reimer, T. Reposeur, J. Ripken, S. Ritz, A. Y. Rodriguez, R. W. Romani, M. Roth, H. F.-W. Sadrozinski, A. Sander, P. M. Saz Parkinson, J. D. Scargle, C. Sgrò, E. J. Siskind, P. D. Smith, G. Spandre, P. Spinelli, J.-L. Starck, Ł. Stawarz, M. S. Strickman, A. W. Strong, D. J. Suson, H. Tajima, H. Takahashi, T. Takahashi, T. Tanaka, J. B. Thayer, J. G. Thayer, L. Tibaldo, O. Tibolla, D. F. Torres, G. Tosti, A. Tramacere, Y. Uchiyama, T. L. Usher, J. Vandenbroucke, V. Vasileiou, N. Vilchez, V. Vitale, A. P. Waite, P. Wang, B. L. Winer, K. S. Wood, Z. Yang, T. Ylinen, and M. Ziegler. GeV Gamma-ray Flux Upper Limits from Clusters of Galaxies. ApJ, 717:L71–L78, July 2010. doi: 10.1088/2041-8205/717/1/L71.

T. Arlen, T. Aune, M. Beilicke, W. Benbow, A. Bouvier, J. H. Buckley, V. Bugaev, K. Byrum, A. Cannon, A. Cesarini, L. Ciupik, E. Collins-Hughes, M. P. Connolly, W. Cui, R. Dickherber, J. Dumm, A. Falcone, S. Federici, Q. Feng, J. P. Finley, G. Finnegan, L. Fortson, A. Furniss, N. Galante, D. Gall, S. Godambe, S. Griffin, J. Grube, G. Gyuk, J. Holder, H. Huan, G. Hughes, T. B. Humensky, A. Imran, P. Kaaret, N. Karlsson, M. Kertzman, Y. Khassen, D. Kieda, H. Krawczynski, F. Krennrich, K. Lee, A. S. Madhavan, G. Maier, P. Majumdar, S. McArthur, A. McCann, P. Moriarty, R. Mukherjee, T. Nelson, A. O'Faoláin de Bhróithe, R. A. Ong, M. Orr, A. N. Otte, N. Park, J. S. Perkins, M. Pohl, H. Prokoph, J. Quinn, K. Ragan, L. C. Reyes, P. T. Reynolds, E. Roache, J. Ruppel, D. B. Saxon, M. Schroedter, G. H. Sembroski, C. Skole, A. W. Smith, I. Telezhinsky, G. Tešić, M. Theiling, S. Thibadeau, K. Tsurusaki, A. Varlotta, M. Vivier, S. P. Wakely, J. E. Ward, A. Weinstein, R. Welsing, D. A. Williams, B. Zitzer, C. Pfrommer, and A. Pinzke. Constraints on Cosmic Rays, Magnetic Fields, and Dark Matter from Gamma-Ray Observations of the Coma Cluster of Galaxies with VERITAS and Fermi. ApJ, 757:123, October 2012. doi: 10.1088/0004-637X/757/2/123.

S. Banfi, F. Vazza, and C. Gheller. On the alignment of haloes, filaments and magnetic fields in the simulated cosmic web. MNRAS, 503(3):4016–4031, May 2021. doi: 10.1093/mnras/stab655.

F. Vazza, D. Paoletti, S. Banfi, F. Finelli, C. Gheller, S. P. O'Sullivan, and M. Brüggen. Simulations and observational tests of primordial magnetic fields from Cosmic Microwave Background constraintsok. MNRAS, 500(4):5350–5368, January 2021. doi: 10.1093/mnras/staa3532.

N. Locatelli, F. Vazza, A. Bonafede, S. Banfi, G. Bernardi, C. Gheller, A. Botteon, and T. Shimwell. New constraints on the magnetic field in cosmic web filaments. A&A, 652:A80, August 2021. doi: 10.1051/0004-6361/202140526.

A. M. Bykov, F. Vazza, J. A. Kropotina, K. P. Levenfish, and F. B.S. Paerels. Shocks and Non-thermal Particles in Clusters of Galaxies, jan 2019. ISSN 15729672.

F. Miniati, D. Ryu, H. Kang, T. W. Jones, R. Cen, and J. P. Ostriker. ApJ, 542:608–621, October 2000. doi: 10.1086/317027.

C. Pfrommer, V. Springel, T. A. Enßlin, and M. Jubelgas. MNRAS, 367:113–131, March 2006. doi: 10.1111/j.1365-2966.2005.09953.x.

F. Vazza, G. Brunetti, and C. Gheller. Shock waves in Eulerian cosmological simulations: main properties and acceleration of cosmic rays. MNRAS, 395:1333–1354, May 2009. doi: 10.1111/j.1365-2966. 2009.14691.x.

S. Planelles and V. Quilis. Cosmological shock waves: clues to the formation history of haloes. MNRAS, 428:1643–1655, January 2013. doi: 10.1093/mnras/sts142.

H. Kang and T. W. Jones. Self-similar evolution of cosmic-ray-modified quasi-parallel plane shocks. *Astroparticle Physics*, 28:232–246, October 2007. doi: 10.1016/j.astropartphys.2007.05.007.

F. Vazza and M. Brüggen. Do radio relics challenge diffusive shock acceleration? MNRAS, 437: 2291–2296, January 2014. doi: 10.1093/mnras/stt2042.

G. Brunetti and T. W. Jones. Cosmic Rays in Galaxy Clusters and Their Nonthermal Emission. *International Journal of Modern Physics D*, 23:1430007-98, March 2014. doi: 10.1142/S0218271814300079.

A. R. Bell. The acceleration of cosmic rays in shock fronts. I. MNRAS, 182:147–156, January 1978.

D. Caprioli and A. Spitkovsky. Simulations of Ion Acceleration at Non-relativistic Shocks. I. Acceleration Efficiency. ApJ, 783:91, March 2014b. doi: 10.1088/0004-637X/783/2/91.

S. Matsukiyo, Y. Ohira, R. Yamazaki, and T. Umeda. Relativistic Electron Shock Drift Acceleration in Low Mach Number Galaxy Cluster Shocks. ApJ, 742(1):47, Nov 2011. doi: 10.1088/0004-637X/742/1/47.

D. Wittor, F. Vazza, and M. Brüggen. Testing cosmic ray acceleration with radio relics: a high-resolution study using MHD and tracers. MNRAS, 464:4448–4462, February 2017. doi: 10.1093/mnras/stw2631.

Ji-Hoon Ha, Dongsu Ryu, and Hyesung Kang. Gamma-ray and Neutrino Emissions due to Cosmic-Ray Protons Accelerated at Intracluster Shocks in Galaxy Clusters. *arXiv e-prints*, art. arXiv:1910.02429, Oct 2019.

Dongsu Ryu, Hyesung Kang, and Ji-Hoon Ha. A Diffusive Shock Acceleration Model for Protons in Weak Quasi-parallel Intracluster Shocks. *The Astrophysical Journal*, 883(1):60, 2019. ISSN 1538-4357. doi: 10.3847/1538-4357/ab3a3a.

R.W. Hockney and J.W. Eastwood. *Computer simulation using particles*. Bristol: Hilger, 1988, 1988.

M. J. Berger and P. Colella. Local adaptive mesh refinement for shock hydrodynamics. *Journal of Computational Physics*, 82:64–84, May 1989. doi: 10.1016/0021-9991(89)90035-1.

P. Colella and H. M. Glaz. Efficient Solution Algorithms for the Riemann Problem for Real Gases. *Journal of Computational Physics*, 59(2):264–289, Jun 1985. doi: 10.1016/0021-9991(85)90146-9.

C.-W. Shu and S. Osher. Efficient Implementation of Essentially Non-oscillatory Shock-Capturing Schemes. *Journal of Computational Physics*, 77:439–471, August 1988. doi: 10.1016/0021-9991(88)90177-5.

F. A. Stasyszyn, K. Dolag, and A. M. Beck. A divergence-cleaning scheme for cosmological SPMHD simulations. MNRAS, 428(1):13–27, Jan 2013. doi: 10.1093/mnras/sts018.

Philip F. Hopkins and Matthias J. Raives. Accurate, meshless methods for magnetohydrodynamics. MNRAS, 455(1):51–88, Jan 2016. doi: 10.1093/mnras/stv2180.

Terrence S. Tricco, Daniel J. Price, and Christoph Federrath. A comparison between grid and particle methods on the small-scale dynamo in magnetized supersonic turbulence. MNRAS, 461(2):1260–1275, Sep 2016. doi: 10.1093/mnras/stw1280.

J. Donnert, F. Vazza, M. Brüggen, and J. ZuHone. Magnetic Field Amplification in Galaxy Clusters and Its Simulation. Space Sci. Rev., 214(8):122, December 2018. doi: 10.1007/s11214-018-0556-8.

K. Dolag, A. M. Bykov, and A. Diaferio. Non-Thermal Processes in Cosmological Simulations. Space Sci. Rev., 134:311–335, February 2008. doi: 10.1007/s11214-008-9319-2.

C. Federrath, J. Schober, S. Bovino, and D. R. G. Schleicher. The Turbulent Dynamo in Highly Compressible Supersonic Plasmas. ApJ, 797:L19, December 2014. doi: 10.1088/2041-8205/797/2/L19.

J.-h. Kim, J. H. Wise, M. A. Alvarez, and T. Abel. Galaxy Formation with Self-consistently Modeled Stars and Massive Black Holes. I. Feedback-regulated Star Formation and Black Hole Growth. ApJ, 738:54, September 2011. doi: 10.1088/0004-637X/738/1/54.

A. V. Kravtsov. On the Origin of the Global Schmidt Law of Star Formation. ApJ, 590:L1–L4, June 2003. doi: 10.1086/376674.

Planck Collaboration, P. A. R. Ade, N. Aghanim, M. Arnaud, M. Ashdown, J. Aumont, C. Baccigalupi, A. J. Banday, R. B. Barreiro, J. G. Bartlett, and et al. Planck 2015 results. XIII. Cosmological parameters. A&A, 594:A13, September 2016. doi: 10.1051/0004-6361/201525830.

Oliver Hahn and Tom Abel. Multi-scale initial conditions for cosmological simulations. MNRAS, 415 (3):2101–2121, Aug 2011. doi: 10.1111/j.1365-2966.2011.18820.x.

Planck Collaboration, N. Aghanim, Y. Akrami, M. Ashdown, J. Aumont, C. Baccigalupi, M. Ballardini, A. J. Banday, R. B. Barreiro, N. Bartolo, S. Basak, R. Battye, K. Benabed, J. P. Bernard, M. Bersanelli, P. Bielewicz, J. J. Bock, J. R. Bond, J. Borrill, F. R. Bouchet, F. Boulanger, M. Bucher, C. Burigana, R. C. Butler, E. Calabrese, J. F. Cardoso, J. Carron, A. Challinor, H. C. Chiang, J. Chluba,

L. P. L. Colombo, C. Combet, D. Contreras, B. P. Crill, F. Cuttaia, P. de Bernardis, G. de Zotti, J. Delabrouille, J. M. Delouis, E. Di Valentino, J. M. Diego, O. Doré, M. Douspis, A. Ducout, X. Dupac, S. Dusini, G. Efstathiou, F. Elsner, T. A. Enßlin, H. K. Eriksen, Y. Fantaye, M. Farhang, J. Fergusson, R. Fernandez-Cobos, F. Finelli, F. Forastieri, M. Frailis, A. A. Fraisse, E. Franceschi, A. Frolov, S. Galeotta, S. Galli, K. Ganga, R. T. Génova-Santos, M. Gerbino, T. Ghosh, J. González-Nuevo, K. M. Górski, S. Gratton, A. Gruppuso, J. E. Gudmundsson, J. Hamann, W. Handley, F. K. Hansen, D. Herranz, S. R. Hildebrandt, E. Hivon, Z. Huang, A. H. Jaffe, W. C. Jones, A. Karakci, E. Keihänen, R. Keskitalo, K. Kiiveri, J. Kim, T. S. Kisner, L. Knox, N. Krachmalnicoff, M. Kunz, H. Kurki-Suonio, G. Lagache, J. M. Lamarre, A. Lasenby, M. Lattanzi, C. R. Lawrence, M. Le Jeune, P. Lemos, J. Lesgourgues, F. Levrier, A. Lewis, M. Liguori, P. B. Lilje, M. Lilley, V. Lindholm, M. López-Caniego, P. M. Lubin, Y. Z. Ma, J. F. Macías-Pérez, G. Maggio, D. Maino, N. Mandolesi, A. Mangilli, A. Marcos-Caballero, M. Maris, P. G. Martin, M. Martinelli, E. Martínez-González, S. Matarrese, N. Mauri, J. D. McEwen, P. R. Meinhold, A. Melchiorri, A. Mennella, M. Migliaccio, M. Millea, S. Mitra, M. A. Miville-Deschênes, D. Molinari, L. Montier, G. Morgante, A. Moss, P. Natoli, H. U. Nørgaard-Nielsen, L. Pagano, D. Paoletti, B. Partridge, G. Patanchon, H. V. Peiris, F. Perrotta, V. Pettorino, F. Piacentini, L. Polastri, G. Polenta, J. L. Puget, J. P. Rachen, M. Reinecke, M. Remazeilles, A. Renzi, G. Rocha, C. Rosset, G. Roudier, J. A. Rubiño-Martín, B. Ruiz-Granados, L. Salvati, M. Sandri, M. Savelainen, D. Scott, E. P. S. Shellard, C. Sirignano, G. Sirri, L. D. Spencer, R. Sunyaev, A. S. Suur-Uski, J. A. Tauber, D. Tavagnacco, M. Tenti, L. Toffolatti, M. Tomasi, T. Trombetti, L. Valenziano, J. Valiviita, B. Van Tent, L. Vibert, P. Vielva, F. Villa, N. Vittorio, B. D. Wand elt, I. K. Wehus, M. White, S. D. M. White, A. Zacchei, and A. Zonca. Planck 2018 results. VI. Cosmological parameters. *arXiv e-prints*, art. arXiv:1807.06209, Jul 2018.

C. Gheller and F. Vazza. A survey of the thermal and non-thermal properties of cosmic filaments. MNRAS, 486(1):981–1002, Jun 2019. doi: 10.1093/mnras/stz843.

Ji-Hoon Ha, Dongsu Ryu, Hyesung Kang, and Allard Jan van Marle. Proton Acceleration in Weak Quasi-parallel Intracluster Shocks: Injection and Early Acceleration. ApJ, 864(2):105, Sep 2018c. doi: 10.3847/1538-4357/aad634.

H. Kang, D. Ryu, R. Cen, and J. P. Ostriker. ApJ, 669:729–740, November 2007. doi: 10.1086/521717.

F. Vazza, M. Brüggen, and C. Gheller. Thermal and non-thermal traces of AGN feedback: results from cosmological AMR simulations. MNRAS, 428:2366–2388, January 2013. doi: 10.1093/mnras/sts213.

H. Kang and D. Ryu. Diffusive Shock Acceleration at Cosmological Shock Waves. ApJ, 764:95, February 2013. doi: 10.1088/0004-637X/764/1/95.

C. Gheller, O. Pantano, and L. Moscardini. Constraining the cosmological baryon density with X-ray clusters. MNRAS, 296:85–99, May 1998. doi: 10.1046/j.1365-8711.1998.01250.x.

Noam I. Libeskind, Yehuda Hoffman, and Stefan Gottlöber. The velocity shear and vorticity across redshifts and non-linear scales. MNRAS, 441(3):1974–1983, July 2014. doi: 10.1093/mnras/stu629.

Weishan Zhu and Long-Long Feng. Evolution of mass and velocity field in the cosmic web: Comparison between baryonic and dark matter. *The Astrophysical Journal*, 838(1):21, mar 2017. doi: 10.3847/1538-4357/aa61f9. URL `https://doi.org/10.3847%2F1538-4357%2Faa61f9`.

J. D. Soler and P. Hennebelle. What are we learning from the relative orientation between density structures and the magnetic field in molecular clouds? *Astronomy and Astrophysics*, 607:1–10, 2017. ISSN 14320746. doi: 10.1051/0004-6361/201731049.

J. Bagchi, T. A. Enßlin, F. Miniati, C. S. Stalin, M. Singh, S. Raychaudhury, and N. B. Humeshkar. Evidence for shock acceleration and intergalactic magnetic fields in a large-scale filament of galaxies ZwCl 2341.1+0000. New A, 7:249–277, July 2002. doi: 10.1016/S1384-1076(02)00137-9.

M. Brüggen, A. Bykov, D. Ryu, and H. Röttgering. Magnetic Fields, Relativistic Particles, and Shock Waves in Cluster Outskirts. Space Sci. Rev., pages 71–+, June 2011. doi: 10.1007/s11214-011-9785-9.

C. Pfrommer, T. A. Enßlin, V. Springel, M. Jubelgas, and K. Dolag. MNRAS, 378:385–408, June 2007. doi: 10.1111/j.1365-2966.2007.11732.x.

R. Fitzpatrick. *Plasma Physics: An Introduction.* CRC Press, 2014. ISBN 9781466594272. URL `https://books.google.it/books?id=5HbSBQAAQBAJ`.

David C. Collins, Hao Xu, Michael L. Norman, Hui Li, and Shengtai Li. Cosmological Adaptive Mesh Refinement Magnetohydrodynamics with Enzo. ApJS, 186(2):308–333, Feb 2010. doi: 10.1088/0067-0049/186/2/308.

C. L. Carilli and G. B. Taylor. Cluster Magnetic Fields. ARA&A, 40:319–348, 2002a.

L. Oc. Drury. REVIEW ARTICLE: An introduction to the theory of diffusive shock acceleration of energetic particles in tenuous plasmas. *Reports on Progress in Physics*, 46(8):973–1027, August 1983. doi: 10.1088/0034-4885/46/8/002.

N. Shimada and M. Hoshino. Strong Electron Acceleration at High Mach Number Shock Waves: Simulation Study of Electron Dynamics. ApJ, 543(1):L67–L71, November 2000. doi: 10.1086/318161.

M. Hoshino and N. Shimada. Nonthermal Electrons at High Mach Number Shocks: Electron Shock Surfing Acceleration. ApJ, 572(2):880–887, June 2002. doi: 10.1086/340454.

Tsunehiko N. Kato and Hideaki Takabe. Electrostatic and electromagnetic instabilities associated with electrostatic shocks: Two-dimensional particle-in-cell simulation. *Physics of Plasmas*, 17(3):032114–032114, March 2010. doi: 10.1063/1.3372138.

Jacek Niemiec, Martin Pohl, Antoine Bret, and Volkmar Wieland. Nonrelativistic Parallel Shocks in Unmagnetized and Weakly Magnetized Plasmas. ApJ, 759(1):73, November 2012. doi: 10.1088/0004-637X/759/1/73.

Volkmar Wieland, Martin Pohl, Jacek Niemiec, Iman Rafighi, and Ken-Ichi Nishikawa. Nonrelativistic Perpendicular Shocks Modeling Young Supernova Remnants: Nonstationary Dynamics and Particle Acceleration at Forward and Reverse Shocks. ApJ, 820(1):62, March 2016. doi: 10.3847/0004-637X/820/1/62.

Lorenzo Sironi and Anatoly Spitkovsky. Particle Acceleration in Relativistic Magnetized Collisionless Pair Shocks: Dependence of Shock Acceleration on Magnetic Obliquity. *The Astrophysical Journal*, 698(2):1523–1549, jun 2009. doi: 10.1088/0004-637x/698/2/1523. URL `https://doi.org/10.1088/0004-637x/698/2/1523`.

L. Sironi, U. Keshet, and M. Lemoine. Relativistic Shocks: Particle Acceleration and Magnetization. Space Sci. Rev., 191(1-4):519–544, October 2015. doi: 10.1007/s11214-015-0181-8.

Artem Bohdan, Jacek Niemiec, Martin Pohl, Yosuke Matsumoto, Takanobu Amano, and Masahiro Hoshino. Kinetic simulations of nonrelativistic perpendicular shocks of young supernova remnants. i. electron shock-surfing acceleration. 4 2019b. doi: 10.3847/1538-4357/ab1b6d. URL `http://arxiv.org/abs/1904.13153http://dx.doi.org/10.3847/1538-4357/ab1b6d`.

Yasunobu Uchiyama, Felix A. Aharonian, Takaaki Tanaka, Tadayuki Takahashi, and Yoshitomo Maeda. Extremely fast acceleration of cosmic rays in a supernova remnant. Nature, 449(7162):576–578, October 2007. doi: 10.1038/nature06210.

M. Hoeft and M. Brüggen. Radio signature of cosmological structure formation shocks. MNRAS, 375: 77–91, February 2007. doi: 10.1111/j.1365-2966.2006.11111.x.

F. Vazza, C. Ferrari, M. Brüggen, A. Bonafede, C. Gheller, and P. Wang. Forecasts for the detection of the magnetised cosmic web from cosmological simulations. A&A, 580:A119, August 2015. doi: 10.1051/0004-6361/201526228.

Oliver Hahn, Cristiano Porciani, C. Marcella Carollo, and Avishai Dekel. Properties of dark matter haloes in clusters, filaments, sheets and voids. MNRAS, 375(2):489–499, February 2007. doi: 10.1111/j.1365-2966.2006.11318.x.

Oliver Hahn, Romain Teyssier, and C. Marcella Carollo. The large-scale orientations of disc galaxies. MNRAS, 405(1):274–290, June 2010. doi: 10.1111/j.1365-2966.2010.16494.x.

Noam I. Libeskind, Yehuda Hoffman, Jaime Forero-Romero, Stefan Gottlöber, Alexander Knebe, Matthias Steinmetz, and Anatoly Klypin. The velocity shear tensor: tracer of halo alignment. MNRAS, 428(3):2489–2499, January 2013. doi: 10.1093/mnras/sts216.

Holly E. Trowland, Geraint F. Lewis, and Joss Bland-Hawthorn. The Cosmic History of the Spin of Dark Matter Halos within the Large-scale Structure. ApJ, 762(2):72, January 2013. doi: 10.1088/0004-637X/762/2/72.

Y. Dubois, C. Pichon, C. Welker, D. Le Borgne, J. Devriendt, C. Laigle, S. Codis, D. Pogosyan, S. Arnouts, K. Benabed, E. Bertin, J. Blaizot, F. Bouchet, J. F. Cardoso, S. Colombi, V. de Lapparent, V. Desjacques, R. Gavazzi, S. Kassin, T. Kimm, H. McCracken, B. Milliard, S. Peirani, S. Prunet, S. Rouberol, J. Silk, A. Slyz, T. Sousbie, R. Teyssier, L. Tresse, M. Treyer, D. Vibert, and M. Volonteri. Dancing in the dark: galactic properties trace spin swings along the cosmic web. MNRAS, 444(2): 1453–1468, October 2014. doi: 10.1093/mnras/stu1227.

Jaime E. Forero-Romero, Sergio Contreras, and Nelson Padilla. Cosmic web alignments with the shape, angular momentum and peculiar velocities of dark matter haloes. MNRAS, 443(2):1090–1102, September 2014. doi: 10.1093/mnras/stu1150.

Peng Wang and Xi Kang. A general explanation on the correlation of dark matter halo spin with the large-scale environment. MNRAS, 468(1):L123–L127, June 2017. doi: 10.1093/mnrasl/slx038.

Punyakoti Ganeshaiah Veena, Marius Cautun, Rien van de Weygaert, Elmo Tempel, Bernard J. T. Jones, Steven Rieder, and Carlos S. Frenk. The Cosmic Ballet: spin and shape alignments of haloes in the cosmic web. MNRAS, 481(1):414–438, November 2018. doi: 10.1093/mnras/sty2270.

Punyakoti Ganeshaiah Veena, Marius Cautun, Elmo Tempel, Rien van de Weygaert, and Carlos S. Frenk. The Cosmic Ballet II: spin alignment of galaxies and haloes with large-scale filaments in the EAGLE simulation. MNRAS, 487(2):1607–1625, August 2019. doi: 10.1093/mnras/stz1343.

Punyakoti Ganeshaiah Veena, Marius Cautun, Rien van de Weygaert, Elmo Tempel, and Carlos S. Frenk. Cosmic Ballet III: Halo spin evolution in the cosmic web. MNRAS, 503(2):2280–2299, May 2021. doi: 10.1093/mnras/stab411.

C. Welker, J. Devriendt, Y. Dubois, C. Pichon, and S. Peirani. Mergers drive spin swings along the cosmic web. MNRAS, 445:L46–L50, November 2014. doi: 10.1093/mnrasl/slu106.

Philip E. Bett and Carlos S. Frenk. Spin flips - I. Evolution of the angular momentum orientation of Milky Way-mass dark matter haloes. MNRAS, 420(4):3324–3333, March 2012. doi: 10.1111/j.1365-2966. 2011.20275.x.

Philip E. Bett and Carlos S. Frenk. Spin flips - II. Evolution of dark matter halo spin orientation, and its correlation with major mergers. MNRAS, 461(2):1338–1355, September 2016. doi: 10.1093/mnras/ stw1395.

X. Hernandez and B. Cervantes-Sodi. A dimensional study of disc galaxies. MNRAS, 368(1):351–360, May 2006. doi: 10.1111/j.1365-2966.2006.10115.x.

E. Tempel, R. S. Stoica, and E. Saar. Evidence for spin alignment of spiral and elliptical/S0 galaxies in filaments. MNRAS, 428(2):1827–1836, January 2013. doi: 10.1093/mnras/sts162.

B. Cervantes-Sodi, X. Hernandez, and Changbom Park. Clues on the origin of galactic angular momentum from looking at galaxy pairs. MNRAS, 402(3):1807–1815, March 2010. doi: 10.1111/j.1365-2966. 2009.16001.x.

Elmo Tempel and Noam I. Libeskind. Galaxy Spin Alignment in Filaments and Sheets: Observational Evidence. ApJ, 775(2):L42, October 2013. doi: 10.1088/2041-8205/775/2/L42.

Youcai Zhang, Xiaohu Yang, Huiyuan Wang, Lei Wang, H. J. Mo, and Frank C. van den Bosch. Alignments of Galaxies within Cosmic Filaments from SDSS DR7. ApJ, 779(2):160, December 2013. doi: 10.1088/0004-637X/779/2/160.

Isha Pahwa, Noam I. Libeskind, Elmo Tempel, Yehuda Hoffman, R. Brent Tully, Hélène M. Courtois, Stefan Gottlöber, Matthias Steinmetz, and Jenny G. Sorce. The alignment of galaxy spin with the shear field in observations. MNRAS, 457(1):695–703, March 2016. doi: 10.1093/mnras/stv2930.

A. Hirv, J. Pelt, E. Saar, E. Tago, A. Tamm, E. Tempel, and M. Einasto. Alignment of galaxies relative to their local environment in SDSS-DR8. A&A, 599:A31, March 2017. doi: 10.1051/0004-6361/ 201629248.

Kandaswamy Subramanian. The origin, evolution and signatures of primordial magnetic fields. *Reports on Progress in Physics*, 79(7):076901, July 2016. doi: 10.1088/0034-4885/79/7/076901.

R. de Regt, S. Apunevych, C. von Ferber, Yu Holovatch, and B. Novosyadlyj. Network analysis of the COSMOS galaxy field. MNRAS, 477(4):4738–4748, Jul 2018. doi: 10.1093/mnras/sty801.

F. Vazza and A. Feletti. The quantitative comparison between the neuronal network and the cosmic web. *Frontiers in Physics*, 8:491, November 2020. doi: 10.3389/fphy.2020.525731.

C. Gheller and F. Vazza. Multiwavelength cross-correlation analysis of the simulated cosmic web. MNRAS, 494(4):5603–5618, April 2020. doi: 10.1093/mnras/staa1032.

G. R. Blumenthal, S. M. Faber, R. Flores, and J. R. Primack. Contraction of Dark Matter Galactic Halos Due to Baryonic Infall. ApJ, 301:27, February 1986. doi: 10.1086/163867.

Philip Bett, Vincent Eke, Carlos S. Frenk, Adrian Jenkins, John Helly, and Julio Navarro. The spin and shape of dark matter haloes in the Millennium simulation of a Λ cold dark matter universe. MNRAS, 376(1):215–232, March 2007. doi: 10.1111/j.1365-2966.2007.11432.x.

S. E. Bryan, S. T. Kay, A. R. Duffy, J. Schaye, C. Dalla Vecchia, and C. M. Booth. The impact of baryons on the spins and shapes of dark matter haloes. MNRAS, 429(4):3316–3329, March 2013. doi: 10.1093/mnras/sts587.

Jörg M. Colberg, K. Simon Krughoff, and Andrew J. Connolly. Intercluster filaments in a ΛCDM Universe. MNRAS, 359(1):272–282, May 2005. doi: 10.1111/j.1365-2966.2005.08897.x.

T. Vernstrom, B. M. Gaensler, S. Brown, E. Lenc, and R. P. Norris. Low-frequency radio constraints on the synchrotron cosmic web. MNRAS, 467(4):4914–4936, June 2017. doi: 10.1093/mnras/stx424.

Takuya Akahori, Hiroyuki Nakanishi, Yoshiaki Sofue, Yutaka Fujita, Kiyotomo Ichiki, Shinsuke Ideguchi, Osamu Kameya, Takahiro Kudoh, Yuki Kudoh, Mami Machida, Yoshimitsu Miyashita, Hiroshi Ohno, Takeaki Ozawa, Keitaro Takahashi, Motokazu Takizawa, and Dai G. Yamazaki. Cosmic magnetism in centimeter- and meter-wavelength radio astronomy. PASJ, 70(1):R2, January 2018. doi: 10.1093/pasj/psx123.

C. L. Carilli and G. B. Taylor. Cluster Magnetic Fields. ARA&A, 40:319–348, January 2002b. doi: 10.1146/annurev.astro.40.060401.093852.

S. P. O'Sullivan, J. Machalski, C. L. Van Eck, G. Heald, M. Brüggen, J. P. U. Fynbo, K. E. Heintz, M. A. Lara-Lopez, V. Vacca, M. J. Hardcastle, T. W. Shimwell, C. Tasse, F. Vazza, H. Andernach, M. Birkinshaw, M. Haverkorn, C. Horellou, W. L. Williams, J. J. Harwood, G. Brunetti, J. M. Anderson, S. A. Mao, B. Nikiel-Wroczyński, K. Takahashi, E. Carretti, T. Vernstrom, R. J. van Weeren, E. Orrú, L. K. Morabito, and J. R. Callingham. The intergalactic magnetic field probed by a giant radio galaxy. A&A, 622:A16, February 2019. doi: 10.1051/0004-6361/201833832.

Hideki Tanimura, Gary Hinshaw, Ian G. McCarthy, Ludovic Van Waerbeke, Nabila Aghanim, Yin-Zhe Ma, Alexander Mead, Alireza Hojjati, and Tilman Tröster. A search for warm/hot gas filaments between pairs of SDSS Luminous Red Galaxies. MNRAS, 483(1):223–234, February 2019b. doi: 10.1093/mnras/sty3118.

F. Govoni, E. Orrù, A. Bonafede, M. Iacobelli, R. Paladino, F. Vazza, M. Murgia, V. Vacca, G. Giovannini, and L. Feretti. A radio ridge connecting two galaxy clusters in a filament of the cosmic web. *Science*, 364(6444):981–984, Jun 2019. doi: 10.1126/science.aat7500.

A. Bonafede, F. Vazza, M. Brüggen, M. Murgia, F. Govoni, L. Feretti, G. Giovannini, and G. Ogrean. Measurements and simulation of Faraday rotation across the Coma radio relic. MNRAS, 433(4): 3208–3226, August 2013. doi: 10.1093/mnras/stt960.

Nicola Locatelli, Franco Vazza, and Paola Domínguez-Fernández. The Challenge of Detecting Intracluster Filaments with Faraday Rotation. *Galaxies*, 6(4):128, November 2018. doi: 10.3390/galaxies6040128.

Marius Cautun, Rien van de Weygaert, and Bernard J. T. Jones. NEXUS: tracing the cosmic web connection. MNRAS, 429(2):1286–1308, February 2013. doi: 10.1093/mnras/sts416.

Takuya Akahori, Dongsu Ryu, and B. M. Gaensler. Fast Radio Bursts as Probes of Magnetic Fields in the Intergalactic Medium. ApJ, 824(2):105, June 2016. doi: 10.3847/0004-637X/824/2/105.

F. Vazza, M. Brüggen, P. M. Hinz, D. Wittor, N. Locatelli, and C. Gheller. Probing the origin of extragalactic magnetic fields with Fast Radio Bursts. MNRAS, 480:3907–3915, November 2018b. doi: 10.1093/mnras/sty1968.

S. Hackstein, M. Brüggen, F. Vazza, and L. F. S. Rodrigues. Redshift estimates for fast radio bursts and implications on intergalactic magnetic fields. MNRAS, 498(4):4811–4829, August 2020. doi: 10.1093/mnras/staa2572.